N° d'ordre: 2089

THÈSE

présentée pour obtenir le titre de

DOCTEUR DE L'INSTITUT NATIONAL POLYTECHNIQUE DE TOULOUSE

Spécialité: Dynamique des Fluides

par

André Kaufmann

VERS LA SIMULATION DES GRANDES ECHELLES EN FORMULATION EULER-EULER DES ECOULEMENTS REACTIFS DIPHASIQUES

soutenue le 23 mars 2004 devant le jury composé de:

Professeur J.P. Bertoglio	Président
Professeur K. Squires	Rapporteur
Professeur L. Vervisch	Rapporteur
Dr. B. Nkonga	Examinateur
Professeur O. Simonin	Examinateur
Dr. B. Cuenot	Directeur de thèse

Réf. CERFACS TH/CFD/04/11

PhD THESIS

André Kaufmann

TOWARDS EULERIAN-EULERIAN LARGE EDDY SIMULATION OF REACTIVE TWO-PHASE FLOWS

defended 23rd of march 2004

Professor J.P. Bertoglio	President
Professor K. Squires	Referee
Professor L. Vervisch	Referee
Dr. B. Nkonga	
Professor O. Simonin	
Dr. B. Cuenot	Thesis director

Réf. CERFACS TH/CFD/04/11

Ce travail de thèse a été réalisé au sein de l'équipe Computational Fluid Dynamics du CERFACS.
Mes remerciements vont en premier lieu à Madame Bénédicte Cuenot, Monsieur Olivier Simonin et Monsieur Thierry Poinsot, qui m'ont initié à la combustion, aux instabilités thermo-acoustiques et au diphasique. Ils m'ont permis d'apprendre dans une atmosphère agréable et m'ont poussé à découvrir de nouveaux domaines sans tenir compte de mes dérives à certains moments de ma thèse.
J'adresse toute ma reconnaissance à Messieurs Kyle Squires et Luc Vervisch pour avoir accepté d'être rapporteurs et pour l'intérêt qu'ils ont su manifester pour ce travail de thèse. Cette reconnaissance s'adresse également à Monsieur Jean-Pierre Bertoglio, président de ce jury de thèse, et à Messieurs Boniface N'Konga et Olivier Simonin, examinateurs, qui, par leurs questions, ont su mettre en évidence les points essentiels de mon travail de thèse.
Je remercie toute l'équipe CFD pour son soutien, spécialement Madame Marie Labadens qui m'a rendu la vie agréable en s'occupant des tâches administratives, et toute l'équipe CSG qui m'a facilité les calculs.
Je remercie aussi ceux qui, dans des discussions parfois longues, au tableau m'ont aidé à éclaircir le contenu de certaines équations et de comprendre les phénomenes physiques.

Abstract

Particle laden flows occur in industrial applications ranging from droplets in gas turbines to fluidized bed in chemical industry. Prediction of the dispersed phase properties such as concentration and dynamics are crucial for the design of more efficient devices that meet the new pollutant regulations of the European community.

Numerical simulation coupling Lagrangian tracking of discrete particles with DNS or LES of the carrier phase provide a well established powerful tool to investigate particle laden flows. Such numerical methods have the drawback of being numerically very expensive for practical applications. Numerical simulations based on separate Eulerian balance equations for both phases, coupled through inter-phase exchange terms might be an effective alternative approach.

This approach has been validated for the case of tracer particles with very low inertia that follow the carrier phase almost instantaneously due to their small response time compared with the microscale time scales of the carrier phase.

Objective of this thesis is to extend this approach to more inertial particles that occur in practical applications such as fuel droplets in gas turbine combustors. Existing results suggest a separation of the dispersed phase velocity into a correlated and an uncorrelated component. The energy related to the uncorrelated component is about 30% of the total particle kinetic energy when the particle relaxation time is comparable to the Lagrangian integral time scale. The presence of this uncorrelated motion leads to stress terms in the Eulerian balance equation for the particle momentum. Models for this stress terms are proposed and tested. Numerical simulations in the Eulerian framework are validated by comparison with simulations using Lagrangian particle tracking. Additionally coupling of the Eulerian transport equations for the particles to combustion models is tested.

Resumé

De nombreuses applications industrielles mettent en jeu des écoulements gaz-particules. On peut citer, entre autres, les turbines aéronautiques et les réacteurs à lit fluidisé de l'industrie chimique. Dès lors, l'amélioration de ces dispositifs, imposée par les nouvelles normes européennes sur les émissions polluantes, nécessite une connaissance prédictive de la dynamique de ce type d'écoulements ainsi que l'évaluation de ses grandeurs caractéristiques telles que la ségrégation spatiale des particules.

La simulation numérique est aujourd'hui largement utilisée à cet effet. Les équations de la phase gazeuse sont résolues par Simulation Numérique Directe (SND) ou par Simulation des Grandes Echelles (SGE). Le couplage avec la phase dispersée peut être envisagé de deux manières. Une première approche, dite lagrangienne, consiste à calculer les trajectoires des particules. Communément utilisée et précise, son coût numérique ne permet cependant pas d'envisager son application à des géométries complexes réalistes. Une seconde approche est fondée sur un formalisme eulérien du mouvement des particules, le couplage entre les deux phases est alors assuré par des termes d'échange interfacial.

Cette méthode a d'ores et déjà été validée pour des particules dont le temps de réponse est faible comparé à la micro-échelle de temps turbulent. L'extension de cette approche à des particules plus inertielles s'avère nécessaire dans les applications industrielles de

type turbines à gaz. Ceci constitue l'objectif principal de cette thèse. Les résultats fournis par l'approche lagrangienne suggèrent de décomposer la vitesse des particules en une composante corrélée et une composante décorrélée. En outre, il apparaît que l'énergie décorrélée sélève à 30% de l'énergie totale de la phase dispersée lorsque le temps de relaxation des particules et l'échelle de temps lagrangienne sont du même ordre. La prise en compte de ce mouvement décorrélé requiert l'introduction d'un tenseur de contraintes dans l'équation de quantité de mouvement. Ce travail propose différents modèles qui sont validés au travers de simulations numériques eulériennes par comparaison avec des SND lagrangiennes. Enfin, une étude du couplage entre les équations de transport des particules et des modèles de combustion est proposée.

Lapin leijonaani vartem

Contents

Introduction

Das schönste Glück des denkenden Menschen ist, das Erforschliche erforscht zu haben und das Unerforschliche zu verehren.
Goethe

Reactive two-phase flows occur in a wide span of domestic and industrial applications: Most terrestrial or airborne vehicles rely on internal combustion engines or gas turbines, since the specific energy of liquid fuels exceed most other forms of fuels, in which energy is stocked in chemical form. A very large amount of todays electrical power is obtained by burning liquid fuels or other (Hydro)Carbon fuels. Domestic applications are typically warm water or heating boilers. Black liquor combustion in paper industry is another example for industrial use of reactive two phase flow. Spatial vehicles use powder boosters and/or liquid oxygen-hydrogen rockets to overcome the gravitational force of the earth.

The extensive use of fossil energy begins to make an impact on todays environment. CO_2 emission modifies the climate on the long term. Even on short terms, the non-flight-days after tragic September 11, 2001 showed that aircraft contrails can trigger cloud formation under certain atmospheric conditions [71] and therefore alter daily weather.

In every days life the impact of fossil energy shows in pollutant formation due to car emissions along intensively used roads leading to formation of nitric oxides and ozone for instance. This has led to the study of atmospheric pollution. Predicting pollutant concentrations in urban areas can then be used to reduce human pollutant exposure.

Trying to reduce pollutant formation, new technologies have come up in gas turbine combustors. These technologies use for example lean premixed pre-vaporized injectors to inject, vaporize and mix kerosene with air. Unfortunately such technologies often lead to combustion instabilities.

Recent changes in legislation impose strict regulations concerning pollutant emission of airborne and terrestal combustion devices. Current technologies do not fulfill all of the above regulations. Therefore the design of future combustion devices needs to be revised. Knowledge on the detailed physical phenomena occurring in the combustion system allow altered and new design. The necessary knowledge can mostly be obtained by experimental measurement. In some cases however the environment is rather hostile and typical measurement devices such as hot wire probes can not be used. Then comparably expensive experimental methods, often using Laser techniques, need to be introduced to measure the physical properties in the combustion system. Numerical simulation offers an additional

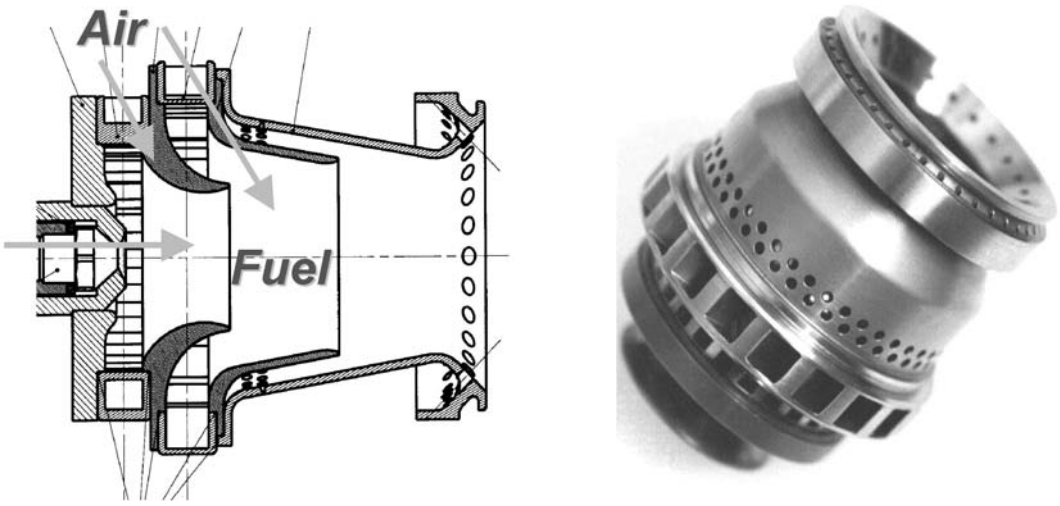

Figure 1: Sketch and image of a lean premixed pre-vaporized (LPP) injector.

tool for the understanding of physical phenomena. Unfortunately today most numerical simulations do not yet have predictive character in combustion devices and research in this field is necessary.

Most industrial and domestic applications use turbulent combustion to produce the desired thermal power. Therefore the study of pollutant formation goes hand in hand with research on turbulent combustion. When non-gaseous fuels are used this adds to the complexity of two-phase flow. The study of turbulent flows has a long history and in the last 30 years of the last century computers have become an increasingly powerful tool in the research of turbulence. The study of turbulent combustion has developed with the use of internal combustion engines and gas turbines. Research has been intense especially for airborne devices, that have very strict safety requirements such as altitude re-ignition capabilities. Research on two-phase flow has concentrated on applications such as fluidized beds, which is the workhorse of chemical procedures and an increasingly interesting way to burn low quality coal or domestic waste.

Therefore reactive two-phase flows combine the difficulties of turbulence, combustion and multi-phase flow. Many of the physical phenomena occurring in reactive two phase flow have been studied independently and put together in complex models. The interaction of such physical phenomena (for example turbulent flow around a droplet and evaporation of the droplet) have been formulated by semi-empirical correlation laws. For many such semi-empirical correlations the validity range is not clear and sometimes even the correlation is doubtful.

Numeric simulation allows to study many of the complicated phenomena in detail, such as the modification of drag by the presence of neighboring particles [60]. However, it is

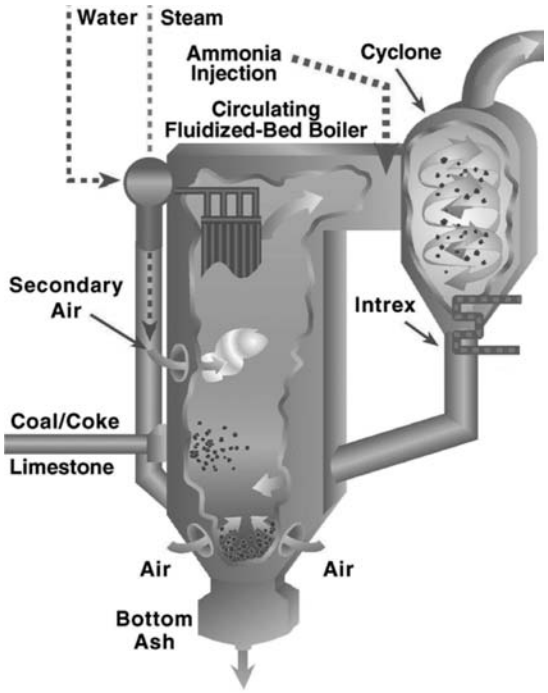

Figure 2: Sketch of a fluidized bed application.

still impossible to calculate with nowadays computing power the exact flow around several million droplets in an air-blast injector of a gas turbine. It is therefore still necessary to model this interaction, so that the properties of the two-phase flows in such a device can be estimated. When the flow is dilute, one possibility is to assume that the particles occupy a small volume compared to the carrier phase and to make a point force approximation. Numerical computations of dispersed two-phase flow can be divided roughly in two methods: Lagrangian particle tracking and Eulerian methods. When using Lagrangian Particle tracking, point forces on an inclusion with or without interaction with the carrier phase are usually assumed. In such a simulation the carrier phase is typically simulated using the Navier-Stokes equations. The interaction forces are computed from the local flow field. Since the location of the discrete particle does not necessarily coincide with the numerical grid of the carrier phase, the flow field at the particle location is obtained by interpolation methods. The other method consists of one of the diverse Eulerian methods that rely on averaging procedures such as volume or ensemble averaging to obtain continuous fields.
Lagrangian particle tracking is a rather intuitive tool and has been used extensively to obtain many interesting results on two-phase flows. Still such methods have the drawback of being numerically expensive when dealing with realistic particle numbers in industrial devices. One possibility to overcome this is to track numerical particles that represent a certain number of physical particles. In a strict mathematical sense this comes down to

calculating the Lagrangian probability density function.
Eulerian methods capture only averaged quantities. The information on the individual particle path and status is lost in the averaging procedure. In industrial applications mean values sometimes already provide valuable information and the status of the individual particle is unimportant. On the other hand Eulerian methods have the advantage of being numerically well understood from the viewpoint of single-phase flows. This is especially true for parallel methods on supercomputers.
Large Eddy Simulations (LES) have emerged into the domain of turbulent combustion and shown their potential through various comparison with experimental measurements. Therefore the question arises, whether Eulerian two-phase flow Large Eddy Simulation can be developed and used for predicting the features and pollutant behavior of reactive two-phase flow. Such methods do exist for Reynolds Averaged Navier- Stokes (RANS) and give promising results [41][111].
Extension of the Reynolds averaged models to unsteady Large Eddy Simulations are however not trivial since a number of length and time scales averaged and modeled in Reynolds averaged computations must be resolved in Large Eddy Simulations. Reynolds averaged equations for two-phase flows are typically obtained by volume filtering or by ensemble average. When deriving the Eulerian equations that are supposed to resolve some important time and length scales special attention has to be taken to derive the appropriate models. A brief sketch of the conservation equations is given in the first chapter. The Eulerian models previously developed by Simonin [110] or Drew [24] are typically of steady character. Modeling assumption for such RANS type Eulerian equations for two phase flows have been validated using Lagrangian particle tracking in forced, statistically stationary turbulence [22][52][32] [92]. This has lead to many interesting results such as the identification of an uncorrelated component of the particle velocity that can be isolated from the total velocity and plays an important role in the Eulerian equations.
In order to avoid conceptual difficulties and to study nevertheless the feasibility of the Eulerian approach, some drastic restrictions and assumptions have been made deriving the equations for the discussed test cases. For reactive two-phase flows some essential basic test cases have been identified. The contents of the thesis can be summarized by the following points:

- The first chapter presents the equations of particle motion in a carrier fluid. The Lagrangian particle tracking method is described very briefly. Two methods for the derivation of a set of Eulerian equations for the dispersed phase are presented: ensemble averaging and volume filtering.

- An important validation step is to check if and to what extent the dynamics and the dispersion of the dispersed phase are represented by an Eulerian-Eulerian description. An essential test case for particle dynamics is the particle laden isotropic turbulence (no combustion). This test case has been studied in three ways: First a simulation of Lagrangian particle tracking (performed by J. Helie,IMFT,Toulouse) with a large number of particles has been volume filtered and post-processed in an

Eulerian framework. Then the ensemble averaged equations are investigated. The Eulerian framework introduces a stress term that needs to be closed. In this part special attention is attributed to the modeling of this stress tensor. The closed equations are then used to predict independently the properties of the dispersed phase. In a third step the Lagrangian and Eulerian results obtained are compared. This serves to evaluate the quality of the Eulerian predictions in terms of particle dispersion and segregation.

- A central question for LES of two-phase flow combustion is the coupling of two phase flow models with combustion models. This is a major difficulty for Lagrange approaches which require large numbers of particles to produce smooth fuel mass fractions and reaction fields. On the other hand, Eulerian approaches should be better suited to reactive cases because they produces continuous fields of all flow parameters. This point is verified in Chapter 6 by computing a laminar one-dimensional two phase flame. This test case gathers enough phenomena to study the interaction behavior of models proper to reactive flows such as the Arrhenius law for heat production and species production/consumption and the models proper to two-phase flows such as drag and evaporation (Bendaklia [18], Versavel [108] and Gutheil [39]).

- The one dimensional flame is usually computed on a mesh that resolves the important length scales. Going to Large Eddy Simulation, the resolved meshes are usually by far too coarse to resolve the length scales of the (turbulent) flames and a turbulent combustion model is needed. It is therefore interesting to study how a turbulent combustion model can be married to a turbulent combustion model such as the thickened flame model [17]. This is done in the second part of Chapter 6.

Those basic test cases (Homogeneous Turbulence and 1d flame) are studied within this thesis. Whereas those test cases do not guarantee the success of complex two-phase-flow simulations in realistic geometries, they provide a fundamental study of the feasibility of this particular approach. Many difficult subjects related to the Eulerian description of two-phase-flows such as polydispersed particle laden flow, particle collisions, coalescence and boundary conditions, to give only some examples, have not been addressed and ensure interesting research for years to come.

Introduction

Les écoulements diphasiques réactifs apparaissent dans une large gamme d'applications domestiques et industrielles. Ils sont présents dans la vie quotidienne, que ce soit dans des appareils domestiques courants tels que les chauffe-eaux ou les systèmes de chauffage, ou dans les moyens de transport, les véhicules terrestres comme les avions, propulsés par des moteurs a piston ou des turbines.

Les écoulements diphasiques réactifs sont également très présents dans l'industrie du secteur énergétique, comme la production d'électricité en grande partie obtenue par combustion des hydrocarbures, mais aussi dans d'autres secteurs comme la chimie, l'industrie du papier (combustion du "black liquor") ou le spatial (propulsion des véhicule spatiaux)

En fait la grande majorité des systèmes de production d'énergie est basée sur la combustion de combustible liquide. Ce choix est dicté par la facilité de stockage de l'énergie sous forme chimique dans un combustible liquide, qui dépasse la densité énergétique de la plupart des autres moyens de stockage chimique.
Cependant il est maintenant avéré que l'utilisation massive des énergies fossiles change notre environement (citer le rapport IPCC). Les émissions d'oxydes de carbone et d'oxydes d'azote sont non seulement dangereuses pour la santé mais elles changent aussi l'évolution de notre climat au travers de processus complexes. On peut citer par exemple l'impact des traînées de condensation derrière les avions qui, dans certaines situations météorologiques, peuvent déclencher la formation de nuages "artificiels" [71]. Ces nuages ont alors un impact sur le bilan radiatif de l'atmosphère, conduisant à une augmentation de la température nocturne et une baisse de la température diurne. Une observation directe de cet effet a été possible pendant les jours sans vols après le 11 septembre 2001 aux Etats-Unis.

Dans la vie de tous les jours l'impact de l'utilisation de l'énergie fossile se manifeste par la formation de polluants tels que l'oxyde d'azote ou l'ozone sur les axes routiers et les zones industrielles. La pollution atmosphérique locale est devenue une vraie préoccupation de santé publique. De nombreuses études ont vu le jour pour tenter de prédire les niveaux de concentration de polluants dans les zones urbaines et minimiser l'exposition de la population. Ces études ont également abouti à la mise en place de réglementations nationales ou européennes sévères sur lémission de polluants.

Dans le but de réduire la formation des polluants à la source de nouvelles technologies ont donc vu jour dans la communauté des turbines à gaz. C'est par exemple le cas du système d'injection LPP (Lean Premixed Prevaporized) qui maintient le prémélange de gaz frais à un faible niveau de richesse. Malheureusement la combustion en régime pauvre

est souvent très instable et de tels systèmes n'ont pas encore atteint un niveau de fiabilité satisfaisant.
Ainsi les technologies disponibles aujourd'hui ne sont pas capable de suivre les dernières réglementations. Il faut pour cela réviser entièrement la conception des chambres de combustion, en se basant sur une connaissance approfondie de la physique de la combustion turbulente. Une partie de cette connaissance peut être obtenue par l'expérience. Cependant la zone de mesure est souvent exposée à des températures élevées et les techniques de mesures simples comme le fil chaud ne peuvent pas être utilisées. On a alors recours à de nouvelles méthodes de mesure, souvent couteuses car utilisant des techniques laser. La simulation numérique offre une alternative intéressante et complémentaire pour la compréhension des phénomènes complexes. Cet outil a déjà fait la preuve de son efficacité et de son potentiel. Cependant la simulation numérique n'a pas encore atteint un caractère predictif dans certaines domaines et de nouveaux développements sont encore nécessaires.

Toutes les applications domestiques et industrielles évoquées précédemment utilisent la combustion turbulente pour obtenir l'énergie thermique désirée, et la formation de polluants en est une conséquence. Il est donc nécessaire de développer des outils pour l'étude de la combustion turbulente. Si les carburants sont liquides, il faut y ajouter la complexité des écoulements diphasiques.
L'étude des écoulements turbulents a évolué dans les trente dernières années grâce à l'utilisation des ordinateurs. D'abord centrée sur les turbines aéronautiques qui sont soumises à des contraintes sévères comme la réallumage en altitude, la recherche en combustion turbulente s'est ensuite développée avec les moteurs à piston et les turbines à gaz. Concernant les écoulements diphasiques, de nombreux travaux ont été menés pour les applications de l'industrie chimique (lits fluidisés). Si ces applications peuvent avoir un intérêt direct pour le secteur énergétique (combustion de déchets ou de charbons de mauvaise qualité en lits fluidisés dans les centrales thermiques), le contexte des turbines nécessite des études spécifiques.
Enfin, il existe très peu d'études sur la combustion turbulente diphasique, qui implique deux domaines jusqu'à présent séparés. Le couplage des phénomènes physiques et l'interaction des modèles sont encore un point obscur.
La simulation numérique permets d'étudier beaucoup des phénomenes precisement. Une example est la modification de la trainée par la presence des particules voisines [60]. Neamoins il est aujourd'hui impossible de calculer avec la puissance actuelle des ordinateurs l'écoulement proche autour des quelques millions de gouttelettes qui apparaissent par exemple dans un injecteur de turbine à gaz. Il est donc toujours nécessaire de modéliser la zone proche de la goutte pour que l'écoulement plus lointain résultant puisse être simulé. Globalement on peut distinguer alors deux classes de simulations. La première est le suivi lagrangien des particules, où on fait une hypothèse de point force pour une inclusion avec ou sans interaction avec le fluide voisin. Comme la particule n'est pas forcement localisé sur un noed du maillage de la phase porteuse, une interpolation du champ de vitesse sur l'endroit de la particule est souvent utilisé. La deuxième méthode est une méthode eulérienne, qui utilise une moyenne d'ensemble ou un filtrage en volume pour obtenir des champs continus.

La méthode du suivi Lagrangien est un outil plutôt intuitif et a permis détablir de nombreux résultats intéressants sur les écoulements diphasiques. Cette méthode a néanmoins l'inconvénient d'être numériquement cher quand il s'agit du transport d'un nombre réaliste de particules dans une application industrielle. Une possibilité pour contourner ce désavantage est de grouper les particules en paquets, tels que un paquet, traité comme une particule, représente un certain nombre de particules réelles. D'un point de vue strictement mathématique, cela revient à transporter une densité de probabilité lagrangienne.
La méthode Eulérienne ne capte que des grandeurs moyennes. L'information sur la trajectoire individuelle et le statut d'une seule particule est perdue dans la prodédure de moyenne. Pour les applications industrielles les valeurs moyennes sont souvent déjà une information intéressante et le statut de la particule individuelle a peu d'importance. D'un autre côté, la méthode Eulérienne a l'avantage d'être bien comprise pour les écoulements monophasiques. Ceci est particulièrement vrai concernant l'application des méthodes de calcul parallèle.
La simulation aux grandes échelles (SGE, ou LES) est récemment entrée dans le domaine de la combustion numérique et commence à montrer son potentiel face aux comparaisons avec les études expérimentales. Ceci amène a la question de l'appliation de la SGE aux écoulements diphasiques réactifs. De telles extensions ont déjà été faites pour les méthodes numériques qui prédisent les écoulements stationnaires moyennés (type moyenne de Reynolds, RANS) [111][41].
L'extension des méthodes pour les écoulements stationnaires aux simulations des grandes échelles n'est pas immédiate car de nouvelles échelles de longeur et de temps apparaissent dans ces dernières, qui sont modélisées dans les simulations stationnaires. Les grandeurs moyennes de type RANS sont obtenues par une moyenne temporelle. Dans la dérivation des modèles pour la simulation aux grandes échelles les variations spatiales et temporelles des différentes grandeurs sont calculées. Deux dérivations possibles sont évoquées dans le premier chapitre.
Les modèles Euleriennes jusque à present par Simonin [110] ou Drew [24] sont plutôt d'un charactere stationaire. Les hypotheses de modélisation pour les equations Euleriennes de type RANS pour les écoulements diphasiques ont étè validé en utilisant des methodes de suivi Lagrangien dans la turbulence stationaire forcé [22][52][32]. Ceci a amene une large gamme de resultats interessants. Une example est la identification de la partie non-correlée de la vitesse des particules qui joue une role importante dans les equations Euleriennes. Dans le but d'éviter des difficultés conceptuelles et pour être néanmoins capable de faire une étude de faisabilité d'une approche Eulérienne, des restrictions sévères ont été faites pour la dérivation des équations et des cas tests. Pour les écoulements turbulents réactifs quelques cas tests principaux ont été identifiés.

- Le premier chapitre place l'étude dans le contexte des particules suspendues dans une phase porteuse. La méthode de suivi Lagrangien est résumée. Deux méthodes differentes pour la dérivation des differentes équations Eulériennes sont évoquées: la moyenne d'ensemble et la moyenne en volume. Ils n'amenent pas strictement ou meme ensemble equations de transport pour les quantites physiques.

- Aujourd'hui il n'est pas clair à quel point la dynamique de l'ensemble des particules (la phase dispersée) est bien représentée par une approche Eulérienne. Un cas test essentiel est celui de l'étude de la dynamique des particules dans une turbulence homogène isotrope sans combustion. Ce cas test est étudié dans ce travail de trois façons. D'abord une simulation avec un suivi lagrangien est moyennée par une opération de filtrage en volume pour obtenir des champs continus. Ces champs continus sont ensuite analysés dans un formalisme Eulérien. Dans une deuxième étape les équations obtenues par une moyenne d'ensemble sont utilisées dans les simulations Eulériennes pour prédire les quantités moyennes. La formulation Eulérienne introduit un nouveau tenseur de contraintes. Une grande partie est consacrée à la modélisation de ce tenseur. Une fois fermées, les équations Eulériennes sont utilisées pour la prédiction des quantités moyennes qui sont ensuite comparées aux résultats Eulériens.

- Un cas test instructif est le cas de la flamme laminaire monodimensionelle. Ce cas test rassemble suffisamment de phénomènes physiques pour étudier le comportement et la compabilité des modèles diphasiques avec ceux de la combustion. (Bendaklia [18], Versavel [108] et Gutheil [39]).

- Une flamme laminaire est d'une manière générale simulée sur un maillage suffisamment raffiné pour simuler les échelles de longeur impliquées. Dans la simulation des grandes échelles, ce n'est plus le cas et un modèle de combustion diphasique turbulente est nécessaire. Il est donc intéressant de regarder comment une modèle de combustion turbulente se marie avec le modèle de la flamme épaissie[17]. Ceci est évoqué dans la deuxième partie du dernier chapitre.

Le cas test évoqués précédemment sont étudiés dans cette thèse. Ces cas tests n'assurent pas la qualité d'une simulation diphasique réactive dans une géométrie complexe réaliste d'une application industrielle, mais établissent une étude fondamentale de faisabilité d'une telle approche. De nombreuses difficultés associées aux simulations dans un cadre Eulérien comme les écoulements polydispersés, les collisions et les conditions limites ne sont pas considérées. Ces sujets assurent des sujets de recherche pour les années à venir.

0.1 List of symbols

Symbol	Signification
index	Signification
ζ	surface property of liquid phase
ϕ	phase index (f, g for gaseous phase or l, p for dispersed phase)
f	carrier phase
g	gaseous phase
l	liquid phase
p	dispersed phase
i	space coordinates
j	second space coordinates or summation index for tensors
k	chemical species or summation index for tensors
F	fuel
QB	quasi-brownian
small letter	Signification
d	droplet diameter
e_s	sensible energy
h_s	sensible enthalpy
h_k	sensible enthalpy of species k
$\Delta h_{f,k}$	formation enthalpy of species k
$\breve{n}$	droplet number per unit volume
n_i	normal vector
$nspecies$	total number of species
p	pressure
p_{cc}	Clausius-Clapeyron reference pressure
q_f^2	carrier phase turbulent kinetic energy
q_{fp}	carrier phase dispersed phase velocity correlation
q_p^2	dispersed phase turbulent kinetic energy
q_i	heat flux vector
s_l	laminar flame speed
u_i	velocity vector
$\breve{u}_{p,i}$	mesoscopic velocity vector
δu_i	uncorrelated particle velocity
Capital letter	Signification
A	pre exponential for Arrhenius law
B_m	Spalding mass coefficient
C_d	drag coefficient
C_L	liquid heat capacity
C_p	heat capacity of gas at constant pressure
C_v	heat capacity of gas at constant volume

Symbol	Signification
$C_{p,k}$	heat capacity of species k at constant pressure
$C_{v,k}$	heat capacity of species k at constant volume
C_V	fuel vapor heat capacity
D_{kj}	binary diffusion coefficients
D_k	diffusion coefficient of species k
D_{th}	heat diffusion coefficient
D_Γ	diffusion coefficient used for evaporation
E	total non chemical energy
E_{activ}	activation energy in Arrhenius law
F	thickening factor of thickened flame model
$F_{d,i}$	drag force
G_i	gravity
H	total non chemical Enthalpy
ΔH	latent heat of evaporation
I_i	momentum exchange term
K_j^f	forward rate of reaction j
K_j^b	backward rate of reaction j
L_V	latent heat of evaporation
N	total droplet number
P	pressure
P_ϕ	pressure of phase ϕ in the two fluid model
$\mathcal{Q}_j$	progress rate of reaction j
S_{ij}	Boussinesq tensor $S_{ij} = \left(\frac{\partial u_i}{\partial x_j} + \frac{\partial u_i}{\partial x_j}\right)$
S_{ij}^T	Boussinesq tensor without trace $S_{ij} = \left(\frac{\partial u_i}{\partial x_j} + \frac{\partial u_j}{\partial x_i} - \frac{2}{3}\delta_{ij}\frac{\partial u_k}{\partial x_k}\right)$
$\breve{S}_{ij}$	Mesoscopic Boussinesq tensor $S_{ij} = \left(\frac{\partial \breve{u}_{p,i}}{\partial x_j} + \frac{\partial \breve{u}_{p,i}}{\partial x_j}\right)$
$\breve{S}_{ij}^T$	Mesoscopic Boussinesq tensor without trace $S_{ij} = \left(\frac{\partial \breve{u}_{p,i}}{\partial x_j} + \frac{\partial \breve{u}_{p,j}}{\partial x_i} - \frac{2}{3}\delta_{ij}\frac{\partial \breve{u}_{p,k}}{\partial x_k}\right)$
T	temperature
T_{cc}	Clausius Clapeyron reference temperature
T_f	characteristic time of the gas flow
T_l	droplet (liquid) temperature
$U_{\phi,i}$	velocity of phase ϕ in the two-fluid model
$V_{i,k}$	diffusion velocity vector of species k
V_i^c	correction diffusion velocity vector
$V_{i,r}, \quad V_{rel}$	relative velocity between phases
W_k	molar mass of species k
W_m	mean molar mass
Y_k	mass fraction of species k
Y_F	fuel mass fraction

Symbol	Signification
Y_{O_2}	oxygen mass fraction

small Greek symbols	Signification
α	volume fraction
α_ϕ	volume fraction of phase ϕ
χ_ϕ	characteristic (phase indicator) function
δ_{ij}	Kronecker symbol
δ_l	laminar flame thickness
δ_{th}	thermal flame thickness
ε	turbulent dissipation
ε_{QB}	Quasi Brownian dissipation
γ	compressibility coefficient
λ	heat diffusivity coefficient
λ_Γ	heat diffusivity used for evaporation
μ	dynamic viscosity
ν	kinematic viscosity
ν_{kj}	stoichiometric coefficient of species k in reaction j
ν_{QB}	quasi brownian viscosity
ν_{SGS}	subgrid viscosity
ν_t	turbulent viscosity
$\dot{\omega}_k$	net reaction rate of species k
$\dot{\omega}_{k,j}$	contribution of reaction j to the reaction rate of species k
$\dot{\omega}_T$	heat release
ϕ	equivalence ratio, phase indicator
ϕ_g	gaseous equivalence ratio
ϕ_l	liquid equivalence ratio
ϕ_t	total equivalence ratio
ρ	(gaseous) density
ρ_ϕ	density of phase ϕ in the two fluid model
σ_{ij}	stress tensor $\sigma_{ij} = \tau_{ij} - p\delta_{ij}$
$\breve{\sigma}_{ij}$	mesoscopic stress tensor $\breve{\sigma}_{ij} = \breve{\tau}_{ij} - P_{QB}\delta_{ij}$
τ_{ij}	viscous tensor
$\breve{\tau}_{ij}$	mesoscopic viscous tensor
$\bar{\tau}_{ij}$	(LES) filtered viscous tensor
τ_p	particle relaxation time
τ_c	chemical time scale
τ_t	turbulent time scale
$\delta\theta_p$	quasi brownian energy
ξ	bulk viscosity (second viscosity)
ξ_{SGS}	subgrid bulk viscosity

capital Greek symbols	Signification
Γ	mass exchange due to evaporation

Symbol	Signification
Γ_ϕ	mass exchange of phase ϕ
$\Gamma_{\phi,k}$	mass exchange of phase ϕ and species k
Π	enthalpy exchange terms
Σ	interface area density
Σ_{ij}	stress tensor in the two-fluid model
Φ	heat exchange terms
$\dot{\Omega}$	reaction rate in the two-fluid model

non-dimensional Numbers	Signification
Da	Damköhler number
Kn	Knudsen number
Le_k	Lewis number of species k
Nu	Nusselt number
Ma	Mach number
Pr	Prandtl number
Re	Reynolds number
Re_d	droplet (or particle) Reynolds number (based on the diameter and relative velocity)
Sc_k	Schmidt number of species k
Sh	Sherwood number
St	Stokes number

operator notation	
$\langle . \rangle$	ensemble averaging operator
$\prec . \succ_p$	contitional ensemble averaging operator
$\mathcal{F}_{\boldsymbol{\kappa}} \{.\}$	fourier transform bracked
$\bar{.}$	reynolds averaged quantity
$\tilde{.}$	favre averaged quantity
$\breve{.}$	mesocopic quantity
$\hat{.}$	fourier transformed quantity
$.'$	fluctuating quantity
$.''$	favre averaged subgrid fluctuation

shortcuts	
CZ	Combustion Zone
DNS	Direct Numerical Simulation
EZ	Evaporation Zone
HIT	Homogeneous Isotropic Turbulence
IZ	Injection Zone
LES	Large Eddy Simulation
PDF	Probability Density Function
PIV	Particle Image Velocimetry
QB	Quasi Brownian
QBE	Quasi Brownian Energy

Symbol	Signification
QBM	Quasi Brownian Motion
QBP	Quasi Brownian Pressure
RANS	Reynolds Averaged Navier-Stokes
SGS	SubGrid Scale
TF	Thickened Flame
TPTF	Two Phase Thickened Flame

Table 1: List of Symbols,Notations and shortcuts

Chapter 1

Transport Equations for dispersed two phase flows

Wie alles sich zum Ganzen webt,
Ein in dem andern wirkt und lebt !
Wie Himmelskräfte auf und nieder steigen
Und sich die goldnen Eimer reichen.
Mit segenduftenden Schwingen
Vom Himmel durch die Erde dringen,
Harmonisch all das All durchklingen !
Welch Schauspiel ! Ach ach ! ein Schauspiel nur !
Wo faßich dich, unendliche Natur ?
Goethe Faust 1.Teil

In this chapter forces acting on a single particle or inclusion are briefly recalled from a bibliographic study. The approach of Lagrangian Particle Tracking is also sketched since it is used as a reference for Eulerian-Eulerian equations.

Two methods are presented to obtain Eulerian-Eulerian conservation equations for dispersed two phase flows. The first method (section 1.3) is based on ensemble averaging supposing low mass and volume charge, so that the carrier phase is undisturbed by the presence of the dispersed phase. This approach is exact in the sense that the conservation equations are derived from the Boltzman equation like the Navier-Stokes equations. Since the carrier phase is supposed undisturbed, this approach leads to a system of equations with one-way coupling.

The second approach (section 1.4) is based on the method of volume filtering. This approach can be compared to the derivation of filtered equations in the sense of Large Eddy Simulations (LES). The method is usefull for deriving conservation equations for reactive flows since source terms and phase exchange terms for the carrier phase and the dispersed phase appear explicitely in the filtering operation. Therefore it leads easily to a system of equations with two-way coupling.

Both approaches result in similar conservation equations. The method of ensemble averaging gives information concerning the modeling and interpretation of pressure and dissipative terms, whereas the method of volume averaging gives information about source and phase interface exchange terms. Both methods may be applied to mono and polydispersed systems. In the case of monodispersed systems, modeling is much easier. Extensions to polydispersed systems are briefly discussed. Detailed information on the volume filtering method may be found in [24], [110] or [68]. The method of ensemble avergaging with application to dispersed flows is discussed by [31], [64] and [91].

1.1 Flow around an isolated particle and the Forces acting upon it

Particle man, Particle man,
doing things a particle can
What's he like ? It's not important
Particle man
Is he a dot or is he a speck ?
When he's underwater does he get wet ?
Or does the water get him instead ?
Nobody knows, Particle man
They might be Giants

Before deriving Eulerian models for dispersed two phase flows a brief review of the flow around an isolated particle and the forces acting upon a particle is given. When particle concentration is hight, the flow around one particle significantly influences the neighboring particle. In this case ssimple models break down and a precise analysis is necessary. This is also true, when the interaction of the particle with the surrounding carrier phase is not limited to forces that can be expressed in the momentum equation, but include mass and heat exchange. Simple models for mass and heat exchange will be considered in the chapter of the one dimensional two-phase-flame. Here the analysis will be limited to basic interaction forces that occur on a single particle without heat and mass exchange.

The interaction forces between the carrier phase and an isolated particle has been studied by many authors. A detailed overview on the forces on an isolated particle can be found in the course [30]. Here a brief overview on the forces on an isolated spherical inclusion is given.

1.1.1 Drag Force

A fundamental relation for the drag force related to a sphere was derived by Stokes [104]. It assumes that the Reynolds number of the particle, given by the ratio of diameter and relative velocity to dynamic viscosity, ($Re_d = d * V_{rel}/\nu$) is much smaller than one. Assuming in the steady case, that the viscous term dominates over the inertial term, one

obtains the Stokes relations:

$$\frac{\partial}{\partial x_j} u_j = 0, \qquad \frac{\partial}{\partial x_i} P = \mu \frac{\partial}{\partial x_k} \frac{\partial}{\partial x_k} u_i \tag{1.1}$$

Then using spherical coordinates one can obtain an analytical solution for the flow leading to drag force consisting of a pressure contribution and a viscous contribution. Since the boundary condition for velocity at the surface of the sphere changes the velocity field, drag force is different for solid particles in a fluid and air bubbles in a liquid.

$$F_{d,particle} \propto 3\pi\mu d V_{rel} \qquad F_{d,bubble} \propto 2\pi\mu d V_{rel} \tag{1.2}$$

Here V_{rel} is the relative velocity of the sphere compared to the velocity of the fluid in absence of the sphere at the location of the sphere. In the case of a liquid droplet the internal flow is important for the boundary condition and needs to be solved. The internal flow depends on the internal Reynolds numbers and therefore the internal viscosity. Therefore the drag force for a liquid droplet depends on the ratio of the liquid viscosity μ_p to the fluid viscosity μ_f ($\Phi_\mu = \mu_p/\mu_f$).

$$F_{d,droplet} \propto 3\pi\mu d V_{rel} \frac{2 + 3\Phi_\mu}{3 + 3\Phi_\mu} \tag{1.3}$$

Oseen Correction

When using a linearized version of the Navier-Stokes equation and taking into account the linearized inertial term the Stokes relation (eq.1.1) becomes:

$$\frac{\partial}{\partial x_j} u_j = 0, \qquad \rho u_{j,\infty} \frac{\partial}{\partial x_j} u_i + \frac{\partial}{\partial x_i} P = \mu \frac{\partial}{\partial x_k} \frac{\partial}{\partial x_k} u_i \tag{1.4}$$

This allows to define a correction as a function of the droplet Reynolds number for the drag coefficient C_d when using a drag law in the form of:

$$F_{d,droplet} \propto C_d \frac{\pi d^2}{8} \rho ||V_{rel}|| V_{rel} \tag{1.5}$$

This drag law is equivalent to the Stokes drag of a solid sphere when using $C_d = 24/Re_d$. The Oseen correction of the drag coefficient is then of the form

$$C_d = \frac{24}{Re_d} \left(\frac{2 + 3\Phi_\mu}{3 + 3\Phi_\mu} \right) \left(1 + \frac{3}{16} \frac{2 + 3\Phi_\mu}{3 + 3\Phi_\mu} Re_d + O(Re_d^2) \right) \tag{1.6}$$

When the particle Reynolds number is bigger than one, it is difficult to obtain analytical solutions. The flow pattern behind the inclusion admits several topologies depending on the particle Reynolds number. For small particle Reynolds numbers (< 20) the flow before and behind the inclusion becomes asymmetric. Further increase in the particle Reynolds number (< 210) leads to axisymetric stationary recirculation zone behind the inclusion.

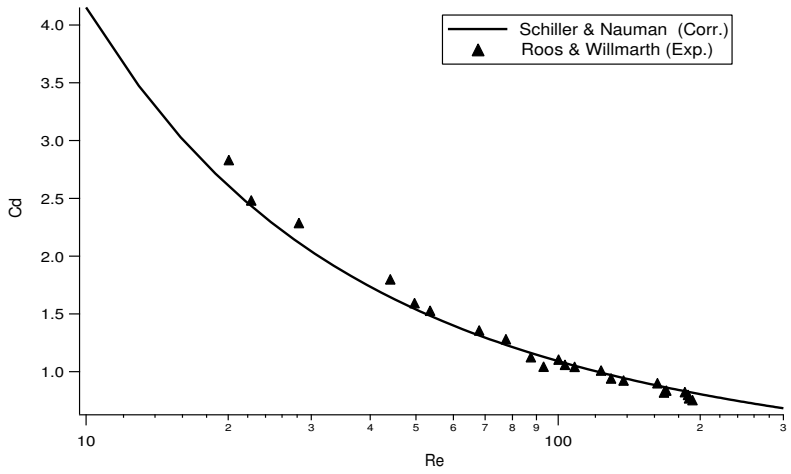

Figure 1.1: Empirical correlation for the drag coefficient of Schiller & Naumann [87] and the experimental results of Roos & Willmarth [83].

For particle Reynolds number bigger then 210, the zone behind the inclusion becomes first asymmetric, then unsteady, destabilizes and finally becomes turbulent. With increasing particle Reynolds number the drag coefficient C_d becomes smaller up to a critical particle Reynolds number of $3.7{*}10^5$ where the boundary layer around the inclusion becomes turbulent. Up to the critical particle Reynolds number the drag coefficient can be approximated by the empirical correlation credited to Schiller and Naumann [87]:

$$C_d = \frac{24}{Re_d}\left(1 + 0.15 \quad Re_d^{0.687}\right) \tag{1.7}$$

This empirical correlation is shown in Fig. 1.1 and compared to experimental results for the drag coefficient measured by Roos and Willmarth [83].

1.1.2 Forces related to acceleration

If the inclusion has a changing relative velocity, additional forces on the inclusion occur. One of them is related to the fluid viscosity and is called Basset or history force. It can be easily explained by the Fourier problem related to kinematic viscosity of the velocity field over a flat plane positioned at $y = 0$. The initially non-moving plane is supposed to attain suddenly the constant velocity V.

$$\frac{\partial}{\partial t}u = \nu\frac{\partial}{\partial x_j}\frac{\partial}{\partial x_j}u \begin{cases} u(t,0) = V \\ u(t,\infty) = 0 \\ u(0,y) = 0 \end{cases} \tag{1.8}$$

The problem in eq. 1.8 admits an analytical solution for constant V. The local stresses on the plane can be expressed by a temporal integral [30]:

$$\tau_{plane} = \sqrt{\frac{\rho\mu}{\pi}} \int_0^t \frac{dV}{d\tau} \frac{d\tau}{\sqrt{t-\tau}} \tag{1.9}$$

For the solid spherical particle in the small particle Reynolds number limit (Stokes drag) this leads to an additional force, which can be expressed in the following form:

$$F_H \propto \frac{3}{2}\pi\mu d \int_0^t \frac{d}{\sqrt{\pi\nu(t-\tau)}} \frac{\partial V_{rel}}{\partial \tau} d\tau \tag{1.10}$$

For increasing particle Reynolds numbers, or for bubbles and liquid droplets the integration kernel is somewhat different but does not change the characteristic behavior of this force. Another force related to acceleration is the so-called added mass force. When the inclusion is accelerated a certain quantity of fluid around the inclusion is accelerated with it.

$$F_{am} \propto C_M \rho \frac{1}{6}\pi d^3 \frac{dV_{rel}}{dt} \tag{1.11}$$

A remaining force related to an accelerated inclusion is the Tchen force. It takes into account the forces of the fluid on the fluid volume in the absence of the particle :

$$F_{Tchen} \propto \frac{1}{6}\rho\pi d^3 \frac{dU}{dt} \tag{1.12}$$

1.1.3 Other forces

When the particle is big enough to see a velocity field with a velocity gradient from one side to the other an effective lift force is introduced. This is for example the case in shear flow where the carrier phase velocity is larger on one side of the particle than the other. This effective lift force due to the vorticity can be expressed by :

$$F_L \propto C_L \rho \frac{1}{6}\pi d^3 \; V_{rel}|_{x_p} \times \Omega \tag{1.13}$$

When the particle is allowed to rotate, the relative slip velocity is unequally distributed. This is the origin of a force known as the Magnus effect, the velocity difference causes a pressure difference and therefore leads to an effective force :

$$F_R \propto C_L \rho \frac{1}{6}\pi d^3 \tag{1.14}$$

The difference in the carrier phase density ρ and the particle density ρ_p induces a buoyancy force when exposed to a gravity field of magnitude g directed in the vertical direction. This buoyancy force can be expressed by :

$$F_b \propto \frac{1}{6}\pi d^3 \left(\rho_p - \rho\right) g \tag{1.15}$$

1.1.4 Comparison of forces on a particle

The equation of motion of a single particle including the forces related to gravity, drag, Tchen contribution, added mass and history contribution with the particle velocity v_p and the particle density ρ_p can be written as [58] :

$$\begin{aligned} \rho_p \frac{dv_p}{dt} &= [\rho_p - \rho]\, g_i - \rho \frac{3}{4} \frac{C_d}{d} |V_{rel}| V_{rel} + \rho \frac{D}{Dt} u \\ &- \rho C_M \frac{d}{dt} V_{rel} - C_H \frac{6}{d} \sqrt{\frac{\nu}{\pi}} \int_0^t \frac{dV_{rel}}{d\tau} \frac{d\tau}{\sqrt{t-\tau}} \end{aligned} \tag{1.16}$$

In order to determine dominant forces it is useful to rewrite eq.1.16 in terms of the density ratio ρ/ρ_p ([12],[93]). Using the definitions of the drag coefficient $C_d = 24f/Re_d$ (f is the turbulent correction $f = 1 + 0.15Re_d^{0.689}$), dividing the relative velocity into the individual velocity components $V_{rel} = v_p - u$ and rearranging the contributions of the added mass force, this leads to a modified differential equation for the particle velocity v_p.

$$\begin{aligned} \frac{dv_p}{dt} &= \frac{(\rho_p - \rho)}{(\rho_p + \rho C_M)} g_i - \frac{\rho 18 \nu f}{d^2 (\rho_p + \rho C_M)} (v_p - u) + \frac{\rho (1 + C_M)}{(\rho_p + \rho C_M)} \frac{D}{Dt} u \\ &- \frac{C_H}{(\rho_p + \rho C_M)} \frac{6}{d} \sqrt{\frac{\nu}{\pi}} \int_0^t \left(\frac{dv_p}{d\tau} - \frac{du}{dt} \right) \frac{d\tau}{\sqrt{t-\tau}} \end{aligned} \tag{1.17}$$

It is interesting to analyze this equation for typical situations such as bubbles in water, heavy solid particles in air (such as coal in a fluidized bed) or fuel droplets in air (such as in a gas turbine combustor). In the limit $\rho/\rho_p \to 0$ the remaining part of the added mass force tends to zero whereas the gravity force coefficient tends to one. The remaining forces of drag and history scale like the inverse of the inclusion density $(1/\rho_p)$. The history force scales like the inverse of the inclusion diameter $(1/d)$ and the drag force as the square of the inverse diameter $(1/d^2)$. In the small particle limit $d \to 0$ the dominant force besides gravity in a gravity field is therefore drag. The drag force can be characterized by a relaxation time τ_p:

$$\tau_p = \frac{\rho_p d^2}{18 \mu f} \tag{1.18}$$

Ignoring all other forces but drag, the particle velocity equation can then be written as:

$$\frac{d}{dt} v_p = -\frac{1}{\tau_p} (v_p - u) \tag{1.19}$$

Eq. 1.19 allows to interpret the relaxation time as the time it takes a particle to attain 63 % of the carrier phase velocity when the particle is initially at rest and the carrier phase velocity is constant. The carrier phase flows admit usually typical time scales such as a flow through time $T = L/U$ (L macroscopic length scale,U mean velocity) in a laminar flow, a turbulent time scale like an eddy turn over time $T = l/u'$ (l turbulent integral

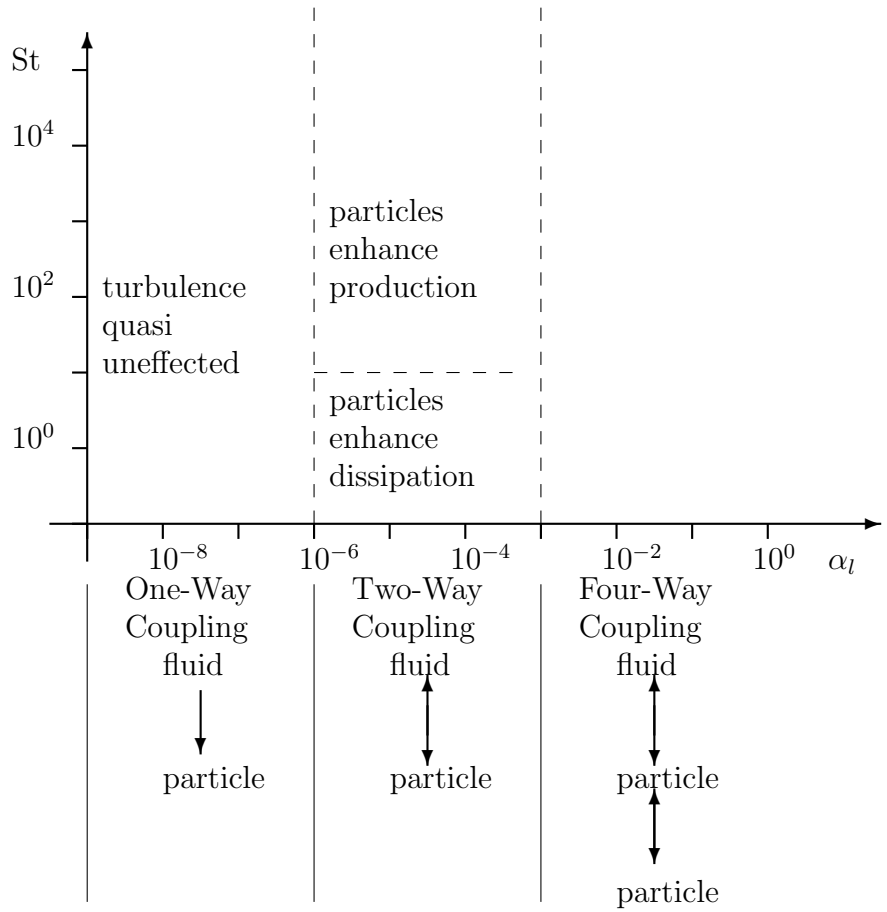

Figure 1.2: Zoology of turbulent particle laden flow regimes [28]

length scale,u' turbulent rms velocity) or a turbulent dissipative time scale $\tau^+ = k/\varepsilon$ (k turbulent kinetic energy, ε turbulent dissipation). Those carrier phase time scales can then be compared to the relaxation time of the particle. The non-dimensional number that compares such time scales is the *Stokes number* defined as :

$$St = \frac{\tau_p}{T} \tag{1.20}$$

The Stokes number gives an information about the qualitative behavior of particles in the flow. Small Stokes numbers ($St \ll 1$) indicate that particles behave as tracers ([32]), whereas large Stokes numbers ($St \gg 1$) qualify the particles to be inertial in the flow and to perform an almost random motion depending on their trajectory history. Effects of maximal segregation in turbulent flow occur at Stokes numbers around unity ([32][61][112][103]). Then particles have enough inertia to be ejected from a vortex and not follow the fluid particle like a tracer, but not enough inertia to cross the vortices without undergoing significant changes compared to their inertial trajectory.

When sufficiently many particles are present, the carrier phase flow is altered by the particle presence. How much the carrier phase flow is altered by the particle presence depends on volume, mass loading and on the particles diameters. For particles that admit a Reynolds number smaller than unity and that are significantly smaller than the Kolmogorov scale in turbulent flow, the single particle presence is believed to have no significant impact on the carrier phase. When the particle is larger than the Kolmogorov scale or has a Reynolds number higher than unity its presence may change the structure of the flow: for example, turbulence will be produced at small scales in the wake of the particle. When the particle number density is high enough, the mean flow structure is altered by the particle presence. As demonstrated by Druzhini and Elghobashi [26] in a Eulerian computation of decreasing homogeneous isotropic turbulence (HIT), a turbulent flow laden with microparticles with very small relaxation times may behave like as if the carrier phase density was increased. Therefore the effective dynamic viscosity is decreased with respect to the initial kinematic viscosity.

At high particle number density, inter particle collisions become important and alter the dynamics of the dispersed phase. Collisions may be inelastic, partially inelastic or elastic. In the simplest case of elastic collisions, total energy and momentum are conserved. The distribution of momentum is however altered by collisions and tends towards a Maxwellian in the ideal case.

A sketch of different flow regimes is given in fig. 1.2 taken from Elghobashi [28]. This two-dimensional sketch takes into account the Stokes number and the volume loading. It can be interpreted as a projection of a three-dimensional graph that includes the density ratio as an additional parameter.

Here only the most simple case is considered. Volume and mass loading are supposed to be so small that the carrier phase is unaltered and particle collisions can be neglected Furthermore particles are considered solid and so small that Stokes drag is a good approximation.

1.2 The Lagrangian Particle Tracking Method

The Lagrangian particle tracking method is a well understood tool for the numerical investigation of particle laden turbulence. In the case of Stokes drag the particle coordinate and velocities of the individual particle with index (k) are advanced in time with the following set of differential equations.

$$\frac{\partial}{\partial t} X_i^{(k)} = V_i^{(k)} \tag{1.21}$$

$$\frac{\partial}{\partial t} V_i^{(k)} = \frac{1}{\tau_p} \left(u_i - V_i^{(k)} \right) \tag{1.22}$$

Here $X_i^{(k)}$ is the location of the particle (k) in space and $V_i^{(k)}$ is its velocity. u_i is the carrier phase velocity at the particle location and τ_p the particle relaxation time. In realistic applications particle numbers are so large that it is not possible to track all particles

individually and particles are advanced as "numerical" particles, that are supposed to represent a large number of "physical" particles. In order not to bias the result by such a procedure, here all particles are computed individually. Special care has to be taken to evaluate the gaseous velocity u_i at the particle location for the drag force. This can be done by using high order interpolation methods [117]. If two-way coupling is used, the repartition of the source terms on the gaseous carrier phase is a supplementary difficulty. If particle sampling for numerical particles is poor, the source terms for instance for fuel evaporation may vary strongly from one computational cell to another. In the case of reactive two-phase flow this may lead to difficulties for the computation of chemical source terms and oscillating behavior for properties like the flame speed.

1.3 Eulerian-Eulerian conservation equations by ensemble averaging

In this part the Eulerian-Eulerian field equations are deduced from kinetic theory. This is largely based on kinetic theory of gases. Here especially the publication of Grad [37] on rarefied gases and the framework of Chapman and Cowling [13] on kinetic theory are used. A concentrated version containing nevertheless the essential framework can also be found in the lecture notes of Sommerfeld [98](Chapter 5,§41,42,43).
The idea of an ensemble average conditioned on one carrier phase realization was adopted from Simonin [92]. The initial work on the concept of Quasi-Brownian Motion was done by Simonin and Fevrier [92].
This approach makes two important hypothesises:

1. volume and mass loading are so small, that the carrier phase flow is not altered by dispersed phase presence.

2. particle diameters are so small, that Stokes drag is a good approximation for the fluid force acting on the particle.

The approach differs significantly from the statistical approach using a joint probability density function for carrier and dispersed phase, typically used in a Reynolds averaged approach like the two-fluid model [31]. The hypothesis made imply, that this is more a preliminary, study since both hypothesises are rarely fulfilled in industrial applications.

1.3.1 The Transport equation for the probability density function

The time development of a Boltzmann-type Eulerian probability density function (pdf) $f_p(c_{p,i}, x_i, t)$ of a particle ensemble $\mathcal{P}$ can be expressed by [13] [52]:

$$\frac{\partial}{\partial t} f_p + \frac{\partial}{\partial x_j} c_{p,j} f_p + \frac{\partial}{\partial c_{j,p}} \frac{F_{p,j}}{m_p} f_p = \left(\frac{\partial}{\partial t} f_p \right)_{coll} \tag{1.23}$$

Here $c_{p,j}$ is the particle velocity in phase space, m_p is the individual particle mass and $F_{p,j}$ is an external force on the particle. The term on the right hand side of equation 1.23 represents the change of the particle distribution due to inter-particle collisions. In order to obtain the Mesoscopic Eulerian conservation equations the carrier phase is supposed to be undisturbed by the dispersed phase. This assumption is satisfied in dilute flows where volume and mass loading are small. To derive local instantaneous Eulerian equations in dilute flows (without turbulence modification by the particles), Février [32], [92] proposes to use an averaging over all dispersed-phase realizations conditioned by one carrier-phase realization. Such an averaging procedure leads to a conditional velocity pdf for the dispersed phase,

$$\breve{f}_p^{(1)}\left(\mathbf{c}_p;\mathbf{x},t,H_f\right)=\left\langle W_p^{(1)}\left(\mathbf{c}_p;\mathbf{x},t\right)|H_f\right\rangle. \tag{1.24}$$

$W_p^{(1)}$ are the realizations of position and velocity in time of any given particle [79] and H_f is the unique carrier flow realization. The transport equation for the new probability density function (pdf)

$$\frac{\partial}{\partial t}\breve{f}_p+\frac{\partial}{\partial x_j}c_{p,j}\breve{f}_p+\frac{\partial}{\partial c_{j,p}}\frac{F_{p,j}}{m_p}\breve{f}_p=\left(\frac{\partial}{\partial t}\breve{f}_p\right)_{coll} \tag{1.25}$$

can then be used to derive Eulerian conservation laws for the moments of the pdf. The dependence of the pdf $\breve{f}_p$ on the carrier phase realization $\mathcal{H}_f$ is not recalled from here on. For any function possibly depending on the particle velocity $\psi_p\left(c_{p,j}\right)$ the corresponding transport equation is obtained by multiplying Eq. 1.25 with $\psi_p\left(c_{p,j}\right)$ and integrating over particle velocity space. This procedure is used as in kinetic theory, assuming that the product $\psi_p\left(c_{p,j}\right)\breve{f}_p$ is finite and tends to zero as at least one velocity component tends to infinity. The corresponding conservation law then has the form:

$$\frac{\partial}{\partial t}\breve{n}_p\langle\psi_p\left(c_{p,i}\right)\rangle_p+\frac{\partial}{\partial x_j}\breve{n}_p\langle c_{p,j}\psi_p\left(c_{p,i}\right)\rangle_p=\breve{n}_p\langle\frac{F_{p,j}}{m_p}\frac{\partial}{\partial c_{j,p}}\psi_p\left(c_{p,i}\right)\rangle_p+\mathcal{C}_p\left(\psi_p\right) \tag{1.26}$$

Eq. 1.26 is the equivalent of what is known as Maxwells equation of transfer in kinetic theory [37]. Integration over particle velocity space is abbreviated by $\langle.\rangle_p$. Collision Integrals are abbreviated by $\mathcal{C}_p$.
Number density weighted (or Favre averaged) type quantities can then be defined as for the Navier Stokes equations.

$$\breve{n}_p = \int\breve{f}_p dc_{p,j} \tag{1.27}$$

$$\breve{\psi}_p=\langle\psi_p\left(c_{p,j}\right)\rangle_p = \frac{1}{\breve{n}_p}\int\psi_p\left(c_{p,j}\right)\breve{f}_p dc_{p,j} \tag{1.28}$$

$$\langle\delta\psi_p\delta\phi_p\rangle_p = \langle\Big(\psi_p\left(c_{p,j}\right)-\breve{\psi}_p\Big)\Big(\phi_p\left(c_{p,j}\right)-\breve{\phi}_p\Big)\rangle_p \tag{1.29}$$

When ψ_p depends on space and time, additional terms arise in the moment transport equation:

$$\frac{\partial}{\partial t}\breve{n}_p\langle\psi_p\left(c_{p,i}\right)\rangle_p+\frac{\partial}{\partial x_j}\breve{n}_p\langle c_{p,j}\psi_p\left(c_{p,i}\right)\rangle_p = \breve{n}_p\langle\frac{F_{p,j}}{m_p}\frac{\partial}{\partial c_{j,p}}\psi_p\left(c_{p,i}\right)\rangle_p \tag{1.30}$$

$$+\mathcal{C}_p\left(\psi_p\right)+\breve{n}_p\langle\frac{\partial}{\partial t}\psi_p+c_{p,j}\frac{\partial}{\partial x_j}\psi_p\rangle_p$$

Eq. 1.30 is the equivalent to Enskog's *general equation of change* in kinetic theory.

In kinetic theory one important property is the *H-Theorem*. Inter-molecule collisions satisfy energy and momentum conservation and ensure a redistribution of particle velocities in phase space. This has important consequences: First, one may define a kinetic entropy equation that satisfies the *Boltzmann-inequality* and second, at equilibrium the phase space velocity distribution is Maxwellian. This opens the possibility to a series development in Hermite polynomials around the Maxwellian [37],[24]. When dealing with particles that are submitted to drag force, the total particle momentum and energy are not conserved, since the particles exchange momentum with the carrier phase. Neglecting furthermore collisions, particle momentum is not redistributed and the phase space velocity distribution is not necessarily Maxwellian.
This can be formalized by construction of the equivalent of the kinetic entropy equation. For simplicity the only interaction force is supposed to be the Stokes drag (1.37). The equivalent of the entropy equation is obtained by multiplication of Eq. 1.25 with $(1+\ln\breve{f}_p)$ and integration over particle velocity:

$$\begin{aligned}\frac{\partial}{\partial t}\int\breve{f}_p\ln\breve{f}_p dc_p \;+\; \frac{\partial}{\partial x}\int c_p\breve{f}_p\ln\breve{f}_p dc_p \\ +\int\left(\frac{1}{\tau_p}\left(u_g-c_p\right)\frac{\partial}{\partial c_p}\breve{f}_p\ln\breve{f}_p-\frac{1}{\tau_p}\left(1+\ln\breve{f}_p\right)\breve{f}_p\right)dc_p=0\end{aligned}\tag{1.31}$$

In the kinetic theory of gases the forces acting on the molecules are independent of the molecular velocity and therefore the integral over velocity space vanishes. In the case of particles, where drag force explicitly depends on the particle velocity, this is not true. Physically the coupling to the carrier phase velocity will push the particle velocity distribution towards the carrier phase velocity.

1.3.2 Mesoscopic Eulerian Particle Velocity and Quasi Brownian Velocity Distribution

When the velocities of different particle realizations $\mathcal{H}_p$ are averaged with conditioning on the one given carrier phase realization $\mathcal{H}_f$ the local instantaneous mean particle velocity is defined by :

$$\breve{u}_{p,i}=\frac{1}{\breve{n}_p}\int c_{p,i}\breve{f}_p dc_{p,j}\tag{1.32}$$

Then the individual particle velocity $V_i^{(k)}$ of a single particle located at $X_j^{(k)}(t)$ at the time t can formally be expressed in terms of an ensemble averaged instantaneous Eulerian particle velocity $\breve{u}_{p,i}$ named *Mesoscopic Eulerian Particle Velocity Field* from here on and a residual velocity component $\delta u_{p,i}^{(k)}$.

$$V_i^{(k)}=\breve{u}_{p,i}(X_j^{(k)}(t),t)+\delta u_{p,i}^{(k)}(t)\tag{1.33}$$

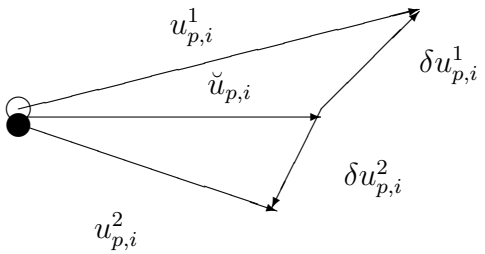

Figure 1.3: Individual particle velocity $V_i^{(k)}$, instantaneous Eulerian particle velocity $\breve{u}_{p,i}$ and residual velocity components $\delta u_{p,i}^{(k)}$.

By definition the conditional ensemble average of the residual velocity component $\delta u_{p,i}^{(k)}$ is zero. It is essential for the following derivation of the conservation equations, that $\breve{u}_{p,i}$ is an Eulerian velocity field shared by all dispersed phase realizations, whereas the individual particle velocities $V_i^{(k)}$ and the residual velocities $\delta u_{p,i}^{(k)}$ are proper to each particle in each realization. In kinetic theory $\delta u_{p,i}^{(k)}$ is referred to as the *peculiar velocity*. Then, as stated in [45], the pressure tensor $\breve{n}_p \langle \delta u_{p,i} \delta u_{p,j} \rangle_p$ in kinetic theory represents the momentum flux through the gas.
By analogy to kinetic theory, the ensemble average of the correlation tensor of the residual velocities $\langle \delta u_{p,i} \delta u_{p,j} \rangle_p$ is defined by"

$$\langle \delta u_{p,i} \delta u_{p,j} \rangle_p = \frac{1}{\breve{n}_p} \int \left(c_{p,i} - \breve{u}_{p,i} \right) \left(c_{p,j} - \breve{u}_{p,j} \right) \breve{f}_p dc_{p,k} \tag{1.34}$$

It gives a measure of the mean particle momentum flux. The diagonal elements represent the normal stresses whereas the non-diagonal elements represent the shear stresses. The concept related to the residual velocities δu_p is from here on referred to as *Quasi Brownian Motion (QBM)*. The trace of the tensor of the residual velocities $\delta \breve{\theta}_p = 1/2 \langle \delta u_{p,k} \delta u_{p,k} \rangle_p$ is referred to as *Quasi Brownian Energy (QBE)*.

1.3.3 Eulerian Conservation Equations for Monodispersed Particle Systems

Using Eq. 1.26 and Eq. 1.30 various conservation laws can be deduced. Choosing $\psi_p = 1$ one obtains the conservation law for particle number density:

$$\frac{\partial}{\partial t} \breve{n}_p + \frac{\partial}{\partial x_j} \breve{n}_p \breve{u}_{p,j} = \mathcal{C}_p \tag{1.35}$$

Excluding particle breakup and coalescence the right hand side of Eq. 1.35 is zero. For $\psi_p = c_{p,i}$ the mean particle momentum equation is recovered.

$$\frac{\partial}{\partial t}\breve{n}_p\breve{u}_{p,i} + \frac{\partial}{\partial x_j}\breve{n}_p\breve{u}_{p,j}\breve{u}_{p,i} = -\frac{\partial}{\partial x_j}\breve{n}_p\langle\delta u_{p,j}\delta u_{p,i}\rangle_p + \breve{n}_p\langle\frac{F_{p,i}}{m_p}\rangle_p + \mathcal{C}_p\left(c_{p,i}\right) \tag{1.36}$$

Without particle division, coalescence and collisions the right hand side of Eq. 1.36 reduces to the force term and the stress term related to QBM. Here the force term considered is limited to Stokes drag :

$$\frac{F_{p,i}}{m_p} = \frac{1}{\tau_p}\left(u_i - c_{p,i}\right) \tag{1.37}$$

The particle relaxation time τ_p is defined as :

$$\tau_p = \frac{\rho_p d_p^2}{18\mu_g} \tag{1.38}$$

Here u_i is the local instantaneous carrier phase velocity at the particle location. A key-point is the determination of the second order term $\breve{n}_p\langle\delta u_{p,j}\delta u_{p,i}\rangle_p$ in the momentum eqn. 1.36. This second order term which arises from the ensemble average corresponds to σ_{ij} in the Navier-Stokes equations. Physically, in a gas, it translates the influence of the peculiar velocity on the transport of the ensemble averaged velocity. In the same manner particles, which have different histories, may have individual particle velocities that are significantly different and alter the mesoscopic velocity. A detailed analysis of the stress term is given in section 3.1.

Modeling of the Quasi Brownian Stress $\langle\delta u_{p,j}\delta u_{p,i}\rangle_p$

The general idea of modeling the unresolved stresses is to relate them to known quantities and their gradients. The known quantities are the number density ($\breve{n}_p$) and the mesoscopic velocity ($\breve{u}_{p,i}$).
In a statistical framework the modeling for the stress tensor $\langle\delta u_{p,j}\delta u_{p,i}\rangle_p$ in gas-particle simulations is done in analogy to modling of the stress tensor in the Navier Stokes equations (Simonin [92][91]). The diagonal terms are modeled by a pressure like term and the non-diagonal terms by making a viscous assumption.

$$\breve{n}_p\langle\delta u_{p,j}\delta u_{p,i}\rangle_p = P_{QB}\delta_{ij} - \mu_{QB}\left(\frac{\partial u_{p,i}}{\partial x_j} + \frac{\partial u_{p,j}}{\partial x_i} - \frac{2}{3}\frac{\partial u_{p,k}}{\partial x_k}\delta_{ij}\right) \tag{1.39}$$

According to Hirschfelder-Curtis-Bird [45] the viscous term of Eq. 1.39 is one of the two linear combinations of velocity gradients based on the Onsager relations ([20]), that satisfy the necessary symmetry relations. The other linear term would be a bulk viscosity.

Quasi Brownian Pressure (QBP)

The quasi brownian energy $\delta\breve{\theta}_p$ is defined by:

$$\delta\breve{\theta}_p = \frac{1}{2}\langle \delta u_{p,k}\delta u_{p,k}\rangle_p \tag{1.40}$$

and is the equivalent of temperature in the Navier Stokes equations *. One key point is the definition of P_{QB}. The quasi brownian pressure P_{QB} is linked by an equation of state to the quasi brownian energy $\delta\breve{\theta}_p$ of the type:

$$P_{QB} = \frac{2}{3}\breve{n}_p\delta\breve{\theta}_p \tag{1.41}$$

This approach requires therefore the knowledge of $\delta\breve{\theta}_p$. Several possibilties for the estimation of this QBE are given in section 3.1. One of the possibilities is to use the corresponding transport equation. This is briefly described below.

The Quasi Brownian viscosity assumption

The viscous stress tensor in Eq. 1.39 contains a viscosity parameter. In the Navier Stokes equations the viscosity depends on the collision frequency between molecules (τ_c). The characteristic time scale concerning particles is the particle relaxation time τ_p. In statistical gaz-particle simulations without collisions the QB viscosity is defined by the following relation.

$$\nu_{QB} = \frac{\tau_p}{3}\delta\breve{\theta}_p \tag{1.42}$$

A physical motivation for this quantity is given in section 11. The dynamic QB viscosity (μ_{QB}) and the kinetic QB viscosity (ν_{QB}) are related by $\mu_{QB} = \breve{n}_p\nu_{QB}$. Like the QBP the QB viscosity depends on the QBE. In the following the transport equation for QBE is briefly presented.

The transport equation for Quasi Brownian Energy

In the case of the dispersed phase, $\delta\breve{\theta}_p$ is a measure of the uncorrelated particle movement. Since the uncorrelated particle movement is not uniform in space, an additional transport equation for this property is needed. With the definition of $\delta\breve{\theta}_p$ and taking $\psi_p = \delta u_{p,k}\delta u_{p,k}$ in Eq. 1.30 yields:

$$\frac{\partial}{\partial t}\breve{n}_p\langle \delta u_{p,k}\delta u_{p,k}\rangle_p + \frac{\partial}{\partial x_j}\breve{n}_p\breve{u}_{p,j}\langle \delta u_{p,k}\delta u_{p,k}\rangle_p = -\frac{\partial}{\partial x_j}\breve{n}_p\langle \delta u_{p,j}\delta u_{p,k}\delta u_{p,k}\rangle_p \tag{1.43}$$
$$-\breve{n}_p\langle\frac{2}{\tau_p}\delta u_{p,k}\delta u_{p,k}\rangle_p$$

* Note that even though $\delta\breve{\theta}_p$ is sometimes called temperature, it characterizes the uncorrelated particle motion and has no link with the temperature of the particle matter, which must be obtained through the enthalpy equation of the dispersed phase.

$$-2\breve{n}_p\langle\delta u_{p,j}\delta u_{l,p}\rangle\frac{\partial\breve{u}_{p,j}}{\partial x_l}$$
$$+\mathcal{C}_p\left(c_{p,k}c_{p,k}\right)$$

In the transport equations of the second order correlation arises a third order correlation. In statistical simulation of gaz-particle simulation this term is usually modeled by a diffuse term similar to Ficks law in the temperature equation [91].

$$\langle\delta u_{p,j}\delta u_{p,k}\delta u_{p,k}\rangle_p = -\breve{k}_{QB}\frac{\partial}{\partial x_j}\delta\breve{\theta}_p \tag{1.44}$$

The diffusion coefficient $\breve{k}_{QB}$ is modeled in analogy to the diffusion coefficient used in the fluctuating particle kinetic energy in the two-fluid formulation by (Simonin [92][91]) :

$$\breve{k}_{QB} = \frac{10}{27}\breve{n}_p\tau_p\delta\breve{\theta}_p \tag{1.45}$$

The influence of modeling the third order correlation of the QBE equation by a diffusive term is discussed in section 3.1.5.

Transport equations for Mesoscopic Momentum and Quasi Brownian Energy

The equations for mesoscopic Eulerian particle velocity field (Eq. 1.36) and the quasi brownian energy distribution (Eq. 1.43) can then be written as follows :

$$\frac{\partial}{\partial t}\breve{n}_p\breve{u}_{p,i} + \frac{\partial}{\partial x_j}\breve{n}_p\breve{u}_{p,j}\breve{u}_{p,i} = -\frac{\partial}{\partial x_i}P_{QB} + \frac{\partial}{\partial x_j}\breve{\tau}_{p,ij} + \frac{\breve{n}_p}{\tau_p}\left(u_i - \breve{u}_{p,i}\right) \tag{1.46}$$

$$\frac{\partial}{\partial t}\breve{n}_p\delta\breve{\theta}_p + \frac{\partial}{\partial x_j}\breve{n}_p\breve{u}_{p,j}\delta\breve{\theta}_p = -2\frac{\breve{n}_p}{\tau_p}\delta\breve{\theta}_p - \left[P_{QB}\delta_{ij} - \breve{\tau}_{p,ij}\right]\frac{\partial\breve{u}_{p,i}}{\partial x_j} + \frac{\partial}{\partial x_j}\breve{n}_p\breve{k}_{QB}\frac{\partial}{\partial x_j}\delta\breve{\theta}_p \tag{1.47}$$

Here the viscous part of the Quasi Brownian Stress tensor is abbreviated by :

$$\breve{\tau}_{p,ij} = \mu_{QB}\left(\frac{\partial\breve{u}_{p,i}}{\partial x_j} + \frac{\partial\breve{u}_{p,j}}{\partial x_i} - \frac{2}{3}\frac{\partial\breve{u}_{p,k}}{\partial x_k}\delta_{ij}\right) \tag{1.48}$$

The physical signification of the three terms on the right hand side of Eq. 1.47 are as follows :

- $-2\frac{\breve{n}_p}{\tau_p}\delta\breve{\theta}_p$ is the dissipation of Quasi Brownian Energy by drag with with the carrier phase,
- $-P_{QB}\delta_{ij}\frac{\partial\breve{u}_{p,i}}{\partial x_j}$ is the production of Quasi Brownian Energy by compression,
- $\left[\frac{2}{3}\mu_{QB}\frac{\partial\breve{u}_{p,k}}{\partial x_k}\delta_{ij} - \mu_{QB}\left(\frac{\partial\breve{u}_{p,i}}{\partial x_j} + \frac{\partial\breve{u}_{p,j}}{\partial x_i}\right)\right]\frac{\partial\breve{u}_{p,i}}{\partial x_j}$ is the production of Quasi Brownian Energy by shear and

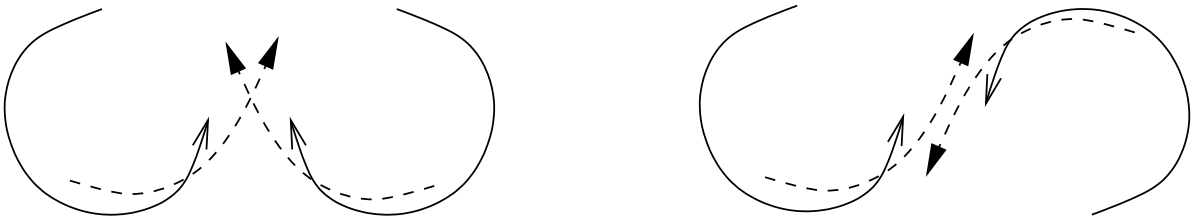

Figure 1.4: Production of Quasi Brownian Motion by compression and shear. The continuous lines give the carrier phase fluid particle and the dashed lines the particle trajectory.

- $\frac{\partial}{\partial x_j}\breve{n}_p\breve{k}_{QB}\frac{\partial}{\partial x_j}\delta\breve{\theta}_p$ is the diffusion of Quasi Brownian Energy in analogy to heat diffusion in the Navier Stokes equations.

In Fig. 1.4 two production mechanisms of QBM are illustrated. The sketch on the left shows two counter rotating vortices of the carrier phase that entrain the particles. Due to their inertia particles are ejected from the carrier phase vortices and meet in a region between the two carrier phase vortices. This compression of particle density leads to an increase in QBM like the compression of a gas leads to an increase in temperature. Whereas in a gas molecules collide and the particle velocities are redistributed, in the dispersed phase particle velocities are not redistributed and particles tend to penetrate into the neighboring carrier phase vortex as far as the counteracting drag force allows the particle to do so. The sketch on the right of Fig. 1.4 shows two co-rotating vortices of the carrier phase and corresponds to a situation, where shear produces an increase in temperature in the Navier-Stokes equations. The dispersed phase acts correspondingly, when particles penetrate a depth proportional to the product of the residual velocity and the particle relaxation time $\delta u * \tau_p$ into the opposite carrier phase vortex. This analogy to the Prandtl mixing layer assumption illustrates, how the shear of the mesoscopic velocity field induces the production of QBM.

Transport equation for the total kinetic energy

For practical applications it is sometimes more convenient to transport the total kinetic energy of the dispersed phase. This quantity can be obtained by multiplication of Eq. 1.46 with $\breve{u}_{p,i}$ and summing with Eq. 1.47. The transport equation for the total kinetic energy $\breve{e}_{cin,p} = 1/2\breve{u}_{p,i}\breve{u}_{p,i} + \delta\breve{\theta}_p$ is then :

$$\begin{aligned}\frac{\partial}{\partial t}\breve{n}_p\breve{e}_{cin,p} + \frac{\partial}{\partial x_j}\breve{n}_p\breve{u}_{p,j}\breve{e}_{cin,p} &= \frac{\breve{n}_p}{\tau_p}\left(u_i\breve{u}_{p,i} - 2\breve{e}_{cin,p}\right) \\ &- \frac{\partial}{\partial x_j}\left[P_{QB}\delta_{ij} - \breve{\tau}_{p,ij}\right]\breve{u}_{p,i} + \frac{\partial}{\partial x_j}\breve{n}_p\breve{k}_{QB}\frac{\partial}{\partial x_j}\delta\breve{\theta}_p\end{aligned} \tag{1.49}$$

The conservation equation for total kinetic energy can also be derived using $\psi_p = c_{p,i}c_{p,i}$ and applying the previous procedure of ensemble averaging.

Transport equations for passive quantities

Other equations for passive or active scalars corresponding to particle properties such as particle temperature T_p or particle enthalpy $h_{p,s}$ can be derived as the other conservation equations. In the following the conservation equation for particle enthalpy is presented. It may be obtained by setting $\psi_p = h_{p,s}$. Here it is pointed out, that particle temperature is a property of a single particle and not related to the uncorrelated motion of particles.

$$\frac{\partial}{\partial t}\breve{n}_p\breve{h}_{p,s} + \frac{\partial}{\partial x_j}\breve{n}_p\breve{u}_{p,j}\breve{h}_{p,s} = +\frac{\partial}{\partial x_j}\left(\breve{n}_p\breve{u}_{p,j}\breve{h}_{p,s} - \breve{n}_p\langle c_{p,j}h_{p,s}\rangle_p\right) \tag{1.50}$$

$$+\breve{n}_p\langle\frac{\partial}{\partial t}h_{p,s} + c_{p,j}\frac{\partial}{\partial x_j}h_{p,s}\rangle_p + \mathcal{C}\left(h_{p,s}\right) \tag{1.51}$$

The first term on the right hand side of Eq. 1.50 is the diffusion of enthalpy due to uncorrelated particle velocity. The second term on the right hand side of Eq. 1.50 corresponds to the enthalpy exchange of the particles with the carrier phase and needs to be modeled. Modeling of such terms is discussed in the chapter of the one-dimensional two-phase flame (chapter 6).

1.3.4 Eulerian Equations for Polydispersed Two-Phase Flows

The difficulty of polydispersed particle size distributions is proper to the Eulerian formulation. In the Lagrangian Particle tracking method every particle has its own inertia and diameter and it is therefore independent on the particle velocity distribution. For the treatment of polydispersed two-phase flows in the Eulerian formulation several strategies exist. Among the most popular are the two following:

1. Particle class methods: The particle size distribution is divided into fixed particle size classes and transport equations are derived for each particle class. Particle class exchange terms due to evaporation, collision and other physical phenomena need to be modeled for every particle class. Furthermore inter-class exchange terms need to be formulated, if the particle diameter per class is static and evaporation, particle-breakup or coalescence are considered. Since momentum transport equations are considered individually, there is no necessity for the hypothesis that all particles follow the same velocity distribution. This model is numerically expensive, if a realistic particle size distribution shall be transported.

2. Presumed Particle distribution with distribution moment transport: Supposing that the particle size distribution is independent of the particle velocity distribution this method allows to take into account the different particle sizes for phase exchange terms such as evaporation. The hypothesis of decoupled size and velocity distribution is clearly questionable, since for instance the particle relaxation time varies as the square of the particle diameter and therefore particle of different sizes should be subject to significantly different dynamics. The advantage of this approach is the limited number of additional transport equations compared to the Particle Class method.

1.4 Eulerian-Eulerian conservation equations by volume filtering

This approach is based on the idea of volume filtering and is therefore close to a spatial filter in the sense of Large Eddy Simulations (LES) for mono-phase flows. It supposes the existence of the Navier-Stokes equations (conservation of mass, mass fractions, momentum and energy) in each phase [91]. This is a simple approach, that leads to two-way coupled set of equations for the two phases. The drawback of the approach is however, that is does not give information about the modeling of phase interchange and fluctuating terms. The interest in the presentation of the volume filtered equations is double fold: First volume filtered results are used in sections 4.2.1 and 4.3.1 to compare the Eulerian-Eulerian results to the Lagrangian results. Secondly the volume filtered approach is used in the chapter for the one dimensional two-phase flame with two-way coupling for mass, momentum and enthalpy terms (chapter 6). The Navier-Stokes equations as they are used for volume filtering are:

$$\frac{\partial}{\partial t}\rho + \frac{\partial}{\partial x_j}\rho u_j = 0 \tag{1.52}$$

$$\frac{\partial}{\partial t}\rho Y_k + \frac{\partial}{\partial x_j}\rho Y_k u_j = \frac{\partial}{\partial x_j}\rho D_k \frac{\partial}{\partial x_j} Y_k + \dot{\omega}_k \tag{1.53}$$

$$\frac{\partial}{\partial t}\rho u_i + \frac{\partial}{\partial x_j}\rho u_i u_j = -\frac{\partial}{\partial x_i}P + \frac{\partial}{\partial x_j}\tau_{ij} = \frac{\partial}{\partial x_j}\sigma_{ij} \tag{1.54}$$

$$\frac{\partial}{\partial t}\rho h + \frac{\partial}{\partial x_j}\rho h u_j = \frac{\partial}{\partial t}P + u_j\frac{\partial}{\partial x_j}P - \frac{\partial}{\partial x_i}q_i + \tau_{ij}\frac{\partial}{\partial x_j}u_i + \dot{\omega}_T \tag{1.55}$$

where the variables ρ, u_j and h correspond to the gaseous density, gaseous velocity and gaseous enthalpy,if in the gas phase and liquid density, liquid velocity and liquid enthalpy, if in the liquid phase. The kernel of the filter function is then a convolution of the characteristic function with the volume filter. This approach is different from the ensemble average approach. Certain hypothesis like one-way coupling are not necessary and different assumptions become necessary. One of the necessary hypothesis is, that the volume filter is larger than the particle diameter and that particles are significantly smaller than the length scales that are to be resolved by the computation. One important feature of the two-fluid model is, that it allows to construct consistent equations. The volume fractions of the different phases always add up to one and summing of the corresponding transport equations of the different phases lead to equations that are globally conserved.

1.4.1 The characteristic function χ_ϕ

For two-phase flows the original system is composed of two distinct phases (liquid droplets in a gas for example) [69]. The interface between the phases is assumed to have zero thickness and each phase is identified by the characteristic function (or component indicator

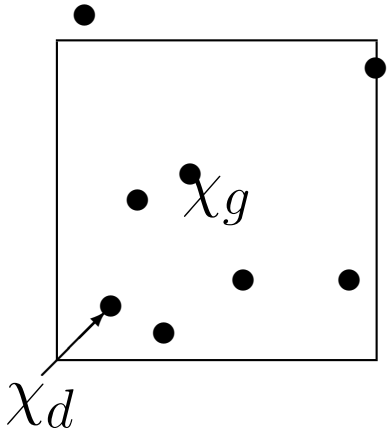

Figure 1.5: The concept of volume averaging: The black line represents the boundaries of the control volume and the black dots the inclusions.

function [24]) χ_ϕ, such that [110]:

$$\chi_\phi = \begin{cases} 1 & \text{if phase } \phi \\ 0 & \text{else} \end{cases} \tag{1.56}$$

Multiplication of any quantity with the characteristic function then allows to identify the corresponding phase quantity.

1.4.2 Derivation operator and commutation relations

Under the conditions of a sharply defined interface of zero thickness, the interface may be transported by an isosurface transport equation known from level-set methods or the G equation in combustion [73].

$$\frac{D}{Dt_\zeta} G = \frac{\partial}{\partial t} G + w_{i,\zeta} \frac{\partial}{\partial x_i} G \tag{1.57}$$

The index ζ signifies that the differential operator $\frac{D}{Dt_\zeta}$ and the displacement speed $w_{i,\zeta}$ are related to the interface. Conservation of the indicator function χ_ϕ and of the surface in between the phases represented by the delta function δ_ζ requires:

$$\frac{D}{Dt_\zeta} \chi_\phi = 0 \quad \text{and} \quad \frac{D}{Dt_\zeta} \delta_\zeta = 0 \tag{1.58}$$

The derivation of interface transport and commutation relations is discussed in detail in the publications of Whitaker [46][114],Gray [113], Simonin [110] and Drew [24]. The resulting commutation relations are :

$$\left[\frac{d}{dt}, \chi_\phi\right] = (w_{\phi,j} - u_{\phi,j}) n_{\phi,j} \delta_{\zeta,\phi}, \tag{1.59}$$

$$\left[\frac{\partial}{\partial t}, \chi_\phi\right] = w_{\phi,j} n_{\phi,j} \delta_{\zeta,\phi}, \tag{1.60}$$

$$\left[\frac{\partial}{\partial x_j}, \chi_\phi\right] = -n_{\phi,j} \delta_{\zeta,\phi}. \tag{1.61}$$

Here commutation bracket was defined as $[a, b] = a \bullet b - b \bullet a$. w_i is the velocity of the interface and $n_{\phi,i}$ is the normal of the interface with respect to the phase.

1.4.3 Properties of Volume averaging with characteristic function

Here one supposes the existence of a fictive control volume Ω. In the language of LES filters this corresponds to a top hat filter for the integration kernel [†]. Then one obtains immediately the phase fraction of the control volume, α_ϕ, that is the control volume integral over the characteristic function :

$$\alpha_\phi = \langle \chi_\phi \rangle_\Omega := \frac{1}{\Omega} \int_\Omega \chi_\phi d\Omega. \tag{1.62}$$

Any scalar or vector function g may be volume averaged by multiplication with the characteristic function χ_ϕ and integration over the control volume Ω to obtain its correspondent phase averaged value G_ϕ.

$$\alpha_\phi G_\phi = \langle \chi_\phi g \rangle_\Omega := \frac{1}{\Omega} \int_\Omega g \chi_\phi d\Omega. \tag{1.63}$$

Note, that this averaging definition corresponds to volume-weighted averages of the selected quantity. Fluctuations of those properties are expressed by:

$$g' \chi_\phi = [g - G_\phi] \chi_\phi. \tag{1.64}$$

If using the Favre averaged (or volume-mass averaged) definition one obtains for the phase averaged value G_ϕ is :

$$\alpha_\phi \rho_\phi G_\phi = \langle \rho g \chi_\phi \rangle_\Omega := \frac{1}{\Omega} \int_\Omega \rho g \chi_\phi d\Omega \tag{1.65}$$

Fluctuations of Favre averaged quantities are noted by double primed symbols g'' and are defined by :

$$\rho_\phi \langle g'' \chi_\phi \rangle_\Omega = -\langle \rho' g'' \chi_\phi \rangle_\Omega, \tag{1.66}$$

$$\langle \rho g'' \chi_\phi \rangle_\Omega = 0. \tag{1.67}$$

To simplify the following averaging properties are assumed, even if they are mathematically not all strictly fulfilled.

[†] see Sagaut [84] for a thorough discussion on filters and consequences for Large Eddy Simultation

1. linearity:

$$\langle a+b\rangle_\Omega = \langle a\rangle_\Omega + \langle b\rangle_\Omega \tag{1.68}$$
$$\langle \lambda a\rangle_\Omega = \lambda \langle a\rangle_\Omega \tag{1.69}$$

2. idempotence:

$$\langle \langle a\rangle_\Omega b\rangle_\Omega = \langle a\rangle_\Omega \langle b\rangle_\Omega \tag{1.70}$$

3. commutation with derivative operators:

$$\left\langle \frac{\partial}{\partial x_i} a \right\rangle_\Omega = \frac{\partial}{\partial x_i} \langle a\rangle_\Omega \tag{1.71}$$
$$\left\langle \frac{\partial}{\partial t} a \right\rangle_\Omega = \frac{\partial}{\partial t} \langle a\rangle_\Omega \tag{1.72}$$

The errors due to the commutation of the filtering process with the derivatives is discussed by Sagaut [84] in the case of mono-phase LES computations.

1.4.4 Navier-Stokes equations in the two fluid model

In the following subsections the equations of the so called two-fluid model are derived by volume averaging of the complete Navier-Stokes equations. The two-fluid model is obtained by applying the following steps to every conservation equation:

1. Multiplication by the indicator function χ_ϕ.
2. Application of the commutation relations to possible terms.
3. Favre Averaging over the control volume.
4. Replacement of unclosed terms by closure models.

For convenience the following convention for notation is applied in this section. Small letters such as $u_i, p, h, e, \sigma_{ij}, \dot{\omega}_k$ describe quantities in each phase before the volume average. Capital letter such as $U_{\phi,i}, P_\phi, H_\phi, E_\phi, \Sigma_{\phi,ij}, \dot{\Omega}_{\phi,k}$ describe the corresponding filtered quantity of the phase ϕ. Mass fractions Y_k are already indicated by capital letter in the Navier Stokes equations. The phase index ϕ serves to identify the phase and therefore also a volume filtered quantity.

Continuity

The continuity equation is obtained from the corresponding Navier-Stokes Eq. 1.52 by applying the the procedure described above and by using the commutation relations Eqs. 1.59

to 1.61 :

$$\frac{\partial}{\partial t}\rho + \frac{\partial}{\partial x_j}\rho u_j = 0 \tag{1.73}$$

$$\chi_\phi \frac{\partial}{\partial t}\rho + \chi_\phi \frac{\partial}{\partial x_j}\rho u_j = 0 \tag{1.74}$$

$$\frac{\partial}{\partial t}\chi_\phi \rho + \frac{\partial}{\partial x_j}\chi_\phi \rho u_j = -\rho(u_j - w_j)n_{\phi,j}\delta_{\zeta,\phi} \tag{1.75}$$

$$\frac{\partial}{\partial t}\alpha_\phi \rho_\phi + \frac{\partial}{\partial x_j}\alpha_\phi \rho_\phi U_{\phi,j} = -\left\langle \rho(u_j - w_j)n_{\phi,j}\delta_\phi \right\rangle_\Omega \tag{1.76}$$

The right hand term of Eq. 1.76 is the mass transport through the interface and is abbreviated henceforth by Γ_ϕ:

$$\Gamma_\phi = -\left\langle \rho(u_j - w_j)n_{\phi,j}\delta_\phi \right\rangle_\Omega \tag{1.77}$$

In the type of application considered in this study (sprays of liquid fuels in gas) Γ_ϕ represents evaporation or condensation.

Species

The species equation is obtained from the corresponding Navier-Stokes Eq. 1.53 like the continuity equation :

$$\frac{\partial}{\partial t}\rho Y_k + \frac{\partial}{\partial x_j}\rho Y_k u_j = \frac{\partial}{\partial x_j}\rho D_k \frac{\partial}{\partial x_j}Y_k + \dot{\omega}_k \tag{1.78}$$

$$\chi_\phi \frac{\partial}{\partial t}\rho Y_k + \chi_\phi \frac{\partial}{\partial x_j}\rho Y_k u_j = \chi_\phi \frac{\partial}{\partial x_j}\rho D_k \frac{\partial}{\partial x_j}Y_k + \chi_\phi \dot{\omega}_k \tag{1.79}$$

$$\frac{\partial}{\partial t}\chi_\phi \rho Y_k + \frac{\partial}{\partial x_j}\chi_\phi \rho Y_k u_j = -\rho Y_k(u_j - w_j)n_{\phi,j}\delta_{\zeta,\phi} \tag{1.80}$$

$$+\chi_\phi \frac{\partial}{\partial x_j}\rho D_k \frac{\partial}{\partial x_j}Y_k + \chi_\phi \dot{\omega}_k \tag{1.81}$$

$$\frac{\partial}{\partial t}\alpha_\phi \rho_\phi Y_{\phi,k} + \frac{\partial}{\partial x_j}\alpha_\phi \rho_\phi Y_{\phi,k} U_{\phi,j} = -\left\langle Y_k \rho(u_j - w_j)n_{\phi,j}\delta_\phi \right\rangle_\Omega + \alpha_\phi \frac{\partial}{\partial x_j}\rho_\phi D_k \frac{\partial}{\partial x_j}Y_{\phi,k} \tag{1.82}$$

$$+\frac{\partial}{\partial x_j}\left(\alpha_\phi \rho_\phi Y_{\phi,k}U_{\phi,j} - \left\langle \chi_\phi \rho Y_k u_j \right\rangle_\Omega\right) + \alpha_\phi \dot{\Omega}_{\phi,k} \tag{1.83}$$

The first term on the right hand side of Eq.1.76 is the mass transport through the interface :

$$\Gamma_{\phi,k} = -\left\langle \rho Y_k(u_j - w_j)n_{\phi,j}\delta_\phi \right\rangle_\Omega \tag{1.84}$$

The mass exchange term then corresponds to the exchange of the mass fraction in between the gaseous carrier phase and the liquid droplets $\Gamma_{\phi,k}$. If for example a mono-component fuel is transported and evaporated, only the corresponding gaseous transport equation has the source term $\Gamma_{\phi,k}$ that is then identical to the source term in the continuity equation Γ_ϕ.

Momentum

The momentum equation (Eq. 1.54) undergoes the same treatment as the continuity/species equation. For simplicity the pressure and viscous stresses are regrouped into the stress tensor $\sigma_{ij} = -\delta_{ij}\frac{\partial}{\partial x_j}p + \tau_{ij}$. The momentum transport equations is then obtained by:

$$\chi_\phi \frac{\partial}{\partial t}\rho u_i + \chi_\phi \frac{\partial}{\partial x_j}\rho u_i u_j = \chi_\phi \frac{\partial}{\partial x_j}\sigma_{ij} \tag{1.85}$$

$$\frac{\partial}{\partial t}\rho u_i \chi_\phi + \frac{\partial}{\partial x_j}\rho u_i u_j \chi_\phi + (\rho u_i)(u_j - w_j)n_{\phi,j}\delta_\phi = \frac{\partial}{\partial x_j}\sigma_{ij}\chi_\phi + \sigma_{ij}n_{\phi,j}\delta_\phi \tag{1.86}$$

$$\frac{\partial}{\partial t}\alpha_\phi\rho_\phi U_{\phi,i} + \frac{\partial}{\partial x_j}\alpha_\phi\rho_\phi U_{\phi,i}U_{\phi,j} = \frac{\partial}{\partial x_j}\left(\alpha_\phi\rho_\phi U_{\phi,i}U_{\phi,j} - \langle\chi_\phi\rho u_i u_j\rangle_\Omega\right) + \left\langle\frac{\partial}{\partial x_j}\chi_\phi\sigma_{ij}\right\rangle_\Omega + \langle\sigma_{ij}n_{\phi,j}\delta_\phi\rangle_\Omega - \langle(\rho u_i)(u_j - w_j)n_{\phi,j}\delta_\phi\rangle_\Omega \tag{1.87}$$

At this place it is useful to introduce some shortcuts to be used later on.

$$\langle\sigma_{ij}\chi_\phi\rangle_\Omega =: \alpha_\phi\Sigma_{\phi,ij} \tag{1.88}$$

$$\langle(\sigma_{ij} - \rho u_i(u_j - w_j))\, n_{\phi,j}\delta_\phi\rangle_\Omega =: I_{\phi,i} \tag{1.89}$$

$$\langle(\rho u_i(u_j - w_j)n_{\phi,j}\delta_\phi\rangle_\Omega =: \Upsilon_{\phi,i} \tag{1.90}$$

$\Sigma_{\phi,ij}$ is the two-fluid version of the stress tensor of the phase ϕ. $I_{\phi,i}$ unites all the forces due to the interaction of the two phases such as drag (and surface tension), momentum exchange due to evaporation etc.

One difficulty in the momentum equation of the dispersed phase is associated to the stress term $\Sigma_{l,ij}$. In the carrier phase, since it can be considered as a continuous medium, this tensor corresponds to the pressure and viscous tensor. In the case of the dispersed phase this tensor corresponds to pressure and viscous stresses in the inclusions. If surface tension is neglected, the pressure within the inclusion is equal to the carrier phase pressure. There are models that consider two different pressure equations for the carrier and dispersed phase (see [86],[36]). It is however common practice to use the carrier phase pressure in the dispersed phase equation [110]. This leads to a term of the form $\alpha_l\frac{\partial}{\partial x_i}P_g$ in the momentum equation of the dispersed phase. This term can be interpreted as the Archimedes force. It can be explained by considering the carrier phase pressure force on the inclusion expressed by its surface integral :

$$F_i = \int_{\partial V} P n_i dA = \int_V \frac{\partial}{\partial x_i} P dV \tag{1.91}$$

Here n_i is the surface normal of the inclusion. This integral can be transformed into a volume integral of the pressure gradient. Then, placing a control volume that includes the particle and the surrounding carrier phase one may extend the volume integral over the particle to the volume integral over the control volume using the characteristic function.

$$\int_V \frac{\partial}{\partial x_i} P dV = \frac{1}{\Omega}\int_\Omega \chi_l \frac{\partial}{\partial x_i} P d\Omega = \alpha_l \frac{\partial}{\partial x_i} P_g \tag{1.92}$$

Care has to be taken if this force is included, since it may cover a part of the forces already considered on a single particle (see section 1.1.4).
The residual viscous stresses of $\Sigma_{l,ij}$ for the dispersed phase are often neglected, since the internal flow of the inclusions are not considered.
Using the idempotence hypothesis one may divide the pressure term into a filtered pressure and a fluctuating pressure and use it to decompose the stress tensor. The fluctuating pressure is however correlated to the local instantaneous carrier phase velocity field. Using $p = P + p'$ one may write the stress tensor component of the forces due to interaction of the fluids as:

$$\begin{aligned} \langle \sigma_{ij} n_{\phi,j} \delta_\phi \rangle_\Omega &= \langle [\tau_{ij} - p\delta_{ij}]\, n_{\phi,j} \delta_\phi \rangle_\Omega && (1.93) \\ &= \langle [\tau_{ij} - p'\delta_{ij}]\, n_{\phi,j} \delta_\phi \rangle_\Omega - P_\phi \langle n_{\phi,i} \delta_\phi \rangle_\Omega && (1.94) \\ &= \langle [\tau_{ij} - p'\delta_{ij}]\, n_{\phi,j} \delta_\phi \rangle_\Omega + P_\phi \frac{\partial}{\partial x_i} \alpha_\phi && (1.95) \end{aligned}$$

Performing the same operation on the term $\Sigma_{\phi,ij}$ yields:

$$\begin{aligned} \frac{\partial}{\partial x_j} \alpha_\phi \Sigma_{\phi,ij} &= \frac{\partial}{\partial x_j} \alpha_\phi \left(\langle \tau_{ij} \rangle_\Omega - P_\phi \delta_{ij} \right) \\ &= \frac{\partial}{\partial x_j} \alpha_\phi \langle \tau_{ij} \rangle_\Omega - \frac{\partial}{\partial x_i} \alpha_\phi P_\phi. && (1.96) \end{aligned}$$

Finally combining the pressure related terms one obtains a term $-\alpha_\phi \frac{\partial}{\partial x_i} P_\phi$.
The tensor $\langle \chi_\phi \rho u_i'' u_j'' \rangle_\Omega = \langle \chi_\phi \rho u_i u_j \rangle_\Omega - \alpha_\phi \rho_\phi U_{\phi,i} U_{\phi,j}$ is for the dispersed phase the two-fluid equivalent of the Quasi Brownian Stress tensor. Modeling of this stress tensor from the volume filtered approach is not clear however. Here, it represents the fluctuating part of the particle velocity in the control volume. The considered particles are not a continuous medium and therefore particles do not have contact forces. The only possible direct interaction are collisions. Neighboring particles see however a similar carrier phase velocity field and undergo therefore a repelling force towards a similar equilibrium. When collisions are neglected this is however not an argument to model the subgrid stresses by a pressure and viscous term.
In the case of the carrier phase the stress tensor (Eq. 1.88) represents the "subgrid" Reynolds stresses. The Tensor $T_{\phi,ij}$ represents the laminar molecular stresses in each phase.
Defining furthermore,

$$\langle [\tau_{ij} - p'\delta_{ij}]\, n_{\phi,j} \delta_\phi \rangle_\Omega := I'_{\phi,i} \tag{1.97}$$

one may rewrite the momentum equation as:

$$\begin{aligned} &\frac{\partial}{\partial t} \alpha_\phi \rho_\phi U_{\phi,i} + \frac{\partial}{\partial x_j} \alpha_\phi \rho_\phi U_{\phi,i} U_{\phi,j} + \frac{\partial}{\partial x_j} \left\langle \rho u_i'' u_j'' \chi_\phi \right\rangle_\Omega = \\ &\quad \frac{\partial}{\partial x_j} \alpha_\phi T_{\phi,ij} - \alpha_\phi \frac{\partial}{\partial x_i} P_\phi + \alpha_\phi \rho_\phi G_i + I'_{\phi,i} - \Upsilon_{ij} && (1.98) \end{aligned}$$

Sensible Enthalpy

The conservation equation for the sensible enthalpy h_s reads:

$$\frac{\partial}{\partial t}\rho h_s + \frac{\partial}{\partial x_j}\rho u_j h_s = \frac{d}{dt}p + \tau_{ij}\frac{\partial}{\partial x_j}u_i - \frac{\partial}{\partial x_j}q_j \tag{1.99}$$

The standard procedure of multiplying by the indicator function yields,

$$\chi_\phi\frac{\partial}{\partial t}\rho h_s + \chi_\phi\frac{\partial}{\partial x_j}\rho u_j h_s = \chi_\phi\frac{d}{dt}p + \chi_\phi\tau_{ij}\frac{\partial}{\partial x_j}u_i - \chi_\phi\frac{\partial}{\partial x_j}q_j, \tag{1.100}$$

and the commutation relation delivers:

$$\begin{aligned}\frac{\partial}{\partial t}\chi_\phi\rho h_s + \frac{\partial}{\partial x_j}\chi_\phi\rho u_j h_s + (\rho h_s)(u_j - w_j)n_{\phi,j}\delta_\phi = \\ \frac{d}{dt}\chi_\phi p + p(u_j - w_j)n_{\phi,j}\delta_\phi + \chi_\phi\tau_{ij}\frac{\partial}{\partial x_j}u_i - \frac{\partial}{\partial x_j}\chi_\phi q_j - q_j n_{\phi,j}\delta_\phi.\end{aligned} \tag{1.101}$$

The final step, averaging over the control volume leads to:

$$\begin{aligned}&\frac{\partial}{\partial t}\alpha_\phi\rho_\phi H_{\phi,s} + \frac{\partial}{\partial x_j}\alpha_\phi\rho_\phi U_{\phi,j}H_{\phi,s} + \langle(\rho h_s)(u_j - w_j)n_{\phi,j}\delta_\phi\rangle_\Omega + \frac{\partial}{\partial x_j}\left\langle\rho u_j'' h_s''\chi_\phi\right\rangle_\Omega = \\ &\quad\frac{d}{dt}\alpha_\phi P_\phi + \langle p(u_j - w_j)n_{\phi,j}\delta_\phi\rangle_\Omega + \left\langle u_j''\frac{\partial}{\partial x_j}\chi_\phi p''\right\rangle_\Omega + \left\langle\chi_\phi\tau_{ij}\frac{\partial}{\partial x_j}u_i\right\rangle_\Omega - \frac{\partial}{\partial x_j}\alpha_\phi q_{\phi,j} \\ &\quad - \langle q_j n_{\phi,j}\delta_\phi\rangle_\Omega\end{aligned} \tag{1.102}$$

At this point one may identify some terms that need to be modeled :

- The term $\langle(\rho h_s)(u_j - w_j)n_{\phi,j}\delta_\phi\rangle_\Omega$ represents the density weighted enthalpy exchange through the interface.
- The term $\langle q_j n_{\phi,j}\delta_\phi\rangle_\Omega$ represents the heat flux through the interface.
- The term representing the phase averaged viscous stresses $\left\langle\chi_\phi\tau_{ij}\frac{\partial}{\partial x_j}u_i\right\rangle_\Omega$ may be decomposed into,

$$\left\langle\chi_\phi\tau_{ij}\frac{\partial}{\partial x_j}u_i\right\rangle_\Omega = \hat{T}_{\phi,ij}\frac{\partial}{\partial x_j}\alpha_\phi U_{\phi,i} - \langle\tau_{ij}u_i n_{\phi,j}\delta_\phi\rangle_\Omega\,. \tag{1.103}$$

Grouping the terms due to interface interactions on the one hand and terms due to viscous, turbulent forces and internal heat diffusion on the other hand, this yields :

$$\begin{aligned}\Pi_\phi = &-\langle(\rho h_s)(u_j - w_j)n_{\phi,j}\delta_\phi\rangle_\Omega + \langle p(u_j - w_j)n_{\phi,j}\delta_\phi\rangle_\Omega \\ &-\langle q_j n_{\phi,j}\delta_\phi\rangle_\Omega - \langle\tau_{ij}u_{\phi,i}n_{\phi,j}\delta_\phi\rangle_\Omega + \left\langle u_j''\frac{\partial}{\partial x_j}\chi_\phi p''\right\rangle_\Omega\end{aligned} \tag{1.104}$$

$$S_\phi^m = \hat{T}_{\phi,ij}\frac{\partial}{\partial x_j}\alpha_\phi U_{\phi,i} - \frac{\partial}{\partial x_j}\alpha_\phi Q_{\phi,j} - \frac{\partial}{\partial x_j}\left\langle\rho u_j'' h_s''\chi_\phi\right\rangle_\Omega \tag{1.105}$$

Finally one deduces a short form for the sensible Enthalpy :

$$\frac{\partial}{\partial t}\alpha_\phi\rho_\phi H_{\phi,s} + \frac{\partial}{\partial x_j}\alpha_\phi\rho_\phi U_{\phi,j}H_{\phi,s} = \Pi_\phi + S_\phi^m + \frac{d}{dt}\alpha_\phi P_\phi. \tag{1.106}$$

Internal Energy

Using the relation between enthalpy and energy $h_s = e_s + p/\rho$ and the development of the pressure :

$$\frac{d}{dt}\alpha_\phi P_\phi = \frac{\partial}{\partial t}\alpha_\phi P_\phi + U_{\phi,j}\frac{\partial}{\partial x_j}\alpha_\phi P_\phi, \tag{1.107}$$

$$= \frac{\partial}{\partial t}\alpha_\phi P_\phi + \frac{\partial}{\partial x_j}\alpha_\phi P_\phi U_{\phi,j} - \alpha_\phi P_\phi\frac{\partial}{\partial x_j}U_{\phi,j}, \tag{1.108}$$

One may rewrite the enthalpy equation as a sensible Energy conservation equation:

$$\frac{\partial}{\partial t}\alpha_\phi(\rho_\phi e_{s,\phi} + P_\phi) + \frac{\partial}{\partial x_j}\alpha_\phi U_{\phi,j}(\rho_\phi e_{s,\phi} + P_\phi) = \Pi_\phi + S_\phi^m + \frac{d}{dt}\alpha_\phi P_\phi. \tag{1.109}$$

Subtraction of the pressure term from both sides leads to the equation for the conservation of sensible energy:

$$\frac{\partial}{\partial t}\alpha_\phi(\rho_\phi e_{s,\phi}) + \frac{\partial}{\partial x_j}\alpha_\phi U_{\phi,j}(\rho_\phi e_{s,\phi}) = \Pi_\phi + S_\phi^m - \alpha_\phi P_\phi\frac{\partial}{\partial x_j}U_{\phi,j}. \tag{1.110}$$

Transport equation for the number density

When evaporation is excluded and the particles are assumed to be spheres of uniform size there exists a simple relation between the volume fraction, the particle number density and the particles ($\alpha_l = n_p\pi d^3\pi/6$). The transport equation for the volume fraction 1.76 can then be used to determine a transport equation for the droplet number density.

$$\frac{\partial}{\partial t}n_p + \frac{\partial}{\partial x_j}n_p U_{l,j} = 0 \tag{1.111}$$

Transport equation for dispersed phase subgrid energy

The transport equation for the dispersed phase subgrid energy is constructed in Appendix A.2. The subgrid kinetic energy is noted by :

$$\Delta q^2_{\Omega,l} = \frac{1}{2}\langle u_k'' u_k''\rangle_{\Omega,l} \tag{1.112}$$

For such a construction some important assumptions need to be made on the properties on the dispersed phase. Notably the particles in one control volume need to have the same mass. Such restrictions can be relaxed in a more complicated derivation which is beyond

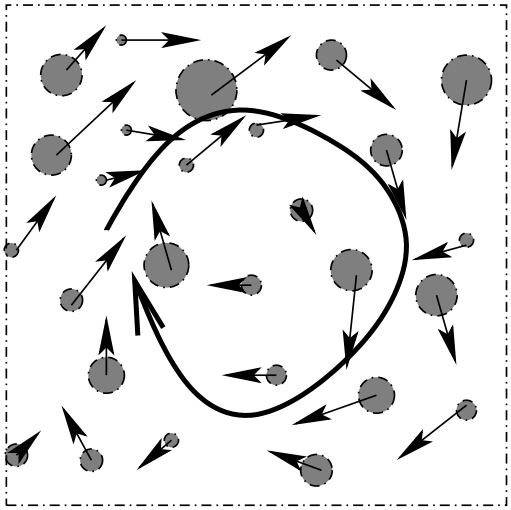

Figure 1.6: A control volume with particles that have an uncorrelated and correlated collective motion. Some part of the collective motion disappears in the volume filtered approach due to the size of the control volume.

the scope of this analysis. The resulting transport equation of the subgrid energy is similar to the QBE but does not contain the same information.

$$\begin{aligned}\frac{\partial}{\partial t}\alpha_l\rho_l\Delta q^2_{\Omega,l} + \frac{\partial}{\partial x_j}\alpha_l\rho_l U_{l,j}\Delta q^2_{\Omega,l} &= -\alpha_l\rho_l\tau_{l,kj}\frac{\partial}{\partial x_j}U_{l,k} + \frac{\alpha_l\rho_l}{\tau_p}\left(\Delta q_{\Omega,fp} - 2\Delta q^2_{\Omega,l}\right) + \Delta q^2_{\Omega,l}\Gamma \\ &\quad -\frac{\partial}{\partial x_k}\alpha_l\rho_l\langle u_i'' u_j'' u_k''\rangle_{\Omega,l}\end{aligned}$$

Here the following shorthand for the stress tensor is used :

$$\tau_{l,ij} = \langle u_i'' u_j''\rangle_{\Omega,l} \tag{1.113}$$

The stress tensor $\tau_{l,ij}$ can be identified with the stress tensor of the momentum equation in the case of particles with identical mass:

$$\alpha_l\rho_l\langle u_i'' u_j''\rangle_{\Omega,l} = \langle\chi_l\rho u_i'' u_j''\rangle_\Omega \tag{1.114}$$

The difference between the QBE and the subgrid kinetic energy is discussed below.

1.4.5 Comparison of ensemble averaged transport equation to volume filtered transport equations

The equations for the dispersed phase (Eqs. 1.35, 1.36) obtained by ensemble averaging can be compared to the equations obtained by volume filtering (Eqs. 1.76, 1.87). At first glance the two sets of equations compare remarkably, if the droplet number density is replaced

by the equivalent volume fraction ($\breve{n}_p = \alpha_l 6/\pi d^3$). It has to be kept in mind however, that even if the structure of the equations is similar, if not identical, the interpretation of the transported quantity is somehow different. In the case of the ensemble average conditioned on one carrier phase realization, the dispersed phase quantities consist of an average of many realizations. The volume filtered equations represent an average of one carrier phase and one dispersed phase realization. One could imagine the existence of more than one combination of carrier phase dispersed phase realization, that lead to the same volume average, but this is not necessarily a representative sub-ensemble of the relevant realizations. This point is discussed further by Drew & Passmann [24].
Another major difference is due to the volume filtering approach. Volume filtered equations are continuous and represent characteristic properties at length scales larger than the control volume used for the filtering operation. Ensemble averaging does not impose a characteristic length scale and ensemble averaged equations are, a priori, valid at all length scales. This has consequences for the construction and interpretation of the stress tensor in the ensemble averaged and volume averaged approaches. Transport equations for both stress tensors are constructed in Appendix A. In the case of volume filtered equations the stress tensor $\langle u_i'' u_j'' \rangle_{\Omega,l}$ contains both, the correlated and the uncorrelated motion of particles at length scales smaller than the filter size. In the case of ensemble averaged equations the stress tensor $\langle \delta u_i \delta u_j \rangle_p$ only contains the uncorrelated motion of particles since there is no length scale associated to the ensemble averaging process. This difference is illustrated in Fig.1.6. It shows a square control volume that contains particles of different sizes. The particles have, at the level of the control volume, a collective vortex like motion. In the ensemble averaged approach this collective motion of the particles is contained in the mesoscopic particle velocity field $\breve{u}_p$. In the volume filtered approach this part of the motion is part of the subgrid stress tensor $\langle u_i'' u_j'' \rangle_{\Omega,l}$. If numerical simulations of the ensemble averaged system of equations is performed, the equations are implicitly filtered at the scale of the numerical grid. Therefore it is necessary to insure that all physical scales are resolved in the numerical computation when choosing the numerical grid.
When the ensemble averaged equations are filtered, a term for the subgrid stress arises. The sum of this subgrid stress and the stress tensor of QBM is equivalent to stress tensor obtained by volume filtering. The ensemble averaged equations allow to separate the QBM stress from the subgrid stress. Therefore the ensemble averaged equations can be used to investigate the uncorrelated motion apart from the correlated motion of subgrid stresses. This will be discussed further in section 5.3.

Eulerian conservation equations for volume fractions obtained by ensemble average

Conservation equations that are equivalent to Eqs.1.35,1.36 and 1.49 can be obtained when the particle mass is included in the conserved variable. For instance $\psi_p = m_p$ where m_p is the particle mass yields a mass conservation equation:

$$\frac{\partial}{\partial t}\breve{n}_p m_p + \frac{\partial}{\partial x_j}\breve{n}_p m_p \breve{u}_{p,j} = \breve{n}_p \langle \frac{\partial}{\partial t} m_p + c_{p,j}\frac{\partial}{\partial x_j} m_p \rangle_p + \frac{\partial}{\partial x_j}\breve{n}_p \left(m_p \breve{u}_{p,j} - \langle m_p c_{p,j} \rangle_p \right) + \mathcal{C}_p \quad (1.115)$$

Using the identities for particle density $\rho_p = m_p/\left(\pi/6d^3\right)$ and particle volume fraction $\alpha_p = \breve{n}_p\pi/6d^3$ one can rewrite the mass conservation Eq. 1.115 as a dispersed phase volume conservation equation:

$$\frac{\partial}{\partial t}\alpha_p\rho_p + \frac{\partial}{\partial x_j}\alpha_p\rho_p\breve{u}_{p,j} = \breve{n}_p\langle\frac{\partial}{\partial t}m_p + c_{p,j}\frac{\partial}{\partial x_j}m_p\rangle_p + \frac{\partial}{\partial x_j}\left(\alpha_p\rho_p\breve{u}_{p,j} - \langle\breve{n}_p m_p c_{p,j}\rangle_p\right) + \mathcal{C}_p \quad (1.116)$$

The first term on the right hand side of Eq. 1.116, $\breve{n}_p\langle\frac{\partial}{\partial t}m_p\rangle$ corresponds to the change of the individual particle mass. In reactive systems with evaporating droplets this term can be modeled by evaporation. The signification of the second on the right hand side, $\langle c_{p,j}\frac{\partial}{\partial x_j}m_p\rangle_p$ becomes clear by replacing m_p by $\rho_l 6/\pi d^3$. For constant particle density, this designates the correlation between particle velocity and change of particle volume and therefore diameter in space. For monodispersed two-phase flows this term is zero. The third term on the right hand side of Eq. 1.116 represents the correlations in mass and velocity fluctuation and is neglected at this point. The fourth term on the right hand side of Eq. 1.116 is zero when collisions are not considered.
For $\psi_p = m_p c_{p,i}$ one recovers an equation for the conservation of inertia:

$$\begin{aligned}\frac{\partial}{\partial t}\alpha_p\rho_p\breve{u}_{p,i} + \frac{\partial}{\partial x_j}\alpha_p\rho_p\breve{u}_{p,j}\breve{u}_{p,i} &= \frac{\partial}{\partial x_j}\left(\alpha_p\rho_p\breve{u}_{p,j}\breve{u}_{p,i} - \breve{n}_p\langle m_p c_{p,j}c_{p,i}\rangle_p\right) \quad (1.117)\\ &+\breve{n}_p\langle F_{p,i}\rangle_p + \breve{n}_p\langle\frac{\partial}{\partial t}m_p c_{p,i} + c_{p,j}\frac{\partial}{\partial x_j}m_p c_{p,i}\rangle_p + \mathcal{C}_p\left(m_p c_{p,i}\right)\end{aligned}$$

The first term on the right hand side of Eq. 1.117 represents the stress term due to uncorrelated particle velocities as in Eq. 1.36. The second term on the right hand side of Eq. 1.117 corresponds to the momentum change due to an an external force such as drag. The third term represents momentum change due to mass change, whereas the last term on the right hand side of Eq. 1.117 represents particle collisions and is neglected.

Eulerian conservation equations : Ensemble average vs Volume average

The Eulerian equations obtained by ensemble and by volume average are summarized in table 1.1. In the case of the ensemble average, the presented equations can be obtained directly as a moment transport from the kinetic equation with exception of the volume fraction that needed the spherical particle assumption. In the case of the volume averaged equations other assumptions are necessary. In the case of the transport equation for the particle number density, the spherical droplet assumption is made and relation between evaporation and particle diameter is assumed. The equation of subgrid kinetic energy is derived making the assumption, that all particles have identical diameter in the control volume.

ensemble averaged	volume averaged
number density	
$\frac{\partial}{\partial t}\breve{n}_p + \frac{\partial}{\partial x_j}\breve{n}_p\breve{u}_{p,j} = 0$ $\psi_p = 1$	$\frac{\partial}{\partial t}n_p + \frac{\partial}{\partial x_j}n_p U_{l,j} = 0$ Navier Stokes continuity + spherical droplet assumption
dispersed phase mass fraction	
$\frac{\partial}{\partial t}\alpha_p\rho_p + \frac{\partial}{\partial x_j}\alpha_p\rho_p\breve{u}_{p,j} = 0$ $\psi_p = m_p +$ spherical droplet assumption	$\frac{\partial}{\partial t}\alpha_l\rho_l + \frac{\partial}{\partial x_j}\alpha_l\rho_l U_{l,j} = 0$ Navier Stokes continuity
species equation	
	$\frac{\partial}{\partial t}\alpha_l\rho_l Y_{l,k} + \frac{\partial}{\partial x_j}\alpha_l\rho_l Y_{l,k}U_{l,j} = \langle\chi_l\rho Y_k'' u_j''\rangle_\Omega$ Navier Stokes species
momentum equation	
$\frac{\partial}{\partial t}\breve{n}_p\breve{u}_{p,i} + \frac{\partial}{\partial x_j}\breve{n}_p\breve{u}_{p,i}\breve{u}_{p,j} = -\frac{\partial}{\partial x_i}P_{QB}$ $\frac{\partial}{\partial x_j}\breve{\tau}_{p,ij} - \frac{1}{\tau_p}\left(\breve{u}_{p,i} - u_i\right)$ $\psi_p = c_{p,i}$	$\frac{\partial}{\partial t}\alpha_l\rho_l U_{l,i} + \frac{\partial}{\partial x_j}\alpha_l\rho_l U_{l,i}U_{l,j} =$ $-\frac{\partial}{\partial x_j}\langle\chi_l\rho u_i'' u_j''\rangle_\Omega - \alpha_l\frac{\partial}{\partial x_i}P_g$ $+\alpha_l\rho_l G_i + I_{l,i} - \Upsilon_{ij}$ Navier Stokes momentum equation
QBE	
$\frac{\partial}{\partial t}\breve{n}_p\delta\breve{\theta}_p + \frac{\partial}{\partial x_j}\breve{n}_p\breve{u}_{p,j}\delta\breve{\theta}_p =$ $-2\frac{\breve{n}_p}{\tau_p}\delta\breve{\theta}_p - \left[P_{QB}\delta_{ij} - \breve{\tau}_{p,ij}\right]\frac{\partial\breve{u}_{p,i}}{\partial x_j}$ $+\frac{\partial}{\partial x_j}\breve{n}_p\breve{k}_{QB}\frac{\partial}{\partial x_j}\delta\breve{\theta}_p$ $\psi_p = c_{p,k}c_{p,k}$	not identified
subgrid energy	
	$\frac{\partial}{\partial t}\alpha_l\rho_l\Delta q_{\Omega,l}^2 + \frac{\partial}{\partial x_j}\alpha_l\rho_l U_{l,j}\Delta q_{\Omega,l}^2 =$ $-\alpha_l\rho_l\tau_{l,kj}\frac{\partial}{\partial x_j}U_{l,k} - \frac{\partial}{\partial x_k}\alpha_l\rho_l\langle u_i'' u_j'' u_k''\rangle_{\Omega,l}$ $+\frac{\alpha_l\rho_l}{\tau_p}\left(\Delta q_{\Omega,fp} - 2\Delta q_{\Omega,l}^2\right)$ see Appendix A.2
dispersed phase sensible enthalpy	
$\frac{\partial}{\partial t}\breve{n}_p\breve{h}_{p,s} + \frac{\partial}{\partial x_j}\breve{n}_p\breve{u}_{p,j}\breve{h}_{p,s} =$ $+\frac{\partial}{\partial x_j}\left(\breve{n}_p\breve{u}_{p,j}\breve{h}_{p,s} - \breve{n}_p\langle c_{p,j}h_{p,s}\rangle_p\right)$ $+\breve{n}_p\langle\frac{\partial}{\partial t}h_{p,s} + c_{p,j}\frac{\partial}{\partial x_j}h_{p,s}\rangle_p + \mathcal{C}\left(h_{p,s}\right)$ $\psi_p = h_{p,s}$	$\frac{\partial}{\partial t}\alpha_\phi\rho_\phi H_{l,s} + \frac{\partial}{\partial x_j}\alpha_\phi\rho_\phi U_{\phi,j}H_{l,s} =$ $\Pi_l + S_l^m + \frac{d}{dt}\alpha_l P_l$ Navier Stokes enthalpy equation

Table 1.1: Comparison of ensemble averaged to volume averaged transport equations in the absence of mass transfer. Note that even if the transport equations have similar form, their physical content is not identical (see section 1.4.5)

1.5 Nature of Eulerian-Eulerian Equations

While mathematical correctness does not imply physical validity, the latter cannot be obtained without the former.
Drew &Passmann [24]

A detailed discussion of the nature of Eulerian-Eulerian Equations is found in the book of Drew and Passman ([24],chap. 19 & 20) and a more fundamental study on conservation laws is found in the book of LeVeque [54].

1.5.1 Fundamental considerations

In the absence of any force on the particle and in the abscence of QBM the Eulerian dispersed phase equation for inertia correspond to the inviscid Burgers equation ([54]).

$$\frac{\partial}{\partial t}u_i + u_j\frac{\partial}{\partial x_j}u_i = 0 \tag{1.118}$$

This equation admits an analytical solution (credited to Hopf and Cole) and it can be shown that, when the characteristics of this equation cross, it admits non-physical triple solutions. Adding a small amount of viscosity changes the nature of the equations and leads to solutions that may admit steep gradients, but stay physical. If the Stokes number is small, the drag force may be sufficient, so that those difficulties do not arise. If the Stokes number is large enough to allow a certain "free path" of the particles this difficulty becomes an issue and pressure and/or viscous terms need to be included to guarantee that physical solutions are obtained.

In the following two sections characteristics of the Eulerian-Eulerian description for dispersed two phase flows are described. The first section considers the ensemble averaged equations. This differs from the two-fluid model approach described in the second section by the phase coupling via pressure and volume fractions as well as the existence of a "sound speed" for the dispersed phase.

1.5.2 Characteristics in ensemble averaged equations

Here the one dimensional equations of the carrier phase and dispersed phase as obtained from ensemble averaging are investigated. Drag force is neglected. The one dimensional set of equations neglecting viscous terms for the two phases is:

$$\frac{\partial}{\partial t}\rho + \frac{\partial}{\partial x}\rho u = 0 \tag{1.119}$$

$$\frac{\partial}{\partial t}\rho u + \frac{\partial}{\partial x}\rho uu + \frac{\partial}{\partial x}P = 0 \tag{1.120}$$

$$\frac{\partial}{\partial t}\rho E + \frac{\partial}{\partial x}\rho uE + \frac{\partial}{\partial x}uP = 0 \tag{1.121}$$

$$\frac{\partial}{\partial t}\breve{n}_p + \frac{\partial}{\partial x}\breve{n}_p\breve{u}_p = 0 \tag{1.122}$$

$$\frac{\partial}{\partial t}\breve{n}_p\breve{u}_p + \frac{\partial}{\partial x}\breve{n}_p\breve{u}_p\breve{u}_p + \frac{\partial}{\partial x}P_{QB} = 0 \tag{1.123}$$

$$\frac{\partial}{\partial t}\breve{n}_p\delta\breve{\theta}_p + \frac{\partial}{\partial x}\breve{n}_p\breve{u}_p\delta\breve{\theta}_p + P_{QB}\frac{\partial}{\partial x}\breve{u}_p = 0 \tag{1.124}$$

This set of conservative equations can be transformed into a primitive set of equations using $\left(\rho E_g = \frac{P_g}{\gamma-1} + \frac{1}{2}\rho_g U_g U_g\right)$ for the gaseous phase and the "equation of state" $P_{QB} = 2/3\breve{n}_p\delta\breve{\theta}_p$ for the dispersed phase.

$$\frac{\partial}{\partial t}\rho + \rho\frac{\partial}{\partial x}u + u\frac{\partial}{\partial x}\rho = 0 \tag{1.125}$$

$$\frac{\partial}{\partial t}u + u\frac{\partial}{\partial x}u + \frac{1}{\rho}\frac{\partial}{\partial x}P = 0 \tag{1.126}$$

$$\frac{\partial}{\partial t}P + \gamma P\frac{\partial}{\partial x}u + u\frac{\partial}{\partial x}P = 0 \tag{1.127}$$

$$\frac{\partial}{\partial t}\breve{n}_p + \breve{n}_p\frac{\partial}{\partial x}\breve{u}_p\breve{u}_p\frac{\partial}{\partial x}\breve{n}_p = 0 \tag{1.128}$$

$$\frac{\partial}{\partial t}\breve{u}_p + \breve{u}_p\frac{\partial}{\partial x}\breve{u}_p + \frac{1}{\breve{n}_p}\frac{\partial}{\partial x}P_{QB} = 0 \tag{1.129}$$

$$\frac{\partial}{\partial t}P_{QB} + \breve{u}_p\frac{\partial}{\partial x}P_{QB} + \frac{5}{2}P_{QB}\frac{\partial}{\partial x}\breve{u}_p = 0 \tag{1.130}$$

This set of equations may be expressed in matrix form.

$$\frac{\partial}{\partial t}\begin{pmatrix}\rho\\ u\\ P\\ \breve{n}_p\\ \breve{u}_p\\ P_{QB}\end{pmatrix} + \begin{pmatrix} u & \rho & 0 & 0 & 0 & 0\\ 0 & u & \frac{1}{\rho} & 0 & 0 & 0\\ 0 & \gamma P & u & 0 & 0 & 0\\ 0 & 0 & 0 & \breve{u}_p & \breve{n}_p & 0\\ 0 & 0 & 0 & 0 & \breve{u}_p & \frac{1}{\breve{n}_p}\\ 0 & 0 & 0 & 0 & \frac{5}{2}P_{QB} & \breve{u}_p \end{pmatrix}\frac{\partial}{\partial x}\begin{pmatrix}\rho\\ u\\ P\\ \breve{n}_p\\ \breve{u}_p\\ P_{QB}\end{pmatrix} = 0 \tag{1.131}$$

The characteristic polynomial of the Jacobian-Matrix is :

$$(u-\lambda)\left((u-\lambda)(u-\lambda) - \frac{\gamma P}{\rho}\right)(\breve{u}_p-\lambda)\left((\breve{u}_p-\lambda)(\breve{u}_p-\lambda) - \frac{\frac{5}{3}P_{QB}}{\breve{n}_p}\right) = 0 \tag{1.132}$$

The eigenvalues of the characteristic polynomial can be divided into two groups: a gaseous and a dispersed phase part. The gaseous part admits the usual values:

$$\lambda_1 = u \tag{1.133}$$

$$\lambda_2 = u + c \tag{1.134}$$

$$\lambda_3 = u - c \tag{1.135}$$

Here the sound speed was defined as $c = \sqrt{\gamma \frac{P}{\rho}}$. The eigenvalues associated to the dispersed phase are:

$$\lambda_1 = \breve{u}_p \tag{1.136}$$

$$\lambda_2 = \breve{u}_p + \sqrt{\frac{5}{2}\frac{P_{QB}}{\breve{n}_p}} \tag{1.137}$$

$$\lambda_3 = \breve{u}_p - \sqrt{\frac{5}{2}\frac{P_{QB}}{\breve{n}_p}} \tag{1.138}$$

Therefore $\sqrt{\frac{5}{2}\frac{P_{QB}}{\breve{n}_p}}$ can be interpreted as the "sound speed" i.e. the velocity of propagation of particles in all directions by Quasi Brownian Motion[‡]. Using the "equation of state" $P_{QB} = 2/3\breve{n}_p\delta\breve{\theta}_p$ one can define this quantity as:

$$\breve{c}_p = \sqrt{\frac{5}{2}\frac{P_{QB}}{\breve{n}_p}} = \sqrt{\frac{5}{3}\delta\breve{\theta}_p} \tag{1.139}$$

Under the assumptions made for the derivation of the ensemble averaged equations for the dispersed phase and neglecting drag force the transport equations do not couple and not influence each other concerning sound speed. Since all eigenvalues are real, this set of equations is hyperbolic and can be treated with the corresponding numerical tools.

1.5.3 Characteristics in the two-fluid model

Here the one-dimensional equations of the two fluid formulation neglecting the viscous terms in the carrier and dispersed phase are used to discuss the behavior of the information propagation in the two-fluid model. The phase coupling via drag force is ignored. The carrier phase pressure is used as pressure for the dispersed phase. It can be seen that this formulation alters the notation of sound speed for the carrier phase depending on the volume/mass loading and the dispersed phase velocity.
The equations of the two-fluid model can be written in a semi-conservative form that shows that the carrier phase pressure couples to the carrier and dispersed phase. The one-dimensional set of equations considered, is:

$$\frac{\partial}{\partial t}\alpha_g\rho_g + \frac{\partial}{\partial x}\alpha_g\rho_g U_g = 0 \tag{1.140}$$

$$\frac{\partial}{\partial t}\alpha_g\rho_g U_g + \frac{\partial}{\partial x}\alpha_g\rho_g U_g U_g + \alpha_g\frac{\partial}{\partial x}P_g = 0 \tag{1.141}$$

$$\frac{\partial}{\partial t}\alpha_g\rho_g E_g + \frac{\partial}{\partial x}\alpha_g\rho_g U_g E_g + \alpha_g\frac{\partial}{\partial x}U_g P_g = 0 \tag{1.142}$$

[‡] Note, that in a gas frequent collisions transfer the information, so that a sound wave can propagate. In the case of the dispersed phase the particles admit a certain "free path length" and, may transport information within this free path. When ignoring collisions one can physically not consider this however as a "sound wave" since after one free path the information is lost.

$$\frac{\partial}{\partial t}\alpha_l\rho_l + \frac{\partial}{\partial x}\alpha_l\rho_l U_l = 0 \quad (1.143)$$

$$\frac{\partial}{\partial t}\alpha_l\rho_l U_l + \frac{\partial}{\partial x}\alpha_l\rho_l U_l U_l + \alpha_l\frac{\partial}{\partial x}P_g = 0 \quad (1.144)$$

$$\frac{\partial}{\partial t}\alpha_l\rho_l E_l + \frac{\partial}{\partial x_j}\alpha_l\rho_l U_l E_l + \alpha_l\frac{\partial}{\partial x}U_l P_g = 0 \quad (1.145)$$

By transformation into primitive form one may express the energy in a pressure transport equation $\left(\rho E_g = \frac{P_g}{\gamma-1} + \frac{1}{2}\rho_g U_g U_g\right)$ [§] and the system may be written as:

$$\frac{\partial}{\partial t}\rho_g + U_g\frac{\partial}{\partial x}\rho_g + \rho_g\frac{\partial}{\partial x}U_g + \frac{\rho_g}{\alpha_g}(U_l - U_g)\frac{\partial}{\partial x}\alpha_l = 0 \quad (1.146)$$

$$\frac{\partial}{\partial t}U_g + U_g\frac{\partial}{\partial x}U_g + \frac{1}{\rho_g}\frac{\partial}{\partial x}P_g = 0 \quad (1.147)$$

$$\frac{\partial}{\partial t}P_g + U_g\frac{\partial}{\partial x}P_g + \gamma P_g\frac{\partial}{\partial x}U_g + \frac{\alpha_l}{\alpha_g}P_g\frac{\partial}{\partial x}U_l + \frac{P_g}{\alpha_g}(U_l - U_g)\frac{\partial}{\partial x}\alpha_l = 0 \quad (1.148)$$

$$\frac{\partial}{\partial t}\alpha_l + \alpha_l\frac{\partial}{\partial x}U_l + U_l\frac{\partial}{\partial x}\alpha_l = 0 \quad (1.149)$$

$$\frac{\partial}{\partial t}U_l + U_l\frac{\partial}{\partial x}U_l + \frac{1}{\rho_l}\frac{\partial}{\partial x}P_g = 0 \quad (1.150)$$

$$\frac{\partial}{\partial t}E_l + U_l\frac{\partial}{\partial x}E_l + \frac{U_l}{\rho_l}\frac{\partial}{\partial x}P_g + \frac{P_g}{\rho_l}\frac{\partial}{\partial x}U_l = 0 \quad (1.151)$$

The previous set of equations may be expressed in matrix form:

$$\frac{\partial}{\partial t}\begin{pmatrix}\rho_g\\U_g\\P_g\\\alpha_l\\U_l\\E_l\end{pmatrix} + \begin{pmatrix}U_g & \rho_g & 0 & \frac{\rho_g}{\alpha_g}(U_l-U_g) & 0 & 0\\0 & U_g & \frac{1}{\rho_g} & 0 & 0 & 0\\0 & \gamma P_g & U_g & \frac{P_g}{\alpha_g}(U_l-U_g) & \frac{\alpha_l}{\alpha_g}P_g & 0\\0 & 0 & 0 & U_l & \alpha_l & 0\\0 & 0 & \frac{1}{\rho_l} & 0 & U_l & 0\\0 & 0 & \frac{U_l}{\rho_l} & 0 & \frac{P_g}{\rho_l} & U_l\end{pmatrix}\frac{\partial}{\partial x}\begin{pmatrix}\rho_g\\U_g\\P_g\\\alpha_l\\U_l\\E_l\end{pmatrix} = 0 \quad (1.152)$$

The characteristic polynomial of the Jacobian Matrix is:

$$(U_g-\lambda)(U_l-\lambda)\left[(U_g-\lambda)^2(U_l-\lambda)^2 - c^2\left((U_l-\lambda)^2 + \frac{\alpha_l\rho_g}{\alpha_g\rho_l\gamma}(U_g-\lambda)^2\right)\right] = 0 \quad (1.153)$$

Here the definition for sound speed $c = \sqrt{\gamma P/\rho}$ has been used. The characteristic polynominal has two trivial eigenvalues:

$$\lambda_1 = U_g$$
$$\lambda_2 = U_l$$

[§]This is valid only for constant heat capacity C_p, mean molar mass W and R

Those two eigenvalues correspond to the entropic modes of the two phases. If α_l is zero the other eigenvalues are:

$$\lambda_{3/4} = U_g \pm c$$
$$\lambda_{5/6} = U_l$$

The first two eigenvalues correspond to the eigenvalues that can be found in the Euler equations. In the case of the absence of the liquid phase the two-fluid formulation therefore has the same sound-speed behavior as the Navier-Stokes equations. In this case all eigenvalues are real and the set of equations is hyperbolic.
If α_l is non-zero there are significantly different roots. For some combinations, the eigenvalues may become complex, and the system may become elliptic and admit non-physical sound speeds.
Considering the same equations without pressure coupling on the liquid phase, (which is just the archimedes force of the gas onto the droplet), the gaseous and liquid phase are decoupled and the eigenvalues of the characterisc polynomial become:

$$\lambda_{1/2} = U_g \pm c$$
$$\lambda_3 = U_g$$
$$\lambda_{4-6} = U_l$$

Those eigenvalues are real and the system is hyperbolic. This shows that if Archimedes force is taken into account, the set of equations couple through the gaseous pressure and the volume fraction. This can lead to non-physical sound speeds that are related to the Eulerian formulation of the dispersed phase. In computations that aim at computing a steady state, such as RANS methods, the coupling of sound speed between the two phases is probably less important. In unsteady computations however, in which for example the link between combustion and acoustic modes is studied, it is questionable whether to include the Archimedes force into the transport equations. Indeed a modification of sound speed alters for instance the eigenmodes of a combustion chamber. The second drawback of a modified sound speed and phase coupling concerns the boundary conditions. Unsteady boundary conditions, in which volume varying volume fractions occur, alter the momentum equation of the carrier phase, since the pressure gradient is pondered by the volume fraction.
In section 1.1.4 the Archimedes force was neglected from the equation of motion of an isolated particle, which density is significantly larger than the density of the carrier phase ($\rho_p \gg \rho_g$). In such cases the pressure term due to Archimedes force can be retracted from the conservation equation.

1.6 Numerical implementation for dispersed two phase flows

The Eulerian equations for the dispersed phase have been implemented into the Navier-Stokes Solver AVBP (V 4.6) [88]. It is based on a 2D/3D finite Volume/ finite Element

method for unstructured, structured and hybrid meshes. The carrier phase conservation equations for density, mass fractions, velocities and total energy (kinetic + internal) ($w = (\rho, \rho Y_k, \rho u, \rho v, \rho w, \rho E)$) are presented in the compact form:

$$\frac{\partial}{\partial t} w_i + \frac{\partial}{\partial x_j} F_{ij} = S_i \tag{1.154}$$

where S_i are source terms in the case of reactive flow and phase coupling. The fluxes F_{ij} are then divided into a non-viscous part, the Euler fluxes F^I_{ij}, and a viscous part F^V_{ij}. The inviscid fluxes are defined as

$$F^I_{ij} = \begin{pmatrix} \rho u & \rho v & \rho w \\ \rho Y_k u & \rho Y_k v & \rho Y_k w \\ \rho u^2 + P & \rho uv & \rho uw \\ \rho uv & \rho v^2 + P & \rho vw \\ \rho uw & \rho vw & \rho w^2 + P \\ (\rho E + P)u & (\rho E + P)v & (\rho E + P)w \end{pmatrix} \tag{1.155}$$

where P is the thermodynamic pressure given by the ideal gas law $P = \rho r T$ and E is the total (kinetic + internal) energy. The viscous fluxes are defined as

$$F^V_{ij} = \begin{pmatrix} 0 & 0 & 0 \\ J_{x,k} & J_{y,k} & J_{z,k} \\ -\tau_{xx} & -\tau_{xy} & -\tau_{xz} \\ -\tau_{yx} & -\tau_{yy} & -\tau_{yz} \\ -\tau_{zx} & -\tau_{zy} & -\tau_{zz} \\ -(u\tau_{xx} + v\tau_{xy} + w\tau_{xz}) + q_x & -(u\tau_{yx} + v\tau_{yy} + w\tau_{zx}) + q_y & -(u\tau_{zx} + v\tau_{zy} + w\tau_{zz}) + q_z \end{pmatrix} \tag{1.156}$$

where $J_{j,k}$ are the species fluxes due to species diffusion, τ_{ij} is the stress tensor and q_j are the fluxes due to thermal diffusion. The stress tensor for the carrier phase is modeled as the trace free tensor of the velocity gradients with the dynamic viscosity μ.

$$\tau_{ij} = \mu \left(\frac{\partial u_i}{\partial x_j} + \frac{\partial u_j}{\partial x_i} - \frac{2}{3} \frac{\partial u_k}{\partial x_k} \delta_{ij} \right) \tag{1.157}$$

The transported moments of the dispersed phase are number density, mesoscopic particle velocity fields, and quasi brownian energy (QBE). $w_{p,i} = \left(\breve{n}_p, \breve{n}_p \breve{u}_p, \breve{n}_p \breve{v}_p, \breve{n}_p \breve{w}_p, \breve{n}_p \delta\breve{\theta}_p\right)$. The conservations equations are then of the same form as in the case of the Navier-Stokes equations

$$\frac{\partial}{\partial t} w_{p,i} + \frac{\partial}{\partial x_j} F_{p,ij} = S_{p,i} \tag{1.158}$$

where $S_{p,i}$ are source terms as drag force and production of quasi brownian energy (QBE). Again the fluxes $F_{p,ij}$ are then divided into the non viscous part, the Euler fluxes $F^I_{p,ij}$, and

the viscous part $F^V_{p,ij}$. The inviscid fluxes are defined as

$$F^I_{p,ij} = \begin{pmatrix} \breve{n}_p\breve{u}_p & \breve{n}_p\breve{v}_p & \breve{n}_p\breve{w}_p \\ \breve{n}_p\breve{u}_p^2 + P_{QB} & \breve{n}_p\breve{u}_p\breve{v}_p & \breve{n}_p\breve{u}_p\breve{w}_p \\ \breve{n}_p\breve{u}_p\breve{v}_p & \breve{n}_p\breve{v}_p^2 + P_{QB} & \breve{n}_p\breve{v}_p\breve{w}_p \\ \breve{n}_p\breve{u}_p\breve{w}_p & \breve{n}_p\breve{v}_p\breve{w}_p & \breve{n}_p\breve{w}_p^2 + P_{QB} \\ \breve{n}_p\delta\breve{\theta}_p\breve{u}_p & \breve{n}_p\delta\breve{\theta}_p\breve{v}_p & \breve{n}_p\delta\breve{\theta}_p\breve{w}_p \end{pmatrix} \tag{1.159}$$

The viscous fluxes for the dispersed phase are defined as

$$F^V_{p,ij} = \begin{pmatrix} 0 & 0 & 0 \\ -\breve{\tau}_{p,xx} & -\breve{\tau}_{p,xy} & -\breve{\tau}_{p,xz} \\ -\breve{\tau}_{p,yx} & -\breve{\tau}_{p,yy} & -\breve{\tau}_{p,yz} \\ -\breve{\tau}_{p,zx} & -\breve{\tau}_{p,zy} & -\breve{\tau}_{p,zz} \\ +\breve{q}_{p,x} & +\breve{q}_{p,y} & +\breve{q}_{p,z} \end{pmatrix} \tag{1.160}$$

where $q_{p,i}$ are the fluxes of QBE by diffusion.
The source term $S_{p,i}$ includes drag and production of QBE by mean gradients.

$$S_{p,i} = \begin{pmatrix} 0 \\ \frac{\breve{n}_p}{\tau_p}\left(u_i - \breve{u}_{p,i}\right) \\ \frac{\breve{n}_p}{\tau_p}\left(v_i - \breve{v}_{p,i}\right) \\ \frac{\breve{n}_p}{\tau_p}\left(w_i - \breve{w}_{p,i}\right) \\ \left(-P_{QB}\delta_{ij} + \breve{\tau}_{p,ij}\right)\frac{\partial \breve{u}_{p,i}}{x_j} - \frac{2\breve{n}_p}{\tau_p}\delta\breve{\theta}_p \end{pmatrix} \tag{1.161}$$

The conservative variables w are then advanced using a standard finite Volume cell-vertex Lax-Wendroff approach [88]. The code AVBP is parallel and based on the COUPL library using MPI for communication.

1.6.1 The Lax Wendroff scheme

The Lax-Wendroff scheme available in AVBP aims to solve the Navier-Stokes equations in the form

$$\frac{\partial}{\partial t}w_i + \frac{\partial}{\partial x_j}F_{ij} = S_i \tag{1.162}$$

Then the Lax-Wendroff approach consists of a Taylor development of the conservative-variable vector in time.

$$w_i\left(t_0 + \Delta t\right) = w_i\left(t_0\right) + \Delta t\frac{\partial}{\partial t}w_i\left(t_0\right) + \frac{1}{2}\left(\Delta t\right)^2\frac{\partial^2}{\partial t^2}w_i\left(t_0\right) + O\left(\Delta t^3\right) \tag{1.163}$$

Assuming $\frac{\partial}{\partial t}w_i + \frac{\partial}{\partial x_j}F_{ij} = 0$, in the previous equation one may replace $\frac{\partial}{\partial t}w_i$ directly by $-\frac{\partial}{\partial x_j}F_{ij}$. For the second order derative one has, $\frac{\partial^2}{\partial t^2}w_i = -\frac{\partial}{\partial t}\frac{\partial}{\partial x_j}F_{ij}$. Devellopping the second order term into

$$\frac{\partial}{\partial t}\frac{\partial}{\partial x_j}F_{ij} = \frac{\partial}{\partial x_j}\frac{\partial}{\partial t}F_{ij} = \frac{\partial}{\partial x_j}\left[\left(\frac{\partial}{\partial w_k}F_{ij}\right)\frac{\partial}{\partial t}w_k\right] = -\frac{\partial}{\partial x_j}\left[\left(\frac{\partial}{\partial w_k}F_{ij}\right)\frac{\partial}{\partial x_l}F_{kl}\right] \tag{1.164}$$

and substituting the new equalities into the Taylor development one gets a second order temporal scheme:

$$w_i\left(t_0+\Delta t\right)=w_i\left(t_0\right)-\Delta t\frac{\partial}{\partial x_j}F_{ij}+\frac{1}{2}\left(\Delta t\right)^2\frac{\partial}{\partial x_j}\left[\left(\frac{\partial}{\partial w_k}F_{ij}\right)\left(\frac{\partial}{\partial t}w_k\right)\right]+O\left(\Delta t^3\right) \quad (1.165)$$

Here it is question to explicitely calculate the jacobi matrices $\frac{\partial}{\partial w_k}F_{ij}$. The divergence of the term is taken care of by the gaussian integral in the finite Volume approach:

$$\int_V\frac{\partial}{\partial x_j}\left(\frac{\partial F_{ij}}{\partial w_k}\frac{\partial w_k}{\partial t}\right)dV=\int_{\partial V}\left(\frac{\partial F_{ij}}{\partial w_k}\frac{\partial w_k}{\partial t}\right)n_j dA \quad (1.166)$$

This allows to advance the conservative variable in time:

$$w_i\left(t_0+\Delta t\right)\approx w_i\left(t_0\right)+\Delta t\frac{1}{\Delta V}\int_{\partial V}F_{ij}n_j dA+\frac{1}{2}\left(\Delta t\right)^2\frac{1}{\Delta V}\int_{\partial V}\left(\frac{\partial F_{ij}}{\partial w_k}\frac{\partial w_k}{\partial t}\right)n_j dA+\Delta t S_i \quad (1.167)$$

The time step is chosen according to the usual CFL conditions for the gaseous phase, supposing that the gaseous sound speed is always large compared to the dispersed phase "sound speed" ($c\gg\breve{c}_p$) (see Eq.1.139).

$$\Delta t<\frac{\Delta l}{||u||+||c||} \quad (1.168)$$

1.6.2 Source term correction in the small τ_p limit

If the characteristic particle relaxation time τ_p is small compared the characteristic time scale of the carrier phase T_f, ie. in the case of small Stokes numbers, the particle relaxation time may be of the order of the carrier phase time step or smaller. In such cases the source term related to drag force causes the dispersed phase velocity to oscillate around the carrier phase target velocity. In order to avoid this unphysical oscillation one has to reduce the numerical time step of the carrier phase to a fraction of the particle relaxation time τ_p. This can increase significantly computational cost. If particles are considered as tracers, one way to circumvent the reduction of the time step is, to integrate the dispersed phase velocity exactly.

In order to obtain an analytical solution for the source term correction one may assume the carrier phase velocity field to be constant $u=const$ for one time step. Here the sketch of the source term correction is given for the one-dimensional case. The one-dimensional equation of motion is:

$$\frac{\partial}{\partial t}\breve{u}_p=\frac{1}{\tau_p}\left[u-\breve{u}_p\right] \quad (1.169)$$

The analytical solution of Eq. 1.169 in the case of a constant carrier phase velocity is:

$$\breve{u}_p=\breve{u}_{p,0}\exp\left(\frac{-\left(t-t_0\right)}{\tau_p}\right)+u_0\left(1-\exp\left(\frac{\left(-\left(t-t_0\right)\right)}{\tau_p}\right)\right) \quad (1.170)$$

$\breve{u}_{p,0}$ is the initial particle velocity. If the initial start time is taken to be zero $t_0 = 0$ then Eq. 1.170 reduces to:

$$\breve{u}_p = u_g + (\breve{u}_p - u) \exp\left(-\frac{t}{\tau_p}\right) \tag{1.171}$$

The finite difference discretisation of Eq. 1.171 is:

$$\frac{\breve{u}_p(t+\delta t) - \breve{u}_p(t)}{\delta t} = (u_g - \breve{u}_p(t)) \left(\frac{1 - \exp\left(-\frac{\delta t}{\tau_p}\right)}{\delta t}\right) \tag{1.172}$$

With the Taylor development of $\exp\left(-\frac{\delta t}{\tau_p}\right)$ this yields for the finite difference version:

$$\frac{\breve{u}_p(t+\delta t) - \breve{u}_p(t)}{\delta t} = (u_g - \breve{u}_p(t)) \left(\frac{1}{\tau_p} - \frac{1}{2}\frac{\delta t}{\tau_p^2} + \frac{1}{6}\frac{\delta t^2}{\tau_p^3} \ldots\right) \tag{1.173}$$

Then, in the large Stokes number limit, one finds the original drag law $\propto 1/\tau_p$ and in the small Stokes number limit one finds the exact integration value. The only change in the source term is to replace $1/\tau_p$ by:

$$\frac{1 - \exp\left(-\frac{\delta t}{\tau_p}\right)}{\delta t} \tag{1.174}$$

to attain exact temporal integration.
This method can be extended to the source term part of the total kinetic energy equation. There the differential equation without convective and dissipative terms becomes the analogon of the drag equation.

$$\frac{\partial}{\partial t}\breve{q}_p^2 = \frac{1}{\tau_p}\left(q_{fp} - 2\breve{q}_p^2\right) \tag{1.175}$$

The discrete equivalent of Eq. 1.175 with exact temporal integration is :

$$\frac{\breve{q}_p^2(t+\delta t) - \breve{q}_p^2(t+\delta t)}{\delta t} = \left(q_{fp} - 2\breve{q}_p^2\right)\frac{1}{2}\frac{1 - \exp\left(-\frac{2\delta t}{\tau_p}\right)}{\delta t} \tag{1.176}$$

As in the case of the drag equation it is sufficient to replace $1/\tau_p$ by the following term:

$$\frac{1}{2}\frac{1 - \exp\left(-\frac{2\delta t}{\tau_p}\right)}{\delta t} \tag{1.177}$$

An extension of this method to third order Runge-Kutta time stepping was developed by E. Riber [82][81].

Chapter 2

Particle dynamics in homogeneous isotropic turbulence

Von Nostradamus' eigner Hand,
Ist dir es nicht Geleit genug ?
Erkennest dann der Sterne Lauf,
Und wenn Natur dich unterweist,
Dann geht die Seelenkraft dir auf,
Wie spricht ein Geist zum anderen Geist.
Goethe, Faust 1. Teil

The dynamics of particles in turbulence have been studied for quite some time. It is at the same time a challenging academic problem as well as an industrial problem. It arises in a wide variety of industrial applications ranking from pneumatic transport of grain to fluidized bed which is the workhorse of the chemical industry. Theoretical considerations on particle dispersion have been undertaken by Tchen [12] among others ([79],[80]). This lead to a definition of time and length scales that characterize the behavior of the particles in turbulence. Analytical methods (Maxey [61]) even permit to predict that inertial particles will accumulate in regions of low vorticity and high strain. Experimental measurements have been made by Snyder and Lumley [97] among others. Studying particles in grid generate turbulence with and without influence of gravity leads to the discovery and understanding of many phenomena of particle dynamics. Using massively computation power Lagrangian Particle tracking is a very powerful tool to precisely analyze the dynamics of particles in turbulent flow. Since the information of every single particle trajectory is computed, very detailed statistics can be extracted from such computations performed among others by Squires and Eaton [102] or Elghobashi and Truesdell [27].

From these theoretical considerations, experimental measurements and Lagrangian computations a certain level of understanding of the physical phenomena has been attained. As in the previous work of Février [32] and Simonin [92] here the Eulerian viewpoint is being emphasized. The motivation for the Eulerian viewpoint is double-fold:

*Lagrangian Simulations were performed with NTMIX by J. Helie

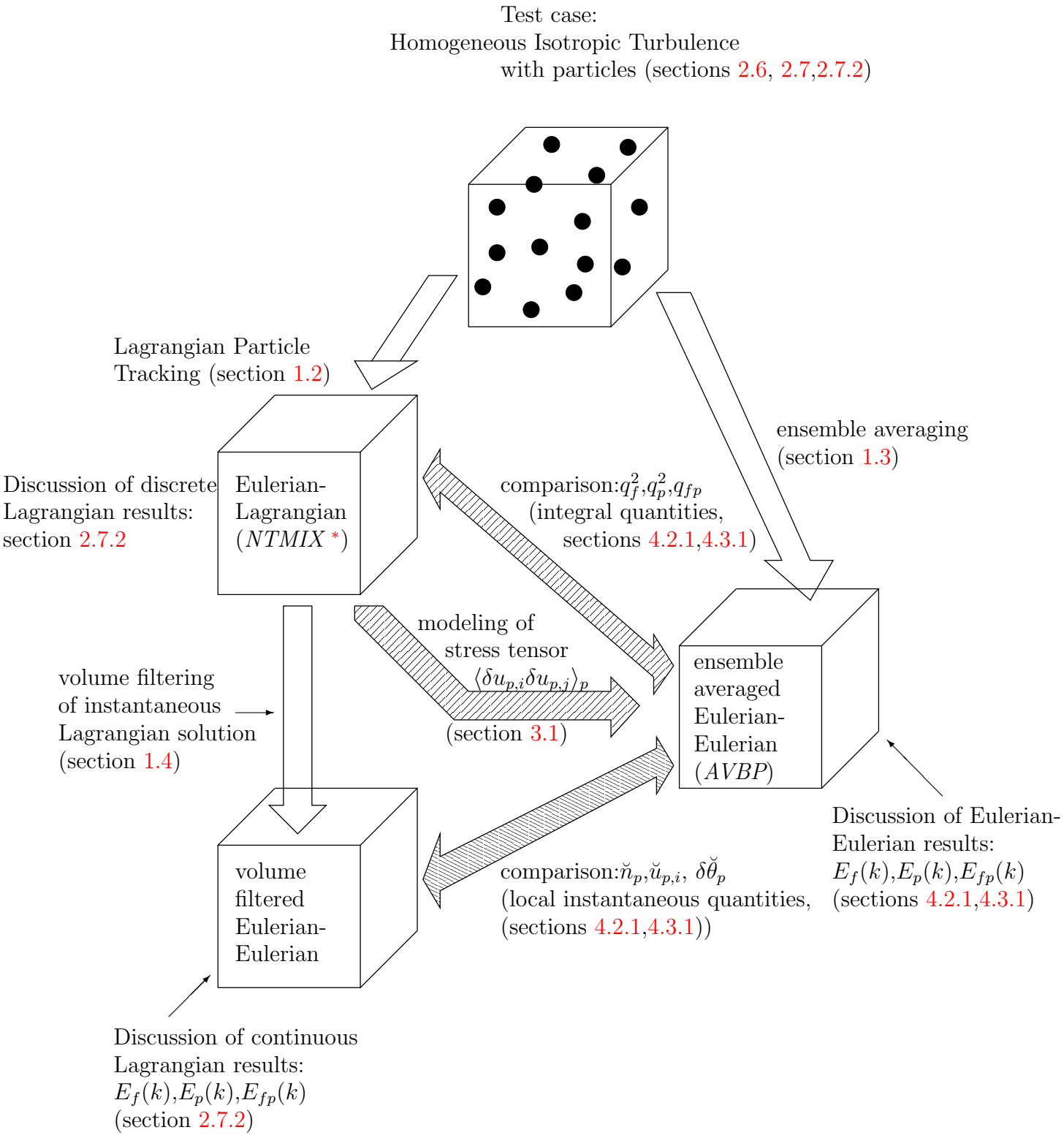

Figure 2.1: Concept of the test case and the analysis of particle dynamics in homogeneous turbulence.

- First it is interesting to consider the Eulerian viewpoint to check if the Eulerian-Eulerian formulation can capture effects, that were observed in experiments and Lagrangian simulations.
- The second motivation for the Eulerian viewpoint is related to the Eulerian formulation itself: Segregation effects for instance can be interpreted using the number density field and studying the divergence of the associated flow field. Other effects can be interpreted relying on the similarities to the compressible Navier-Stokes equations.

A plan for the analysis and comparison of Lagrangian and Eulerian simulations is sketched in Fig. 2.1. In this chapter the necessary tools for the analysis of Lagrangian simulations are introduced and applied to the results of the Lagrangian simulations performed by J. Helie (IMFT). The results of the Lagrangian simulations are volume filtered and the resulting continuous fields are then post processed, as if they were obtained from an ensemble averaged computation (section 2.7.2 of this chapter). Comparison between the Lagrangian and Eulerian simulations will be done in chapter 4. This comparison can be made using the ergodicity theorem. Supposing, that Lagrangian simulations are performed with sufficiently many particles and that the control volume for the filtering operation can be made sufficiently small, the volume filtered quantities are identical to the ensemble averaged quantities. In order not to contradict this assumption, particles where assumed to be point particles, that respond to a Stokes drag law in the Lagrangian simulation.

2.1 Dynamics of particles in turbulence

A rough classification of particle laden flow concerning Stokes number and volume fraction (or particle number) was given in the first chapter. Here, the behavior of dispersed flow whose particle loadings are small, so that one way coupling can be assumed, is further discussed. As mentioned in the first chapter, a wide range of length and time scales exists in the turbulent carrier phase. Those time and length scales need to be compared to the characteristic time and length scales of the dispersed phase. It is necessary to assume, that the particle diameter is much smaller than the Kolmogorov length scale. Since ensemble averaged quantities are considered in the dispersed phase, there is no small scale limit for the Eulerian length scales. This property of the Eulerian interpretation illustrates furthermore one of its characteristics : the Eulerian description gives ensemble-averaged quantities and not individual particle/droplet properties and can therefore have length scales smaller than the particle diameter.

2.2 Time and Length scales for particle properties

In this section some integral properties of the turbulent carrier phase are recalled. They are used later in this chapter when defining the test cases. Then, turbulent length and time scales are introduced in the framework of both, Lagrangian and Eulerian approaches.

2.2.1 Mesoscopic approach and its time and length scales

Integral properties of a flow are defined independent in space. If the considered realization of the flow is isotropic, in exploitation of numerical simulations it is common use to define integral properties by the normalized space integral over the computational domain. Here the volume average is defined as:

$$\langle \psi \rangle_V = \frac{1}{V} \int \psi dV \tag{2.1}$$

The correlations presented in the following are not proper to this averaging operator and of more general validity.

Autocorrelation functions and integral length scales of the carrier phase

An important tool to investigate the velocity field in homogeneous turbulence is autocorrelation functions. The normalized velocity autocorrelation function for incompressible turbulence is usually named $\mathcal{R}_{ij}$ and defined by the following relations [77]:

$$\hat{\mathcal{R}}^f_{ij}(\boldsymbol{r}) = \langle u_i(\boldsymbol{x}) u_j(\boldsymbol{x}+\boldsymbol{r}) \rangle \tag{2.2}$$

$$\mathcal{R}^f_{ij}(\boldsymbol{r}) = \hat{\mathcal{R}}^f_{ij}(0)^{-1} \hat{\mathcal{R}}^f_{ij}(\boldsymbol{r}) \tag{2.3}$$

In homogeneous isotropic turbulence, rotation and translation invariance lead to the interesting feature, that the autocorrelation functions can be separated into a longitudinal and a transverse autocorrelation [14]:

$$f(r) = \mathcal{R}^f_{ii}(r\boldsymbol{e}_i) \tag{2.4}$$

$$g(r) = \mathcal{R}^f_{ii}(r\boldsymbol{e}_j) \quad \text{with} \quad i \neq j \tag{2.5}$$

Here $r = \sqrt{r_i r_i}$ is the distance. This allows to write the autocorrelation function in the following form:

$$\mathcal{R}^f_{ij}(\boldsymbol{r}) = g(r)\delta_{ij} + \frac{f(r) - g(r)}{r^2} r_i r_j \tag{2.6}$$

If the fluid is incompressible, which is the case for the considered carrier phase, specific relations can be obtained between the parallel and normal components of the autocorrelation functions [57]:

$$g(r) = f(r) + \frac{r}{2} \frac{df(r)}{dr} \tag{2.7}$$

A hand-waving physical interpretation of the normal and parallel components can be given by the following argument: if a fluid particle in a vortex looks in the direction of its velocity, its velocity component will decrease. Then the correlation will decrease as well. If the same fluid particle looks normal to its velocity, for instance into the center of a vortex, it will see a decrease of the velocity correlation and will eventually become negative, since the vortex

velocity is in the opposite direction.
The autocorrelation function Eq. 2.2 allows to define an integral length scale :

$$\mathcal{L}^f_{ij,k} = \int_0^\infty \mathcal{R}^f_{ij}(r\boldsymbol{e}_k)dr \tag{2.8}$$

Longitudinal and transversal integral length scales can be defined with respect to the definitions of the longitudinal and transversal autocorrelation functions.

$$\mathcal{L}^f_{11} = \int_0^\infty \mathcal{R}^f_{ii}(r\boldsymbol{e}_i)dr \tag{2.9}$$

$$\mathcal{L}^f_{22} = \int_0^\infty \mathcal{R}^f_{ii}(r\boldsymbol{e}_j)dr \qquad i \neq j \tag{2.10}$$

According to the hand-waving explication above, the integral length scales $\mathcal{L}_{ij}$ characterize the length scales associated to the big structures of the flow. When additionally defining a turbulent velocity by $u' = \sqrt{\frac{1}{3}\langle u_i u_i \rangle}$ one can define an integral time scale, or an eddy turn over time as:

$$T^f_u = \frac{L}{u'} \tag{2.11}$$

Other important length scales are given by the longitudinal and horizontal Taylor micro-scales [5] that can be obtained by a spatial Taylor development of the velocity in the autocorrelation functions. The longitudinal Taylor micro-scale λ_1 is defined by:

$$\lambda_1 = \left(-\frac{1}{2}\frac{d^2\mathcal{R}_{11}}{dr_1^2}\bigg|_{r=0} \right)^{-1/2} \tag{2.12}$$

and the transversal Taylor micro-scale λ_2 by:

$$\lambda_2 = \left(-\frac{1}{2}\frac{d^2\mathcal{R}_{11}}{dr_2^2}\bigg|_{r=0} \right)^{-1/2} \tag{2.13}$$

The Taylor micro-scale therefore measures the curvature of the autocorrelation function at the origin.
These integral properties describe the carrier phase turbulence. In the following section those definitions - with their limitations - are transposed to the dispersed phase and the carrier-phase dispersed-phase correlation.

Lagrangian autocorrelation functions

In the case of Lagrangian simulations one does not dispose of continuous fields and it is not obvious to define the equivalent of the velocity autocorrelation function. In the Lagrangian framework it is more natural to define a temporal correlation function [12]. If $V_i^{(k)}(X_i^{(k)}, t)$

is the velocity of an individual particle k at location $X(t_0)$ at time t_0, one may define the correlation with the velocity of the same particle at time t_1 and location $X(t_1)$ [100]:

$$\hat{\mathcal{R}}_{L,ij}(\tau) = \frac{1}{N}\sum_{k}\int_{-\infty}^{\infty} V_i^{(k)}(t)V_j^{(k)}(t+\tau)dt \tag{2.14}$$

$$\mathcal{R}_{L,ij}(\tau) = \hat{\mathcal{R}}_{L,ij}(0)^{-1}\hat{\mathcal{R}}_{L,ij}(\tau) \tag{2.15}$$

As expected, the normal terms of this correlation terms depend very much on the particle relaxation time [32]. If the particle relaxation time is small compared to the characteristic time scale of the turbulence, the particle will rapidly adapt to the carrier phase turbulence and one finds the Lagrangian correlation function of a fluid particle. If the particle relaxation time is large compared to the characteristic time scale of the turbulence, the particle will persist on its trajectory for a longer time and the correlation function will drop less rapidly than the Lagrangian correlation function of a fluid particle.
Following the definition of Février [32] one may define a spatial correlation function:

$$R_{ij}^{pp}(\boldsymbol{r}) = \langle V_i^{(m)}V_j^{(n)} \mid \boldsymbol{x} = X^{(m)}, X^{(n)} = \boldsymbol{x}+\boldsymbol{r}, m \neq n\rangle \tag{2.16}$$

In this definition Février used the conditional averaging operator $\langle|\rangle$ for the particles.

Eulerian autocorrelation functions and integral length scales of the dispersed phase

In order to construct the Eulerian definition equivalent to Eq. 2.16 one has to account for the particle presence : it requires to define a probability density of two particles present at two distinct locations. Février used the following definitions for the presence of the two-point number density :

$$\breve{n}_{pp}(\boldsymbol{x}, \boldsymbol{x}+\boldsymbol{r}, t) = \langle \delta(\boldsymbol{x} - X^{(m)})\delta(\boldsymbol{x}+\boldsymbol{r}-X^{(n)}) \mid m \neq n\rangle \tag{2.17}$$

This allows then to define Eulerian spatial correlation functions for the dispersed phase, the carrier-phase dispersed-phase correlation and the particle weighted carrier phase correlation:

$$\hat{\breve{R}}_{ij}^{pp} = \frac{\langle \breve{n}_{pp}(\boldsymbol{x}, \boldsymbol{x}+\boldsymbol{r}, t)\breve{u}_{p,i}(\boldsymbol{x}, t)\breve{u}_{p,j}(\boldsymbol{x}+\boldsymbol{r}, t)\rangle}{\langle \breve{n}_{pp}(\boldsymbol{x}, \boldsymbol{x}+\boldsymbol{r}, t)\rangle} \tag{2.18}$$

$$\hat{\breve{R}}_{ij}^{fp} = \frac{\langle \breve{n}_{pp}(\boldsymbol{x}, \boldsymbol{x}+\boldsymbol{r}, t)u_i(\boldsymbol{x}, t)\breve{u}_{p,j}(\boldsymbol{x}+\boldsymbol{r}, t)\rangle}{\langle \breve{n}_{pp}(\boldsymbol{x}, \boldsymbol{x}+\boldsymbol{r}, t)\rangle} \tag{2.19}$$

$$\hat{\breve{R}}_{ij}^{ff} = \frac{\langle \breve{n}_{pp}(\boldsymbol{x}, \boldsymbol{x}+\boldsymbol{r}, t)u_i(\boldsymbol{x}, t)u_j(\boldsymbol{x}+\boldsymbol{r}, t)\rangle}{\langle \breve{n}_{pp}(\boldsymbol{x}, \boldsymbol{x}+\boldsymbol{r}, t)\rangle} \tag{2.20}$$

The Lagrangian correlation (Eq. 2.16)) takes into account the correlated and uncorrelated part of the particle velocity, whereas the Eulerian correlation (Eq. 2.18) takes only into

account the mesoscopic particle velocity. Therefore Lagrangian and Eulerian correlations differ by the uncorrelated part of the velocity as pointed out by Février [32].
The two point number density $\breve{n}_{pp}(\boldsymbol{x}, \boldsymbol{x}+\boldsymbol{r}, t)$ allows furthermore to define a normalized function that measures segregation effects :

$$g^{pp}(\boldsymbol{r}) = \frac{\langle \breve{n}_{pp}(\boldsymbol{x}, \boldsymbol{x}+\boldsymbol{r}, t)\rangle}{\langle \breve{n}_{p}(\boldsymbol{x}, t)\rangle \langle \breve{n}_{p}(\boldsymbol{x}+\boldsymbol{r}, t)\rangle} \tag{2.21}$$

In the ensemble averaged Eulerian computation one does not have access to the two point number density probability $\langle \breve{n}_{pp}(\boldsymbol{x}, \boldsymbol{x}+\boldsymbol{r}, t)\rangle$. If the probabilities of finding a particle at point $\boldsymbol{x}$ and at point $\boldsymbol{x}+\boldsymbol{r}$ are completely uncorrelated the two point probability can be expressed as the product of the two one point probabilities. Even if this does not allow to compare totally the Lagrangian correlation functions, here the normalized Eulerian autocorrelation functions are defined as :

$$\hat{\breve{\mathcal{R}}}^{pp}_{ij}(\boldsymbol{r}) = \frac{\langle \breve{n}_{p}(\boldsymbol{x}, t)\breve{u}_{p,i}(\boldsymbol{x}, t)\breve{n}_{p}(\boldsymbol{x}+\boldsymbol{r}, t)\breve{u}_{p,j}(\boldsymbol{x}+\boldsymbol{r}, t)\rangle}{\langle \breve{n}_{p}(\boldsymbol{x}, t)\breve{n}_{p}(\boldsymbol{x}+\boldsymbol{r}, t)\rangle} \tag{2.22}$$

$$\breve{\mathcal{R}}^{pp}_{ij}(\boldsymbol{r}) = \hat{\breve{\mathcal{R}}}^{pp}_{ij}(0)^{-1}\,\hat{\breve{\mathcal{R}}}^{pp}_{ij}(\boldsymbol{r}) \tag{2.23}$$

$$\hat{\breve{\mathcal{R}}}^{fp}_{ij}(\boldsymbol{r}) = \frac{\langle \breve{n}_{p}(\boldsymbol{x}, t)u_{i}(\boldsymbol{x}, t)\breve{n}_{p}(\boldsymbol{x}+\boldsymbol{r}, t)\breve{u}_{p,j}(\boldsymbol{x}+\boldsymbol{r}, t)\rangle}{\langle \breve{n}_{p}(\boldsymbol{x}, t)\breve{n}_{p}(\boldsymbol{x}+\boldsymbol{r}, t)\rangle} \tag{2.24}$$

$$\breve{\mathcal{R}}^{fp}_{ij}(\boldsymbol{r}) = \hat{\breve{\mathcal{R}}}^{fp}_{ij}(0)^{-1}\,\hat{\breve{\mathcal{R}}}^{fp}_{ij}(\boldsymbol{r}) \tag{2.25}$$

$$\hat{\breve{\mathcal{R}}}^{ff}_{ij}(\boldsymbol{r}) = \frac{\langle \breve{n}_{p}(\boldsymbol{x}, t)u_{i}(\boldsymbol{x}, t)\breve{n}_{p}(\boldsymbol{x}+\boldsymbol{r}, t)u_{j}(\boldsymbol{x}+\boldsymbol{r}, t)\rangle}{\langle \breve{n}_{p}(\boldsymbol{x}, t)\breve{n}_{p}(\boldsymbol{x}+\boldsymbol{r}, t)\rangle} \tag{2.26}$$

$$\breve{\mathcal{R}}^{ff}_{ij}(\boldsymbol{r}) = \hat{\breve{\mathcal{R}}}^{ff}_{ij}(0)^{-1}\,\hat{\breve{\mathcal{R}}}^{ff}_{ij}(\boldsymbol{r}) \tag{2.27}$$

In analogy to the longitudinal and transversal autocorrelations functions one can define the corresponding longitudinal and transversal autocorrelations functions of the dispersed phase.

$$\breve{f}^{pp}(r) = \breve{\mathcal{R}}^{pp}_{ii}(r\boldsymbol{e}_i) \tag{2.28}$$

$$\breve{g}^{pp}(r) = \breve{\mathcal{R}}^{pp}_{ii}(r\boldsymbol{e}_j) \quad \text{with} \quad i \neq j \tag{2.29}$$

$$\breve{f}^{fp}(r) = \breve{\mathcal{R}}^{fp}_{ii}(r\boldsymbol{e}_i) \tag{2.30}$$

$$\breve{g}^{fp}(r) = \breve{\mathcal{R}}^{fp}_{ii}(r\boldsymbol{e}_j) \quad \text{with} \quad i \neq j \tag{2.31}$$

$$\breve{f}^{ff}(r) = \breve{\mathcal{R}}^{ff}_{ii}(r\boldsymbol{e}_i) \tag{2.32}$$

$$\breve{g}^{ff}(r) = \breve{\mathcal{R}}^{ff}_{ii}(r\boldsymbol{e}_j) \quad \text{with} \quad i \neq j \tag{2.33}$$

The Eulerian autocorrelation function Eq. 2.22 allows to define an integral length scale of the correlated motion of the dispersed phase:

$$\breve{\mathcal{L}}^{p}_{ij,k} = \int_0^\infty \breve{\mathcal{R}}^{pp}_{ij}(r\boldsymbol{e}_k)dr \tag{2.34}$$

As in the case of the carrier phase, this length scale gives information about the large scale structures of correlated motion. In analogy to the carrier phase one can define a longitudinal Taylor micro-scale λ_{p1}:

$$\lambda_{p1} = \left(-\frac{1}{2}\frac{d^2\breve{\mathcal{R}}^{pp}_{11}}{dr_1^2}\bigg|_0 \right)^{-1/2} \tag{2.35}$$

and a horizontal Taylor micro-scale λ_{p2} :

$$\lambda_{p2} = \left(-\frac{1}{2}\frac{d^2\breve{\mathcal{R}}^{pp}_{11}}{dr_2^2}\bigg|_0 \right)^{-1/2} \tag{2.36}$$

This Taylor micro-scale then gives information about the curvature of the mesoscopic particle velocity autocorrelation function at the origin. As in the case of the autocorrelation function for the mesoscopic velocity one can use two one point number density functions to define the segregation function:

$$\breve{g}^{pp}(\boldsymbol{r}) = \frac{\langle \breve{n}_p(\boldsymbol{x},t)\breve{n}_p(\boldsymbol{x}+\boldsymbol{r},t)\rangle}{\langle \breve{n}_p(\boldsymbol{x},t)\rangle\langle \breve{n}_p(\boldsymbol{x}+\boldsymbol{r},t)\rangle} \tag{2.37}$$

Eq. 2.37 is the autocorrelation function of the number density field. It allows, as in the case of the velocity autocorrelation function, to define a length scale associated to the curvature at the origin :

$$\lambda_{\breve{n}_p} = \left(-\frac{1}{2}\frac{d^2\breve{g}^{pp}}{dr_2^2}\bigg|_0 \right)^{-1/2} \tag{2.38}$$

In the carrier phase turbulence the Taylor micro-scale can be associated to the pseudo-dissipation [14]. A priori it is not clear how to interpret physically the mesoscopic Taylor micro-scale or the length scale associated to the number density autocorrelation function. The length scale from the number density autocorrelation function $\breve{g}_{pp}$ gives information about the stiffness of the number density gradients. Some care has to be taken when interpreting the autocorrelation functions. Since the mesoscopic velocity field is compressible not all the relations used in incompressible turbulence are valid.

One dimensional spectra

Making use of the longitudinal and transverse autocorrelation functions one may define one dimensional energy spectra [78] for the incompressible carrier phase.

$$E_{11}(\kappa) = \int f(r)e^{i\kappa r}dr \tag{2.39}$$

$$E_{22}(\kappa) = \int g(r)e^{i\kappa r}dr \tag{2.40}$$

The autocorrelation functions $f(r)$ and $g(r)$ are real and even functions. Therefore the Fourier transform can actually be reduced to a cosine transform and the resulting spectra are also real and even.
The previously defined autocorrelation functions for the dispersed phase are conditioned by the particle presence since they include the number density. One dimensional spectra obtained from the dispersed phase autocorrelation function include therefore this information. The one dimensional spectra of the dispersed phase are here defined in analogy to the one dimensional carrier phase spectra.

$$\breve{E}_{11}^{pp}(\kappa) = \int \breve{f}^{pp}(r)e^{i\kappa r}dr \tag{2.41}$$

$$\breve{E}_{22}^{pp}(\kappa) = \int \breve{g}^{pp}(r)e^{i\kappa r}dr \tag{2.42}$$

$$\breve{E}_{11}^{fp}(\kappa) = \int \breve{f}^{fp}(r)e^{i\kappa r}dr \tag{2.43}$$

$$\breve{E}_{22}^{fp}(\kappa) = \int \breve{g}^{fp}(r)e^{i\kappa r}dr \tag{2.44}$$

$$\breve{E}_{11}^{ff}(\kappa) = \int \breve{f}^{ff}(r)e^{i\kappa r}dr \tag{2.45}$$

$$\breve{E}_{22}^{ff}(\kappa) = \int \breve{g}^{ff}(r)e^{i\kappa r}dr \tag{2.46}$$

One dimensional spectra can later be compared to the three dimensional spectra obtained from the usual spectral definition of kinetic energy.

In the incompressible carrier phase the essential quantity is the velocity field. Since the dispersed phase has a compressible behavior, the autocorrelation function of number density (eq. 2.37) gives some information on segregation. The fourier transform of this quantity allows then to investigate the length scales important in the segregation process.

$$\breve{N}^{pp}(\kappa) = \int \breve{g}^{pp}(r)e^{i\kappa r}dr \tag{2.47}$$

A hand-waving physical interpretation of this spectral quantity can be obtained by considering a vortex such that the turnover time is of the same order than the particle relaxation time. Particles will be entrained by the vortex, but inertia will carry particles to the regions of shear outside the vortex. Therefore the dominant wave number contribution of the spectral quantity $\breve{N}^{pp}$ should correspond to the length scales down to the size of the vortex.

2.2.2 Particle dynamic length scales

The length scale down to which particles follow the carrier phase flow can be estimated by $\lambda_p = \tau_p v_p$. This corresponds to the mean path length particles need to adapt to the carrier phase flow. Below this length scale particle-fluid correlation is weak or inexistent. Another

dynamic length scale can be defined as $\delta\lambda_p = \tau_p \delta u_p$. This corresponds to the kinetic viscous length scale. This length scale can be interpreted like the Kolmogorov length scale in turbulent flow : the correlated particle velocity $\breve{u}_p$ undergoes viscous dissipation. Between those two length scales, λ_p and $\delta\lambda_p$, there is no effective viscous mechanism and yet there is a non-negligible amount of correlated particle motion. If all the correlated dynamics of the dispersed phase has to be resolved, it should be resolved to the viscous length scale of the dynamics as there is the Kolmogorov length scale for the carrier phase. If the Stokes number is small enough however, the length scale up to which particle drag dominates the dynamics (λ_p), may be smaller than the Kolmogorov length scale η and the particles behave as perfect tracers. Difficulties in spatial resolution due to the dispersed phase dynamics arise, if λ_p is larger than the Kolmogorov length scale η and if $\delta\lambda_p$ is significantly smaller than the Kolmogorov length scale. Then, in a true "DNS", spatial resolution needs to go down to the dissipative length scale $\delta\lambda_p$. The dynamic length scales $\lambda_p, \delta\lambda_p$ are not the only limiting factors however. Due to the correlated motion at small length scales with "weak" pressure due to QBE, compressibility effects are very important for the number density field: particles tend to accumulate in zones of high strain and low vorticity as it has been observed in Lagrangian computations [103].

2.3 The Dynamical System of Particles in Turbulence: Integral Properties

2.3.1 Carrier phase properties

Integral properties of incompressible decaying homogeneous isotropic turbulence can be summarized to a simple set of ordinary differential equations of the integral kinetic energy,

$$q_f^2 = \frac{1}{V}\frac{1}{2}\int u_k u_k dV \tag{2.48}$$

and the dissipation of kinetic energy

$$\varepsilon = \frac{1}{V}\frac{\nu}{2}\int \frac{\partial u_i}{\partial x_j}\frac{\partial u_j}{\partial x_i} dV \tag{2.49}$$

where ν is the kinematic viscosity.

$$\frac{\partial}{\partial t} q_f^2 = -\varepsilon \tag{2.50}$$

$$\frac{\partial}{\partial t}\varepsilon = -C_2 \frac{\varepsilon^2}{q_f^2} \tag{2.51}$$

Those equations can be obtained from the Navier-Stokes equations with some assumptions on the properties of the flow ([14],[44],[5]) satisfied in incompressible decaying homogeneous turbulence. Eq. 2.50 is exact while Eq. 2.51 is a model based on a characteristic time scale for dissipation proportional to q_f^2/ε.

2.3.2 Dispersed phase properties

This simple system of two coupled ordinary differential equations that describes the global development of the carrier phase can be extended to the dispersed phase and the fluid particle correlation. The discrete formulation in the Lagrangian description of the dispersed phase and continuous formulation in the Eulerian description require a separate definition of the integral properties. This is presented in the two following subsections. Since the following analysis of the behavior is strictly limited to the case of one way coupling, the carrier phase system for the kinetic energy and dissipation is not influenced by the dispersed phase and does not need modification.

Dispersed phase Lagrangian properties

Using the Lagrangian equations of particle transport with Stokes drag (Eqs. 1.21,1.22) a corresponding set of ordinary differential equations for the fluid-particle correlation,

$$q_{fp} = \frac{1}{N} \sum_{k=1}^{N} u_i(X_i^{(k)}(t), t) V_i^{(k)} \tag{2.52}$$

and the particle kinetic energy,

$$q_p^2 = \frac{1}{2} \frac{1}{N} \sum_{k=1}^{N} V_i^{(k)} V_i^{(k)} \tag{2.53}$$

can be obtained for the dispersed phase and the fluid-particle correlation. It uses the definition of the carrier phase kinetic energy "seen" by the particle, i.e. the carrier phase kinetic energy conditioned by the particle presence [22],[52] :

$$q_{f@p} = \frac{1}{N} \sum_{k=1}^{N} u_i(X^{(k)}(t), t) u_i(X^{(k)}(t), t) \tag{2.54}$$

This differs from the carrier phase energy q_f^2 since it takes into account the non-uniform distribution of the particle number density. The dynamical system for the fluid particle correlation and the particle kinetic energy is :

$$\frac{\partial}{\partial t} q_{fp} = -\varepsilon_{fp} - \frac{1}{\tau_p} \left[q_{fp} - 2 q_{f@p}^2 \right] \tag{2.55}$$

$$\frac{\partial}{\partial t} q_p^2 = -\frac{1}{\tau_p} \left[2 q_p^2 - q_{fp} \right] \tag{2.56}$$

Here ε_{fp} is the dissipation of the fluid particle correlation.

$$\begin{aligned} \varepsilon_{fp} = \frac{1}{N} \sum_{k=1}^{N} \Bigg\{ & V_i^k u_j(X_i^{(k)}(t), t) \left. \frac{\partial}{\partial x_j} \right|_{x_l = X_l^{(k)}(t)} u_i(x_l, t) + \frac{V_i^{(k)}}{\rho} \left. \frac{\partial}{\partial x_i} \right|_{x_l = X_l^{(k)}(t)} P(x_l, t) \\ & - \nu V_i^{(k)} \left. \frac{\partial}{\partial x_j} \right|_{x_l = X_l^{(k)}(t)} \tau_{ij}(x_l, t) \Bigg\} \end{aligned} \tag{2.57}$$

The dissipation of the fluid-particle correlation ε_{fp} can be used to introduce a dissipative time-scale for the fluid particle correlation τ^t_{fp}:

$$\tau^t_{fp} = \frac{q_{fp}}{\varepsilon_{fp}} \tag{2.58}$$

Theoretical arguments (Simonin []) show that this time scale should be approximative half of the carrier phase dissipative time scale.

Dispersed phase Eulerian properties

In the case of Eulerian simulations the particle velocity is divided into two parts, one corresponding to the mesoscopic Eulerian velocity field ($\breve{u}_{p,i}$) and a residual velocity ($\delta u_{p,i}$) of quasi brownian motion. Then the equivalent set of differential equations for the fluid particle correlation

$$q_{fp} = \frac{1}{V}\frac{1}{\langle \breve{n}_p \rangle_V} \int \breve{n}_p u_i \breve{u}_{p,i} dV, \tag{2.59}$$

the resolved integral kinetic energy of the dispersed phase,

$$\breve{q}^2_p = \frac{1}{V}\frac{1}{2}\frac{1}{\langle \breve{n}_p \rangle_V} \int \breve{n}_p \breve{u}_{p,i} \breve{u}_{p,i} dV, \tag{2.60}$$

and the integral quasi brownian energy,

$$\delta q^2_p = \frac{1}{V}\frac{1}{\langle \breve{n}_p \rangle_V} \int \breve{n}_p \delta\breve{\theta}_p dV \tag{2.61}$$

can be obtained from the Eulerian conservation eqs. 1.35, 1.46, 1.47 and using the fact that the simulations are performed in a periodic domain, such that the terms preceding a spatial derivative vanishes:

$$\frac{\partial}{\partial t} q_{fp} = -\frac{q_{fp}}{\tau^t_{fp}} - \frac{1}{\tau_p}\left[q_{fp} - 2q^2_f\right] \tag{2.62}$$

$$\frac{\partial}{\partial t} \breve{q}^2_p = -\frac{1}{\tau_p}\left[2\breve{q}^2_p - q_{fp}\right] - \varepsilon_{QB} \tag{2.63}$$

$$\frac{\partial}{\partial t} \delta q^2_p = -\frac{1}{\tau_p}\delta q^2_p + \varepsilon_{QB} \tag{2.64}$$

Comparing Eq. 2.63 to the equivalent relation obtained from the Lagrangian Eq. 2.56, a supplementary dissipation term ε_{QB} related to the quasi brownian motion arises.

$$\varepsilon_{QB} = \frac{1}{V} \int \breve{u}_{p,i} \frac{\partial}{\partial x_j} \breve{n}_p \langle \delta u_{p,i} \delta u_{p,j} \rangle_p dV \tag{2.65}$$

Conservation of the energy balance implies the transfer of the dissipated correlated energy into the uncorrelated quasi brownian energy.

One important assumption made in the derivation of the integral properties is that the particle relaxation time remains constant. In realistic flows this is not true however. As discussed in the first chapter the particle relaxation time changes with the Reynolds number of the particle. Since the present study is limited to Stokes drag, the relaxation time is assumed constant.

The set of differential equations for the integral properties (Eqs.2.62 to 2.64) can not be solved independently, since for the closure of the equations expressions for ε_{fp} and ε_{QB} have to be specified. On the other hand, if solving for ε_{fp} and ε_{QB} in the ODE system and measuring the integral properties, the dissipative time scale τ^t_{fp} can be measured and checked to analytical results. A second application for the integral properties is to check the computational results by evaluating explicitly ε_{fp} and ε_{QB} during the numerical computation and to check whether the total behavior of the integral system is consistent.

2.4 Spectrum Analysis

The spectral behavior of an incompressible gas in homogeneous isotropic turbulence is a classical problem [78]. In a rough sketch, the non-linear terms in the transport equation ensure a transport from the energetic length scales to the rest of the spectrum. Since dissipation is proportional to the second spatial derative, it is most efficient at small length scales. Molecular viscosity dissipates therefore kinetic energy in the range of the smallest length scales. The smallest length scale in a turbulent viscous flow is normally associated to the Kolmogorov length scale η [57].
In the case of the dispersed phase the picture is somewhat not as clear. In a gas one can imagine, that the continuous field description of the gaseous molecules is well adapted due to the high collision frequency. Then from the spectral view-point an energy cascade from the energetic length scales to the dissipative length scales by the non-linear terms of the transport equation can be understood. In the dispersed phase without collisions it is not clear, to what point the continuous formulation can reproduce the behavior of the dispersed phase and whether such an energy cascade exists. Coupling of the dispersed phase to the carrier phase by drag force via the carrier-phase dispersed-phase correlation suggests however - if the Stokes number is not too large - that the dispersed phase should admit a behavior similar to the one of the gaseous carrier phase.
The subject of the current section therefore is to introduce the necessary spectral tools to investigate the behavior of the dispersed-phase kinetic energy and to understand its temporal development in an Eulerian framework. The description is introduced in three steps. First the spectral transfer in an incompressible fluid is recalled. This is the traditional technique to investigate the turbulent transfer in incompressible homogeneous isotropic turbulence. It is then extended to compressible fluids. Transfer terms related to transport and pressure are treated separately to study the effect of compressibility in the dispersed phase. Finally the compressible analysis is extended by separating the velocity into a compressible and an incompressible component. Since those velocities are orthogonal in spectral space, this allows to construct a compressible and an incompressible spectral en-

ergy development.
The presented tools are limited to the case of one-way coupling. The influence of the dispersed phase on the carrier phase spectrum has been investigated by Truesdell [27], Boivin [9], Squires [101] and others ([105][2]).
Here the notation of Pope [78] is used. Other discussion on spectral development can for example be found in [44], [8].
The spectral tools presented here are first used in section 2.7.2 for the analysis of the gaseous carrier phase, dispersed phase and their correlation for the results of the volume-filtered Lagrangian results. They are then used in section 3.1 to evaluate and interpret the different models of the QB stress tensor. Finally some aspects are recalled when evoking the necessary qualities of a LES model for Eulerian-Eulerian two phase flows.

2.4.1 Governing Equations in incompressible analysis

The governing equations consist of the incompressible Navier-Stokes Equations for the carrier phase and the transport equations for the dispersed phase.
Temporal and spatial dependence on variables are suppressed if their dependence is not ambigious. One way coupling is explicitely assumed. For the carrier phase and the dispersed phase the viscosity is assumed spatially uniform. The carrier phase equations reduce in this simple case to the following equations : (The supplementary index for the carrier phase is again suppressed.)

$$\frac{\partial}{\partial t}u_i + \frac{\partial}{\partial x_j}u_i u_j = -\frac{1}{\rho}\frac{\partial}{\partial x_i}P + \nu\frac{\partial}{\partial x_k}\frac{\partial}{\partial x_k}u_i \tag{2.66}$$

$$\frac{\partial}{\partial x_j}u_j = 0 \tag{2.67}$$

Here the incompressibility condition $\partial u_j/\partial x_j$ has been used to write $u_j \partial u_i/\partial x_j$ as $\partial/\partial x_j(u_i u_j)$.
The equivalent for the transport equation with constant number density of the dispersed phase is:

$$\frac{\partial}{\partial t}\breve{u}_{p,i} + \frac{\partial}{\partial x_j}\breve{u}_{p,i}\breve{u}_{p,j} = -\frac{1}{\breve{n}_p}\frac{\partial}{\partial x_i}P_{QB} + \nu_{QB}\frac{\partial}{\partial x_k}\frac{\partial}{\partial x_k}\breve{u}_{p,i} + \frac{1}{\tau_p}\left(u_i - \breve{u}_{p,i}\right) \tag{2.68}$$

$$\frac{\partial}{\partial x_j}\breve{u}_{p,j} = 0 \tag{2.69}$$

The spatial fourier transform of any variable is here defined as:

$$\mathcal{F}_{\boldsymbol{\kappa}}\left\{f(x)\right\} = \hat{f}(\boldsymbol{\kappa}) = \frac{1}{L}\int f(x)e^{-i\boldsymbol{\kappa}x}dx \tag{2.70}$$

The fourier transform of the dynamic pressure is defined by:

$$\hat{P}(\boldsymbol{\kappa}) = \mathcal{F}_{\boldsymbol{\kappa}}\left\{\frac{1}{\rho}P(x,t)\right\}, \qquad \hat{P}_{QB}(\boldsymbol{\kappa}) = \mathcal{F}_{\boldsymbol{\kappa}}\left\{\frac{1}{\breve{n}_p}P_{QB}(x,t)\right\}. \tag{2.71}$$

Fourier transform of the two transport equations (2.66,2.68) yields :

$$\left(\frac{\partial}{\partial t}+\nu\kappa^2\right)\hat{u}_i(\boldsymbol{\kappa}) = -i\kappa_i\hat{P}(\boldsymbol{\kappa})-i\kappa_j\mathcal{F}_{\boldsymbol{\kappa}}\left\{u_i(x)u_j(x)\right\} \tag{2.72}$$

$$\left(\frac{\partial}{\partial t}+\nu_{QB}\kappa^2\right)\hat{u}_{p,i}(\boldsymbol{\kappa}) = -i\kappa_i\hat{P}_{QB}(\boldsymbol{\kappa})-i\kappa_j\mathcal{F}_{\boldsymbol{\kappa}}\left\{u_{p,i}(x)u_{p,j}(x)\right\}-\frac{1}{\tau_p}\left(\hat{u}_{p,i}-\hat{u}_i\right) \tag{2.73}$$

These equations contain the Fourier transform of the correlations $u_i(x)u_j(x)$ (and $u_{p,i}(x)u_{p,j}(x)$ respectively). The Fourier transforms of these correlations are:

$$\mathcal{F}_{\boldsymbol{\kappa}}\left\{u_i(x)u_j(x)\right\}=\frac{1}{L}\int\hat{u}_i(\boldsymbol{\kappa}')\hat{u}_j(\boldsymbol{\kappa}-\boldsymbol{\kappa}')d\boldsymbol{\kappa}' \tag{2.74}$$

Making use of the incompressibility condition $\left(\frac{\partial}{\partial x_j}u_j\right)$ for the carrier phase, the right hand side of Eq. 2.72 can be isolated by multiplication of Eq. 2.72 with κ_i. It can be seen that the pressure then balances the components parallel to $\boldsymbol{\kappa}$ in the derivative of the convective term [78]. To shorten notation, it is useful to define the projection operator $\hat{\mathcal{P}}_{ij}(\boldsymbol{\kappa})$ as:

$$\hat{\mathcal{P}}_{ij}(\boldsymbol{\kappa})=\left(\delta_{ij}-\frac{\kappa_i\kappa_j}{\kappa^2}\right) \tag{2.75}$$

and the fourier transform of the convection term derivative as:

$$\hat{G}_k(\boldsymbol{\kappa})=\mathcal{F}_{\boldsymbol{\kappa}}\left\{\frac{\partial}{\partial x_j}u_k(x)u_j(x)\right\}=i\kappa_j\frac{1}{L}\int\hat{u}_k(\boldsymbol{\kappa}')\hat{u}_j(\boldsymbol{\kappa}-\boldsymbol{\kappa}')d\boldsymbol{\kappa}' \tag{2.76}$$

Then the fourier transformed incompressible Navier-Stokes equation can formally be written as:

$$\left(\frac{\partial}{\partial t}+\nu\kappa^2\right)\hat{u}_i\left(\boldsymbol{\kappa}\right)=-\hat{\mathcal{P}}_{ij}(\boldsymbol{\kappa})\hat{G}_j(\boldsymbol{\kappa}) \tag{2.77}$$

For the following analysis the dispersed phase is considered incompressible like the carrier phase. Then the pressure term balances the velocity divergence in the momentum equation and the spectral momentum transport can be expressed in analogy to the carrier phase momentum Eq. 2.77 with a remaining term related to particle drag:

$$\left(\frac{\partial}{\partial t}+\nu_{QB}\kappa^2\right)\hat{u}_{p,i}\left(\boldsymbol{\kappa}\right)=-\hat{\mathcal{P}}_{ij}(\boldsymbol{\kappa})\hat{G}_{p,j}(\boldsymbol{\kappa})+\frac{1}{\tau_p}\left(\hat{u}_i(\boldsymbol{\kappa})-\hat{u}_{p,i}(\boldsymbol{\kappa})\right) \tag{2.78}$$

In this equation the term due to dissipation is a model since ν_{QB} is assumed constant. Eqs. 2.77 and 2.78 can then be used to obtain transport equations for the spectral kinetic energy of the carrier phase:

$$E_f(\boldsymbol{\kappa})=\frac{1}{2}\hat{u}_i(\boldsymbol{\kappa})\hat{u}_i^*(\boldsymbol{\kappa}) \tag{2.79}$$

the kinetic Energy of the dispersed phase:

$$E_p(\boldsymbol{\kappa})=\frac{1}{2}\hat{u}_{p,i}(\boldsymbol{\kappa})\hat{u}_{p,i}^*(\boldsymbol{\kappa}) \tag{2.80}$$

and the spectral carrier-phase dispersed-phase correlation:

$$E_{fp}(\boldsymbol{\kappa}) = \frac{1}{2}\left(\hat{u}_i(\boldsymbol{\kappa})\hat{u}^*_{p,i}(\boldsymbol{\kappa}) + \hat{u}_{p,i}(\boldsymbol{\kappa})\hat{u}^*_i(\boldsymbol{\kappa})\right) \tag{2.81}$$

The corresponding transport equations for the gaseous and dispersed phase velocity correlation are:

$$\left(\frac{\partial}{\partial t} + 2\nu\kappa^2\right)\hat{u}_i(\boldsymbol{\kappa})\hat{u}^*_i(\boldsymbol{\kappa}) = -\hat{u}_i(\boldsymbol{\kappa})\hat{\mathcal{P}}_{ik}(-\boldsymbol{\kappa})\hat{G}_k(-\boldsymbol{\kappa}) - \hat{u}^*_i(\boldsymbol{\kappa})\hat{\mathcal{P}}_{ik}(\boldsymbol{\kappa})\hat{G}_k(\boldsymbol{\kappa}) \tag{2.82}$$

$$\begin{aligned}\left(\frac{\partial}{\partial t} + 2\nu_{QB}\kappa^2\right)\hat{u}_{p,i}(\boldsymbol{\kappa})\hat{u}^*_{p,i}(\boldsymbol{\kappa}) &= -\hat{u}_{p,i}(\boldsymbol{\kappa})\hat{\mathcal{P}}_{ik}(-\boldsymbol{\kappa})\hat{G}_{p,k}(-\boldsymbol{\kappa}) - \hat{u}^*_{p,i}(\boldsymbol{\kappa})\hat{\mathcal{P}}_{ik}(\boldsymbol{\kappa})\hat{G}_{p,k}(\boldsymbol{\kappa}) \\ &+ \frac{1}{\tau_p}\left(\left(\hat{u}_i(\boldsymbol{\kappa})\hat{u}^*_{p,i}(\boldsymbol{\kappa}) + \hat{u}^*_i(\boldsymbol{\kappa})\hat{u}_{p,i}(\boldsymbol{\kappa})\right) - 2\hat{u}_{p,i}(\boldsymbol{\kappa})\hat{u}^*_{p,i}(\boldsymbol{\kappa})\right)\end{aligned} \tag{2.83}$$

Here $\hat{G}_{p,k}$ is defined in analogy to the carrier phase operator:

$$\hat{G}_{p,k}(\boldsymbol{\kappa}) = \mathcal{F}_{\boldsymbol{\kappa}}\left\{\frac{\partial}{\partial x_j}\breve{u}_{p,k}(x)\breve{u}_{p,j}(x)\right\} = i\kappa_j\frac{1}{L}\int \hat{u}_{p,k}(\boldsymbol{\kappa}')\hat{u}_{p,j}(\boldsymbol{\kappa}-\boldsymbol{\kappa}')d\boldsymbol{\kappa}' \tag{2.84}$$

The transport equation for the carrier-dispersed phase correlation is:

$$\begin{aligned}\left(\frac{\partial}{\partial t} + (\nu+\nu_{QB})\,\kappa^2\right)\left(\hat{u}_{p,i}(\boldsymbol{\kappa})\hat{u}^*_i(\boldsymbol{\kappa}) + \hat{u}^*_{p,i}(\boldsymbol{\kappa})\hat{u}_i(\boldsymbol{\kappa})\right) = \\ -\hat{u}_{p,i}(\boldsymbol{\kappa})\hat{\mathcal{P}}_{ik}(-\boldsymbol{\kappa})\hat{G}_k(-\boldsymbol{\kappa}) - \hat{u}^*_{p,i}(\boldsymbol{\kappa})\hat{\mathcal{P}}_{ik}(\boldsymbol{\kappa})\hat{G}_k(\boldsymbol{\kappa}) \\ -\hat{u}_i(\boldsymbol{\kappa})\hat{\mathcal{P}}_{ik}(-\boldsymbol{\kappa})\hat{G}_{p,k}(-\boldsymbol{\kappa}) - \hat{u}^*_i(\boldsymbol{\kappa})\hat{\mathcal{P}}_{ik}(\boldsymbol{\kappa})\hat{G}_{p,k}(\boldsymbol{\kappa}) \\ +\frac{1}{\tau_p}\left(2\hat{u}_i(\boldsymbol{\kappa})\hat{u}^*_i(\boldsymbol{\kappa}) - \left(\hat{u}_i(\boldsymbol{\kappa})\hat{u}^*_{p,i}(\boldsymbol{\kappa}) + \hat{u}^*_i(\boldsymbol{\kappa})\hat{u}_{p,i}(\boldsymbol{\kappa})\right)\right)\end{aligned} \tag{2.85}$$

The different terms of the transport equation are developed separately. They are identified as:

- the inter-scale transport of the carrier phase:

$$\hat{T}_f(\boldsymbol{\kappa}) = -\frac{1}{2}\left(\hat{u}_i(\boldsymbol{\kappa})\hat{\mathcal{P}}_{ik}(-\boldsymbol{\kappa})\hat{G}_k(-\boldsymbol{\kappa}) + \hat{u}^*_i(\boldsymbol{\kappa})\hat{\mathcal{P}}_{ik}(\boldsymbol{\kappa})\hat{G}_k(\boldsymbol{\kappa})\right) \tag{2.86}$$

- the dissipation of carrier phase kinetic energy:

$$\hat{\mathcal{E}}_f = \nu\kappa^2\hat{u}_i(\boldsymbol{\kappa})\hat{u}^*_i(\boldsymbol{\kappa}) \tag{2.87}$$

- the inter-scale transport of the dispersed phase:

$$\hat{T}_p(\boldsymbol{\kappa}) = -\frac{1}{2}\left(\hat{u}_{p,i}(\boldsymbol{\kappa})\hat{\mathcal{P}}_{ik}(-\boldsymbol{\kappa})\hat{G}_{p,k}(-\boldsymbol{\kappa}) + \hat{u}^*_{p,i}(\boldsymbol{\kappa})\hat{\mathcal{P}}_{ik}(\boldsymbol{\kappa})\hat{G}_{p,k}(\boldsymbol{\kappa})\right) \tag{2.88}$$

- the phase exchange (drag) term in the dispersed phase:

$$\hat{\Pi}_p(\boldsymbol{\kappa}) = \frac{1}{2}\frac{1}{\tau_p}\left(\left(\hat{u}_i(\boldsymbol{\kappa})\hat{u}^*_{p,i}(\boldsymbol{\kappa}) + \hat{u}^*_i(\boldsymbol{\kappa})\hat{u}_{p,i}(\boldsymbol{\kappa})\right) - 2\hat{u}_{p,i}(\boldsymbol{\kappa})\hat{u}^*_{p,i}(\boldsymbol{\kappa})\right) \tag{2.89}$$

- the dissipation of dispersed phase kinetic energy by QB diffusion:

$$\hat{\mathcal{E}}_p = \nu_{QB}\kappa^2\hat{u}_{p,i}(\boldsymbol{\kappa})\hat{u}^*_{p,i}(\boldsymbol{\kappa}) \tag{2.90}$$

- the inter-scale transfer term in the carrier-dispersed phase correlation:

$$\begin{aligned}\hat{T}_{fp} &= -\frac{1}{2}\Big(\hat{u}_{p,i}(\boldsymbol{\kappa})\hat{\mathcal{P}}_{ik}(-\boldsymbol{\kappa})\hat{G}_k(-\boldsymbol{\kappa}) + \hat{u}^*_{p,i}(\boldsymbol{\kappa})\hat{\mathcal{P}}_{ik}(\boldsymbol{\kappa})\hat{G}_k(\boldsymbol{\kappa}) \\ &\quad + \hat{u}_i(\boldsymbol{\kappa})\hat{\mathcal{P}}_{ik}(-\boldsymbol{\kappa})\hat{G}_{p,k}(-\boldsymbol{\kappa}) + \hat{u}^*_i(\boldsymbol{\kappa})\hat{\mathcal{P}}_{ik}(\boldsymbol{\kappa})\hat{G}_{p,k}(\boldsymbol{\kappa})\Big)\end{aligned} \tag{2.91}$$

- the term related to drag in the fluid-particle correlation:

$$\hat{\Pi}_{fp} = \frac{1}{2}\frac{1}{\tau_p}\left(2\hat{u}_i(\boldsymbol{\kappa})\hat{u}^*_i(\boldsymbol{\kappa}) - \left(\hat{u}_i(\boldsymbol{\kappa})\hat{u}^*_{p,i}(\boldsymbol{\kappa}) + \hat{u}^*_i(\boldsymbol{\kappa})\hat{u}_{p,i}(\boldsymbol{\kappa})\right)\right) \tag{2.92}$$

- and the dissipation of fluid-particle correlation:

$$\hat{\mathcal{E}}_{fp} = (\nu + \nu_{QB})\kappa^2\left(\hat{u}_{p,i}(\boldsymbol{\kappa})\hat{u}^*_i(\boldsymbol{\kappa}) + \hat{u}_i(\boldsymbol{\kappa})\hat{u}^*_{p,i}(\boldsymbol{\kappa})\right) \tag{2.93}$$

This allows to write the equations for the temporal development of the spectra as:

$$\frac{\partial}{\partial t}E_f(\boldsymbol{\kappa}) - \hat{T}_f(\boldsymbol{\kappa}) + \hat{\mathcal{E}}_f(\boldsymbol{\kappa}) = 0 \tag{2.94}$$

$$\frac{\partial}{\partial t}E_p(\boldsymbol{\kappa}) - \hat{T}_p(\boldsymbol{\kappa}) + \hat{\mathcal{E}}_p(\boldsymbol{\kappa}) - \hat{\Pi}_p(\boldsymbol{\kappa}) = 0 \tag{2.95}$$

$$\frac{\partial}{\partial t}E_{fp}(\boldsymbol{\kappa}) - \hat{T}_{fp}(\boldsymbol{\kappa}) + \hat{\mathcal{E}}_{fp}(\boldsymbol{\kappa}) - \hat{\Pi}_{fp}(\boldsymbol{\kappa}) = 0 \tag{2.96}$$

In incompressible homogeneous isotropic turbulence the expression $\hat{T}_f(\boldsymbol{\kappa})$ is a transfer term in the sense that the wave number integral of this quantity is zero.

$$\int \hat{T}_f(\boldsymbol{\kappa})d\boldsymbol{\kappa} = 0 \tag{2.97}$$

By analogy the expressions $\hat{T}_p(\boldsymbol{\kappa})$ and $\hat{T}_p(\boldsymbol{\kappa})$ were also named transfer terms since they redistribute kinetic energy. However they do not necessarily satisfy the transport condition in the sence that the wave number integral vanishes.

Dissipative quantities containing Quasi Brownian viscosity ν_{QB} are actually models since in contrary to the carrier phase viscosity ν the dispersed phase viscosity varies in space with $\delta\breve{\theta}_p$ and is therefore not constant.

When the QBE is small or comparable to the correlated particle kinetic energy $\breve{u}_p^2 \geq 2/3\delta\breve{\theta}_p$ the situation can be compared to gaseous flows at Mach numbers ≥ 1. Then the behavior of the dispersed phase can not be considered as incompressible and a compressible analysis of the dispersed phase becomes necessary. This compressible analysis is presented in the following section.

2.4.2 Governing Equations in compressible analysis

Since the gaseous equations can be treated as incompressible ($Ma \ll 1$) the compressible analysis is limited to the dispersed phase. The primitive transport equations of the compressible dispersed phase are:

$$\frac{\partial}{\partial t}\breve{n}_p + \frac{\partial}{\partial x_j}\breve{n}_p\breve{u}_{p,j} = 0 \tag{2.98}$$

$$\frac{\partial}{\partial t}\breve{u}_{p,i} + \breve{u}_{p,j}\frac{\partial}{\partial x_j}\breve{u}_{p,i} = -\frac{1}{\breve{n}_p}\frac{\partial}{\partial x_i}P_{QB} + \nu_{QB}\frac{\partial}{\partial x_j}\left(\frac{\partial \breve{u}_{p,i}}{\partial x_j} + \frac{\partial \breve{u}_{p,j}}{\partial x_i} - \frac{2}{3}\delta_{ij}\frac{\partial u_{p,k}}{\partial x_k}\right) \tag{2.99}$$

$$+\frac{1}{\tau_p}\left(u_i - \breve{u}_{p,i}\right) \tag{2.100}$$

Fourier transform of Eq. 2.99 is then:

$$\frac{\partial}{\partial t}\hat{u}_{p,i}(\boldsymbol{\kappa}) = -\mathcal{F}_k\left\{\frac{1}{\breve{n}_p}\frac{\partial}{\partial x_i}P_{QB}\right\} \tag{2.101}$$

$$-\nu_{QB}\left(\kappa^2\hat{u}_{p,i}(\boldsymbol{\kappa}) + \kappa_j\left(\kappa_i\hat{u}_{p,j}(\boldsymbol{\kappa})\right) - \frac{2}{3}\delta_{ij}\kappa_j\left(\kappa_k\hat{u}_{p,k}(\boldsymbol{\kappa})\right)\right) \tag{2.102}$$

$$-\mathcal{F}_{\boldsymbol{\kappa}}\left\{u_{p,j}(x)\frac{\partial}{\partial x_j}u_{p,i}(x)\right\} - \frac{1}{\tau_p}\left(\hat{u}_{p,i} - \hat{u}_i\right)$$

For the ease of notation some definitions for transport, pressure and viscous term are introduced:

- the fourier transform of the transport term is abbreviated by:

$$\hat{H}_i\left(\boldsymbol{\kappa}\right) = \mathcal{F}_{\boldsymbol{\kappa}}\left\{\breve{u}_{p,j}(x)\frac{\partial}{\partial x_j}\breve{u}_{p,i}(x)\right\} \tag{2.103}$$

- The fourier transform of the pressure gradient term is abbreviated by:

$$\hat{Q}_i\left(\boldsymbol{\kappa}\right) = \mathcal{F}_{\boldsymbol{\kappa}}\left\{\frac{1}{\breve{n}_p}\frac{\partial}{\partial x_i}P_{QB}\right\} \tag{2.104}$$

- The viscous term is abbreviated by [†]:

$$\hat{\mathcal{S}}_i(\boldsymbol{\kappa}) = \nu_{QB}\left(\kappa^2\hat{u}_{p,i}(\boldsymbol{\kappa}) + \kappa_i\left(\kappa_j\hat{u}_{p,j}(\boldsymbol{\kappa})\right) - \frac{2}{3}\delta_{ij}\kappa_j\left(\kappa_k\hat{u}_{p,k}(\boldsymbol{\kappa})\right)\right) \tag{2.105}$$

Then the fourier transformed transport equation is:

$$\frac{\partial}{\partial t}\hat{u}_{p,i}(\boldsymbol{\kappa}) = -\hat{Q}_i(\boldsymbol{\kappa}) - \hat{H}_i\left(\boldsymbol{\kappa}\right) - \hat{\mathcal{S}}_i\left(\boldsymbol{\kappa}\right) - \frac{1}{\tau_p}\left(\hat{u}_{p,i} - \hat{u}_i\right) \tag{2.106}$$

[†]This form is only valid when ν_{QB} is constant. This is not necessarily true. This formulation is only chosen for simplicity and is therefore a model and not the exact dissipation due to QBM.

Note that the difference between Eq. 2.73 and Eq. 2.106 is due to the pressure compensation of the nonlinear term $\hat{H}_k(\boldsymbol{\kappa})$ parallel to $\boldsymbol{\kappa}$. The other difference arises from the viscous operator that takes into account the compressible component of the velocity. The transport equations for spectral kinetic energy of the dispersed phase and fluid-particle correlation take therefore a somewhat different form:

$$\begin{aligned}\frac{\partial}{\partial t}\hat{u}_{p,i}(\boldsymbol{\kappa})\hat{u}^*_{p,i}(\boldsymbol{\kappa}) &= -\hat{u}_{p,i}(\boldsymbol{\kappa})\hat{Q}^*_i(\boldsymbol{\kappa}) - \hat{u}^*_{p,i}(\boldsymbol{\kappa})\hat{Q}_i(\boldsymbol{\kappa}) \\ &- \hat{u}_{p,i}(\boldsymbol{\kappa})\hat{H}^*_i(\boldsymbol{\kappa}) - \hat{u}^*_{p,i}(\boldsymbol{\kappa})\hat{H}_i(\boldsymbol{\kappa}) \\ &- \hat{u}_{p,i}(\boldsymbol{\kappa})\hat{\mathcal{S}}^*_i(\boldsymbol{\kappa}) - \hat{u}^*_{p,i}(\boldsymbol{\kappa})\hat{\mathcal{S}}_i(\boldsymbol{\kappa}) \\ &+ \frac{1}{\tau_p}\left(\left(\hat{u}_i(\boldsymbol{\kappa})\hat{u}^*_{p,i}(\boldsymbol{\kappa}) + \hat{u}^*_i(\boldsymbol{\kappa})\hat{u}_{p,i}(\boldsymbol{\kappa})\right) - 2\hat{u}_{p,i}(\boldsymbol{\kappa})\hat{u}^*_{p,i}(\boldsymbol{\kappa})\right)\end{aligned} \tag{2.107}$$

$$\begin{aligned}\left(\frac{\partial}{\partial t} + (\nu+\nu_{QB})\,\kappa^2\right)\left(\hat{u}_{p,i}(\boldsymbol{\kappa})\hat{u}^*_i(\boldsymbol{\kappa}) + \hat{u}^*_{p,i}(\boldsymbol{\kappa})\hat{u}_i(\boldsymbol{\kappa})\right) = \\ -\hat{u}_{p,i}(\boldsymbol{\kappa})\hat{\mathcal{P}}_{ik}(-\boldsymbol{\kappa})\hat{G}_k(-\boldsymbol{\kappa}) - \hat{u}^*_{p,i}(\boldsymbol{\kappa})\hat{\mathcal{P}}_{ik}(\boldsymbol{\kappa})\hat{G}_k(\boldsymbol{\kappa}) \\ -\hat{u}_i(\boldsymbol{\kappa})\hat{Q}^*_i(\boldsymbol{\kappa}) - \hat{u}^*_i(\boldsymbol{\kappa})\hat{Q}_i(\boldsymbol{\kappa}) \\ -\hat{u}_i(\boldsymbol{\kappa})\hat{H}^*_i(\boldsymbol{\kappa}) - \hat{u}^*_i(\boldsymbol{\kappa})\hat{H}_i(\boldsymbol{\kappa}) \\ +\frac{1}{\tau_p}\left(2\hat{u}_i(\boldsymbol{\kappa})\hat{u}^*_i(\boldsymbol{\kappa}) - \left(\hat{u}_i(\boldsymbol{\kappa})\hat{u}^*_{p,i}(\boldsymbol{\kappa}) + \hat{u}^*_i(\boldsymbol{\kappa})\hat{u}_{p,i}(\boldsymbol{\kappa})\right)\right)\end{aligned} \tag{2.108}$$

Since the compressible term in the viscous dissipation of the carrier-phase dispersed-phase correlation vanishes, the viscous component can be written as in the incompressible case. Like in the incompressible case the different terms of the transport equation can be isolated. Spectral interscale transport of the dispersed equation can be divided into the nonlinear transport contribution due to $\hat{H}_i$ and the dynamic pressure contribution due to $i\kappa_i\hat{P}_{QB}$ for the spectral kinetic energy of the dispersed phase:

$$\hat{T}^c_p(\boldsymbol{\kappa}) = -\frac{1}{2}\left(\hat{u}_{p,i}(\boldsymbol{\kappa})\hat{H}^*_i(\boldsymbol{\kappa}) + \hat{u}^*_{p,i}(\boldsymbol{\kappa})\hat{H}_i(\boldsymbol{\kappa})\right) \tag{2.109}$$

$$\hat{T}^{pc}_p(\boldsymbol{\kappa}) = -\frac{1}{2}\left(\hat{u}_{p,i}(\boldsymbol{\kappa})\hat{Q}^*_i(\boldsymbol{\kappa}) + \hat{u}^*_{p,i}(\boldsymbol{\kappa})\hat{Q}_i(\boldsymbol{\kappa})\right) \tag{2.110}$$

and for the case of the spectral fluid-particle correlation :

$$\begin{aligned}\hat{T}^c_{fp}(\boldsymbol{\kappa}) &= -\frac{1}{4}\left(\hat{u}_{p,i}(\boldsymbol{\kappa})\hat{\mathcal{P}}_{ik}(-\boldsymbol{\kappa})\hat{G}_k(-\boldsymbol{\kappa}) + \hat{u}^*_{p,i}(\boldsymbol{\kappa})\hat{\mathcal{P}}_{ik}(\boldsymbol{\kappa})\hat{G}_k(\boldsymbol{\kappa})\right. \\ &\left. +\hat{u}_i(\boldsymbol{\kappa})\hat{H}^*_i(\boldsymbol{\kappa}) + \hat{u}^*_i(\boldsymbol{\kappa})\hat{H}_i(\boldsymbol{\kappa})\right)\end{aligned} \tag{2.111}$$

$$\hat{T}^{pc}_{fp}(\boldsymbol{\kappa}) = -\frac{1}{4}\left(\hat{u}_i(\boldsymbol{\kappa})\hat{Q}^*_i(\boldsymbol{\kappa}) + \hat{u}^*_i(\boldsymbol{\kappa})\hat{Q}_i(\boldsymbol{\kappa})\right) \tag{2.112}$$

The compressible viscous component is abbreviated by $\hat{\mathcal{E}}^c_p$:

$$\hat{\mathcal{E}}^c_p = \frac{1}{2}\left(\hat{u}_{p,i}(\boldsymbol{\kappa})\hat{\mathcal{S}}^*_i(\boldsymbol{\kappa}) + \hat{u}^*_{p,i}(\boldsymbol{\kappa})\hat{\mathcal{S}}_i(\boldsymbol{\kappa})\right) \tag{2.113}$$

The temporal development in compressible analysis of the dispersed phase can then be written as:

$$\frac{\partial}{\partial t}E_p(\boldsymbol{\kappa}) - \hat{T}_p^c(\boldsymbol{\kappa}) - \hat{T}_p^{pc}(\boldsymbol{\kappa}) + \hat{\mathcal{E}}_p^c(\boldsymbol{\kappa}) - \hat{\Pi}_p(\boldsymbol{\kappa}) = 0 \tag{2.114}$$

$$\frac{\partial}{\partial t}E_{fp}(\boldsymbol{\kappa}) - \hat{T}_{fp}^c(\boldsymbol{\kappa}) - \hat{T}_{fp}^{pc}(\boldsymbol{\kappa}) + \hat{\mathcal{E}}_{fp}(\boldsymbol{\kappa}) - \hat{\Pi}_{fp}(\boldsymbol{\kappa}) = 0 \tag{2.115}$$

2.4.3 Detailed analysis of the incompressible and compressible behavior

Following the approach of Bertoglio [8][6] one can decompose the mesoscopic particle velocity field into a purely compressible part $\hat{u}_p^c$ and an incompressible solenoidal part $\hat{u}_p^s$. In spectral space the velocity field can be split using the projection operators introduced by Kraichnan [51] so that the velocity components can be written as follows:

$$\hat{u}_{p,i}^c = \frac{\kappa_i\kappa_j}{k^2}\hat{u}_{p,j} \tag{2.116}$$

$$\hat{u}_{p,i}^s = \left(\delta_{ij} - \frac{\kappa_i\kappa_j}{k^2}\right)\hat{u}_{p,j} \tag{2.117}$$

$$\hat{u}_{p,i} = \hat{u}_{p,i}^c + \hat{u}_{p,i}^s \tag{2.118}$$

By construction $\hat{u}_p^c$ and $\hat{u}_p^s$ are orthogonal in Fourier space. This allows therefore to decompose the particle kinetic energy into a compressible part and an incompressible part :

$$E_p^c(\boldsymbol{\kappa}) = \frac{1}{2}\hat{u}_{p,i}^c(\boldsymbol{\kappa})\hat{u}_{p,i}^{c*}(\boldsymbol{\kappa}) \tag{2.119}$$

$$E_p^s(\boldsymbol{\kappa}) = \frac{1}{2}\hat{u}_{p,i}^s(\boldsymbol{\kappa})\hat{u}_{p,i}^{s*}(\boldsymbol{\kappa}) \tag{2.120}$$

In the same way one may define a solenoidal carrier-phase dispersed-phase correlation.

$$E_{fp}^s(\boldsymbol{\kappa}) = \frac{1}{2}\left(\hat{u}_i^s(\boldsymbol{\kappa})\hat{u}_{p,i}^{s*}(\boldsymbol{\kappa}) + \hat{u}_i^{s*}(\boldsymbol{\kappa})\hat{u}_{p,i}^s(\boldsymbol{\kappa})\right) \tag{2.121}$$

Since $\hat{u}_i \neq \hat{u}_{p,i}$ the compressible component of the dispersed phase velocity is not necessarily orthogonal to the purely solenoidal carrier phase velocity. This justifies the introduction of a solenoidal carrier-phase dispersed phase correlation $E_{fp}^s \neq E_{fp}$.
In order to simplify the notation, the projection operator (Eq.2.75) is used to obtain the solenoidal part of the dispersed phase velocity and a new projection operator Π_{ij} [‡] is defined for the compressible part as :

$$\Pi_{ij} = \frac{\kappa_i\kappa_j}{\kappa^2} \tag{2.122}$$

[‡]The projection operator is defined by Π and the drag force component in the energy transport equation is defined by $\hat{\Pi}$. Both notations are chosen in accordance to literature.

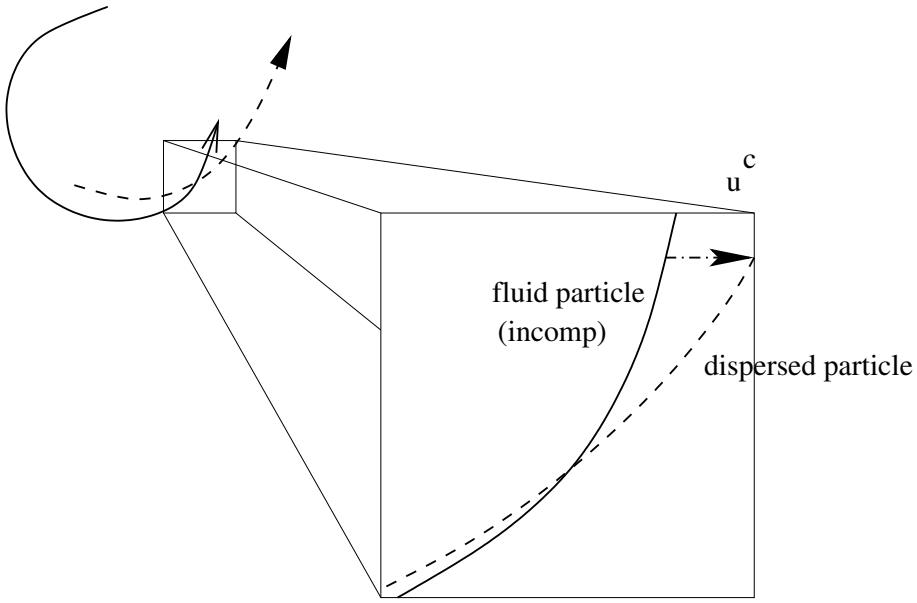

Figure 2.2: Sketch of the decomposition of the dispersed phase velocity into an incompressible component following the "fluid" particle (line) and a compressible component (u^c,vector) due to inertia, taking the particle out of the carrier phase vortex.

Compressible kinetic energy

Application of the projection operator Π_{ij} to the spectral velocity transport Eq. 2.106 leads then to a transport equation for the compressible part of the velocity field:

$$\begin{aligned}\frac{\partial}{\partial t}\hat{u}^c_{p,i}(\boldsymbol{\kappa}) &= -\Pi_{ij}\mathcal{F}_k\left\{\frac{1}{\breve{n}_p}\frac{\partial}{\partial x_j}P_{QB}\right\} - \nu_{QB}\frac{4}{3}\kappa_i\left(\kappa_j\hat{u}^c_{p,j}(\boldsymbol{\kappa})\right) \\ &\quad -\Pi_{ij}\mathcal{F}_{\boldsymbol{\kappa}}\left\{u_{p,k}(x)\frac{\partial}{\partial x_k}u_{p,j}(x)\right\} - \frac{1}{\tau_p}\left(\hat{u}^c_{p,i}\right)\end{aligned} \tag{2.123}$$

Since the carrier phase velocity field is assumed incompressible, the carrier phase velocity vanishes from the drag force term. The spectral transport Eq.2.123, allows already some interpretation on the nature of the compressible flow field. There is no coupling of the compressible flow field via drag force with the carrier phase. QBP, if present, counteracts the compressible velocity and therefore the only production of compressible velocity is due to the nonlinear term in the transport equation. Drag force on the other hand only diminishes the compressible velocity. From the physical viewpoint this is consistent since one expects a heavy particle (i.e. with a large relaxation time) to be centrifuged out of a carrier phase vortex leading to compressibility effects in the Eulerian description whereas a particle with a small relaxation time to follow the carrier phase vortex, here due to the strong repellent force in the drag force term. This example is sketched in Fig. 2.2.

Eqn. 2.123 can then be used to construct the transport equation for the compressible kinetic energy. Here also the definitions of eqns. 2.103,2.104 are used:

$$\begin{aligned}\frac{\partial}{\partial t}\hat{u}^{c}_{p,i}(\boldsymbol{\kappa})\hat{u}^{c*}_{p,i}(\boldsymbol{\kappa}) &= -\hat{u}^{c}_{p,i}(\boldsymbol{\kappa})\Pi_{ij}\hat{Q}^{*}_{j}(\boldsymbol{\kappa}) - \hat{u}^{c*}_{p,i}(\boldsymbol{\kappa})\Pi_{ij}\hat{Q}_{j}(\boldsymbol{\kappa}) \qquad (2.124)\\ &- \hat{u}^{c}_{p,i}(\boldsymbol{\kappa})\Pi_{ij}\hat{H}^{*}_{j}(\boldsymbol{\kappa}) - \hat{u}^{c*}_{p,i}(\boldsymbol{\kappa})\Pi_{ij}\hat{H}_{j}(\boldsymbol{\kappa})\\ &- 2\frac{4}{3}\nu_{QB}\left(\kappa_i\hat{u}^{c*}_{p,i}\right)\left(\kappa_j\hat{u}^{c}_{p,j}\right) - \frac{2}{\tau_p}\left(\hat{u}^{c}_{p,i}(\boldsymbol{\kappa})\hat{u}^{c*}_{p,i}(\boldsymbol{\kappa})\right)\end{aligned}$$

To shorten notation for the spectral energy equation the transport terms are defined as :

$$\hat{T}^{\Pi c}_{p}(\boldsymbol{\kappa}) = -\frac{1}{2}\left(\hat{u}^{c}_{p,i}(\boldsymbol{\kappa})\Pi_{ij}\hat{H}^{*}_{j}(\boldsymbol{\kappa}) + \hat{u}^{c*}_{p,i}(\boldsymbol{\kappa})\Pi_{ij}\hat{H}_{j}(\boldsymbol{\kappa})\right) \qquad (2.125)$$

$$\hat{T}^{\Pi pc}_{p}(\boldsymbol{\kappa}) = -\frac{1}{2}\left(\hat{u}^{c}_{p,i}(\boldsymbol{\kappa})\Pi_{ij}\hat{Q}^{*}_{j}(\boldsymbol{\kappa}) + \hat{u}^{c*}_{p,i}(\boldsymbol{\kappa})\Pi_{ij}\hat{Q}_{j}(\boldsymbol{\kappa})\right) \qquad (2.126)$$

The dissipative term due to drag force is abbreviated as :

$$\hat{\Pi}^{\Pi c}_{p}(\boldsymbol{\kappa}) = -\frac{1}{\tau_p}\left(\hat{u}^{c}_{p,i}(\boldsymbol{\kappa})\hat{u}^{c*}_{p,i}(\boldsymbol{\kappa})\right) \qquad (2.127)$$

and the dissipative term due to QB viscosity as :

$$\hat{\mathcal{E}}^{\Pi c}_{p} = \frac{4}{3}\nu_{QB}\left(\kappa_i\hat{u}^{c*}_{p,i}\right)\left(\kappa_j\hat{u}^{c}_{p,j}\right) \qquad (2.128)$$

Using the previous abbreviations one can write the spectral transport equation for the compressible energy of the dispersed velocity as :

$$\frac{\partial}{\partial t}E^{c}_{p}(\boldsymbol{\kappa}) - \hat{T}^{\Pi c}_{p}(\boldsymbol{\kappa}) - \hat{T}^{\Pi pc}_{p}(\boldsymbol{\kappa}) + \hat{\mathcal{E}}^{\Pi c}_{p}(\boldsymbol{\kappa}) - \hat{\Pi}^{\Pi c}_{p}(\boldsymbol{\kappa}) = 0 \qquad (2.129)$$

Since the gaseous carrier phase is considered as incompressible the compressible carrier-phase dispersed-phase correlation is zero.

Solenoidal kinetic energy

Application of the projection operator $\hat{\mathcal{P}}_{ij}$ to the spectral velocity transport Eq. 2.106 leads then to a transport equation for the incompressible part of the velocity field:

$$\frac{\partial}{\partial t}\hat{u}^{s}_{p,i}(\boldsymbol{\kappa}) = -\hat{\mathcal{P}}_{ij}\hat{Q}_{j}(\boldsymbol{\kappa}) - \hat{\mathcal{P}}_{ij}\hat{H}_{j}(\boldsymbol{\kappa}) - \hat{\mathcal{P}}_{ij}\hat{S}_{j}(\boldsymbol{\kappa}) - \frac{1}{\tau_p}\left(\hat{u}^{s}_{p,i} - \hat{u}^{s}_{i}\right) \qquad (2.130)$$

Eqn. 2.130 can then be used to construct the transport equation for the incompressible kinetic energy.

$$\begin{aligned}\frac{\partial}{\partial t}\hat{u}^{s}_{p,i}(\boldsymbol{\kappa})\hat{u}^{s*}_{p,i}(\boldsymbol{\kappa}) &= -\hat{u}^{s}_{p,i}(\boldsymbol{\kappa})\hat{\mathcal{P}}_{ij}\hat{Q}^{*}_{j}(\boldsymbol{\kappa}) - \hat{u}^{s*}_{p,i}(\boldsymbol{\kappa})\hat{\mathcal{P}}_{ij}\hat{Q}_{j}(\boldsymbol{\kappa}) \qquad (2.131)\\ &- \hat{u}^{s}_{p,i}(\boldsymbol{\kappa})\hat{\mathcal{P}}_{ij}\hat{H}^{*}_{j}(\boldsymbol{\kappa}) - \hat{u}^{s*}_{p,i}(\boldsymbol{\kappa})\hat{\mathcal{P}}_{ij}\hat{H}_{j}(\boldsymbol{\kappa}) \qquad (2.132)\\ &- \hat{u}^{s}_{p,i}(\boldsymbol{\kappa})\hat{\mathcal{P}}_{ij}\hat{S}^{*}_{j}(\boldsymbol{\kappa}) - \hat{u}^{s*}_{p,i}(\boldsymbol{\kappa})\hat{\mathcal{P}}_{ij}\hat{S}_{j}(\boldsymbol{\kappa})\\ &- \frac{1}{\tau_p}\left(2\hat{u}^{s}_{p,i}(\boldsymbol{\kappa})\hat{u}^{s*}_{p,i}(\boldsymbol{\kappa}) - \hat{u}^{s}_{p,i}(\boldsymbol{\kappa})\hat{u}^{s*}_{i}(\boldsymbol{\kappa}) - \hat{u}^{s*}_{p,i}(\boldsymbol{\kappa})\hat{u}^{s}_{i}(\boldsymbol{\kappa})\right)\end{aligned}$$

To shorten notation for the spectral energy equation the transport terms are defined as :

$$\hat{T}_p^{\mathcal{P}c}(\boldsymbol{\kappa}) = -\frac{1}{2}\left(\hat{u}_{p,i}^s(\boldsymbol{\kappa})\hat{\mathcal{P}}_{ij}\hat{H}_j^*(\boldsymbol{\kappa}) + \hat{u}_{p,i}^{s*}(\boldsymbol{\kappa})\hat{\mathcal{P}}_{ij}\hat{H}_j(\boldsymbol{\kappa})\right) \tag{2.133}$$

$$\hat{T}_p^{\mathcal{P}pc}(\boldsymbol{\kappa}) = -\frac{1}{2}\left(\hat{u}_{p,i}^s(\boldsymbol{\kappa})\hat{\mathcal{P}}_{ij}\hat{Q}_j^*(\boldsymbol{\kappa}) + \hat{u}_{p,i}^{s*}(\boldsymbol{\kappa})\hat{\mathcal{P}}_{ij}\hat{Q}_j(\boldsymbol{\kappa})\right) \tag{2.134}$$

The dissipative term due to drag force is abbreviated as :

$$\hat{\Pi}_p^{\mathcal{P}c}(\boldsymbol{\kappa}) = -\frac{1}{2\tau_p}\left(\hat{u}_{p,i}^s(\boldsymbol{\kappa})\hat{u}_{p,i}^{s*}(\boldsymbol{\kappa}) - \hat{u}_{p,i}^s(\boldsymbol{\kappa})\hat{u}_i^{s*}(\boldsymbol{\kappa}) - \hat{u}_{p,i}^{s*}(\boldsymbol{\kappa})\hat{u}_i^s(\boldsymbol{\kappa})\right) \tag{2.135}$$

and the dissipative term due to QB viscosity as :

$$\hat{\mathcal{E}}_p^{\mathcal{P}c} = \hat{u}_{p,i}^s(\boldsymbol{\kappa})\hat{\mathcal{P}}_{ij}\hat{S}_j^*(\boldsymbol{\kappa}) + \hat{u}_{p,i}^{s*}(\boldsymbol{\kappa})\hat{\mathcal{P}}_{ij}\hat{S}_j(\boldsymbol{\kappa}) \tag{2.136}$$

Using the previous abbreviations one can write the spectral transport equation for the incompressible energy of the dispersed velocity as :

$$\frac{\partial}{\partial t}E_p^s(\boldsymbol{\kappa}) - \hat{T}_p^{\mathcal{P}c}(\boldsymbol{\kappa}) - \hat{T}_p^{\mathcal{P}pc}(\boldsymbol{\kappa}) + \hat{\mathcal{E}}_p^{\mathcal{P}c}(\boldsymbol{\kappa}) - \hat{\Pi}_p^{\mathcal{P}c}(\boldsymbol{\kappa}) = 0 \tag{2.137}$$

This evolution equation differs from the incompressible treatment in Eq. 2.94 by the separate treatment of transport and pressure effect. Here it is not explicitly assumed, that the flow field is divergence free but the solenoidal components of the velocity field are used. Hence the E_p^s differs from the total kinetic energy by the compressible component. [§]

Application of projection procedure as before to the dispersed phase spectral velocity equation and multiplication with the carrier phase velocity allows to construct together with the equivalent gaseous equation the solenoidal spectral transport equation of carrier phase- dispersed phase correlation.

$$\begin{aligned}\left(\frac{\partial}{\partial t} + (\nu + \nu_{QB})\,\kappa^2\right)\left(\hat{u}_{p,i}^s(\boldsymbol{\kappa})\hat{u}_i^{s*}(\boldsymbol{\kappa}) + \hat{u}_{p,i}^{s*}(\boldsymbol{\kappa})\hat{u}_i^s(\boldsymbol{\kappa})\right) = \\ -\hat{u}_{p,i}^s(\boldsymbol{\kappa})\hat{\mathcal{P}}_{ik}(-\boldsymbol{\kappa})\hat{G}_k(-\boldsymbol{\kappa}) - \hat{u}_{p,i}^{s*}(\boldsymbol{\kappa})\hat{\mathcal{P}}_{ik}(\boldsymbol{\kappa})\hat{G}_k(\boldsymbol{\kappa}) \\ -\hat{u}_i^s(\boldsymbol{\kappa})\hat{\mathcal{P}}_{ik}\hat{Q}_k^*(\boldsymbol{\kappa}) - \hat{u}_i^{s*}(\boldsymbol{\kappa})\hat{\mathcal{P}}_{ik}\hat{Q}_k(\boldsymbol{\kappa}) \\ -\hat{u}_i^s(\boldsymbol{\kappa})\hat{\mathcal{P}}_{ik}\hat{H}_k^*(\boldsymbol{\kappa}) - \hat{u}_i^{s*}(\boldsymbol{\kappa})\hat{\mathcal{P}}_{ik}\hat{H}_k(\boldsymbol{\kappa}) \\ +\frac{1}{\tau_p}\left(2\hat{u}_i^s(\boldsymbol{\kappa})\hat{u}_i^{s*}(\boldsymbol{\kappa}) - \left(\hat{u}_i^s(\boldsymbol{\kappa})\hat{u}_{p,i}^{s*}(\boldsymbol{\kappa}) + \hat{u}_i^{s*}(\boldsymbol{\kappa})\hat{u}_{p,i}^s(\boldsymbol{\kappa})\right)\right)\end{aligned} \tag{2.138}$$

The following notations are introduced for the transport equations of solenoidal carrier phase dispersed phase correlation :

$$\begin{aligned}\hat{T}_{fp}^{\mathcal{P}c}(\boldsymbol{\kappa}) \;=\; -\frac{1}{4}\Big(&\hat{u}_{p,i}^s(\boldsymbol{\kappa})\hat{\mathcal{P}}_{ik}(-\boldsymbol{\kappa})\hat{G}_k(-\boldsymbol{\kappa}) + \hat{u}_{p,i}^{s*}(\boldsymbol{\kappa})\hat{\mathcal{P}}_{ik}(\boldsymbol{\kappa})\hat{G}_k(\boldsymbol{\kappa}) \\ &+\hat{u}_i^s(\boldsymbol{\kappa})\hat{\mathcal{P}}_{ik}(-\boldsymbol{\kappa})\hat{H}_k^*(\boldsymbol{\kappa}) + \hat{u}_i^{*s}(\boldsymbol{\kappa})\hat{\mathcal{P}}_{ik}(\boldsymbol{\kappa})\hat{H}_k(\boldsymbol{\kappa})\Big)\end{aligned} \tag{2.139}$$

[§]The superscript s at the carrier phase velocity is not necessary, since the carrier phase is considered incompressible. The notation is kept for clarity only.

$$\hat{T}_{fp}^{\mathcal{P}pc}(\boldsymbol{\kappa}) = -\frac{1}{4}\left(\hat{u}_i^s(\boldsymbol{\kappa})\hat{\mathcal{P}}_{ik}(-\boldsymbol{\kappa})\hat{Q}_k^*(\boldsymbol{\kappa}) + \hat{u}_i^{s*}(\boldsymbol{\kappa})\hat{\mathcal{P}}_{ik}(\boldsymbol{\kappa})\hat{Q}_k(\boldsymbol{\kappa})\right) \tag{2.140}$$

$$\hat{\mathcal{E}}_{fp}^{\mathcal{P}}(\boldsymbol{\kappa}) = (\nu + \nu_{QB})\,\kappa^2\left(\hat{u}_{p,i}^s(\boldsymbol{\kappa})\hat{u}_i^{s*}(\boldsymbol{\kappa}) + \hat{u}_{p,i}^{s*}(\boldsymbol{\kappa})\hat{u}_i^s(\boldsymbol{\kappa})\right) \tag{2.141}$$

$$\hat{\Pi}_{fp}^{\mathcal{P}}(\boldsymbol{\kappa}) = \frac{1}{\tau_p}\left(2\hat{u}_i^s(\boldsymbol{\kappa})\hat{u}_i^{s*}(\boldsymbol{\kappa}) - \left(\hat{u}_i^s(\boldsymbol{\kappa})\hat{u}_{p,i}^{s*}(\boldsymbol{\kappa}) + \hat{u}_i^{s*}(\boldsymbol{\kappa})\hat{u}_{p,i}^s(\boldsymbol{\kappa})\right)\right) \tag{2.142}$$

This yields the following transport equation for the carrier phase dispersed phase correlation.

$$\frac{\partial}{\partial t}E_{fp}^s(\boldsymbol{\kappa}) - \hat{T}_{fp}^{\mathcal{P}c}(\boldsymbol{\kappa}) - \hat{T}_{fp}^{\mathcal{P}pc}(\boldsymbol{\kappa}) + \hat{\mathcal{E}}_{fp}^{\mathcal{P}}(\boldsymbol{\kappa}) - \hat{\Pi}_{fp}^{\mathcal{P}}(\boldsymbol{\kappa}) = 0 \tag{2.143}$$

2.4.4 Three dimensional spectra functions

The spectral energies $E_f(\boldsymbol{\kappa}), E_p(\boldsymbol{\kappa}), E_{fp}(\boldsymbol{\kappa})$ and their corresponding transport terms depend on the three dimensional wave vector $\boldsymbol{\kappa}$. Since the turbulent flow investigated in this work is considered isotropic, one can remove the directional information retaining only the wave number. This is done by integration of the three dimensional spectral energies over an iso-wave number surface to obtain the three dimensional spectra functions depending on the scalar wave number only.

$$E_\phi(\kappa) = \iiint E_\phi(\boldsymbol{\kappa})\delta(\kappa - |\boldsymbol{\kappa}|)d\boldsymbol{\kappa} \tag{2.144}$$

Three dimensional spectra functions and transfer terms are used later in this chapter to analyze a volume filtered Lagrangian solution. In the following chapters this tool will as well be used to analyze the Eulerian simulations with different stress tensor models. Finally the spectral tools and results are used to discuss the implications for a future LES model.

2.5 Particle dispersion in turbulence

The uncorrelated molecular movement in a gas tends to render the molecular concentrations of species more uniform. From the viewpoint of a continous field this process is described by what is called molecular diffusion and associated to the Eulerian transport equations. Passing to discrete particles (or fluid particles) the fact that two particles, that are initially very close, gain in distance with time due to the (turbulent) motion is called (turbulent) dispersion.
The definition of dispersion is however not unique. Tchen [12] associates particle dispersion with probability function:

> ... the probability for a particle, which at the instant t_0 started from the region $(y_0, y_0 + dy_0)$ to arrive in the region $(y, y + dy)$ at the instant t.

Other authors associate with dispersion the coefficient that quantifies the dispersive transport like the diffusion coefficient quantifies the diffusive transport.

Turbulent dispersion is driven by the turbulent (correlated) motion of the particles. Assuming drag force as only coupling mechanism, the dispersion coefficient can be related to the integral properties of the carrier phase turbulence and the particle relaxation time []. When particles are subject to supplementary gravity field, particles tend to cross the carrier phase turbulence with a certain settling velocity given by the gravity constant and the particle relaxation time. If the characteristic time for crossing an eddy is significantly shorter than the equivalent integral turbulent time scale, the "effective Stokes number" of the particle concerning dispersion is governed by the time-scale of gravitational settling [119]. This phenomena is known as the crossing trajectory effect.

2.5.1 Lagrangian measurement of particle dispersion coefficient

Particle dispersion is usually measured in Lagrangian simulations by tracking individual particle path and calculating the variance of the relative displacement [102]:

$$\left\langle X_p^2(t) \right\rangle = \frac{1}{N} \sum_{j=1}^{N} \left[X_{p,j}(t) - X_{p,j}(t_0) \right]^2 . \tag{2.145}$$

The particle dispersion can be related to the time derivate of this quantity (see [67])

$$D_p^L(t) = \frac{1}{2} \frac{d}{dt} \left\langle X_p^2(t) \right\rangle \tag{2.146}$$

Using the definition of the Lagrangian particle velocity the particle dispersion coefficient can be related to the Lagrangian velocity autocorrelation [102] (see also eq.2.14).

2.5.2 Eulerian measurement of particle dispersion coefficient

In Eulerian simulations one does not have access to individual particle paths. Particle dispersion can still be measured by a semi-empirical method (see Laviéville [52], Deutsch [22], Simonin [] and Monin [67]): Supposing that the simulation is being carried out with colored particles, a transport equation is written for the fraction of colored particles to total particles ($\tilde{c} = \frac{\tilde{n}_c}{\tilde{n}_p}$). This transport equation is similar to the transport equation for particle number density (Eq. 1.35):

$$\frac{\partial}{\partial t} \tilde{c} \tilde{n}_p + \frac{\partial}{\partial x_i} \tilde{c} \tilde{n}_p \tilde{u}_{p,i} = \frac{\partial}{\partial x_i} \tilde{c} \tilde{n}_p \left(\tilde{u}_{p,i} - \tilde{u}_{p,i}^c \right) \tag{2.147}$$

Here, $\tilde{u}_{p,i}^c$ is the mesoscopic velocity of colored particles. Since only the velocity of the total particle number density is resolved, a supplementary term arises on the rhs of Eq.(2.147). This term takes into account the slip velocity between colored particles and the mesoscopic velocity of the particle ensemble. Comparing to the Navier-Stokes equations, this term is the equivalent of molecular diffusion in a species equation. Since the slip velocity can only arise from uncorrelated movement of the particles, this term can be modeled as a diffusion related to the quasi Brownian motion.

If the ensemble-averaged mean number density fraction of colored particles $\langle\tilde{n}_p\rangle\mathcal{C} = \langle\tilde{n}_p\tilde{c}\rangle$, $(\tilde{c} = \mathcal{C} + c')$ is uniformly stratified in the k-direction and fluctuations are assumed periodic with respect to the computational domain, the fluctuating number density of colored particles $c'\tilde{n}_p$ can be extracted from the total colored number density and one obtains a transport equation for the fluctuations of colored particle concentration:

$$\frac{\partial}{\partial t}c'\tilde{n}_p + \frac{\partial}{\partial x_i}c'\tilde{n}_p\tilde{u}_{p,i} = -\tilde{n}_p\tilde{u}_{p,k}\frac{\partial}{\partial x_k}\mathcal{C} + \frac{\partial}{\partial x_i}\tilde{c}\tilde{n}_p(\tilde{u}_{p,i} - \tilde{u}^c_{p,i}) \tag{2.148}$$

Averaging the colored number density equation (Eq. (2.147)) one obtains a Reynolds averaged type transport equation:

$$\frac{\partial}{\partial t}\langle\tilde{n}_p\rangle\mathcal{C} + \frac{\partial}{\partial x_i}\langle\tilde{n}_p\rangle\mathcal{C}\langle\tilde{u}_{p,i}\rangle_p = -\frac{\partial}{\partial x_i}\langle\tilde{n}_p c'u_{p,i}\rangle + \frac{\partial}{\partial x_i}\left\langle\tilde{c}\tilde{n}_p\left(\tilde{u}_{p,i} - \tilde{u}^c_{p,i}\right)\right\rangle \tag{2.149}$$

Eq.2.148 has been written neglecting the quasi Brownian motion term. Particle dispersion can be measured making a gradient assumption: $(\langle c'\tilde{n}_p\tilde{u}_{p,k}\rangle = \langle\tilde{n}_p\rangle D^t_{p,k}\frac{\partial}{\partial x_k}\mathcal{C})$. A semi-empirical dispersion coefficient is defined by:

$$D^t_{p,k} = \frac{\langle\tilde{n}_p c'u_{p,k}\rangle}{\langle\tilde{n}_p\rangle\frac{\partial}{\partial x_k}\mathcal{C}} \tag{2.150}$$

This dispersion coefficient compares to the Lagrangian dispersion coefficient (2.146) in the long time limit of stationary turbulence. Nevertheless simulations neglecting the quasi Brownian motion should underestimate the Lagrangian dispersion.

As pointed out by Laviéville [52] following an argument of Batchelor [7] of Eq. 2.150 in the case of a pure diffusion equation, the semi-empirical Eulerian Dispersion coefficient is equivalent to the Lagrangian expression (Eq. 2.146).

2.5.3 Measurement of particle dispersion in a gravity field

In the presence of gravity particles are subject to a constant force field. If gravity is balanced by particle drag, particles have attained the so called terminal velocity. The terminal velocity v_t in the case of negligble mean carrier velocity is

$$v_t = g\tau_p \tag{2.151}$$

where $g = 9.806$ is the gravity constant and τ_p is the particle relaxation time. Then Eq. 2.147 has to be modified such as to take into acount the terminal velocity.

$$\frac{\partial}{\partial t}\tilde{c}\tilde{n}_p + \frac{\partial}{\partial x_i}\tilde{c}\tilde{n}_p\left(\tilde{u}_{p,i} + v_t\delta_{i,g}\right) = \frac{\partial}{\partial x_i}\tilde{c}\tilde{n}_p\left(\tilde{u}_{p,i} - \tilde{u}^c_{p,i}\right) \tag{2.152}$$

Since the terminal velocity is constant it the divergence part associated to the terminal velocity is zero. Therefore Eq. 2.152 can be used to write the analogous of Eq. 2.148.

$$\frac{\partial}{\partial t}c'\tilde{n}_p + \frac{\partial}{\partial x_i}c'\tilde{n}_p\tilde{u}_{p,i} = -\tilde{n}_p\tilde{u}_{p,k}\frac{\partial}{\partial x_k}\mathcal{C} - v_t\delta_{k,g}\frac{\partial}{\partial x_k}\tilde{n}_p c' + \frac{\partial}{\partial x_i}\tilde{c}\tilde{n}_p(\tilde{u}_{p,i} - \tilde{u}^c_{p,i}) \tag{2.153}$$

Therefore gravity adds an intrinsic forcing term to the dispersion equation. Whereas in the absence of gravity the dispersion equation is independent on the value of the mean forcing gradient $\frac{\partial}{\partial x_k}\mathcal{C}$, the forcing gradient needs to be significantly larger then the terminal velocity in order to suppress spurious forcing due to gravity.

2.6 Test cases for dynamics of particles in turbulence

A generic test case for the dynamics of a coupled carrier-phase dispersed phase system is particles in homogeneous isotropic turbulence. Such model flows can be classified in three categories:

1. *Decreasing homogeneous turbulence:* This reflects the natural behavior of the Navier-Stokes equations and no artificial forcing terms are needed. This test case has however the drawback of being statistically unsteady and therefore particle relaxation times need to be chosen carefully, so that the decreasing behavior of the carrier phase turbulence does not alter the behavior of the points of interest. The advantage of this setup is, that it can be compared to experiments of spatially decreasing grid turbulence. This approach has been used together with Lagrangian particle tracking to determine particle dynamics and particle dispersion [102][27].

2. *Forced homogeneous isotropic turbulence:* In this setup the most energetic length scales are forced in spectral space [48]. This setup is well suited to study temporally independent quantities, since the turbulence is statistically stationary. This approach has been extensively used to study particles in turbulent flows [32][52][22]

3. *Kinematic Simulation (KS):* This approach is sometimes called artificial (or cheap) turbulence, since it only provides a divergence free flow field with the spectral kinetic energy characteristic of the Navier-Stokes equations [33]. The advantage of this approximation is its low numerical cost. Its biggest drawback is, that the flow field does not satisfy the complete Navier-Stokes equations. As pointed out by Maxey [61] triple correlations vanish and there is no representation of the energy transfer from large scales to dissipative small scales. Furthermore it lacks the temporal advection of small scale turbulent motion by large eddies.

2.6.1 Previous work on the behavior of particles in forced turbulence

Particle behavior in forced homogeneous turbulence was studied among others by Squires [103], Deutsch [22], Laviéville [52] and Février [32]. These studies were made using Lagrangian particle tracking with different particle concentrations and using LES for the carrier phase. These studies revealed some aspects of turbulence seen by the particles, segregation and the existence of an uncorrelated component in the dispersed phase kinetic energy called Quasi Brownian Motion.

Quasi Brownian Energy

The division of the particle kinetic energy into a correlated, *mesoscopic* kinetic energy $\breve{q}_p^2$ and an uncorrelated *Quasi Brownian* energy $\delta\breve{\theta}_p$ was first introduced by Simonin [92] and Février [32]. Février observed in his simulations of forced turbulence a relation between the correlated kinetic energy of the dispersed phase $\breve{q}_p^2$, the carrier phase kinetic energy at the particle location $q_{f@p}^2$, and the total kinetic energy of the particles q_p^2.

$$\frac{\breve{q}_p^2}{q_{f@p}^2} = \left(\frac{q_p^2}{q_{f@p}^2}\right)^{3/2} \tag{2.154}$$

Février used this relation to obtain an expression for the uncorrelated particle kinetic energy using the conservation of total kinetic energy ($\breve{q}_p^2 = q_p^2 - \delta q_p^2$).

$$\frac{\delta q_p^2}{q_{f@p}^2} = \frac{q_p^2}{q_{f@p}^2} - \left(\frac{q_p^2}{q_{f@p}^2}\right)^{3/2} \tag{2.155}$$

Deutsch [23][22] extended the theory of Tchen-Hinze, that relates the particle kinetic energy q_p^2 to the carrier phase dispersed phase correlation q_{fp} and the carrier phase dispersed phase correlation to the carrier phase kinetic energy q_f^2. q_{fp} and q_f^2 are linked using the the characteristic time scales of the carrier phase and the particle relaxation time.

$$2q_p^2 = q_{fp} = 2q_{f@p}^2 \frac{T_L^{f@p}}{T_L^{f@p} + \tau_p} \tag{2.156}$$

Here a Stokes number is defined as the ratio of the particle relaxation time to the carrier phase integral length scale seen by the particle $St = \tau_p / T_L^{f@p}$ [32]. Together with the Eq. 2.156, this allows to express the relations of Février (eqs. 2.154 and 2.155) as a function of the Stokes number.

$$\breve{q}_p^2 = q_{f@p}^2 \left(\frac{1}{1+St}\right)^{3/2} \tag{2.157}$$

$$\delta q_p^2 = q_{f@p}^2 \left(\left(\frac{1}{1+St}\right) - \left(\frac{1}{1+St}\right)^{3/2}\right) \tag{2.158}$$

In Fig. 2.3 the Quasi Brownian Energy divided by the correlated kinetic energy is given as a function of the inverse of the Stokes number. The symbols correspond to results of the Lagrangian computation at different Reynolds numbers of the carrier flow and the continuous line corresponds to the correlation given by P. Février:

$$\frac{\delta q_p^2}{\breve{q}_p^2} = \sqrt{1+St} - 1 \tag{2.159}$$

This shows, that the uncorrelated energy of the dispersed phase can be related to the Stokes number. It shows further more, that at a Stokes number of ≈ 3 the uncorrelated part of

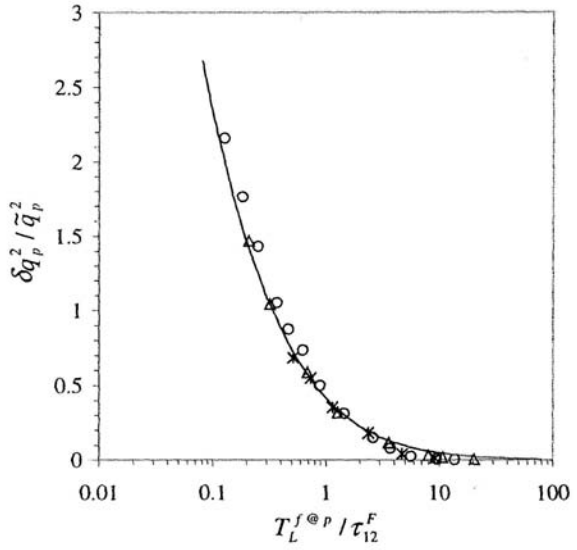

Figure 2.3: Dependence of the Quasi Brownian Energy on the Stokes number (P. Février [32])

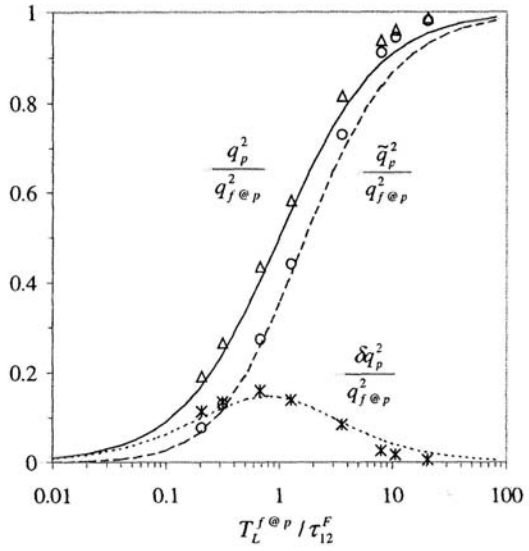

Figure 2.4: Correlated and uncorrelated particle kinetic energy as a function of the inverse of the Stokes number in forced homogeneous isotropic turbulence (P.Février [32]).

the dispersed phase kinetic energy is of the same magnitude than the correlated kinetic energy in forced stationary turbulence. Fig. 2.4 shows the correlated and uncorrelated particle kinetic energy with respect to the carrier phase kinetic energy as a function of the inverse of the Stokes number in forced homogeneous isotropic turbulence (taken from P.Février [32]). This shows, that the dispersed phase kinetic energy can be divided into an uncorrelated and a correlated kinetic energy. The uncorrelated contribution of the kinetic energy becomes increasingly important with increasing Stokes number.

2.7 Simulation test case of decaying Homogeneous Isotropic Turbulence (HIT)

Here the approach of decaying homogeneous isotropic turbulence is chosen. The initial flow field has been obtained by first initializing the velocity field with a divergence free random field, so that the associated kinetic energy $E(k)$ respects a Passot-Pouquet spectrum [72]:

$$E(k) = \frac{16}{3}\sqrt{\frac{2}{\pi}}\frac{u'^2}{k_e}\left(\frac{k}{k_e}\right)^4 \exp\left(-2\left\{\frac{k}{k_e}\right\}^2\right) \tag{2.160}$$

Then, in order to obtain a flow field, that is solution of the Navier-Stokes equations the initial field is computed for some eddy turn over times and the integral properties of the turbulence are measured. Carrier phase turbulence can be qualified by several integral properties ([14],[5],[57]). Among such values are:

- Reynolds number based on a characteristic length scale of the turbulence (Re),
- viscosity (ν),
- integral length scale (l),
- turbulent rms velocity (u'),
- eddy turn over time (T_u),
- dissipation length scale (η).

The integral properties of the carrier phase turbulence are necessary to qualify and quantify the dynamics of the particles in it. The temporal behavior of the kinetic energy for the test cases HIT1 and HIT2 is shown in fig. 2.6. The kinetic energy of the carrier phase decays following the ODE system of Eqs. 2.50,2.51. In the case of HIT1 the carrier phase kinetic energy values are given for the computation with the NTMIX (6th order compact scheme) and AVBP (here 2nd order central scheme). It shows, that the code AVBP has a sufficient numerical accuracy for the carrier phase. A different way to check the dissipation of the numerical scheme compared to the dissipation of the viscous model is to compare the measured dissipation to the temporal derivative of the kinetic energy. This is shown

	HIT 1 DNS	HIT 2 DNS
$Re_l \left(= \frac{u'l}{\nu}\right)$	13.6	70.9
ν	0.005	0.0005
l	0.855	0.647
$\mathcal{L}^f_{11}$	0.945	0.726
$\mathcal{L}^f_{22}$	0.754	0.597
$\mathcal{L}^f_{33}$	0.865	0.618
u'	0.0789	0.0548
ε	0.00104	0.00022
$T_u(= l/u')$	10.91	11.8
$\tau^+(= u'^2/2\varepsilon)$	2.99	6.83
$\eta(= (\nu^3/\varepsilon)^{1/4})$	0.104	0.0274
$\tau_\eta(= \nu^{1/2}\varepsilon^{-1/2})$	2.19	1.506
Reference values:		
$Re_{acc} \left(= \frac{c_{ref}L_{ref}}{\nu_{ref}}\right)$	200	2005.8
L_{ref}	0.001	0.001
c_{ref}	347.0	347.0
T_{ref}	2.8818e-6	2.8818e-6
Computational box (non-dimensional)		
L_x, L_y, L_z	2π	2π
$64^3 : \delta x$	0.098	—
$128^3 : \delta x$	0.049	0.049
$192^3 : \delta x$	0.033	0.033
$64^3 : \delta t$	0.0480	—
$128^3 : \delta t$	0.0239	0.0239
$192^3 : \delta t$	0.0137	0.0137

Table 2.1: Properties of two different initial carrier phase turbulence test cases. All values are non-dimensional and given with three significant digits. In the top box measured values are given, the second boxe gives the deduced quantities, the third box gives information on the values used to convert to non-dimensional properties and the bottom box gives information on the computational domain.

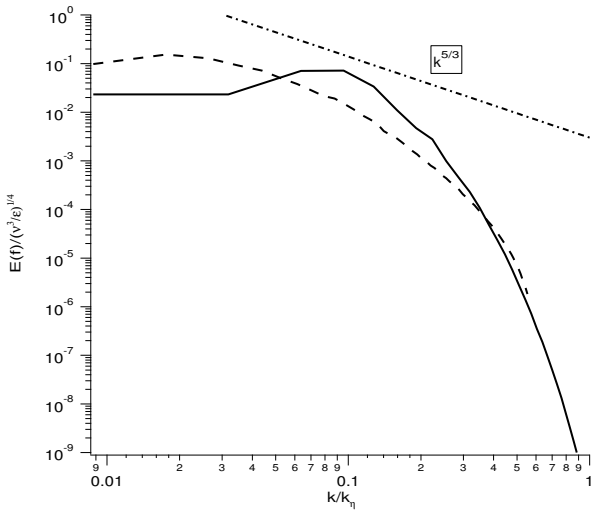

Figure 2.5: Spectrum of the carrier phase kinetic energy of HIT 1 ($Re = 13.6$,line) and HIT 2 ($Re = 70.9$,dashed line) in Kolmogorov scaling at the time particles are injected.

in fig. 2.7. In both cases, HIT1 and HIT2, the temporal derivative of the carrier phase dissipation corresponds to the measured dissipation of the code. Oscillation of the carrier phase derivative occurs, since kinetic energy is measured at every time step.

In Fig. 2.8 the temporal development of the length scales of the carrier phase are shown. Since the box of the computation is of size 2π there are roughly six integral length scales in the computational box.

2.7.1 Dispersed phase properties

The dynamics of particles in homogeneous isotropic turbulence depends on the particle relaxation time τ_p (when only Stokes drag is considered). Stokes numbers for the different test cases are given in table 2.2.
The dynamics depends of course on the initial conditions. Several approaches exist to initialize particle positions and particle velocities:

1. **Dispersed phase velocity equals carrier phase velocity:** If the relaxation time is small compared to the characteristic time scales of the carrier phase, the particles have a velocity field close to the carrier phase velocity field. In this case it is physical to initialize the dispersed phase velocity field with the gaseous velocity field and to initialize the quasi brownian energy field with a value close to zero. The QBE field can not be initialized with zero since shear viscosity and QBE flux coefficients are directly linear in QBE.

2. **Dispersed phase velocity equals zero:** If relaxation times are large compared to the characteristic time scales of the carrier phase, there is much more QBE than

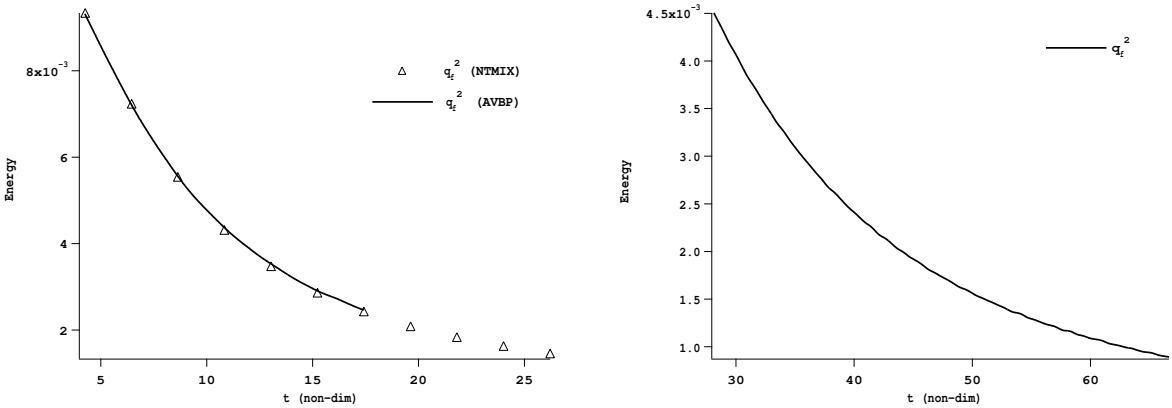

Figure 2.6: Decay of the carrier phase kinetic energy for HIT1 is shown in the left graph. The Symbols indicate the carrier phase energy from the NTMIX code used for the Lagrangian reference computation. The decay of kinetic energy for the case HIT2 is shown in the right graph.

kinetic energy in the mesoscopic particle velocity field. In this case it might be more physical to initialize the dispersed phase velocity field with zero and to initialize the quasi brownian energy field with some fraction of the gaseous kinetic energy.

3. **Dispersed phase velocity is partially correlated to the carrier velocity:** In the intermediate case, which is the most physical approach, a solution is to initialize the dispersed phase velocity field with a fraction of the carrier phase velocity the quasi brownian energy field with the complement of the carrier phase kinetic energy.

2.7.2 Results of Lagrangian Simulations

In this section the results of the Eulerian-Lagrangian simulations of J. Helie are presented, post-processed and discussed. This is done here by two means:
First the integral properties of the carrier phase, dispersed phase and their correlation are discussed. This corresponds to an application of the quantities introduced in section 2.3.
The second analysis of the Lagrangian simulation concerns the temporal evolution of the one dimensional spectra. This is discussed and implications for the modeling of a stress tensor are shown.
Whereas the integral properties of the Lagrangian simulation are obtained from the discrete particles, for the second analysis continuous fields of the correlated velocity, number density and Quasi Brownian Energy are necessary to perform the spectral analysis. The continuous fields are obtained by a volume filtering approach using different kernels for the filter [43]. This corresponds to the approach presented in section 1.4. The continuous fields however are then interpreted as if they were obtained by ensemble average. Volume averaging and ensemble averaging do not necessarily result in the same continuous fields [24]. Here however it is assumed, that if a large number of particles are used, the volume averaged

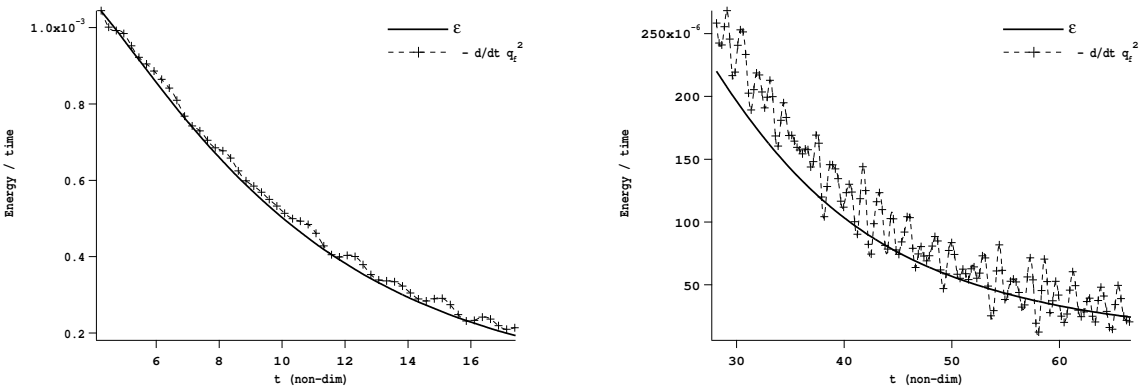

Figure 2.7: Here the decay of the carrier phase kinetic energy $-\partial/\partial t q_f^2$ is compared to the dissipation rate ε. The left graph shows measured dissipation rate and the temporal derivative of kinetic energy for case HIT1. The right graph shows measured dissipation rate and the temporal derivative of kinetic energy for case HIT2.

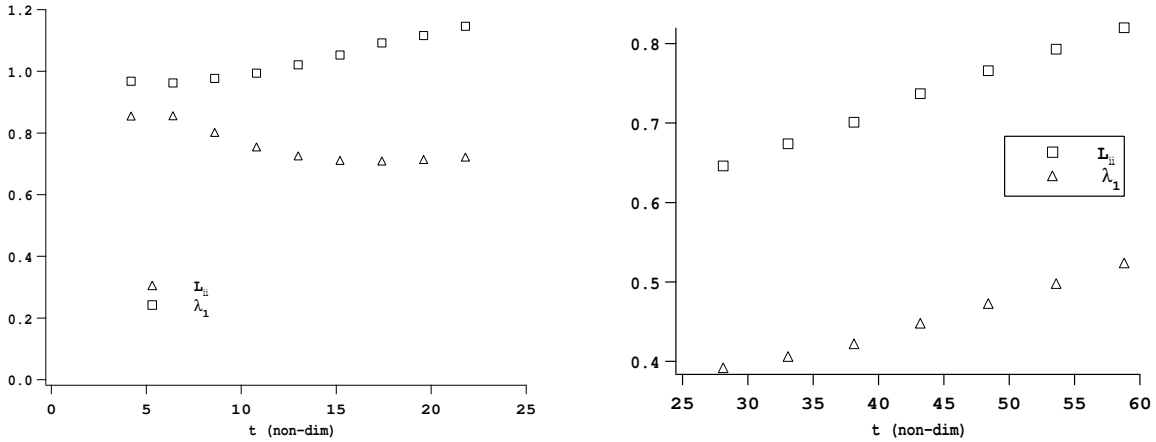

Figure 2.8: Temporal development of the length scales of the carrier phase. Squares represent the Taylor micro-scale λ_1 and the triangles represent the integral length scale $\mathcal{L}_{ii}$. The left graph shows the length scales for HIT1 and the right graph shows the length scales for HIT2.

Test case	τ_p	St_{τ^+} (HIT 1)	St_{T_u} (HIT 1)	St_{τ^+} (HIT 2)	St_{T_u} (HIT 2)
A	0.00287	0.00096	0.000263	0.00042	0.000243
B	0.00574	0.00192	0.000526	0.00084	0.000486
C	0.0115	0.00385	0.00105	0.00168	0.000975
D	0.023	0.00769	0.00211	0.00337	0.00195
E	0.046	0.0154	0.00422	0.00673	0.0039
F	0.092	0.0308	0.00843	0.0135	0.0078
G	0.184	0.0615	0.0169	0.0269	0.0156
H	0.367	0.123	0.0336	0.0537	0.0311
I	0.735	0.246	0.0674	0.108	0.0622
J	1.469	0.491	0.135	0.215	0.124
K	2.938	0.983	0.269	0.43	0.249
L	5.498	1.84	0.504	0.805	0.466
CJ	4.687	1.57	0.430	0.686	0.397
M	0.4485	0.15	0.0411	0.0657	0.038
N	0.538	0.18	0.0493	0.0788	0.0456
V	0.445	0.149	0.0408	0.0651	0.0377
W	0.450	0.151	0.0412	0.0659	0.0381
Z	0.459	0.154	0.0420	0.0672	0.0389
BS 1	5.88	1.97	0.539	0.861	0.498
BS 2	8.61	2.88	0.789	1.26	0.730
BS 3	11.8	3.95	1.08	1.73	1.0
BS 4	23.5	7.86	2.15	3.44	1.99

Table 2.2: The table describes dispersed phase properties of the different test cases. Lagrangian simulations were performed with the parameters (HIT 1,CJ) and (HIT 1,H). The other test cases are computed in the Eulerian simulation only.

Lagrangian results are comparable to the ensemble averaged results. Simulations with a different number of particles per computational cell $(5, 10, 20, 40)$ were performed by J. Helie to investigate the effect of sampling on the continuous fields. By using 40 particles per cell, the error in the fields can be evaluated to be lower then 5% using different type of filter Kernels.
The carrier phase reference solution was produced with *NTMIX*, a cartesian finite difference code with a sixth order compact scheme [53]. This ensures low dispersion/diffusion errors for the carrier phase reference solution and allows to check the precision of the code *AVBP* used for the Eulerian-Eulerian computations.

Properties of the Lagrangian Simulation

In this simulation the carrier phase parameters are given by *HIT1* in table 2.1 and the dispersed phase characteristics correspond to case *CJ* in table 2.2. The Reynolds number

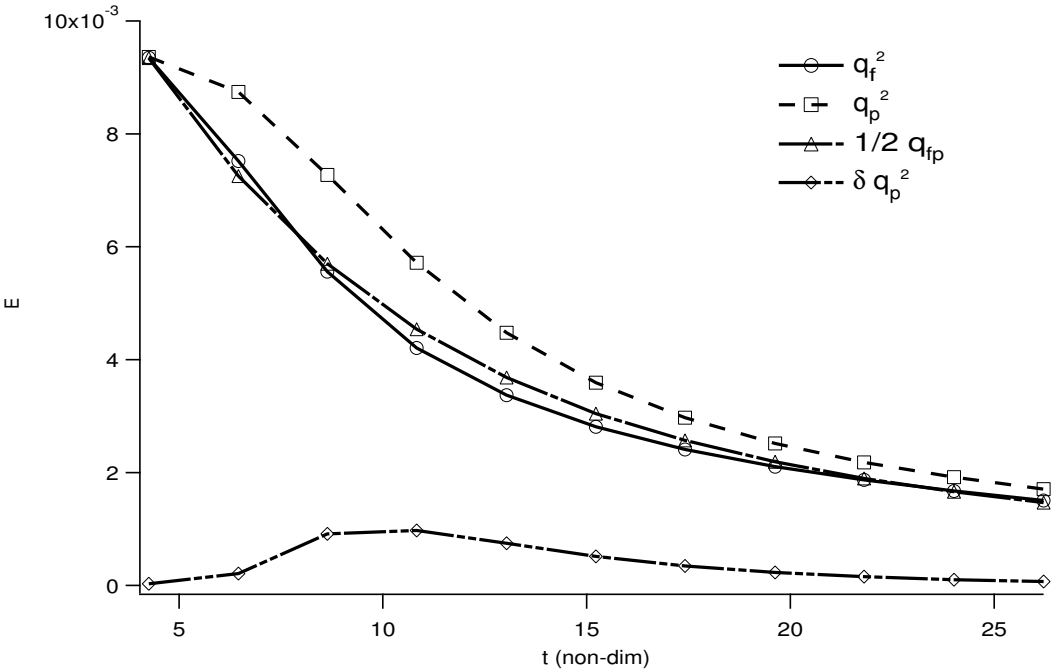

Figure 2.9: Spectral development of the carrier phase kinetic energy, dispersed phase kinetic energy and the dispersed-phase carrier phase correlation in the Lagrangian Simulation (HIT 1,CJ).

was chosen to be small ($Re = 13.6$), so that no subgrid models are needed for the carrier phase and a true "DNS" could be performed. At such low Reynolds numbers the viscous effects are very important. Therefore the usual assumption of separation of scales, made at high Reynolds numbers, is not realistic. This initial flow field is obtained as described in section 2.7.1. In Fig. 2.4 the correlated and uncorrelated kinetic energy of the dispersed phase in forced homogeneous isotropic turbulence is shown. The Lagrangian simulation of J. Helie (HIT1,CJ) can be placed according to Stokes number close to unity in the center of the graph. Here large segregation effects and effects due to uncorrelated particle motion are expected.
Eulerian simulations with a larger range of Stokes numbers are presented in the following chapter.

Integral properties of the Lagrangian Simulation

The dispersed phase is initialized according to the procedure described in section 2.7.1: Particles are randomly distributed in the computational domain, so that initially a homogeneous distribution of particle number density is achieved. The individual particle velocity

is set to the carrier phase velocity at the location of the particle. This implies, that the Quasi Brownian Motion is initially zero. Fig. 2.9 shows the spectral development of the integral properties of the Eulerian-Lagrangian simulation. The carrier phase energy decays due to molecular viscosity (continuous line with circles). The carrier-phase dispersed-phase correlation follows closely the carrier phase energy (dot-dashed line with triangles). Due to particle inertia the dispersed phase energy (dashed line with squares) decays more slowly than the carrier phase energy or the carrier-phase dispersed-phase correlation. The uncorrelated particle kinetic energy (QBE) (line with diamonds) is initially zero. This is due to the initialization, where the particle velocity is initially equal to the gaseous velocity and therefore entirely correlated. The time evolution behavior of the Quasi Brownian energy can be interpreted as follows: Due to its inertia the particle velocity becomes slightly uncorrelated from the gaseous velocity. After about one carrier phase turn over time (≈ 4 non-dimensional time units) some particles have been ejected from the vortices. If such particles from different vortices meet, their velocity is at best partially correlated. This leads to the production of Quasi Brownian Energy in such regions. At large scales dispersed phase velocity diminishes due to drag force, since the carrier phase velocity is effectively decreased by molecular viscosity. Since particle inertia is proportional to its velocity, the production of Quasi Brownian Motion decreases with the decreasing correlated particle velocity. Quasi Brownian Motion decreases as well due to drag with the carrier phase and consequently so does Quasi Brownian Energy.

Autocorrelation Functions

In this part the instantaneous Eulerian quantities of the Lagrangian simulation at the non-dimensional time $t = 10.8$ are used to calculate the different autocorrelation functions. The Eulerian properties of the dispersed phase (number density, "mesoscopic velocity"[¶]) are obtained by volume filtering. The normal and parallel components of the autocorrelation functions are shown in Fig. 2.10. The usual autocorrelation functions of the carrier phase are given in the upper left graph (f,g). Due to the periodicity of the computational domain and the insufficient sampling, the autocorrelation function f does not exactly tend to zero and the autocorrelation function g does not have a negative loop. The autocorrelation functions of the gaseous velocity pondered by the particle presence ("correlation of the gas velocity seen by the particles" f^{ff}, g^{ff}) are significantly steeper at the origin than the purely gaseous autocorrelation functions. This shows the influence of the strongly varying number density field. Autocorrelation functions of the mesoscopic dispersed phase velocity (f^{pp},g^{pp}) are given in the lower left graph and the autocorrelation functions of the carrier-phase dispersed-phase correlation (f^{fp},g^{fp}) in the lower right graph. They both show a behavior similar to the velocity autocorrelation function of the carrier phase pondered by the particle presence.

The autocorrelation function $\breve{g}^{pp}(r)$ associated to the droplet number density field is shown in Fig. 2.11. At the origin this correlation function drops very rapidly to zero

[¶]Volume filtered quantities are not necessarily equal to ensemble averaged quantities. This hypothesis is however made at this point in order to post-process and analyze the continuous quantities.

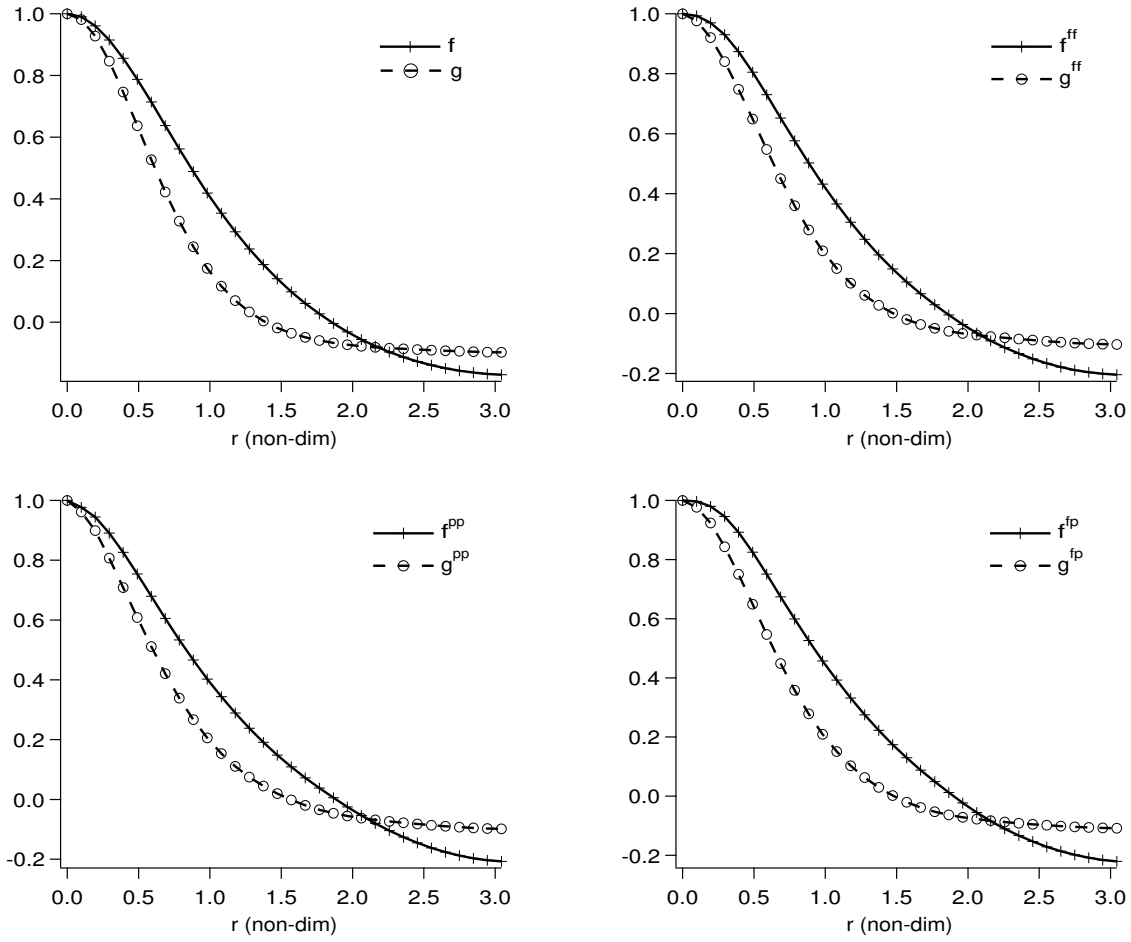

Figure 2.10: Autocorrelation functions of the Lagrangian Simulation from volume filtered dispersed phase quantities (t=10.8, HIT 1, CJ).

indicating a strongly varying particle number density field. Unfortunately the gradient of this correlation function is too steep at the origin to evaluate numerically a meaningful length scale $\lambda_{\check{n}_p}$. Qualitatively this length scale is however significantly smaller than the corresponding Taylor micro-scale of the carrier phase velocity field.

One dimensional spectra

One dimensional spectra as obtained from the fourier transform of the autocorrelation functions are shown in Fig. 2.12. The one dimensional spectra of the carrier phase show the classical behavior of turbulence at low Reynolds numbers. The one dimensional spectra of the dispersed phase show also a decay but a non-negligible remaining contribution at small scales. It is also interesting to notice that the longitudinal component of the one dimensional fluid-particle and fluid-seen spectra disappear at rather small wave numbers

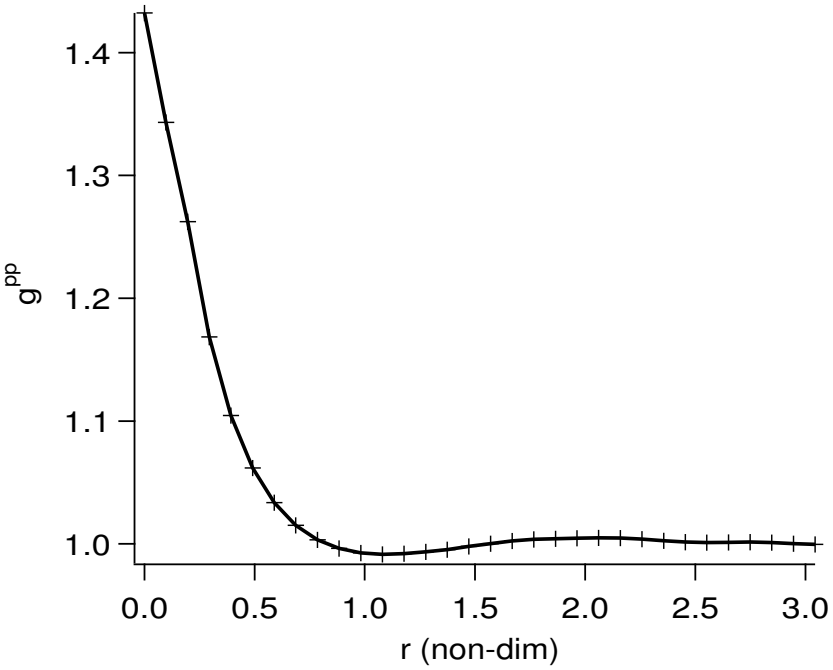

Figure 2.11: number density autocorrelation functions $\breve{g}^{pp}(r)$ of the Lagrangian Simulation from volume filtered dispersed phase quantities (t=10.8, HIT 1, CJ).

whereas the transversal component persists down to small scales with consequent contribution. The difference between the one dimensional spectra of the carrier phase and the carrier phase seen by the particles consists in the conditioning on the number density of the particles. The rapid decay of the longitudinal component reflects therefore the decorrelation due to number density in the direction of the mesoscopic velocity.
The one-dimensional spectrum of the number density autocorrelation $\breve{N}^{pp}$ (Fig. 2.13) decays similar to the one dimensional dispersed phase energy spectrum and admits significant variations at small scales. It has some similarities to the temperature spectrum of turbulent flows with a high Prandtl number. When the diffusion coefficient of temperature is small compared to viscosity, the temperature spectrum follows the turbulent energy spectrum down to the Kolomogov scale. Whereas all kinetic energy is dissipated beyond this scale, the temperature spectrum diverges from the kinetic energy spectrum and small scale temperature fluctuations persist down to the length scale where thermal diffusion dissipates temperature fluctuations. In the case of the number density, the fluctuations decrease with the mesoscopic kinetic energy spectrum. At length scales where particle inertia dominates since the particle relaxation time is comparable or larger than the associated time scale, number density and velocity fluctuations persist since drag force is not an efficient dissipative mechanism at such scales.

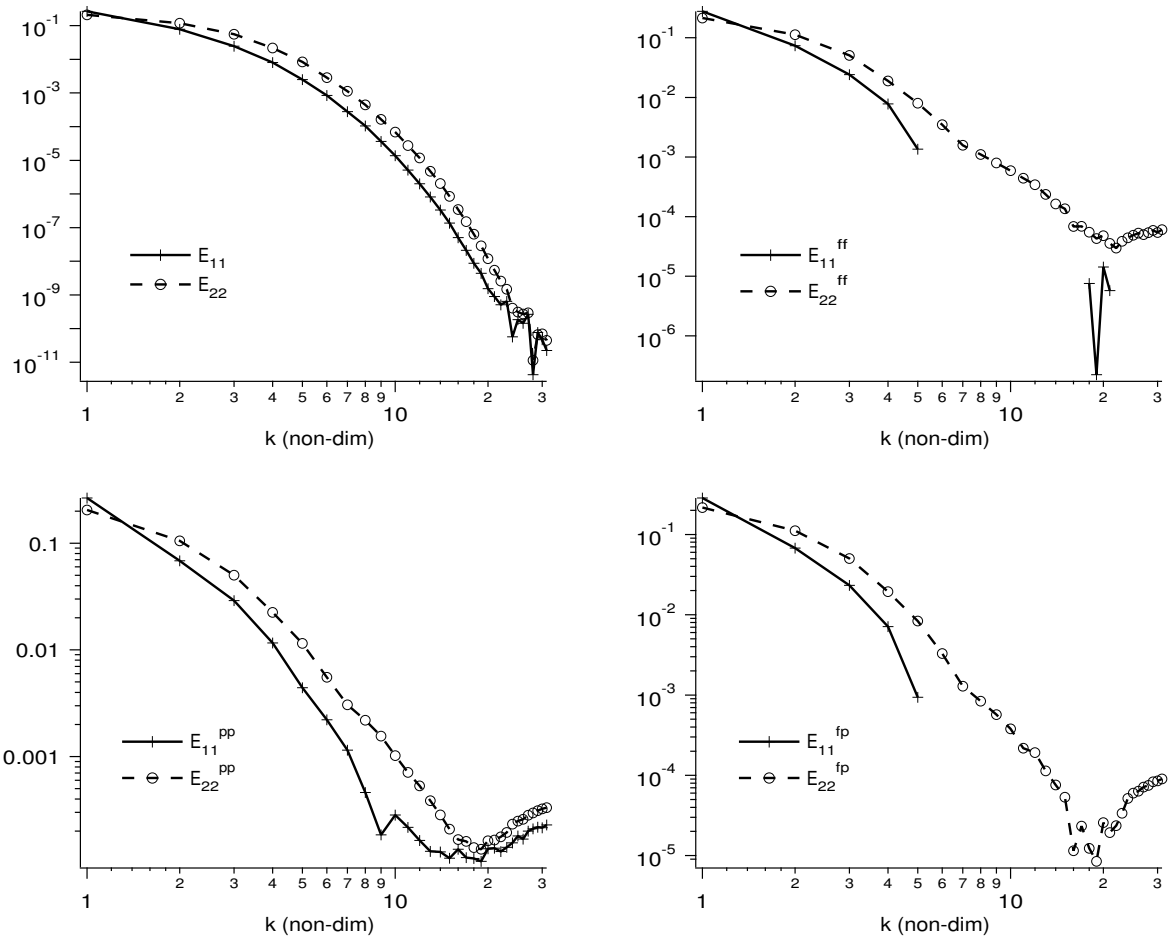

Figure 2.12: One dimensional spectra of the Lagrangian Simulation from volume filtered dispersed phase quantities (t=10.8, HIT 1, CJ).

Three dimensional energy spectra

Here the properties introduced in section 2.4.1 are discussed. They are obtained from the instantaneous carrier phase properties at $(t(non-dim) = 10.8)$ and volume filtering the discrete particle properties as explained above.
In Fig. 2.14 the different energy spectra are compared. The carrier phase energy E_f (lines with +) shows the behavior of a low Reynolds turbulence with a small inertial range and the rapidly decreasing viscous tail (to be compared to the $-5/3$ Kolmogorov decay). As pointed out by Moin et al. [66] it is difficult to obtain a spectrum with a developed inertial range in decaying turbulence. Forced turbulence produces better spectra. The carrier-phase dispersed-phase correlation (dot-dashed line with downward triangle) follows closely the carrier phase kinetic energy up to a wave number of about 12. At smaller length scales the two phases are completely uncorrelated. Correlation between the two

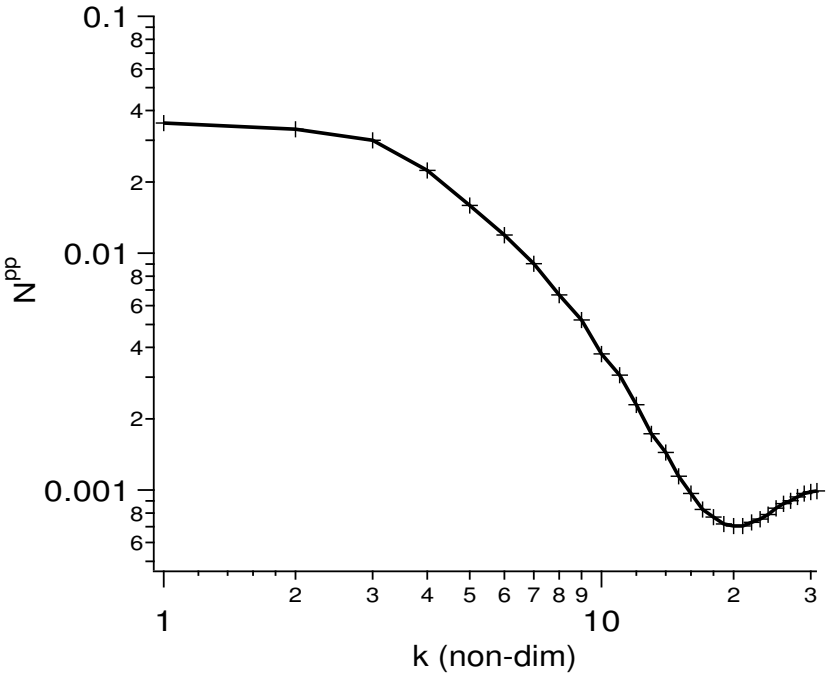

Figure 2.13: number density spectrum $\breve{N}^{pp}(r)$ of the Lagrangian Simulation from volume filtered dispersed phase quantities (t=10.8, HIT 1, CJ).

phases is maintained by drag force. If the characteristic time from the small scales is small compared to the particle relaxation time, drag force is ineffective in coupling the two phases. This effect can be quantified by comparing the length scale $\lambda_p = \tau_p v_p = 0.28$ to the length scale from the spectrum, where carrier phase and dispersed phase become uncorrelated (here $l = \pi/k = 0.26$).
The behavior of the correlated particle kinetic energy (dashed line with standing triangles) is somehow different to the carrier phase spectrum. At large scales (up to a non-dimensional wave number of approximately 7) the correlated particle kinetic energy follows the spectra of the carrier flow. At such large scales the particle relaxation time is small and the dispersed structures can follow the carrier phase. At small scales the particle kinetic energy is larger than the carrier phase kinetic energy. Since the mean Quasi Brownian viscosity as from the model in eq. 1.42 is smaller than the gaseous viscosity ($\nu = 0.005 \gg \nu_{QB} = 0.0019$) one expects a freely developing spectrum to decrease more slowly like the correlated dispersed phase kinetic energy does. Since the dispersed-phase is however coupled to the carrier phase by drag one could expect the dispersed phase energy spectrum to drop faster. An interesting detail in the dispersed phase spectrum is also, that the energy increases slightly at very small scales. Even if this may partially be due to the volume filtering method this tendency is true for the last 6 wave numbers. This is significantly larger than the volume filter. One possibility is, that this is an artifact introduced by the temporally

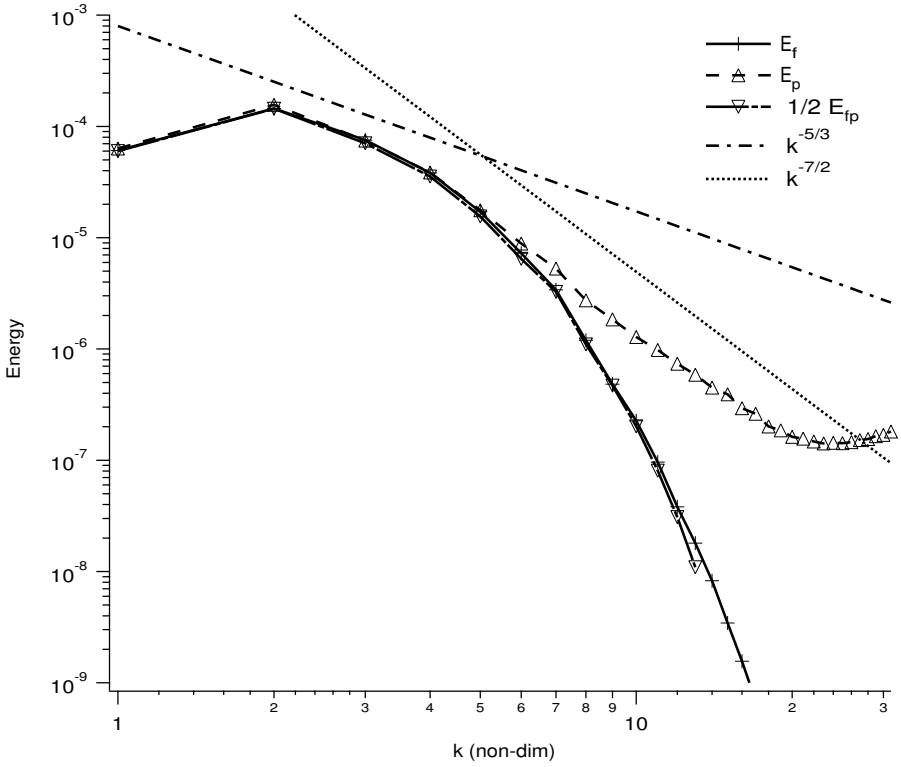

Figure 2.14: Spectra of the carrier phase, dispersed phase and carrier-phase dispersed-phase correlation from the Lagrangian Simulation (t=10.8,HIT 1, CJ).

decreasing turbulence. If the carrier phase energy decreases more rapidly than the correlated dispersed phase kinetic energy, due to viscosity and coupling is effective at large scales, this might be a "left over" from the particle velocity initialization. The dispersed phase kinetic energy at initialization should then be larger or equal to the dispersed phase kinetic energy at the time t = 10.8. In Fig. 2.15 the initial correlated particle kinetic energy is compared to its value at t=10.8. One clearly sees that the correlated energy at small scales is initially smaller than at time t=10.8. Therefore there must exist some kind of transport mechanism to transfer correlated energy to the small scales of the dispersed phase. One possible way to analyze this, is to consider the temporal evolution of the Eulerian spectrum as introduced in section 2.4. In order to choose the appropriate representation (compressible/incompressible formulation) the kinetic energy spectra are analyzed concerning the compressibility of the velocity field.

Compressible and Incompressible kinetic Energy

As discussed in section 2.4.3 the spectral kinetic energies can be decomposed into an incompressible and a compressible part. Fig. 2.16 shows the different components. The carrier phase kinetic energies are given by continuous lines. The incompressible part is

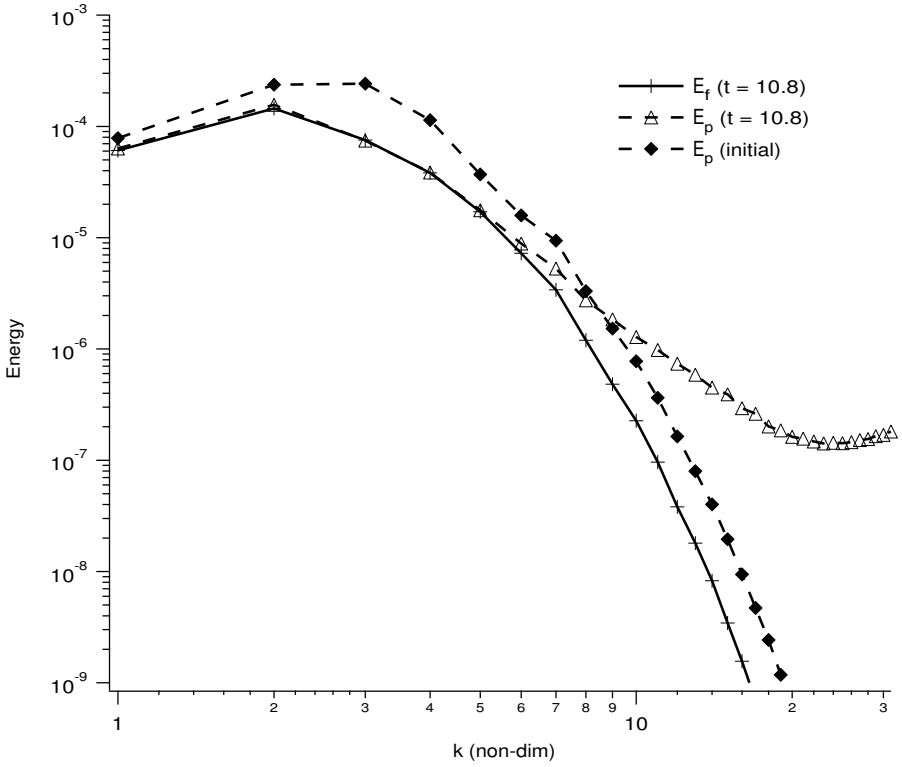

Figure 2.15: Spectra of the carrier phase, dispersed phase and carrier-phase dispersed-phase correlation from the Lagrangian Simulation (t=10.8, HIT 1, CJ).

marked by a circle and the compressible part is marked by a +. Since the compressible kinetic energy of the carrier phase is always at least two orders of magnitude smaller than its incompressible counterpart, the lines of the incompressible and total kinetic energy of the carrier phase superpose on the log-log plot. Therefore an incompressible analysis concerning the temporal evolution of the spectra should be adequate.
The correlated dispersed phase kinetic energies are given by dashed lines, the incompressible part is marked with a circle and the compressible part with a +. In contrary to the carrier phase the dispersed phase compressible kinetic energy is only significantly smaller at the large scales. At small scales the compressible kinetic energy is comparable to the incompressible kinetic energy. In two-dimensional numerical simulations of supersonic turbulence (Passot & Pouquet [72]) similar behavior is reported: kinetic energy related to vorticity dominates the large scales, whereas compressible kinetic energy dominates the small scales. The transient Mach number level for such a behavior is estimated by $Ma \approx 0.3$ [72]. Moin et al. [65] observed similar spectra in three dimensional simulations of compressible turbulence with a fluctuating Mach number of $Ma = 0.4$.
In analogy to gaseous computations one may define a turbulent dispersed phase Mach

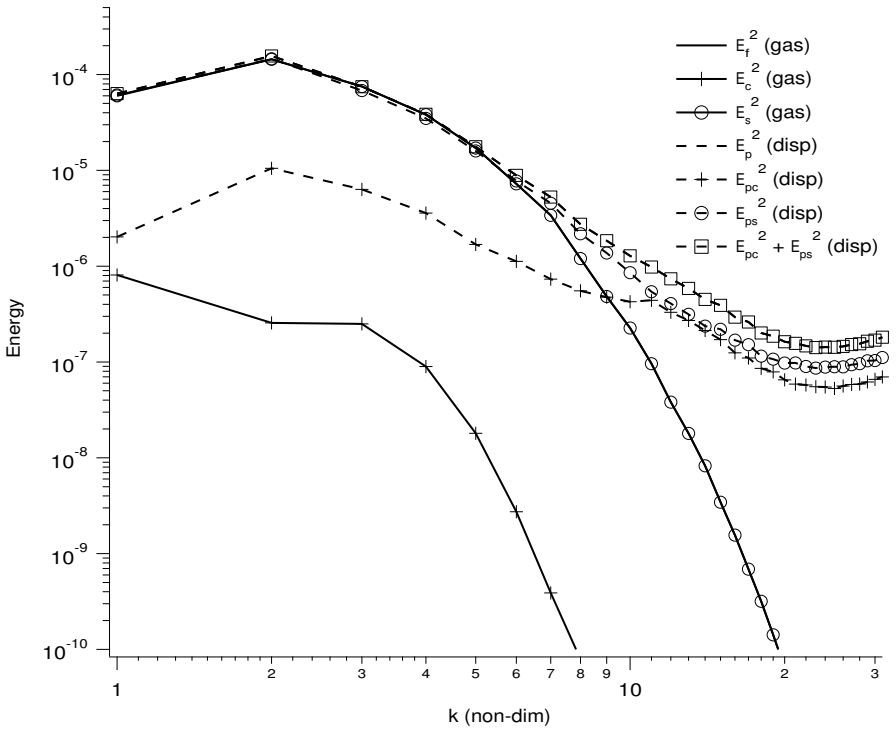

Figure 2.16: Spectra of the incompressible and compressible kinetic Energies from the Lagrangian Simulation (HIT 1, CJ).

number:

$$Ma_p = \frac{\breve{u}'_p}{\sqrt{\delta\breve{\theta}_p}} \tag{2.161}$$

that compares the correlated fluctuating velocity to the uncorrelated fluctuating velocity. Then the ratio of the correlated kinetic energy to the uncorrelated kinetic energy gives the square of this Mach number. Fig. 2.9 then shows, that the dispersed phase can be considered as "supersonic". In gaseous supersonic flows a non-neglecting part of the dissipation is due to the formation of shocks. The dispersed phase can however not directly be interpreted as a supersonic flow: if the Stokes number is sufficiently small, the influence of drag force goes down below the Kolmogorov length scale and the dispersed phase spectrum will follow the carrier phase spectrum.
Due to the behavior of the dispersed phase a compressible treatment seems to be most adequate.

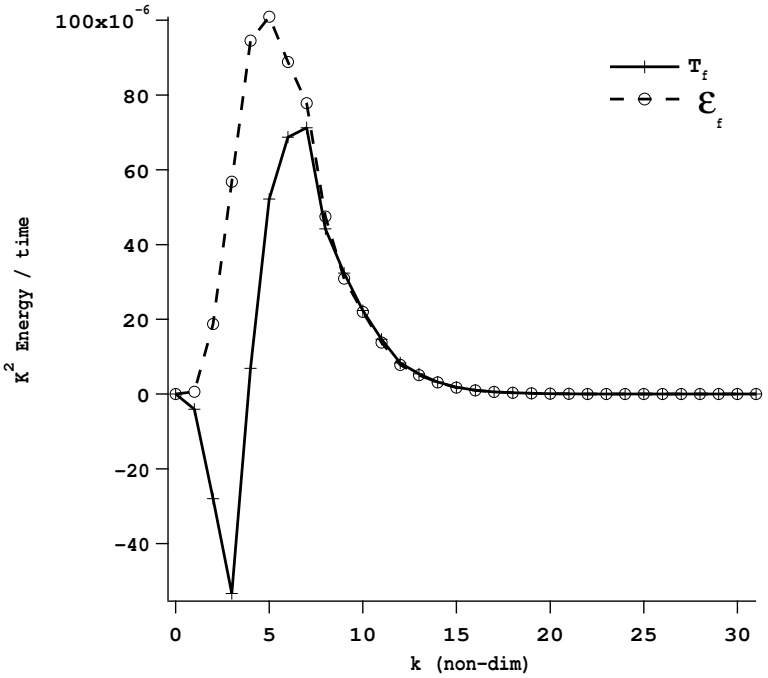

Figure 2.17: Spectral transfer terms for the carrier phase of the Eulerian-Lagrangian Simulation (HIT 1, CJ).

Temporal evolution of the carrier phase spectrum

Here the spectral transfer of energy in the carrier phase is discussed. This is a classical tool in incompressible analysis (Pope [78],Andre [3]). Fig. 2.17 shows the spectral transfer terms for the carrier phase. The continuous line shows the transfer of kinetic energy by T_f from the energy containing part of the spectrum to the small scale dissipative part of the spectrum. The dashed line shows the dissipative term $\mathcal{E}_f$. Since the simulated turbulence acts at small Reynolds numbers, the transfer part and the dissipative part of the spectrum are not separated but overlap. The graph is scaled by the square of the wave number to emphasize the small scales.

Temporal evolution of the carrier-phase dispersed-phase correlation

The upper graph in Fig. 2.18 shows the different terms of the temporal evolution of the carrier-phase dispersed-phase correlation in compressible analysis. The continuous line shows the transfer term $\hat{T}^c_{fp}$. Compared to the incompressible transfer term in the carrier phase equation the transfer persists to small scales. The transfer term related to pressure $\hat{T}^{pc}_{fp}$ is given by a short dashed line with squares and mostly negative. It therefore dissipates correlation. The term related to gaseous and Quasi Brownian viscosity $\hat{\mathcal{E}}^c_{fp}$ given by the dashed lines with circles dissipates correlation in the same range as the gaseous dissipative

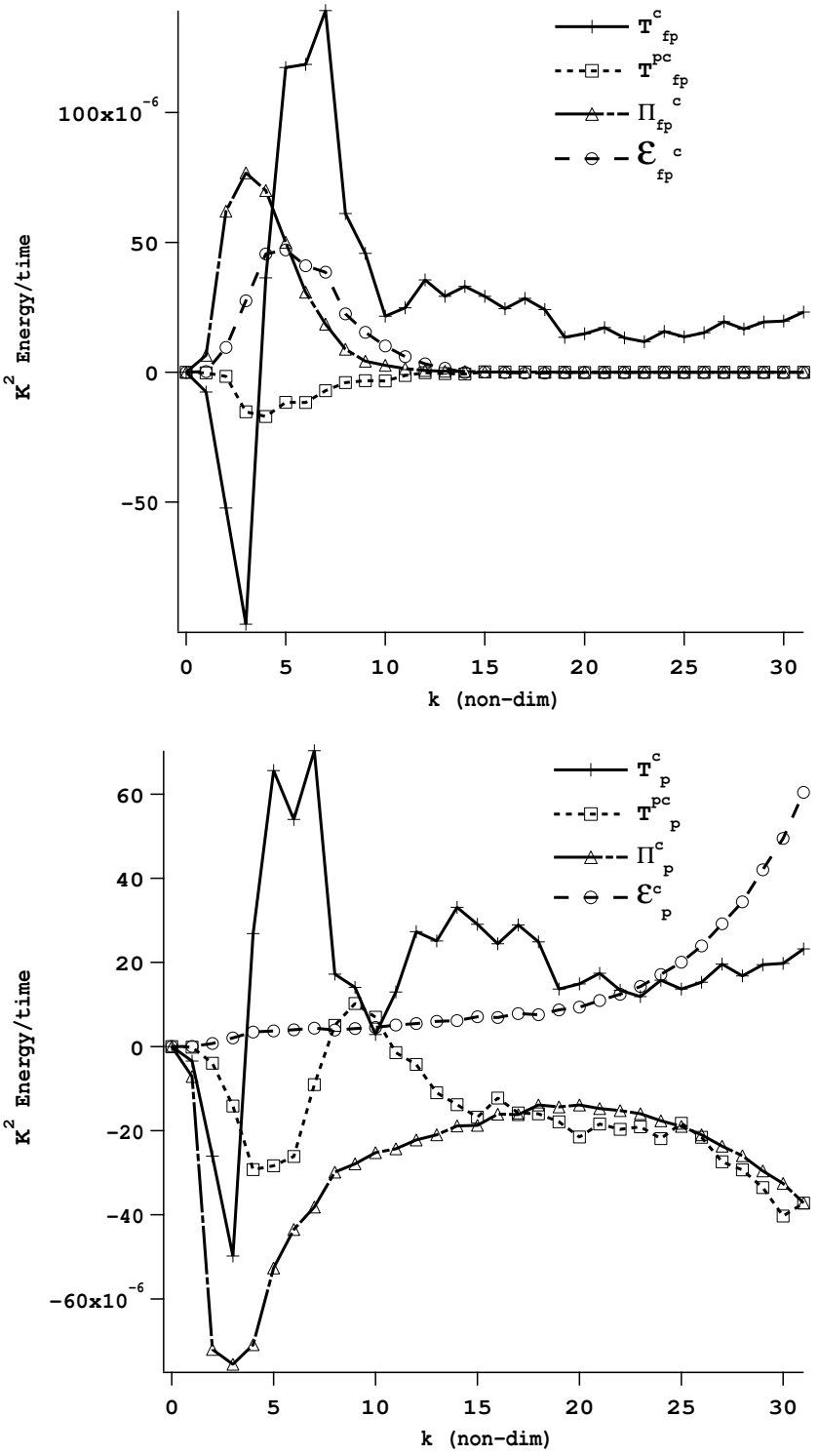

Figure 2.18: The upper graph shows the compressible analysis of the spectrum evolution of the carrier phase - dispersed phase correlation spectrum of the test case (HIT 1, CJ) . whereas the lower graph shows the compressible analysis of the spectrum evolution for dispersed phase in the same case.

term. The term related to drag force $\hat{\Pi}_{fp}$ (interrupted line with triangles) dissipates also correlation at the large energy containing scales, where the particle relaxation time is small or comparable to the characteristic time scale. This is consistent with the fact, that the carrier phase kinetic energy is slightly larger at those scales than the half of the carrier-phase dispersed phase correlation. As in the case of the gaseous plot, small scales are emphasized by scaling with the square of the wave number.

Temporal evolution of the dispersed phase mesoscopic kinetic energy

The temporal evolution of the dispersed phase mesoscopic kinetic energy spectrum is given in the lower graph of Fig. 2.18. The transfer term $\hat{T}_p^c$ is shown by the continuous line. As the transfer term in the carrier-phase dispersed-phase correlation it persists down to the small scales. The transport term related to Quasi Brownian Pressure $\hat{T}_p^{pc}$ compensates partially the transport term, but dissipates more at small scales. The dissipative term related to Quasi Brownian viscosity $\hat{\mathcal{E}}_p^c$ is less dissipative at large or medium scales but very dissipative at small scales due to the relatively flat spectrum. The term related to drag force $\hat{\Pi}_p$ dissipates energy at the large and small scales, but less at medium scales. Since the mesoscopic particle kinetic energy is larger than the fluid particle correlation throughout the spectrum this is a consistent behavior. If the sum of the different transfer terms is made, one obtains a very dissipative behavior at small scales for the dispersed phase kinetic energy. This is not consistent with the observation made previously, that the spectrum increases with time at small scales. This puts into question the spectral balance Eqn. 2.114 made on the basis pressure-viscosity assumption for the unresolved stresses (eqn. 1.39): The spectrum graph (Fig. 2.15)) and the graph showing the transport of the spectral kinetic energy (Fig. 2.18) show, that the behavior of the dispersed phase differs at small scales from the behavior of the carrier phase. Since the transport analysis in the Fig. 2.18 can not explain the balance of mesoscopic kinetic energy at small scales, a somehow different mechanism must be present. The expression related to transport and drag force arise directly from first principles. The terms related to QBP and Quasi Brownian viscosity are models that are expected to mimic the unresolved fluxes related to the stress tensor $\langle \delta u_{p,i} \delta u_{p,j} \rangle_p$. Apparently those unresolved fluxes play a role in the existence of small scale mesoscopic velocity. Fig. 2.15 suggests that there is a mechanism that feeds small scale mesoscopic energy and the unresolved fluxes are not necessarily well represented by a dissipative mechanism.

Temporal evolution of the compressible part of the dispersed phase spectrum

Here the Lagrangian results are discussed concerning the compressible part of the velocity field. The different terms of the compressible energy evolution are presented in Fig. 2.19. The transfer term $\hat{T}_p^{\Pi c}$ is represented by the continuous line. It shows a the feeding of compressible energy over a wide range of length scales. The transfer term related to QBP $\hat{T}_p^{\Pi pc}$, shown by the dashed line with squares, has a more dissipative role concerning the compressible velocity field, especially at small scales. The dissipative term related to QB

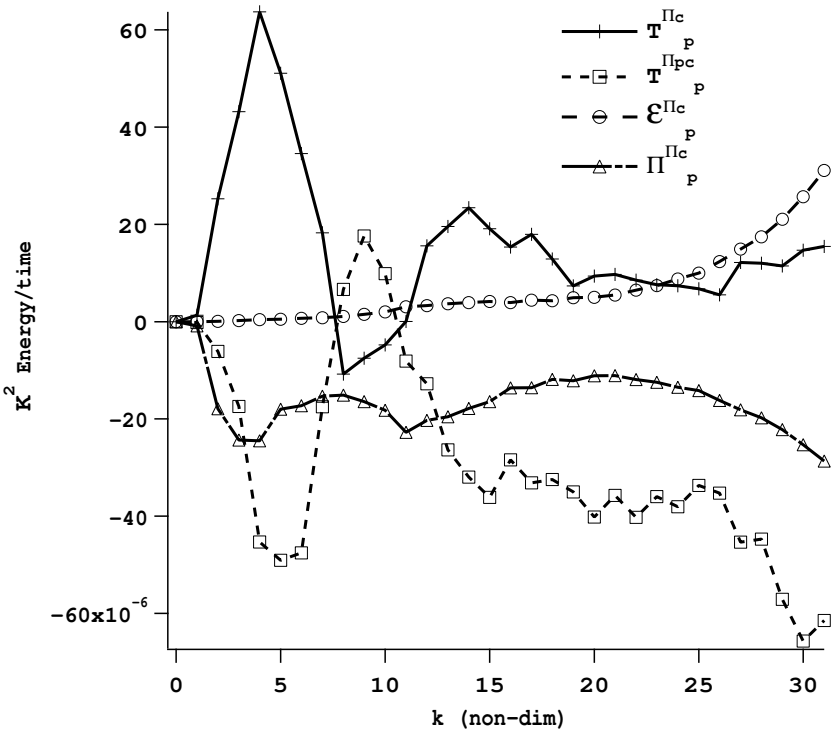

Figure 2.19: Spectral transfer terms for the compressible part of the dispersed phase of the Eulerian-Lagrangian Simulation (HIT 1, CJ).

viscosity $\hat{\mathcal{E}}_p^{\Pi c}$ is given by the dashed line with circles. As in the case of the analysis of the total kinetic energy it is important at the very small scales. The transfer term related to drag $\hat{\Pi}_p^{\Pi c}$ is shown by the interrupted line with triangles. As previously discussed, it is entirely negative. It is interesting to notice its importance at small scales. All terms, except the transfer term related to the square of the velocities, are mostly of dissipative character. This confirms the previous analysis. As in the case of the total kinetic energy, the sum of the transfer terms has a mostly dissipative character, especially at small scales, which is in contradiction to the observed spectrum.

Temporal evolution of the solenoidal part of the carrier phase dispersed phase correlation

The upper graph of Fig. 2.20 shows the components of the temporal evolution equations of the solenoidal component of the carrier-phase dispersed-phase correlation. The transport component $\hat{T}_{fp}^{\mathcal{P}c}$ dominates this evolution equation. In the transport of the total correlation (compressible + incompressible) contribution, there was some more production of fluid particle correlation at small scales. The other components of the evolution equation have a form comparable to the components in the evolution equation of the total carrier phase

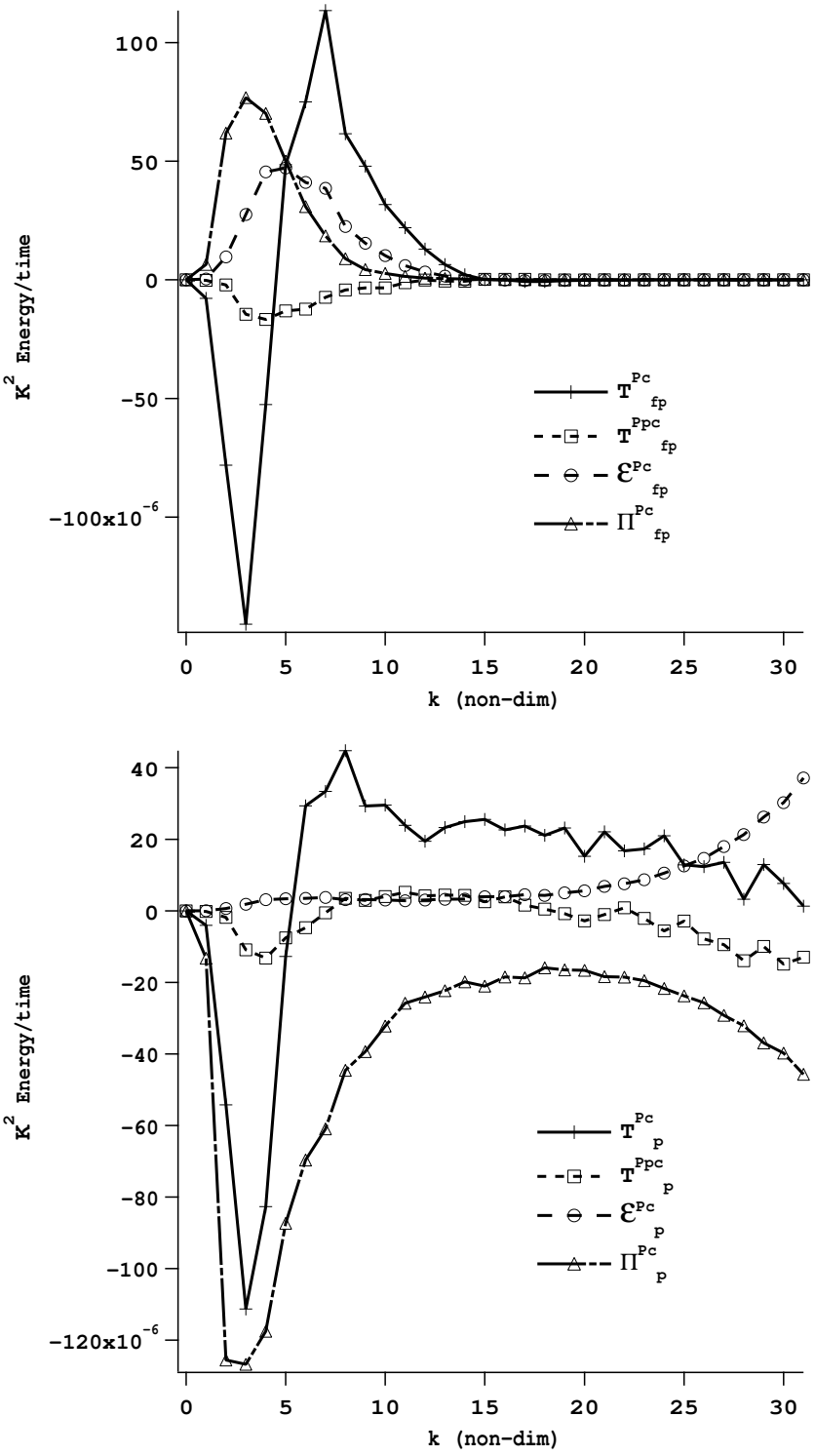

Figure 2.20: The upper graph shows the compressible analysis of the spectrum evolution of the carrier phase - dispersed phase solenoidal correlation spectrum of the test case (HIT 1, CJ). whereas the lower graph shows the compressible analysis of the spectrum evolution for solenoidal dispersed phase kinetic energy in the same case.

dispersed phase correlation.

Temporal evolution of the solenoidal part of the dispersed phase spectrum

The lower graph of Fig. 2.20 shows the components of the temporal evolution equations of the solenoidal component of the solenoidal dispersed phase kinetic energy. The transport component $\hat{T}_p^{\mathcal{P}c}$ differs significantly from the total evolution equation since the compressible component is absent. This is also the case for the dissipation by the drag force component $\hat{\Pi}_p^{\mathcal{P}c}$. The pressure contribution $\hat{T}_p^{\mathcal{P}pc}$ is small, since it acts essentially on the compressible component of the flow.

Chapter 3

Eulerian-Eulerian Prediction of dispersed phase properties

In this chapter the Eulerian-Eulerian system, described in the first chapter, is solved for the test case of decaying homogeneous isotropic turbulence, described in the second chapter. The Stokes number is varied from the case of tracer particles to inertial particles. A detailed comparison of the Eulerian and Lagrangian computation for two different Stokes numbers is given in the fourth chapter.

The main interest of this chapter is the modeling of the Quasi-Brownian stress tensor $\breve{n}\langle \delta u_{p,i} \delta u_{p,j} \rangle$. Modeling for the stress tensor has been introduced in the first chapter without a detailed analysis of the underlying physical phenomena. Here certain aspects of the stress tensor are investigated and different models are proposed. The range of application in terms of Stokes number for the different models is discussed and finally the models are tested. For inertial particles compressibility effects become important (see section 9) and difficulties with numerical solution of the number density field require an increase in spatial resolution and/or filtering of the number density field. Therefore a filtered density approach with a modified pressure is proposed for the case of inertial particles and tested.

Preliminary work of this chapter was performed during the Summer Program at the Center of Turbulence Research in Stanford, Ca. The work was preliminary in the sense that the stress tensor was modeled by an excessive pressure term. In this work the Eulerian predictions were compared to the Experimental measurements of Snyder and Lumley [97] and the Lagrangian simulations of Elghobashi and Truesdell [27]. Results were published in the corresponding proceedings [49].

The concept of Quasi Brownian Motion (QBM) and Quasi Brownian Stress was taken from Simonin [92] and Février [32]. For some part of the modeling of the QBM stress tensor results from Lagrangian simulations in forced homogeneous isotropic turbulence were used.

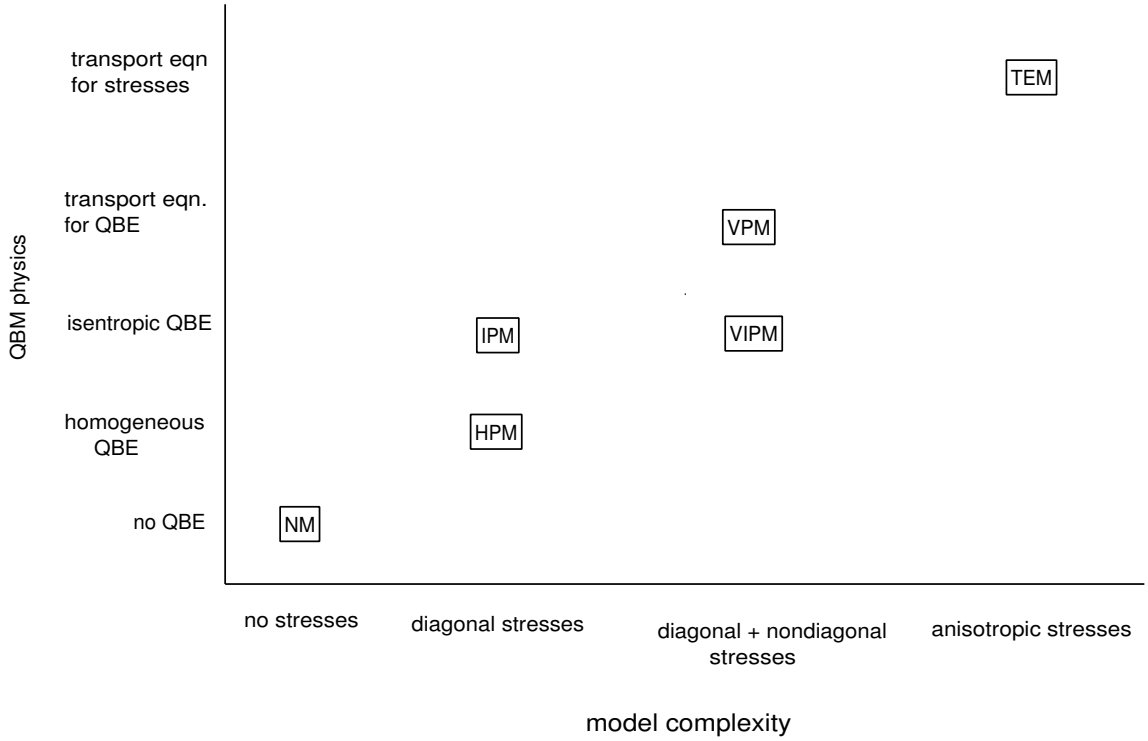

Figure 3.1: Different model approaches for QBE stress $\langle \delta u_{p,i} \delta u_{p,j} \rangle_p$ illustrating computational complexity and physical content of the model.

3.1 Modeling approaches for the Quasi-Brownian Stress tensor

In this section different models of the QB stress tensor are introduced and evaluated with respect to the range of application.
In section 1.3.3, Eq. 1.39 a pressure-viscosity model was proposed for the QB stress tensor $\langle \delta u_{p,i} \delta u_{p,j} \rangle_p$. It was first used in chapter 2 in order to introduce the different tools for the diagnostics in the Eulerian-Eulerian framework such as energy spectra. Then, application to the volume filtered Lagrangian results has shown the mechanisms, that should be reproduced in an Eulerian model. Therefore it is interesting to investigate the stress tensor and the underlying physical phenomena more precesisely.

The results of the Lagrangian computations of P. Février give an idea of the importance of the stress tensor with respect to the Stokes number. In Fig. 2.3 the QBE divided by the correlated kinetic energy is given as a function of the inverse of the Stokes number. Since in the QB stress tensor the magnitude of the off-diagonal elements is always smaller or equal than the trace, QBE can be considered as an indicator of the importance of the QB stress tensor. The two extreme limits of very small and very large Stokes numbers show completely different behavior :

- In the case of very small Stokes numbers ($St \ll 1$, right side of Fig. 2.3) the particle relaxation time is very small compared to the characteristic time scales of the carrier phase and the particles follow almost completely the carrier phase velocity. One application is the experimental measurement of the velocity flow field by PIV (Particle Image Velocimetry) or LDA (Laser Doppler Anemometry). Recalling the definitions of $\delta u_{p,i}$ and taking into account, that the particle velocities of all particles are almost totally aligned with the carrier phase velocities, the residual velocities tend to zero in this case and the effect of the stress tensor becomes negligible. It is drag force is dominant in this range of Stokes numbers.

- In the case of large Stokes numbers ($St \gg 1$, left side of Fig. 2.3) particles have their individual trajectory and are less influenced by the carrier phase velocity field. In this case the elements of the stress tensor are non-negligible. The bigger the Stokes number is, the larger the diagonal components of the stress tensor. Indeed, with increasing Stokes number, each particle follows less the carrier phase (fluid) particle trajectory. Drag force remains a certain large scale driving force, but is less important compared to the case of tracer particles.

In the intermediate range, drag force is as important as the QB stress tensor.
The different models proposed in this section are summarized in table 3.1 and motivated here. A detailed discussion of the different models is found in the following sections (3.1.1 to 3.1.6).

Modeling of the stress tensor is approached from the limit where particles can be considered as tracers. Then, according to Eq. 2.159 the stress tensor is only a small correction in the momentum equation. If the correction is very small the stress tensor can be omitted.

Here this is refered to as the *No Model (NM)* approach. One example can be given by the Eulerian computation of Druzhini and Elghobashi [25][26]. This approach is presented in section 3.1.1.

Most simple models are therefore close to the Euler equations for a gas: Only the diagonal terms are modeled by pressure terms. When QBE is fixed and uniform in space like temperature in a gas, the QBP varies only with the number density distribution. This can be compared to the isothermal Euler equations in which temperature is fixed. This approach is called here *Homogeneous Pressure Model (HPM)* and explained in section 3.1.2.

A different model, taking into account spatial variations of QBE, can be expressed making an isentropic assumption relating the variation of QBE to the number density. If only the diagonal stresses are considered, the stress tensor can be modeled by a pressure assumption. This approach is named here *Isentropic Pressure Model (IPM)*. It is explained in section 3.1.3.

More complex models are close to the Navier Stokes equations in a gas. The diagonal terms are modeled by a pressure model and the non diagonal terms are modeled making a viscosity assumption like the Boussinesque assumption.

An extension of the IPM to a *Viscous Isentropic Pressure Model (VIPM)*, in which the diagonal stresses are modeled by a pressure assumption and the non diagonal terms by viscosity model, is possible. If the Boussinesque assumption is used, a viscosity coefficient is necessary. The physical motivation for such a QB viscosity is detailed in section 3.1.4.

The *Viscous Pressure Model (VPM)* used in Eq. 1.39 was proposed in section 1.3.3 by analogy to gaz-particle flow. It uses a transport equation for the QBE. Diagonal stresses are modeled by a pressure model and non-diagonal stresses by a viscous assumption as in the VIPM model. The transport equation for QBE and the modeling assumptions are detailed in section 3.1.5.

A different approach is to solve explicitly a transport equation for the QB stresses. In this case triple correlations need to be modeled. The computational procedure can be compared to Reynolds averaged Navier Stokes equations that use transport equations for the Reynolds stresses. This model is called the *Transport Equation Model (TEM)* and detailed in section 3.1.6.

A qualification of the different models concerning physics is sketched in Fig. 3.1 in terms of model complexity and the physical content. The computational effort is closely related to the model complexity. The models HPM,IPM and VIPM are purely algebraic concerning the QBE. The VPM model requires a transport equation for QBE and the TEM model requires 6 additional transport equations for the diagonal and non-diagonal stresses.

The models presented here are compared at several instances to the Navier Stokes equations by showing the parallels in the systems of the equations. It has to be kept in mind however, that the equations for the subsonic flow of a gas and the equations of the dispersed phase differ by two important physical properties: collisions and drag force.

Collisions ensure an efficient redistribution of momentum. This mechanism is absent in the case of inertial particles, if collisions are not considered. In the case of a subsonic

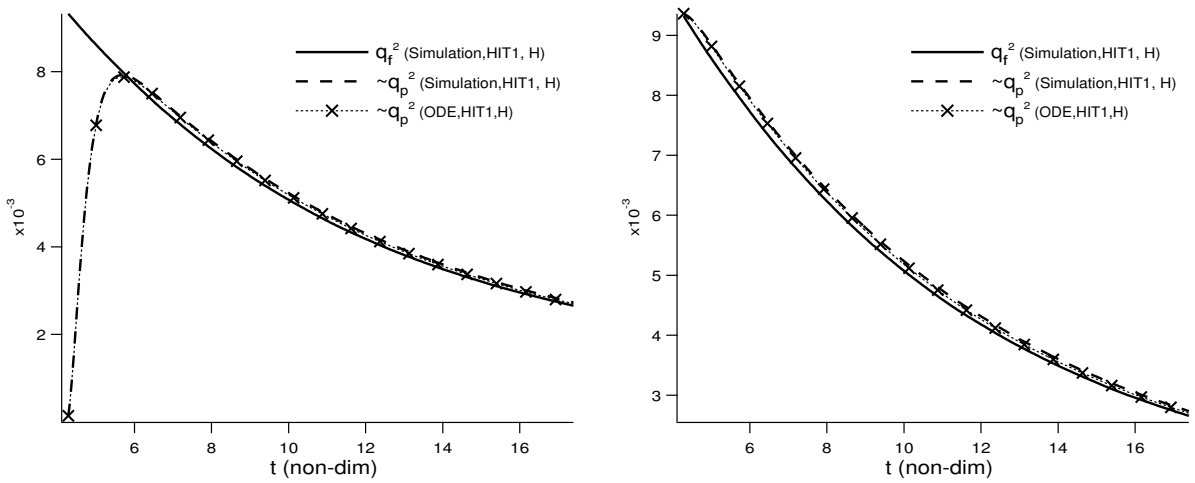

Figure 3.2: Carrier phase kinetic energy q_f^2 and correlated dispersed phase kinetic energy $\breve{q}_p^2$ from the numerical simulation (HIT1,H) as a function of time. The crosses give the correlated dispersed phase kinetic energy from the ODE system with the same particle relaxation time and carrier phase kinetic energy. (Eq. 2.63) The necessary dissipation term was extracted from the Eulerian computation. The left graph shows the temporal development in the case, where particles have initially zero velocity, the right graph shows the case, where particles have initially a velocity identical to the carrier phase velocity at the particle location.

gas, the redistribution of momentum ensures, that the diagonal elements of the stress tensor are almost isotropic and that a Gaussian distribution of molecular velocity is a good approximation. The non-diagonal elements can be interpreted as the deviation from the Gaussian velocity distribution in a gas [37]. In the case of inertial particles however, the velocity distribution is a priori not known and can be different to a Gaussian distribution.

Drag force couples the dispersed phase strongly to the carrier phase at length scales that are such that the particles can respond to the carrier phase. In a very simple picture of a vortex the eddy turn over time $T_u = l/u'$ given approx. by its characteristic length scale l and its velocity u' can be compared to the relaxation time τ_p. Therefore particles may follow the structures of large vortices in a turbulence. Depending on Stokes number the particle relaxation time may be too large for the particles too respond however to the small scale vortices.

3.1.1 No model approach (NM) :

This approach assumes that the QBM stress can be neglected:

$$\breve{n}_p \langle \delta u_{p,i} \delta u_{p,j} \rangle_p = 0 \tag{3.1}$$

In this case the set of equations for the dispersed phase reduces to:

$$\frac{\partial}{\partial t}\breve{n}_p + \frac{\partial}{\partial x_j}\breve{n}_p \breve{u}_{p,i} \quad = \quad 0 \tag{3.2}$$

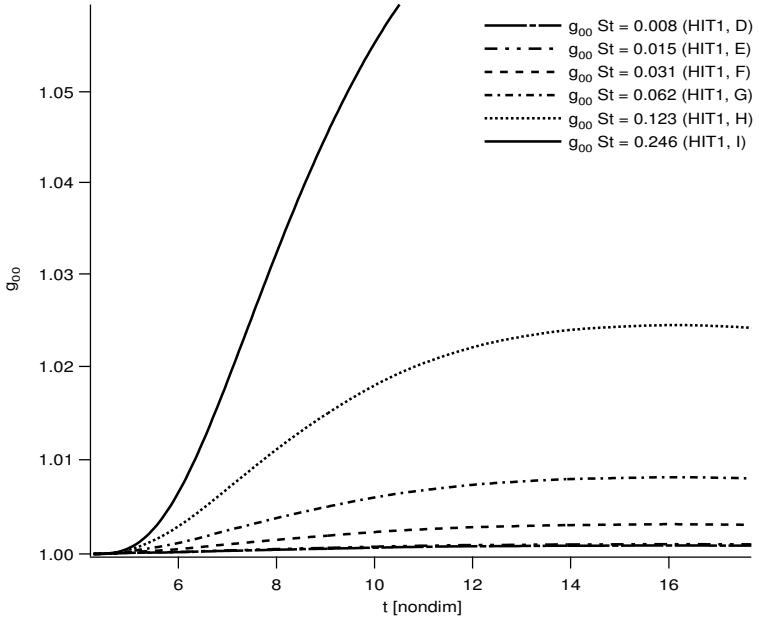

Figure 3.3: Particle segregation without a stress tensor model (NM). The numerical simulation fails for the case (HIT, I) after the non-dimensional time t= 10.36 due to the appearance of difficulties in the number density transport equation.

$$\frac{\partial}{\partial t}\breve{n}_p\breve{u}_{p,i} + \frac{\partial}{\partial x_j}\breve{n}_p\breve{u}_{p,i}\breve{u}_{p,j} \quad = \quad \frac{1}{\tau_p}\left(u_i - \breve{u}_{p,i}\right) \tag{3.3}$$

The no model approach should be valid in the case of very small Stokes numbers. The limits of this case in the Eulerian formulation are explored here and compared to the ODE model for the integral properties presented in section 2.3.2.
The left graph of Fig. 3.2 shows the temporal development of the carrier phase kinetic energy q_f^2, the correlated dispersed phase kinetic energy $\breve{q}_p^2$, and the correlated kinetic energy as obtained from the ODE system in section 2.3.2, Eq. 2.60 for the test case HIT1,H. In this simulation particles are initially at rest (initialisation 2, section 2.7.1). As predicted by the ODE system, particle kinetic energy releases very quickly to the carrier phase kinetic energy. Recalling the ODE system presented in chapter two (Eqs.2.62-2.64) the fluid-particle correlation first increases due to its relaxation towards the carrier phase kinetic energy. Correlated particle kinetic energy then follows the fluid particle correlation and increases. Since the carrier phase turbulence decreases, at one point fluid particle correlation equals twice the carrier phase kinetic energy and the developement is inverted. Coupling to the carrier phase is not any more a driving force but dissipates fluid particle correlation. The same mechanism leads to a decrease in correlated particle kinetic energy once the correlated particle kinetic energy equals half the fluid particle correlation. Then drag force dissipates particle kinetic energy. The right hand graph in Fig. 3.2 shows the temporal development, if particles have initially the same velocity as the carrier phase

(initialisation 1, section 2.7.1) Here the particle kinetic energy is slightly larger than the carrier phase kinetic energy due to particle inertia. The drag force acts therefore as a dissipative term in the particle momentum equation. The effect of drag force is the only dissipative mechanism, since the stress tensor is neglected.

If the Stokes number based on the timescale τ^+ exceeds 0.1, the numerical computation fails since inertia effects lead to strong preferential concentrations with sharp gradients of number density. This causes dispersion in the numerical scheme used to perform the computation and makes the simulation fail.

One method to characterize segregation effects is by the value of the autocorrelation function g_{00}. This value is given as a function of time for the test case HIT1 with different particle relaxation times in Fig. 3.3. Up to a Stokes number (based on the dissipative time scale τ^+) of 0.123, particle seggregation increases first and then becomes steady. This behavior is proper to simulations with decreasing turbulence. Particles are swept out of the regions of high vorticity into the regions of high shear. As the turbulence decreases particles stay in the regions of high shear. Therefore the particle number density shows the history of the carrier phase turbulence. In the case of forced turbulence the total kinetic energy of the carrier phase is statistically stationary. Particles are swept out of the regions of high vorticity but as the carrier phase turbulence is forced with changing modes new vortices arrive in the regions of high particle number density and redistribute the number density. Therefore values for segregation of decreasing turbulence can not directly be transmitted to the case of forced turbulence.

3.1.2 Homogeneous pressure model (HPM) :

As mentioned in the introduction, the HPM only takes into account the local variations of the number density and assumes a spatially uniform QBE. Off-diagonal terms of the stress tensor are assumed in equilibrium. In the case of a homogeneous QBE, it is necessary to have a physical value for this quantity as it is necessary in the case of isothermal Euler simulations to provide a value for temperature.

Using the results of the simulations of P. Février, the average QBE can be estimated from the knowledge of the correlated kinetic energy by the relation given by the following equation (see section 2.6.1).

$$\delta q_p^2 = \eta_{QB} \breve{q}_p^2 \tag{3.4}$$

Here η_{QB} is the proportionality factor between the uncorrelated and the correlated kinetic energy. This correlation factor can be estimated by two means [92]:

1. The first model has proposed by P. Février [32] and is based on the analysis of Tchen-Hinze [23] [22]. Following the argument of Février, two inertial particles, that are located at the same point, have a priori two different trajectory histories. Therefore their velocities are, a priori, not completely correlated. The Lagrangian *rms* velocity of the uncorrelated motion can be estimated by :

$$\delta u'_p = u' \sqrt{\frac{T_L}{\tau_p + T_L}} \tag{3.5}$$

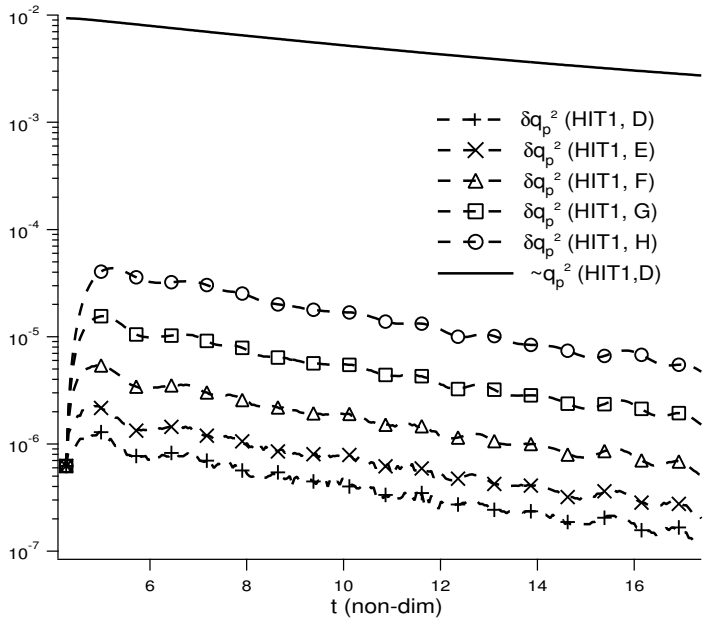

Figure 3.4: QBE obtained from the equilibrium formula (Eq.3.8) for the different Stokes numbers in the simulation HIT1. As a comparison for the order of magnitude, the correlated particle kinetic energy with a Stokes number corresponding to test case D is also given. Note the log scale for the energy.

The time those two particles dispose to correlate their velocity is the time they spend in the location, where they are subject to the same carrier phase velocity field. Février estimates this time by:

$$T_s \approx \sqrt{T_L \tau_p + T_L^2}. \tag{3.6}$$

This characteristic time T_s, where the two particles "see" the same velocity field can be compared to the relaxation time of the particle. This leads to another type of Stokes number, that characterizes the uncorrelated part of the particle motion and leads to an expression for the proportionality factor η_{QB}. For the Lagrangian time scale Février chose the integral Lagrangian time of the particle following the particle trajectory :

$$\eta_{QB} = \frac{\sqrt{\frac{\tau_p}{T_L^{f@p}}}}{1 + \sqrt{\frac{T_L^{f@p}}{\tau_p}}} = \frac{\sqrt{St_{T_L^{f@p}}}}{1 + \sqrt{\frac{1}{St_{T_L^{f@p}}}}} \tag{3.7}$$

The Stokes number of the integral Lagrangian carrier phase time scale is defined as $St_{T_L^{f@p}} = \tau_p / T_L^{f@p}$.

2. This approach is directly based on calculated values of the mesoscopic kinetic energy $\breve{q}_p^2$, the carrier phase kinetic energy "seen" by the particle $q_{f@p}^2$ and the fluid particle

correlation q_{fp}.

$$\eta_{QB} = \frac{4q^2_{f@p}\breve{q}^2_p}{q^2_{fp}} - 1 \tag{3.8}$$

The knowledge of the global instantaneous QB energy δq_p^2 (Eq. 2.61) can then be used to give the local QB energy $\delta\breve{\theta}_p$ (Eq. 1.40) with the hypothesis of a uniform $\delta\breve{\theta}_p$. Then the QB pressure can be written in the following form:

$$P_{QB} = \frac{2}{3}\breve{n}_p\eta_{QB}\breve{q}^2_p \tag{3.9}$$

This leads to a pressure modeling of the QB stress term:

$$\breve{n}_p\langle\delta u_{p,i}\delta u_{p,j}\rangle_p = P_{QB}\delta_{ij} \tag{3.10}$$

In the case of the HPM, the equations that need to be solved for the dispersed phase are:

$$\frac{\partial}{\partial t}\breve{n}_p + \frac{\partial}{\partial x_j}\breve{n}_p\breve{u}_{p,i} = 0 \tag{3.11}$$

$$\frac{\partial}{\partial t}\breve{n}_p\breve{u}_{p,i} + \frac{\partial}{\partial x_j}\breve{n}_p\breve{u}_{p,i}\breve{u}_{p,j} = -\frac{\partial}{\partial x_i}P_{QB} + \frac{1}{\tau_p}\left(u_i - \breve{u}_{p,i}\right) \tag{3.12}$$

This "isothermal" approximation takes into account the variations of the number density field. In contrary to an isothermal Euler approximation of the Navier Stokes equations, the QBE is not assumed constant in time since it depends on the evolution of the resolved dispersed phase kinetic energy.
The temporal development of the QBE δq_p^2 obtained by the equilibrium formulae (Eq. 3.8) is shown in Fig. 3.4 using a linear-log plot. Simulations run with this model, show that at Stokes numbers about $St_{\tau^+} \approx 0.15$, particle segregation effects become again important and the computations fail.

This model was used during the Summer Program 2002 at CTR,Stanford,CA to compare Eulerian-Eulerian computations of decaying homogeneous isotropic turbulence to Eulerian-Lagrangian computations of Elghobashi and Truesdell [27] and the corresponding experimental measurements of Snyder and Lumley [97]. In order to avoid difficulties related to segregation effects, the QBE was assumed to be proportional to several times the correlated kinetic energy of the dispersed phase. This unphysical correction of QBP made the numerical simulation possible by making them "subsonic" and thus limiting compressibility effects. Results are published in the corresponding proceedings [49].

3.1.3 Isentropic pressure model (IPM):

The homogeneous distribution of QBE used in the HPM approach is not very physical. As can be observed in compressible gaseous flow, compression leads to an increase in temperature. This physical phenomena can be translated to the behavior of the dispersed

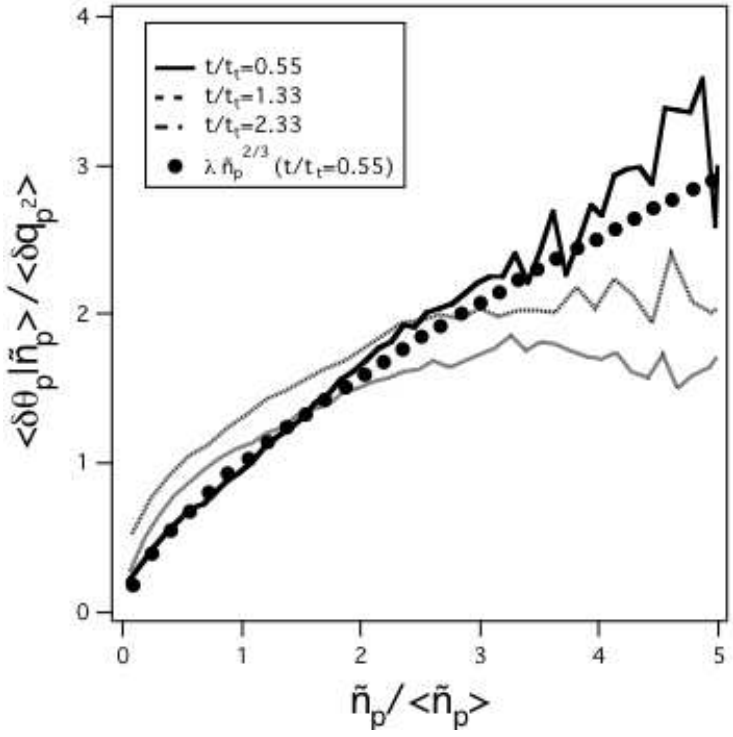

Figure 3.5: Conditional average of QB energy on the number density in the Lagrangian computation at different times (HIT 1,CJ).

phase, where isentropic compression leads to an increase of QBE in regions of high particle number density. This increase of QBE due to compression can be found in Lagrangian computations of particle laden flow in critical Stokes number regime. In the case of small Stokes numbers, drag force is a strong repelling mechanism and strongly diminuishes the compressible component of the correlated velocity (Eq. 2.123) and compressibility effects are weak. To take into acount an increase in QB energy due to compression, it is usefull to to come back to the mechanism, that can be understood using the Chapman-Enskog expansion. Making some simplifications, it can be shown that QBE should be proportional to $n^{2/3}$: Consider the conservation equations for particle number density :

$$\frac{\partial}{\partial t}\breve{n}_p + \frac{\partial}{\partial x_j}\breve{n}_p\breve{u}_{p,j} = 0 \tag{3.13}$$

and a shortened version of the transport equation for QBE :

$$\frac{\partial}{\partial t}\breve{n}_p\delta\breve{\theta}_p + \frac{\partial}{\partial x_j}\breve{n}_p\breve{u}_{j,p}\delta\breve{\theta}_p = -\frac{2}{3}\breve{n}_p\delta\breve{\theta}_p\frac{\partial\breve{u}_{p,j}}{\partial x_j} \tag{3.14}$$

where effects due to particle drag, shear production and diffusion are neglected. This transport equation can also be obtained by the lowest order expression in the Chapman-Enskog expansion with a supplementary solvability condition on the higher order contributions to QB energy *. Multiplication of Eq. 3.13 by $-\frac{2}{3}\breve{n}_p^{-5/3}\delta\breve{\theta}_p$ and summing with the product of Eq. 3.14 with $\breve{n}_p^{-5/3}$ yields:

$$\frac{\partial}{\partial t}\breve{n}_p^{-2/3}\delta\breve{\theta}_p + \breve{u}_{p,j}\frac{\partial}{\partial x_j}\breve{n}_p^{-2/3}\delta\breve{\theta}_p = 0 \tag{3.15}$$

or, using continuity:

$$\frac{\partial}{\partial t}\breve{n}_p\left(\breve{n}_p^{-2/3}\delta\breve{\theta}_p\right) + \frac{\partial}{\partial x_j}\breve{n}_p\breve{u}_{j,p}\left(\breve{n}_p^{-2/3}\delta\breve{\theta}_p\right) = 0 \tag{3.16}$$

Therefore, under the assumptions, that the contributions of diffusion, shear production and dissipation by drag are negligible, the product $\tilde{n}_p^{-2/3}\delta\breve{\theta}_p$ is a conserved quantity. In other words one can estimate local QBE by:

$$\delta\breve{\theta}_p = An_p^{2/3} \tag{3.17}$$

This model can be a posteriori tested by the Lagrangian simulation. The correlation between particle number density and QBE is illustrated in Fig. 3.5. The dotted line shows the theoretical assumption $\delta\breve{\theta}_p = An_p^{2/3}$ and the other lines show the dependence of $\delta\breve{\theta}_p$ on the particle number density $\breve{n}_p$ at different times.

This leads to an equation of state for the quasi brownian pressure (QBP) :

$$P_{QB} = \frac{2}{3}\breve{n}_p^{5/3}\langle\breve{n}_p\rangle^{-2/3}\eta_{QB}\breve{q}_p^2 \tag{3.18}$$

As in the case of the homogeneous pressure model approach, the QB stress tensor is then defined as:

$$\breve{n}_p\langle\delta u_{p,i}\delta u_{p,j}\rangle_p = P_{QB}\delta_{ij} \tag{3.19}$$

QBP takes into account the spatially non uniform distribution of QB energy. In the IPM the final equations that need to be solved for the dispersed phase with the isentropic pressure model are:

$$\frac{\partial}{\partial t}\breve{n}_p + \frac{\partial}{\partial x_j}\breve{n}_p\breve{u}_{p,i} = 0 \tag{3.20}$$

$$\frac{\partial}{\partial t}\breve{n}_p\breve{u}_{p,i} + \frac{\partial}{\partial x_j}\breve{n}_p\breve{u}_{p,i}\breve{u}_{p,j} = -\frac{\partial}{\partial x_i}P_{QB} + \frac{1}{\tau_p}\left(u_i - \breve{u}_{p,i}\right) \tag{3.21}$$

Simulation for a wide range of Stokes numbers were attempted. As in the case of the HPM, simulations failed for Stokes numbers larger than ≈ 0.15, again due to difficulties in the resolution of the number density field.

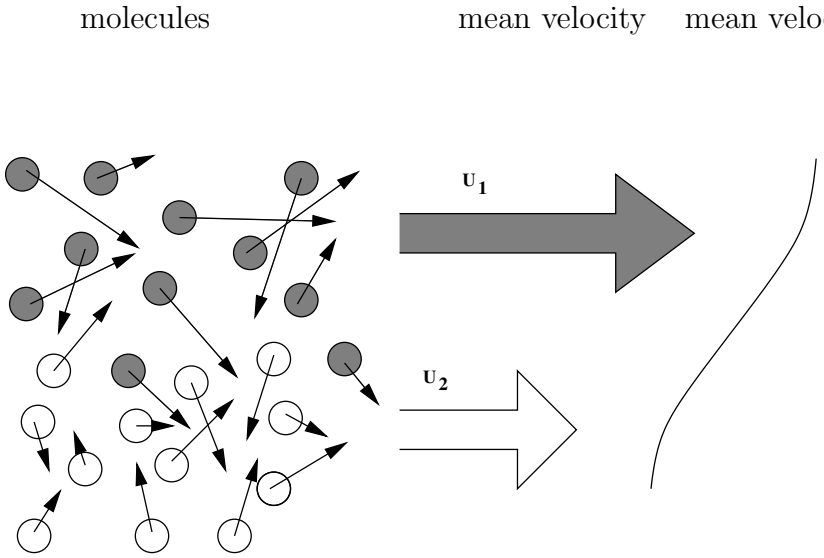

Figure 3.6: kinetic contribution to viscosity in a gas: illustration with a Couette Flow

3.1.4 Viscous Isentropic Pressure model (VIPM) :

In the IPM local variations of QBE are taken into account. The next step is to consider the off-diagonal components of the stress tensor. For these terms, a simple algebraic model compatible with the isentropic approximation, is the the Boussinesque assumption. This requires the introduction of a viscosity for the dispersed phase. This in explained in two steps. First the construction of a viscosity for a gas is briefly sketched. This is then used to construct an equivalent viscosity for the dispersed phase.

In the case of a gas viscous effects have two origins [93]:

1. Kinetic contribution [13]: In a dilute gas, the mean free path of the molecule λ is proportional to the product of molecular velocity v and the inter-collision time τ_c ($\lambda = v\tau_c$), the average time between two collisions of the same molecule τ_c. The rate of exchange of momentum in the ensemble averaged velocity field depends for mono-atomic gases essentially on the peculiar velocity and the penetration depth given by the mean free path length ($\propto \lambda v$). Therefore the kinematic viscosity should be proportional to the product of the mean free path length and the peculiar velocity. This is equivalent to say that kinematic viscosity is roughly proportional to the inter-collision time and the square of the molecular velocity:

$$\nu \propto \lambda_c v = \tau_c v^2 \tag{3.22}$$

   The kinetic contribution depends therefore on the collision frequency, since the collision frequency influences the mean free path length.

*see Chapmann and Cowling [13], par 7.14 p 116 or Dellar [21]

The kinetic contribution to viscosity can be illustrated with a Couette flow (Fig.3.6). Here it is assumed, that the molecules in the upper layer have a mean velocity U_1 and the molecules in the lower layer have a velocity U_2. Due to the penetration of molecules from the upper layer to the lower layer of about one free path length in one inter-collision time, the initially steep gradient between the two ensemble averaged velocities is smoothened out.

2. Collisional contribution: The collision contribution to the kinematic viscosity of a gas becomes important, if the molecular number density (or pressure) is so large that the molecular "diameter" becomes comparable to the free path length. Then inter-molecular collisions efficiently redistribute molecular velocity and the ensemble averaged velocity is altered. This mechanism is different from the viscosity in most liquids. In most liquids viscosity decreases with temperature. This is due to the inter-molecular forces, that are non-negligible.

The contributions to total viscosity in a gas is illustrated in Fig. 3.7. In contrary to the gas phase, the particles in the dispersed phase do not have a "free flight" since they undergo a constant force [†]. Nevertheless the particle relaxation time can be used together with the particle velocity to establish a length scale, that corresponds to an inertia dominated trajectory length of the particle. This length scale is $\lambda = v_p \tau_p$. Even in the absence of collisions the momentum contribution of the particle changes the ensemble averaged velocity field and increases the uncorrelated part of the particle kinetic energy. This motivates the modeling of the non-diagonal terms of the QB stress tensor by a viscosity assumption. As in the case of the gas, the kinetic QB viscosity is then proportional to the particle trajectory length dominated by inertia and the particle velocity. It is the uncorrelated part of the particle kinetic energy that causes a change in the ensemble averaged velocity field. It can be estimated by $\delta u = \sqrt{\delta\breve{\theta}_p}$. This leads to a QB viscosity of the form :

$$\nu_{QB} \approx \frac{1}{3}\tau_p \delta\breve{\theta}_p \tag{3.23}$$

Using the picture of the "Couette Flow" (Fig. 3.6) for the dispersed phase, the demonstration of Grad [37] for the viscosity of a gas can be transposed to the dispersed phase to obtain the expression for viscosity given in Eq. 3.23. Grad takes the second order moment transport equations for a gas. The equivalent equation for the dispersed phase is developed in appendix A.1. Then it is assumed, that the transverse velocities are zero ($\breve{u}_{p,2} = \breve{u}_{p,3} = 0$), that temporal and the other spatial gradients vanish ($\partial f/\partial t = \partial f/\partial x_1 = \partial f/\partial x_3 = 0$), and that the flux of QBE is negligible ($\langle \delta u_{p,i} \delta u_{p,j} \delta u_{p,k} \rangle_p = 0$). Under those assumptions the second order transport equation reduces to the following equation:

$$\breve{n}_p \langle \delta u_{p,1} \delta u_{p,2} \rangle_p \frac{\partial}{\partial x_2} \breve{u}_{p,1} + \breve{n}_p \langle \delta u_{p,2} \delta u_{p,2} \rangle_p \frac{\partial}{\partial x_2} \breve{u}_{p,1} + \frac{2\breve{n}_p}{\tau_p} \langle \delta u_1 \delta u_2 \rangle_p = 0 \tag{3.24}$$

[†] This depends largely on the interaction force between the molecules. If the interaction force is short ranged (that is it drops rapidly with increasing inter-molecular distance, Leonard Jones Potential etc.) molecules undergo an almost free flight.

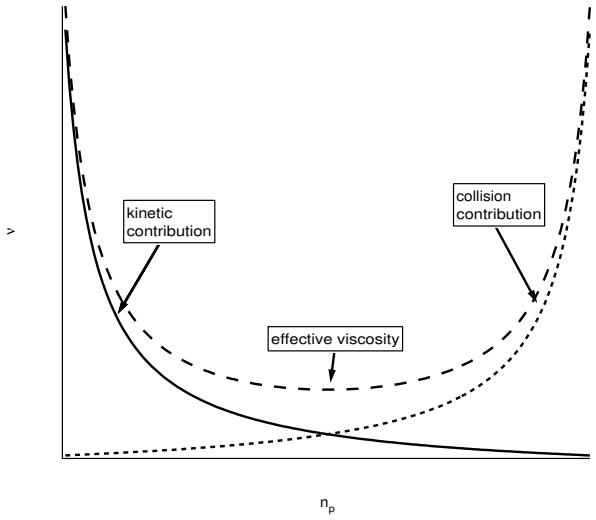

Figure 3.7: Sketch of the origin of viscosity in a gas as a function of molecular number density. At large inter-collision times the kinetic contribution to the viscosity dominates. At small inter-collision times the collision contribution dominates.

If the diagonal stresses are much larger than the off-diagonal stresses ($\langle \delta u_{p,2} \delta u_{p,2} \rangle_p \gg |\langle \delta u_{p,1} \delta u_{p,2} \rangle_p|$) and the diagonal stress is approximated by one third of the trace of the tensor ($\langle \delta u_{p,2} \delta u_{p,2} \rangle_p \approx 2/3 \delta \breve{\theta}_p$) and the off diagonal stress can be approximated by the following expression.

$$\langle \delta u_{p,1} \delta u_{p,2} \rangle_p \approx \frac{1}{3} \tau_p \delta \breve{\theta}_p \frac{\partial}{\partial x_2} \breve{u}_{p,1} \tag{3.25}$$

This reveals the QB viscosity coefficient as the proportionality coefficient between the off-diagonal stress and the mesoscopic velocity gradient.
As Grad pointed out, this is only a demonstrative motivation that lacks mathematical correctness, since a production of QBE by "shear stress" leads to a flux of QBE.

Quasi Brownian viscosity in the Isentropic approximation

Since the local value of the QBE $\delta \breve{\theta}_p$ is not known, here the isentropic approximation (Eq. 3.17) is used to estimate the local value of the QBE.

$$\nu_{QB} \approx \frac{1}{3} \tau_p \frac{\breve{n}_p^{2/3}}{\langle \breve{n}_p \rangle^{2/3}} \delta q_p^2 \tag{3.26}$$

The dynamic QB viscosity is then $\mu_{QB} = \breve{n}_p \nu_{QB}$ and can be used to write the stress tensor model with QBP for the diagonal terms of the QB stress tensor and a viscous assumption for the non-diagonal parts QB stress tensor.

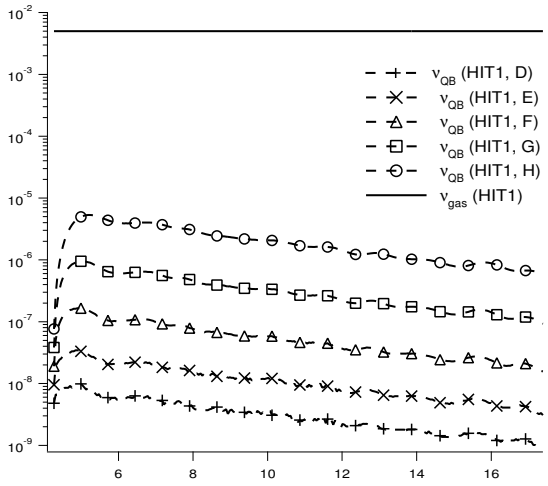

Figure 3.8: QB viscosity obtained by Eq. 3.23 estimating $\delta\breve{\theta}_p$ using the equilibrium formula (Eq.3.8) for different Stokes number in the test case HIT1. For reference, the carrier phase viscosity is given as a continuous line.

$$\breve{n}_p\langle\delta u_{p,i}\delta u_{p,j}\rangle_p = P_{QB}\delta_{ij} - \mu_{QB}\left(\frac{\partial\breve{u}_{p,i}}{\partial x_j} + \frac{\partial\breve{u}_{p,j}}{\partial x_i} - \frac{2}{3}\frac{\partial\breve{u}_{k,p}}{\partial x_k}\delta_{ij}\right) \tag{3.27}$$

The equations required to describe the dispersed phase behavior in the VIPM are :

$$\frac{\partial}{\partial t}\breve{n}_p + \frac{\partial}{\partial x_j}\breve{n}_p\breve{u}_{p,i} = 0 \tag{3.28}$$

$$\frac{\partial}{\partial t}\breve{n}_p\breve{u}_{p,i} + \frac{\partial}{\partial x_j}\breve{n}_p\breve{u}_{p,i}\breve{u}_{p,j} = -\frac{\partial}{\partial x_i}P_{QB} + \frac{\partial}{\partial x_j}\breve{\tau}_{p,ij} + \frac{1}{\tau_p}\left(u_i - \breve{u}_{p,i}\right) \tag{3.29}$$

where $\breve{\tau}_{p,ij}$ is the viscous part of the QB stress tensor as defined by Eq. 1.48. The qualitative order of influence of the viscous components of the QB stress tensor can be estimated by evaluating the temporal development of the QB viscosity and comparing it to the carrier phase viscosity. This is done in Fig. 3.8. The magnitude of QB viscosity increases with the Stokes number but remains several orders of magnitude smaller than the carrier phase viscosity. Therefore the QB dissipation stays significantly smaller than the dissipation in the carrier phase.

3.1.5 Viscous Pressure Model : (VPM)

A different method to take into account local variations of the QBE is to explicitly use the corresponding transport equation. The transport equation for QBE is obtained by taking the trace of the transport equations for the double correlations (appendix A.1).

This approach was presented in section 1.
The knowledge of the local values of QBE allows then to define the QBP and QB viscosity:

$$P_{QB} = \frac{2}{3}\breve{n}_p \delta\breve{\theta}_p \tag{3.30}$$

$$\mu_{QB} = \frac{1}{3}\breve{n}_p \tau_p \delta\breve{\theta}_p \tag{3.31}$$

The transport equations that need to be solved for the dispersed phase in the case of the VPM model are:

$$\frac{\partial}{\partial t}\breve{n}_p + \frac{\partial}{\partial x_j}\breve{n}_p\breve{u}_{p,i} = 0 \tag{3.32}$$

$$\begin{aligned}\frac{\partial}{\partial t}\breve{n}_p\breve{u}_{p,i} + \frac{\partial}{\partial x_j}\breve{n}_p\breve{u}_{p,i}\breve{u}_{p,j} &= -\frac{\partial}{\partial x_i}P_{QB} + \frac{\partial}{\partial x_j}\breve{\tau}_{p,ij} \\ &\quad + \frac{1}{\tau_p}\left(u_i - \breve{u}_{p,i}\right)\end{aligned} \tag{3.33}$$

$$\begin{aligned}\frac{\partial}{\partial t}\breve{n}_p\delta\breve{\theta}_p + \frac{\partial}{\partial x_j}\breve{n}_p\breve{u}_{p,j}\delta\breve{\theta}_p &= -2\frac{\breve{n}_p}{\tau_p}\delta\breve{\theta}_p - \left[P_{QB}\delta_{ij} - \breve{\tau}_{p,ij}\right]\frac{\partial\breve{u}_{p,i}}{\partial x_j} \\ &\quad + \frac{\partial}{\partial x_j}\breve{n}_p\breve{k}_{QB}\frac{\partial}{\partial x_j}\delta\breve{\theta}_p\end{aligned} \tag{3.34}$$

In the transport equation for QBE the triple correlation is modeled by a diffusion assumption using the diffusion coefficient $\breve{k}_{QB}$. It is modeled by analogy to the diffusion coefficient used in the transport equation for the fluctuating particle motion in the two-fluid formulation (see Eq. 1.45).

Initialisation of QBE

One difficulty associated to the VPM model is the initialization of QBE. If particles are initially at rest or have velocities equal to the carrier phase at the particle location, QBM is physically absent. In the transport equation 3.34 all production mechanism for QBE are proportional to QBE. In the case of production of QBE by the viscous elements of the stress tensor, viscosity is proportional to QBE and thus production by shear is impossible with zero QBE. The production of QBE by compression relies as well on the existence of QBE, since it is result of the product of QBE with the divergence of the mesoscopic flow field.
Here this difficulty was circumvented by initializing the QBE field with a value higher than the value given by equilibrium formula (Eq.3.8). In this case dissipation by drag force should decrease the amount of QBE rapidly to its production/dissipation equilibrium.

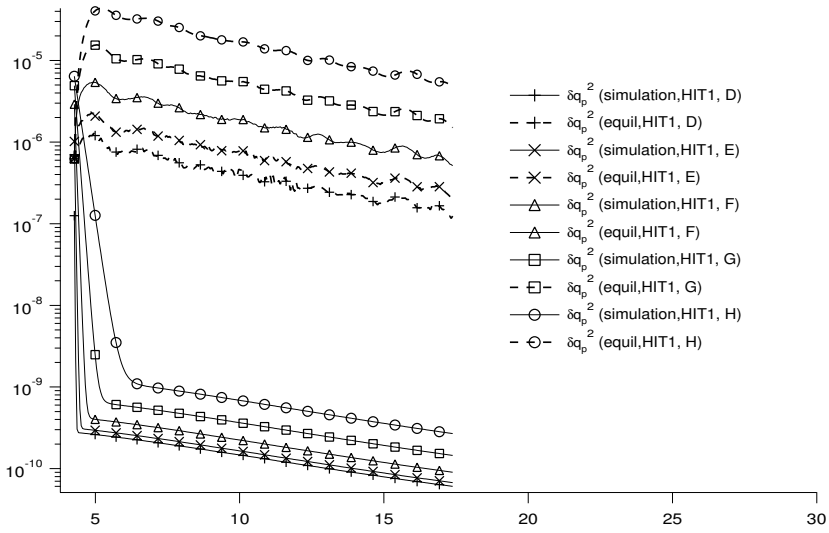

Figure 3.9: The values of $\langle \delta \breve{\theta}_p \rangle$ obtained by the simulation in the VPM model compared to the values of δq_p^2 as obtained from the equilibrium formula (Eq. 3.8) for different Stokes numbers in the test case HIT1.

QBE using the transport equation

The values of QBE can quantitatively be compared to the values obtained from the equilibrium formula. This is shown in Fig. 3.9. The prediction of QBE by the transport equation of QBE predicts values far lower than the values obtained by the equilibrium formula. This may have several origins other than the production model for QBE. One possible origin is that the length scales of the dispersed phase are significantly smaller than the length scales of the carrier phase and that the small scale motion is insufficiently resolved. However a series of simulations with a 64^3, 128^3 and 192^3 grid points show, that the spatial resolution is not responsible for the low values of QBE (Fig. 3.10). It shows that the temporal development of QBE energy is identical in the three cases. Therefore the difficulty of low QBE compared to the equilibrium formula is not due to the spatial resolution.

Effects of initialization on QBE

Another possible cause for the lack of QBE is due to the initialisation of the mesoscopic velocity field. If dispersed phase velocities are aligned with the carrier phase velocity, production of QBE could be very small. In this case an initialisation with a different mesoscopic velocity field should change the rate of production of QBE. In Fig. 3.11 the temporal developement of QBE is compared for two different initialisations. In one case the mesoscopic velocity of the dispersed phase is initially set to zero and in the other case the mesoscopic dispersed phase velocity is equal to the carrier phase velocity (see section 2.7.1). The equilibrium QBE from the first simulation is given as a reference value. The figure

Model	Description
No model approach (NM)	$\breve{n}_p\langle\delta u_{p,i}\delta u_{p,j}\rangle_p = 0$ (section 3.1.1)
Homogeneous pressure model (HPM)	$\breve{n}_p\langle\delta u_{p,i}\delta u_{p,j}\rangle_p = P_{QB}\delta_{ij}$ with uniform algebraic QBE ("Isothermal" approximation, section 3.1.2, algebraic QBE)
Isentropic pressure model (IPM)	$\breve{n}_p\langle\delta u_{p,i}\delta u_{p,j}\rangle_p = P_{QB}\delta_{ij}$ with non-uniform QBE ("Isentropic" approximation, section 3.1.3, algebraic QBE)
Viscous isentropic pressure model (VIPM)	$\breve{n}_p\langle\delta u_{p,i}\delta u_{p,j}\rangle_p = P_{QB}\delta_{ij} - \mu_{QB}S_{ij}^T$ with non-uniform algebraic QBE (section 3.1.4)
Viscous pressure model (VPM)	$\breve{n}_p\langle\delta u_{p,i}\delta u_{p,j}\rangle_p = P_{QB}\delta_{ij} - \mu_{QB}S_{ij}^T$ (section 3.1.5, transport equation for QBE, see also section 1.3.3)
transport equation model (TEM)	$\breve{n}_p\langle\delta u_{p,i}\delta u_{p,j}\rangle_p$ (section 3.1.6, transport equations for stresses)

Table 3.1: Different models of the QBM stress tensor

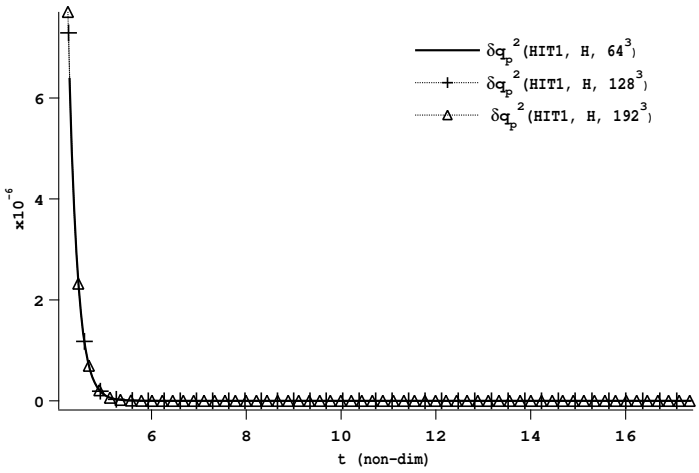

Figure 3.10: QBE with three different spatial resolutions $(64^3, 128^3, 192^3)$ for the test case HIT1,H.

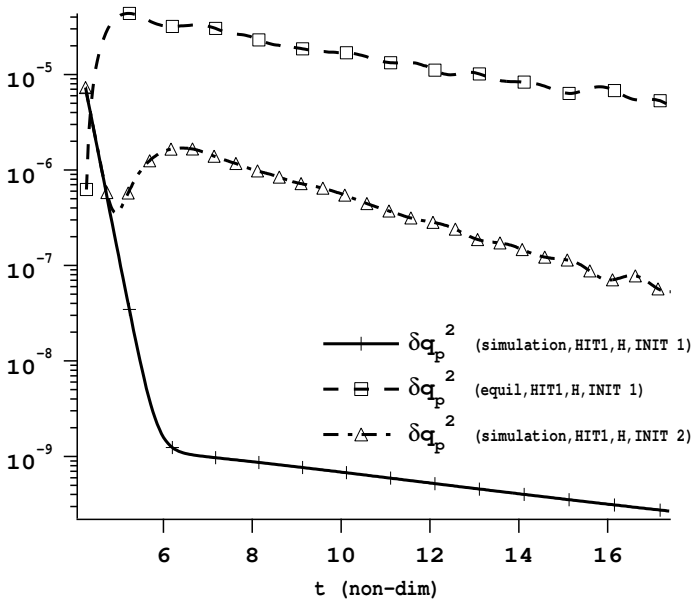

Figure 3.11: QBE with different initial conditions for the test case HIT1,H.

shows that the initialisation has a large impact for the development of QBE. If particles are initially at rest, the mesoscopic velocity is not aligned with the carrier phase velocity and a bigger production of QBE occurs. The value of QBE with the second initialisation is however still one magnitude smaller than the equilibrium QBE.

Effects of carrier phase turbulence on QBE

A third possibility is related to the carrier phase turbulence. Since in the carrier phase test case (HIT1) the Reynolds number is very low, this may be due to an effect of low Reynolds number. In Fig. 3.12 developement for QBE in the test case (HIT2,D) is compared to the QBE from the equilibrium formula. It shows that the same difficulty as in low Reynolds number case arises.

Effect of the diffusion coefficient in the QBE transport equation

Triple correlations $\langle \delta u_{p,i} \delta u_{p,k} \delta u_{p,k} \rangle_p$ were modeled by making a gradient assumption on QBE. When the Navier Stokes equations are developed from kinetic theory, the heat flux term arises by making a perturbation on a gaussian velocity distribution in Hermite polynomials. In the development of the mesoscopic equations no assumptions on the shape of the velocity distribution was made. Therefore such a modeling is questionable. In the test cases previously mentioned QBE is predicted too small compared to the equilibrium formula and the effect of the diffusion coefficient can not be tested. Therefore this test is reported to the section of inertial particle with larger values of QBE (section 12).

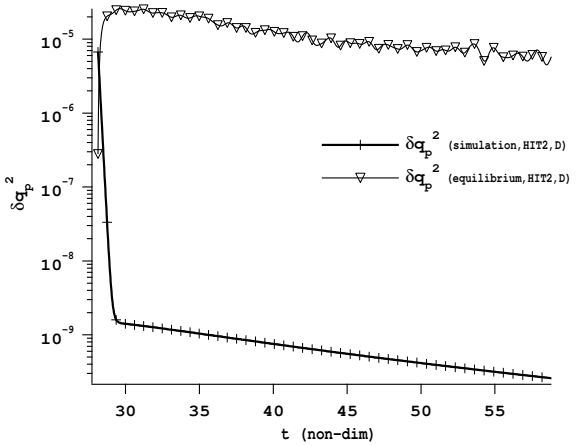

Figure 3.12: QBE in the simulation (HIT 2,D).

3.1.6 Transport equation model for second order terms: (TEM)

Supposing that the residual particle kinetic energy is anisotropic, modeling the diagonal terms of the QB stress tensor by one third of the trace is questionable. In order to take into account such anisotropic effects, one possibility is to transport the second moments of the residual particle velocity distribution. This approach corresponds conceptually to the $R_{2,ij}$ models in gas-particle flow (Simonin [91]). The difference to R_{ij} models in Reynolds averaged (RANS) computations of turbulent gaseous flows is, that the present model is derived from the kinetic equation and not from the Navier-Stokes equations. Furthermore the second order model contains contributions related to drag force absent in the transport equations for gaseous turbulent flows. The derivation of the second order transport equations is done in Appendix A.1. The resulting transport equation is given below:

$$\begin{aligned}\frac{\partial}{\partial t}\breve{n}_p\langle\delta u_{p,i}\delta u_{p,j}\rangle_p + \frac{\partial}{\partial x_k}\breve{n}_p\breve{u}_{p,k}\langle\delta u_{p,i}\delta u_{p,j}\rangle_p &= -\breve{n}_p\langle\delta u_{p,i}\delta u_{p,k}\rangle_p\frac{\partial}{\partial x_k}\breve{u}_{p,j} \\ &\quad -\breve{n}_p\langle\delta u_{p,j}\delta u_{p,k}\rangle_p\frac{\partial}{\partial x_k}\breve{u}_{p,i} + \\ &\quad -\frac{\partial}{\partial x_k}\breve{n}_p\langle\delta u_{p,i}\delta u_{p,j}\delta u_{p,k}\rangle_p - \frac{2}{\tau_p}\breve{n}_p\langle\delta u_{p,i}\delta u_{p,j}\rangle_p\end{aligned} \tag{3.35}$$

The second order transport equations require modeling of the third order correlations $\langle\delta u_{p,i}\delta u_{p,j}\delta u_{p,k}\rangle_p$. By analogy to the statistic two-fluid model [91] the third order correlations are modeled via a diffusion assumption:

$$\frac{\partial}{\partial x_m}\breve{n}_p\langle\delta u_{p,i}\delta u_{p,j}\delta u_{p,m}\rangle_p = -\frac{\partial}{\partial x_m}\breve{n}_p\mathcal{K}_{p,mn}\frac{\partial}{\partial x_n}\langle\delta u_{p,i}\delta u_{p,j}\rangle_p \tag{3.36}$$

with the diffusion coefficients

$$\mathcal{K}_{p,mn} = \frac{5}{9}\tau_p\langle\delta u_{p,m}\delta u_{p,n}\rangle_p \tag{3.37}$$

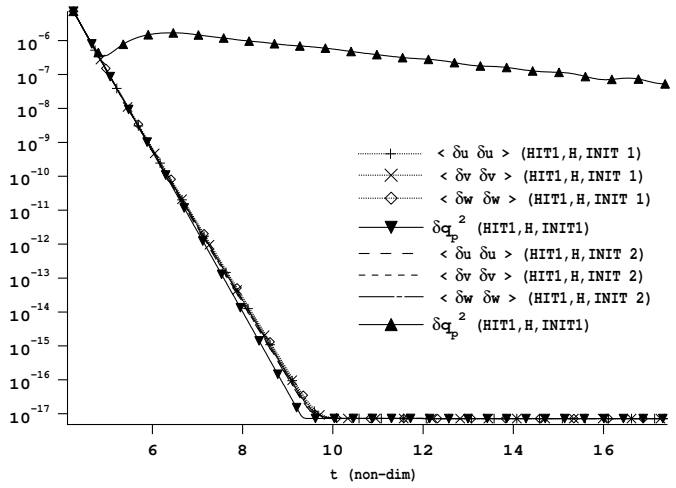

Figure 3.13: Comparison of diagonal stresses from the TEM and QBE from the VPM for two different initializations.

In this model the second order stresses need to be initialized with physical values before the computation. As in the case of the transport equation for QBE, the diagonal terms can be initialized using the equilibrium formula of P. Fevrier (Eq. 3.8). Off-diagonal terms can be initialized with zero, since production terms for the off-diagonal terms are in the contraction of diagonal terms of the stress tensor with the gradients in the mesoscopic velocity field.

3.1.7 Comparison of second order transport models to viscous models

The diagonal stresses can be compared to 2/3 of the QBE obtained from the transport equation in the VPM model and the equilibrium formula in the HPM model. Fig. 3.13 shows the temporal development of the diagonal stresses in comparison with QBE.

Since the stresses are local quantities, it is interesting to see, if the diagonal stresses are isotropic, i.e. to what point the diagonal components have the same value. In Fig. 3.14 the diagonal stresses from QBP and viscous modeling are compared to the diagonal stresses as obtained from the transport equation.

3.1.8 Compressibility Effects

In the cases considered particle inertia leads to strong compressibility effects. This can be illustrated by comparing the system of the dispersed phase to a dilute gas. In a subsonic flow the uncorrelated velocity of the molecules (approximately the soundspeed) is larger than the correlated velocity. This is translated in the Navier-Stokes equations by pressure

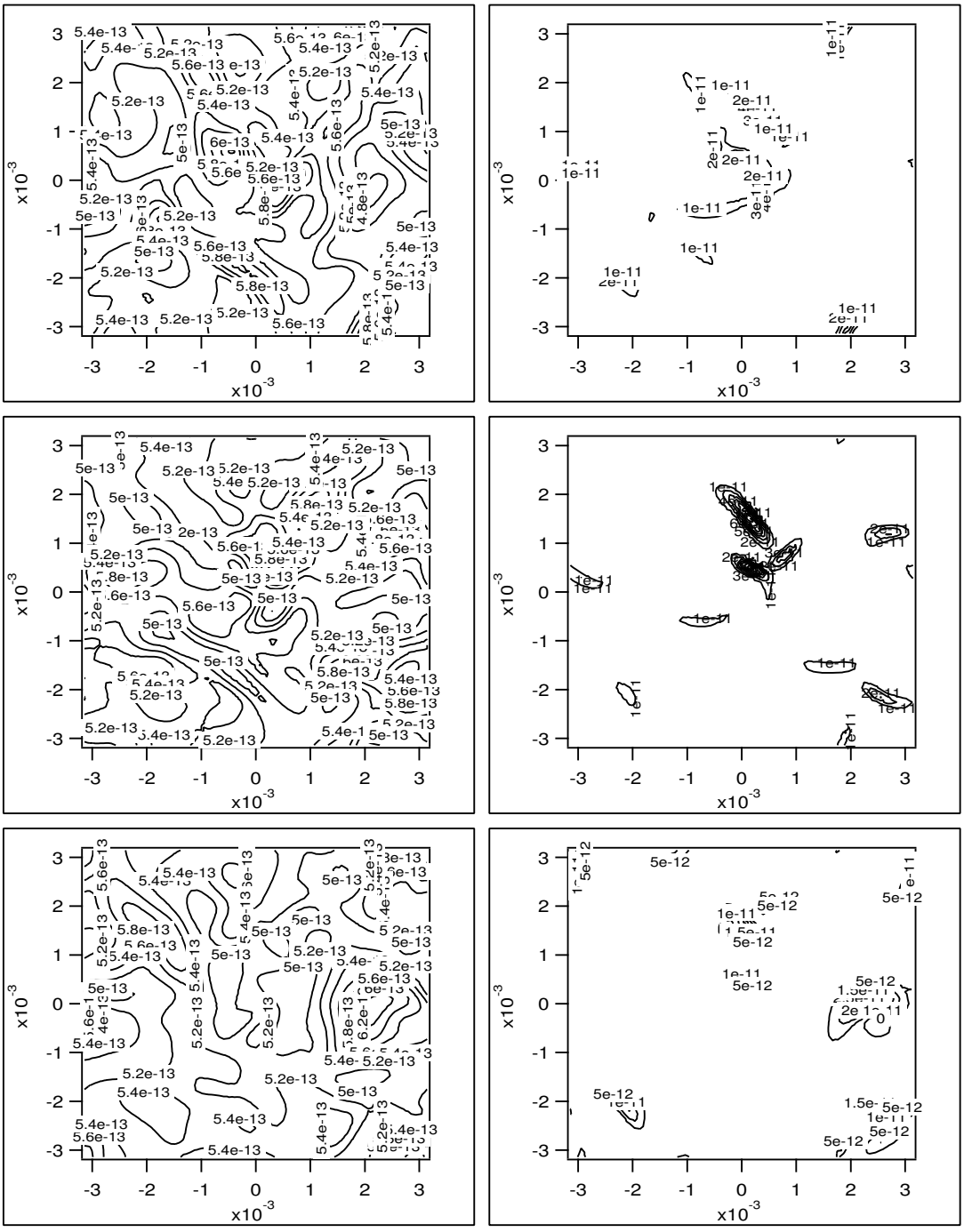

Figure 3.14: Diagonal stresses in the case HIT 1, H. The left column shows the modeled stresses $\langle \delta u_{p,i} \delta u_{p,j} \rangle_p = 2/3 * \delta \breve{\theta}_p \delta_{ij} - \nu_{QB} S_{ij}^T$ from top to bottom $\langle \delta u_p \delta u_p \rangle_p$, $\langle \delta v_p \delta v_p \rangle_p$, $\langle \delta w_p \delta w_p \rangle_p$ and the right column shows the equivalent stress components from the transport equation.

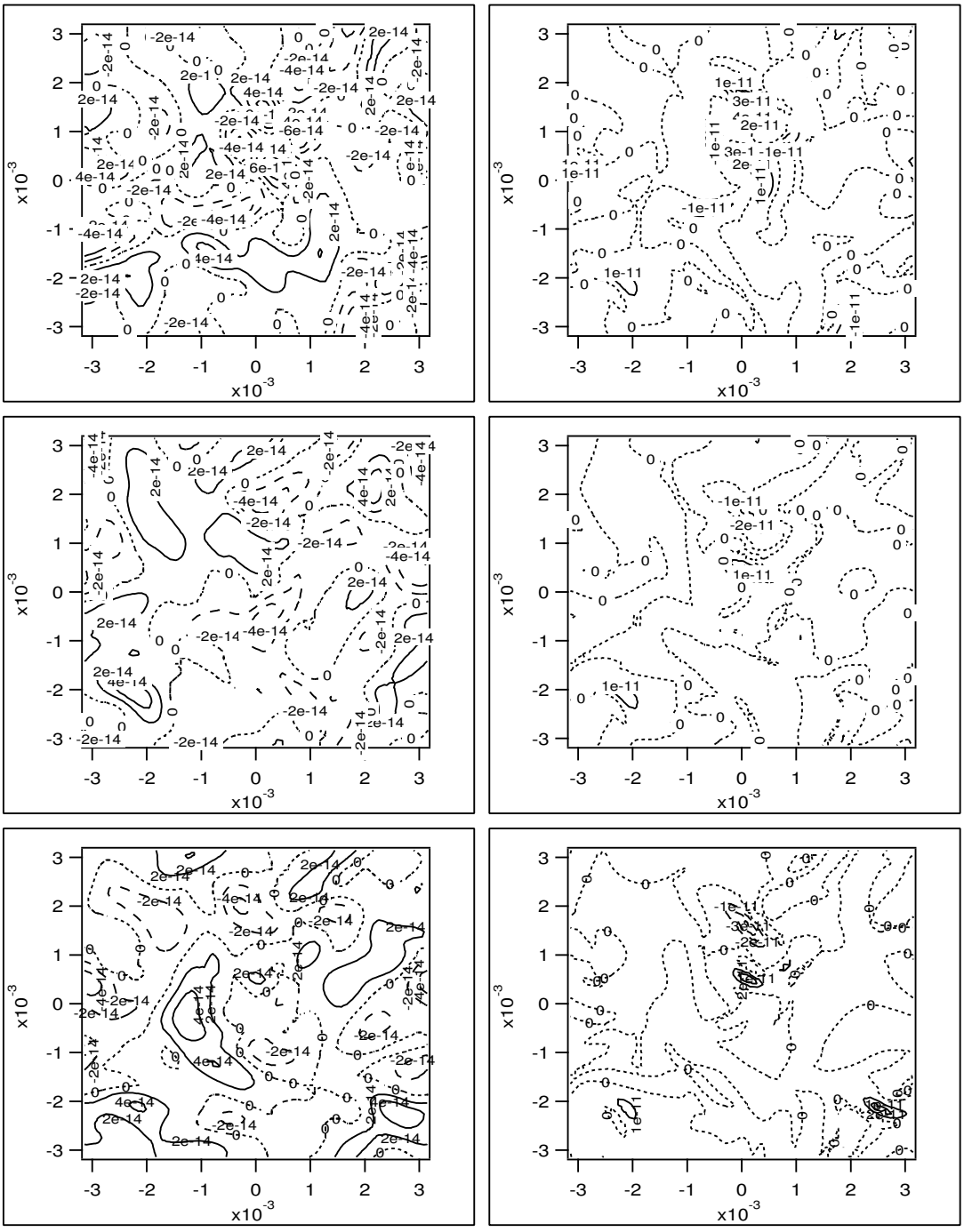

Figure 3.15: Non-Diagonal stresses in the case HIT 1, H. The left column shows the modeled stresses $\langle \delta u_{p,i} \delta u_{p,j} \rangle_p = -\nu_{QB} S_{ij}^T$ from top to bottom $\langle \delta u_p \delta v_p \rangle_p$, $\langle \delta u_p \delta w_p \rangle_p$, $\langle \delta v_p \delta w_p \rangle_p$ and the right column shows the equivalent stress components from the transport equation.

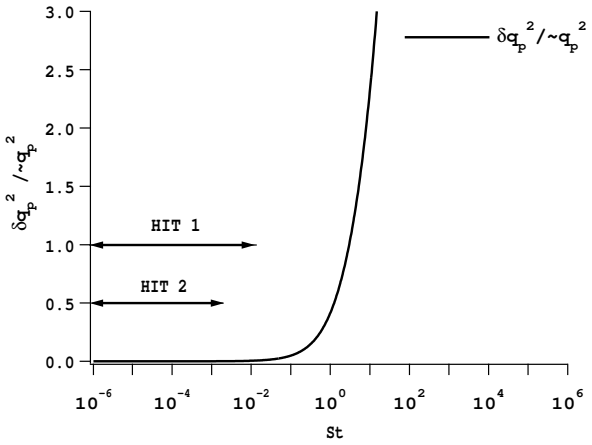

Figure 3.16: Range of Stokes numbers where the simulation could be performed without encountering numerical difficulties with the present models.

which redistributes the molecules such that density variations are small and no shock like structures are generated.
In a supersonic flow the uncorrelated velocity of the molecules (approximately the sound-speed) is smaller than the correlated velocity. Such flows may contain shocks or shock like structures where density variations are large.
If the correlated kinetic energy of the particles is larger than QBE, the QBP does not prevent the creation of large differences in the number density field.
In the case of large Stokes numbers, the dispersed system becomes "subsonic" and QBP effectivly counteracts compressibility effects. In the case of small Stokes numbers, the dispersed phase has the characteristics of a "supersonic" gaseous flow since the correlated velocity is larger than the uncorrelated velocity. In the tracer limit, it is drag force that prevents compressibility effects, since it diminishes the compressible velocity component (see Eq. 2.123). Maximal segregation occurs therefore in the range of Stokes numbers where, both mechanisms are less effective which is the range of unity Stokes numbers.

3.2 Validity of the presented models:

If the Stokes number, based on the dissipative time scale τ^+, exceeds 0.15 in the case HIT1 and 0.0033 in the case HIT2, the numerical computation fails. This is represented in the graph given in fig. 3.16. The origin of this problem is the number density field since compressibility effects lead to strong variations in the number density. In a poorly resolved computation this leads to negative number densities due to dispersion effects. In a typical Navier-Stokes computation, the gaseous density varies too little in the absence of shocks to observe such difficulties. Two possibilities exist to overcome this difficulties: One is to

increase spatial resolution to the point, where the number density field is resolved and a second possibility is to resolve filtered equations for the dispersed phase, comparable to the filtered Navier-Stokes equations in Large Eddy Simulations (LES). Both strategies are investigated in the following section. One difficulty both methods have in common is to estimate the necessary spatial descitiztion of the number density field. This question is considered a posteriori by comparing the simulations of three different spatial resolutions.

3.3 Extension to inertial particles

3.3.1 Increase in spatial resolution

The previously presented test cases were all performed with a spatial resolution of 64^3. At Stokes numbers, where inertial effects become important simulations failed due to poor resolution of the droplet number density field. An increase in spatial resolution should improve the resolution of the number density field and therefore allow to perform computations with more inertial particles. Here spatial resolution is increased from 64^3 to 128^3 and to 192^3. An increase from 64^3 to 128^3 allows to increase the Stokes number from 0.123 (HIT1,H) to 0.149 (HIT1,V). A further increase in spatial resolution to 192^3 allows to perform simulations with a Stokes number of 0.151 (HIT1,W). This shows that the effects due to inertia are strongly dependent on the Stokes number and that an increase in spatial resolution even at such low Reynolds numbers is insufficient to perform simulations at higher Stokes numbers. This leads to the idea of performing simulations with a filtered number density field.

3.3.2 Filtered dispersed phase equations

Here the second approach of filtered equations is presented. Only the resulting set of equations is presented whereas the actual filtering operation is detailed in chapter 5.
Sloppy filtering in Favre averged sense of the dispersed phase equations (eqs.1.35,1.46 and 1.47) then leads to the following set of equations:

1. particle number density:

$$\frac{\partial}{\partial t}\breve{\bar{n}}_p + \frac{\partial}{\partial x_j}\breve{\bar{n}}_p\breve{\tilde{u}}_{p,j} = 0 \tag{3.38}$$

2. mesoscopic particle momentum:

$$\begin{aligned}\frac{\partial}{\partial t}\breve{\bar{n}}_p\breve{\tilde{u}}_{p,i} + \frac{\partial}{\partial x_j}\breve{\bar{n}}_p\breve{\tilde{u}}_{p,j}\breve{\tilde{u}}_{p,i} \;=\; & -\frac{\partial}{\partial x_j}\bar{P}_{QB} + \frac{\partial}{\partial x_j}\breve{\bar{\tau}}_{p,ij} \\ & + \frac{\breve{\bar{n}}_p}{\tau_p}\left(\tilde{u}_i - \breve{\tilde{u}}_{p,i}\right) \\ & - \frac{\partial}{\partial x_j}\left\{\breve{\bar{n}}_p\widetilde{\breve{u}_{p,j}\breve{u}_{p,i}} - \breve{\bar{n}}_p\breve{\tilde{u}}_{p,j}\breve{\tilde{u}}_{p,i}\right\}\end{aligned} \tag{3.39}$$

3. Quasi Brownian Energy:

$$\frac{\partial}{\partial t}\breve{\bar{n}}_p\delta\tilde{\breve{\theta}}_p + \frac{\partial}{\partial x_j}\breve{\bar{n}}_p\tilde{\breve{u}}_{p,j}\delta\tilde{\breve{\theta}}_p = -2\frac{\breve{\bar{n}}_p}{\tau_p}\delta\tilde{\breve{\theta}}_p - \overline{[P_{QB}\delta_{ij} - \breve{\tau}_{p,ij}]\frac{\partial\breve{u}_{p,i}}{\partial x_j}} \tag{3.40}$$

$$+ \frac{\partial}{\partial x_j}\breve{\bar{n}}_p\tilde{\breve{k}}_{QB}\frac{\partial}{\partial x_j}\delta\tilde{\breve{\theta}}_p$$

$$- \frac{\partial}{\partial x_j}\left\{\breve{\bar{n}}_p\widetilde{\breve{u}_{p,j}\delta\breve{\theta}_p} - \breve{\bar{n}}_p\tilde{\breve{u}}_{p,j}\delta\tilde{\breve{\theta}}_p\right\} \tag{3.41}$$

Following the idea that essentially the insufficiently resolved quantity is the droplet number density, the non-diagonal components of the tensor

$$\frac{\partial}{\partial x_j}\left\{\breve{\bar{n}}_p\breve{u}_{p,j}\widetilde{\breve{u}_{p,i}} - \breve{\bar{n}}_p\tilde{\breve{u}}_{p,j}\tilde{\breve{u}}_{p,i}\right\} \tag{3.42}$$

or the tensor

$$\frac{\partial}{\partial x_j}\left\{\breve{\bar{n}}_p\breve{u}_{p,j}\widetilde{\delta\breve{\theta}_p} - \breve{\bar{n}}_p\tilde{\breve{u}}_{p,j}\delta\tilde{\breve{\theta}}_p\right\} \tag{3.43}$$

can be considered as negligible. Density in a gas is primarily influenced by pressure. Here the filtered QB pressure, using the definition for QB pressure, can be expressed in terms of the filtered density and Favre averaged QB energy.

$$\bar{P}_{QB} = \frac{2}{3}\overline{\breve{n}_p\delta\breve{\theta}_p} = \frac{2}{3}\breve{\bar{n}}_p\delta\tilde{\breve{\theta}}_p. \tag{3.44}$$

In the present case the number density field is filtered and admits less variations then the unfiltered number density field. Variations in number density are created by the compressible component of the mesoscopic velocity field. The "subgrid" term for the filtered momentum equation needs to act therefore on the compressible component of the velocity field like a pressure term.
This can be achieved by introducing for the diagonal components of the unresolved stresses a subgrid pressure that compensates partially the compressible component of the mesoscopic velocity field, leading to a filtered number density field. This subgrid term for the diagonal part of the unresolved stresses (Eq. 3.42) can be chosen in the form of a bulk viscosity and one may construct a new pressure for the filtered momentum equation containing the filtered QB pressure and the subgrid pressure resulting from the normal stresses.

$$\tilde{P}_p = \bar{P}_{QB} + P_{sgs} \tag{3.45}$$

The subgrid pressure is chosen as form of the bulk viscosity. [‡]

$$P_{sgs} = -\xi_{sgs} \frac{\partial}{\partial x_j} \breve{\tilde{u}}_{p,j} \tag{3.46}$$

It is still necessary to estimate the subgrid coefficient ξ_{sgs}: In LES simulation of compressible turbulence a subgrid model for the diagonal terms of the stress tensor is sometimes used (Moin et al. [65],Yoshizawa [118]). There the additional diagonal terms are modeled by a type of subgrid pressure that has the form:

$$2C_I \bar{\rho} \Delta^2 \left| \tilde{S}_{ij} \right|^2 \tag{3.47}$$

In the considered case, it is not subject to model small scale vorticity that contributes to the subgrid energy, as is the case in a compressible large eddy simulation. Only the local compressibility effects are targeted. Local compressibility is measured by the divergence of the flow field $\frac{\partial}{\partial x_j} \breve{\tilde{u}}_{p,j}$. This leads to the following coefficient for the subgrid bulk viscosity:

$$\xi_{sgs} = C_{divu} (\Delta)^2 \sqrt{\left(\frac{\partial}{\partial x_j} \breve{\tilde{u}}_{p,j} \right)^2} \tag{3.48}$$

Here Δ is the size of filter. In the simulations presented in the following Δ was chosen as the size of the grid cell. Whereas the constant in the Smagorinsky model for the turbulent subgrid viscosity can be evaluated theoretically, making an assumption on the form of the spectrum, the constant in the subgrid pressure has at this point no theoretical basis and therefore needs to be handled carefully.
The new equation of state (Eq. 3.45) leads to a filtered number density field. Since this terms represents the compressible energy component of the subgrid energy it is questionable whether or not to include it in the production term of the filtered QBE. This point is addressed in the following section.

Filtered Pressure-Strain production of QBE

In the equation for QBE, one filtered term, that needs to be expressed, is the filtered QBP mesoscopic velocity divergence correlation and the strain shear correlation:

$$\overline{P_{QB} \delta_{ij} \frac{\partial \breve{u}_{p,i}}{\partial x_j}} - \overline{\breve{\tau}_{p,ij} \frac{\partial \breve{u}_{p,i}}{\partial x_j}} \tag{3.49}$$

[‡] Following the argument of Kohler [50], a somewhat different interpretation of such an equation of state without filtering is possible. There the divergence term in the equation of state is a first order correction taking into account, that the trace elements of the stress tensor are not necessarily of the same value. In the case of a shock for instance, peculiar velocities normal to the shock differ significantly from the peculiar velocities parallel to the shock. Such an interpretation suggests however that the bulk viscosity is a quasi brownian effect and not a subgrid effect. This is in contradiction to the previous assumption that the simulation of the dispersed phase is only limited by the spatial resolution.

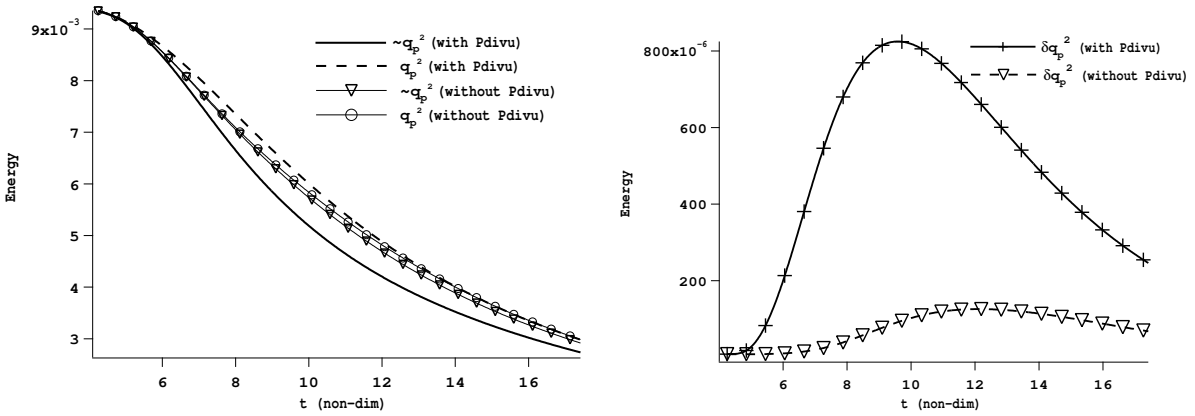

Figure 3.17: QBE when the subgrid pressure is included in the production term of QBE compared to the case where it is excluded.

Since the considered equations show highly compressible behavior, one can not use the standard argument of incompressible LES and neglect the pressure dilatation correlation. The most easy way to handle this term is to assume the filter to be a projector. If the mesoscopic velocity field is considered to be entirely resolved, which is not entirely true, since the subgrid pressure counteracts partially the compressible component, one may approximate this term by :

$$\bar{P}_{QB}\delta_{ij}\frac{\partial\breve{\bar{u}}_{p,i}}{\partial x_j} - \breve{\bar{\tau}}_{p,ij}\frac{\partial\breve{\bar{u}}_{p,i}}{\partial x_j} \tag{3.50}$$

In this case the subgrid pressure does not enter as a production term into the equation for QBE.
Since it is the compressible component of the dispersed phase kinetic energy, that exchanges with QBE by dilatation and compression, the subgrid pressure P_{sgs} effects the local production of QBE. Under the assumption, that the compressible kinetic energy enters directly into QBE, the pressure strain component may be approximated by the following relation.

$$\left(\bar{P}_{QB} + P_{sgs}\right)\delta_{ij}\frac{\partial\breve{\bar{u}}_{p,i}}{\partial x_j} - \breve{\bar{\tau}}_{p,ij}\frac{\partial\breve{\bar{u}}_{p,i}}{\partial x_j} \tag{3.51}$$

Simulations have been performed with and without this supplementary source term in the equation for QBE. Results are shown in fig. 3.17. If the supplementary source term is excluded, production of QBE is significantly smaller, since local compressibility effects are not taken into account.

Reconstruction of the filter kernel

Here it is assumed that $\breve{\bar{n}}_p$ is the filtered number density field of the equivalent resolved number density field $\breve{n}_p$. Formally the filtered number density field is obtained by the

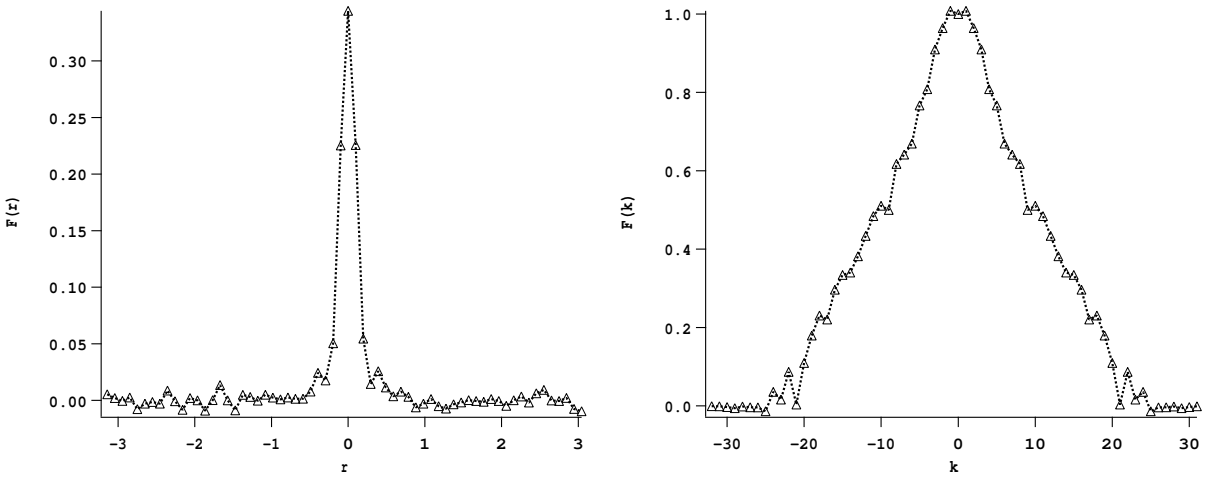

Figure 3.18: Filtering Kernel obtained by backward convolution between the Lagrangian number density field and the Eulerian number density field with a subgrid Pressure term. Simulation parameters are (HIT1, CJ) at t=10.8. The left graph shows the spatial filter and the right graph shows the spectral filter.

following convolution with the filter kernel:

$$\bar{\breve{n}}_p(x) = \int \breve{n}_p(x')F(x'-x)dx' \tag{3.52}$$

Using the Fourier transform property the convolution becomes a product in spectral space:

$$\hat{\bar{\breve{n}}}_p(\boldsymbol{\kappa}) = \hat{\breve{n}}_p(\boldsymbol{\kappa})\hat{F}(\boldsymbol{\kappa}) \tag{3.53}$$

Finally, by the real space filter kernel can be obtained by backward Fourier transform:

$$F(x) = \mathcal{F}^{-1}\left(\frac{\hat{\bar{\breve{n}}}_p(\boldsymbol{\kappa})}{\hat{\breve{n}}_p(\boldsymbol{\kappa})}\right) \tag{3.54}$$

In the present case the unfiltered number density field is not available from the Eulerian computation. Therefore the equivalent Lagrangian number density field is used to obtain the filter kernel. The filter kernel is displayed in fig.3.18 for the case (HIT1,CJ) at $t = 10.8$. Since the filter is considered isotropic in space, averaging over the different directions was performed and only the one dimensional kernel is retained. The figure shows that the convolution kernel averages the Lagrangian number density field a little more than the neighboring grid cells. If interpreting this graph, one has to keep in mind that the Lagrangian number density was already volume filtered to obtain a continuous field.

Unphysical production of QBE by dilatation

A subgrid pressure leads however to an unphysical artifact: By isolating the production term related to pressure in the equation for QBE, one obtains with the filtered pressure

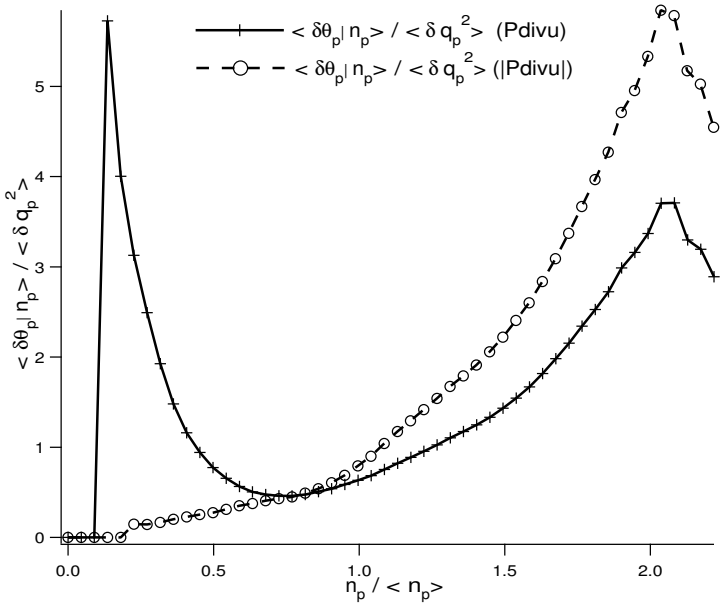

Figure 3.19: Conditional average of QB energy on the number density with a the subgrid pressure term as production in the QBE and a modified production term. The simulation parameters for the gas phase are HIT 1 (table 2.1) and CJ (table 2.2) for the dispersed phase. The analysis was performed at the non dimensional time t = 10.8.

the following expression:

$$\tilde{P}_{QB}\delta_{ij}\frac{\partial \breve{u}_{p,k}}{\partial x_k} = \tilde{\breve{P}}_{QB}\delta_{ij}\frac{\partial \breve{u}_{p,k}}{\partial x_k} + P_{sgs}\delta_{ij}\frac{\partial \breve{u}_{p,k}}{\partial x_k} \tag{3.55}$$

The last term on the right hand side of Eq. 3.55 can be expanded into the detailed expression using the definition of P_{sgs} in Eq. 3.46:

$$C_{divu}(\delta x)^2\sqrt{\left(\frac{\partial \breve{u}_{p,k}}{\partial x_k}\right)^2}\frac{\partial \breve{u}_{p,k}}{\partial x_k}\delta_{ij}\frac{\partial \breve{u}_{p,k}}{\partial x_k} \tag{3.56}$$

This expression has the same sign for positive and negative divergence. In other words, it leads to a production of QBE in the case of dilatation and compression. This is in contradiction to what is expected from the isentropic approximation (see fig. 3.5). In order to illustrate this effect two different computations were performed. The first one with the subgrid pressure as a production term and the other one, where the absolute value of the subgrid pressure was taken in the production term. If the absolute value is taken in the production term, QBE is dissipated in the case of dilatation as expected by the isentropic approximation. The difference is illustrated in fig. 3.19.

Effect of the diffusion coefficient in the QBE transport equation

Triple correlations $\langle \delta u_{p,i} \delta u_{p,j} \delta u_{p,m} \rangle$ occur, if the particle velocity distribution is asymmetric since odd power correlations vanish in symmetric distributions. In a gas spatial variations in double correlations may then produce triple correlations by inter-molecular collisions and therefore ensure a redistribution of kinetic energy and a return to equilibrium. Using Ficks law, triple correlations are modeled by a gradient assumption for the double correlations. This reflects the assumption that a spatially non-homogeneous distribution of double correlations is redistributed by molecular collisions modeled by a diffusion process. A second process of production of triple correlations is non-linear transport production mechanism. This requires, that triple correlations are initially not zero and therefore, that the particle velocity distribution is asymmetric from the beginning.

Concerning particles without collisions, the only production mechanism is due to non-linear transport apart from higher order correlations since drag force is a dissipative term. It is therefore questionable, whether a "kinetic" rather than a "collision" mechanism can ensure the redistribution of the double correlations. Numerically this has been tested and compared to the Lagrangian simulation. The comparison is made in fig. 3.20 and done for two spatial resolutions. In the case of the lower resolution (64^3,left column) production effects due to the subgrid model are important and do not allow a detailed analysis. It is possible to see however, that maxima are lower in the case with QBE diffusion. In the right column (spatial resolution 128^3) results are closest to the Lagrangian solution when QBE diffusion is omitted. Spatial structures in QBE are quite close to the Lagrangian simulation and maximum level are comparable for the case of a spatial resolution of 128^3 and omitting QBE diffusion.

3.4 Summary and Outlook

The limiting factor in performing Eulerian-Eulerian simulations seems to be effects of compressibility in certain Stokes number regimes, as can also be seen in the analysis of the Eulerian-Lagrangian results of J.Helie in section 9: On the one hand it puts into question the modeling of the unresolved stresses $\langle \delta u_{p,i} \delta u_{p,j} \rangle_p$ by a pressure-viscosity model and leads to difficulties in the numerical resolution of the number density field.
Compressibility effects occur for Stokes numbers, where the particle relaxation time is small enough to follow the large structures of the carrier flow and to be large enough, so that a certain inertia persists at small scales. Then the Quasi Brownian Motion of particles is insufficient to make the flow "subsonic" and pressure only weakly equilibrates the compressible transport effects.
The different stress tensor models as well as the extension to inertial particles by a subgrid bulk viscosity are questionable for their suitability for the considered simulation. For future tests it would be interesting to consider algebraic stress models, that are capable of handling anisotropic diagonal stresses such as non-linear stress models for RANS computations (Speziale [99],Gatski [34], Pope [76],Taulbee [106]) and which are able to handle

Lagrangian result:

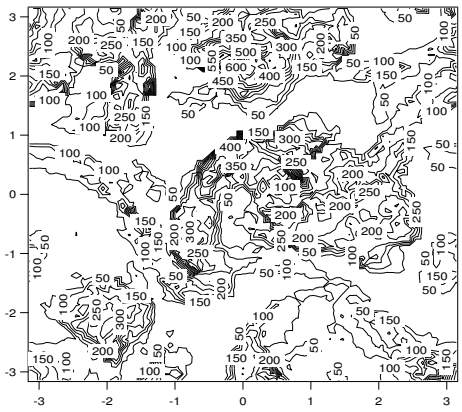

Eulerian simulation without QBE diffusion: $k_{QB} = 0$:

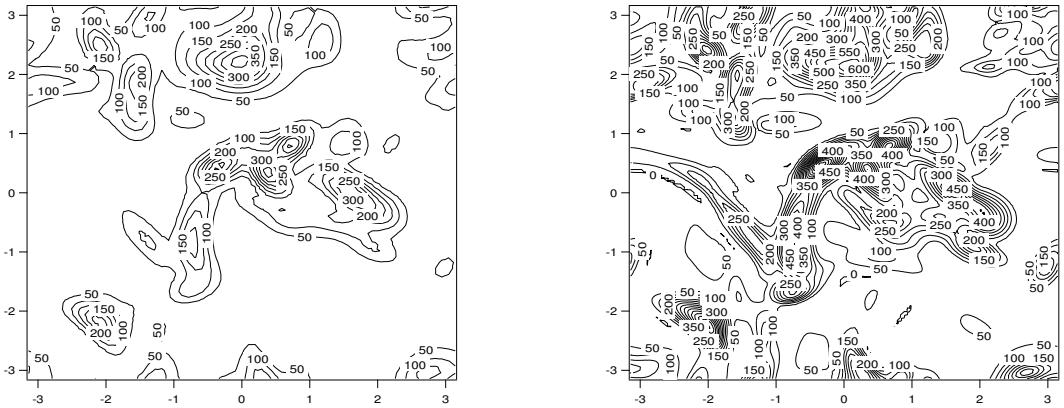

Eulerian simulation with QBE diffusion: $k_{QB} = \frac{5}{3}\tau_p \delta\breve{\theta}_p$

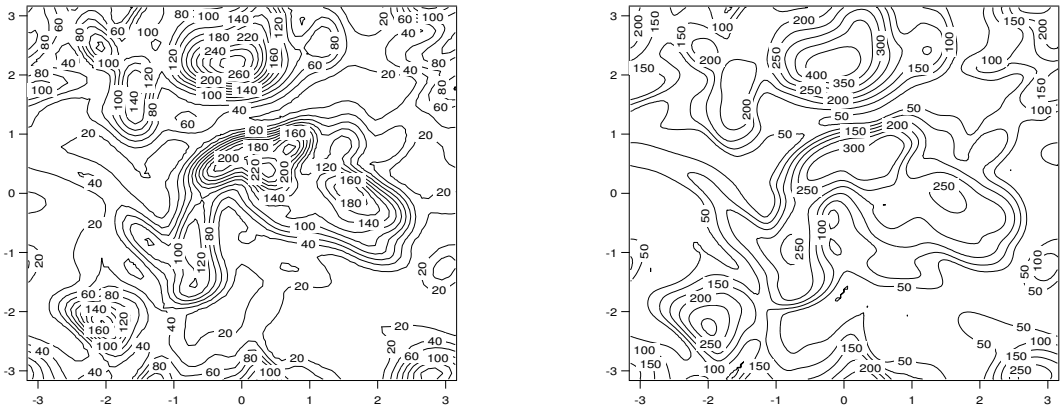

Figure 3.20: Comparison of QBE in two Eulerian computations with different spatial resolution (left column 64^3, right column 128^3). The top graph shows the result of the Lagrangian computation. In the graphs in the middle the diffusion coefficient in the QBE equation was omitted: Without the diffusion coefficient QBE is as expected more localized and forms sharper peeks.

compressibility effects.

Since the Eulerian description of the dispersed phase should be interpreted as a fluid that describes certain properties of the discrete particle phase one can consider modeling as for more exotic fluids such as Reiner-Rivilin fluids [107]. They introduce a natural time scale into the quantities the stress tensor may depend on. A natural time scale for the dispersed phase would be the particle relaxation time. In this case the stress tensor can be a general function of the following arguments: $\left(\tau_p, \breve{n}_p, \breve{S}_{ij}, \delta\breve{\theta}_p\right)$. According to Truesdell, the classical description using the Boussinesque assumption fails, if the characteristic time of the fluid is of the order of the rate of strain or deformation. In such cases the stress tensor requires modeling different from the Boussinesque assumption. In the case of the dispersed phase, this criterion can be expressed by comparing the particle relaxation time to the rate of strain. If the rate of strain in the dispersed phase is comparable to the rate of strain of the carrier phase this fact can easily be expressed in terms of the Stokes number based on the dissipative length scale of the carrier phase. Then, according to the analysis of Truesdell, the classical stress tensor modeling needs to be reviewed.

In the current development of non-Newtonian visco-elastic fluids, such as fluids containing polymers, interesting approaches for the modeling of the stress tensor can be found. Especially the way of including history effects into the stress tensor could be used for the development of a stress tensor, that contains a certain memory of the particle trajectories.

Chapter 4

Application to particle dispersion (Comparison Euler-Lagrange)

The center of this chapter is the comparison between Eulerian and Lagrangian computations. Here the viewpoint is taken that the Lagrangian results reflect the physical behavior of particles in a turbulent carrier phase. The Eulerian equations should, if properly modeled, predict the equivalent physical properties. As previously evoked, in the Eulerian computations the information about every individual particle is lost. Therefore only ensemble (or in this case volume) averaged quantities of the Lagrangian simulation can be compared to the Eulerian results. Here the Lagrangian results were kindly provided by J. Helie and M. Moureau, IMFT. I would like to thank them very much at this point for this fruitfull collaboration. The Lagrangian particle tracking used was briefly presented in the first chapter. A second part of this chapter is devoted to the measurement of particle dispersion.

4.1 Comparison of Eulerian and Lagrangian computations

In this section results of the Eulerian computation are compared to Lagrangian computations. This is done for the two specific cases provided by J. Helie and M. Moureau.
The first case is (HIT1,H). In this case it is not necessary to filter the number density field to perform the numerical computation. In the second case particles are more inertial and only a filtered number density field can be computed. This corresponds to case (HIT1,CJ). Both test cases are defined in sections 2.7 and 2.7.1.
Comparison is done in several steps. In the first step the integral properties introduced in chapter two are compared. In the second step local instantaneous values are compared on cuts of snapshots. At those instantaneous times the spectral development of kinetic energies are than compared to evaluate the modeling of the stress term by a pressure viscosity model.
The Eulerian simulation for the case HIT1,H was performed with the VPM model. For

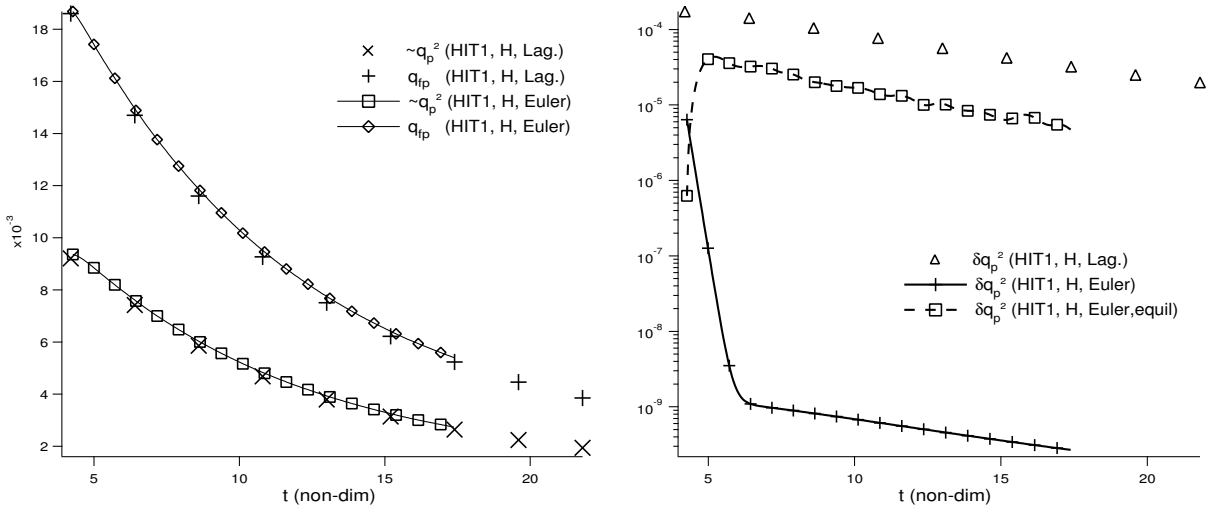

Figure 4.1: Comparison of Lagrangian and Eulerian integral properties in the test case (HIT1, H).

the case of HIT1,CJ the subgrid term was additionally used, such that a filtered number density field is compared to the unfiltered Lagrangian solution.

4.2 Comparison of Lagrangian and Eulerian simulations for tracer like particles

4.2.1 Comparison of integral properties (HIT1,H)

The temporal development of the integral properties of $\breve{q}_p^2, q_{fp}$ and δq_p^2 for the test case (HIT1,H) is shown in Fig. 4.1. Lagrangian results are marked by symbols only and the Eulerian results are marked by lines and symbols.
Concerning fluid-particle correlation and the correlated particle kinetic energy, the two simulations compare rather well. The uncorrelated particle kinetic energy δq_p^2 is however very badly predicted by the Eulerian computation and even the equilibrium assumption shows results far off the Lagrangian results (note the linear-log scale in Fig.4.1 for δq_p^2).
Production of QBE is due to shear in the chosen Eulerian description (VPM, section 3.1.5). Therefore it is assumed, that the lack of production of QBE in the Eulerian simulation is mainly due to badly captured small scale vorticity.
Fig. 4.2 shows the probability density to find a computational cell with a certain particle number density for the Lagrangian and Eulerian computation. The Lagrangian pdf has wider wings than the Eulerian equivalent.

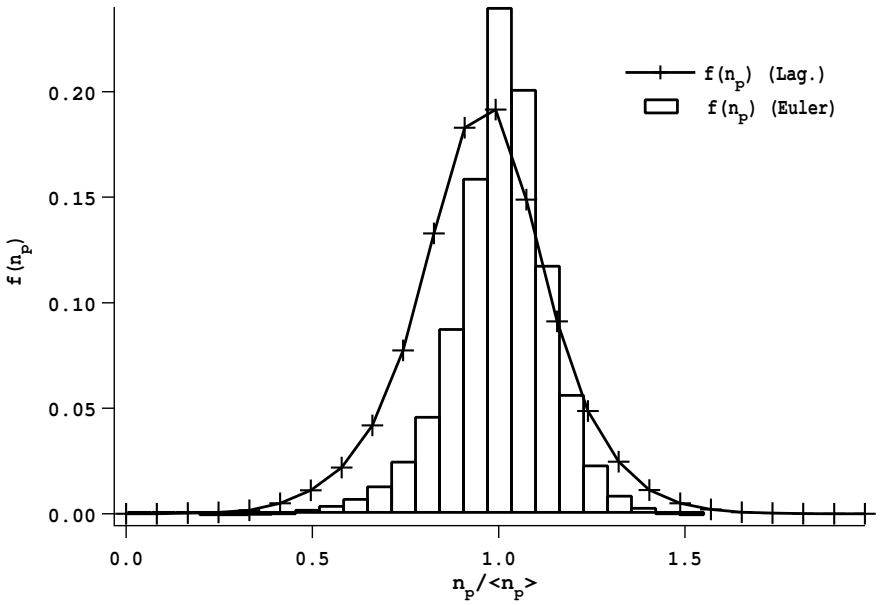

Figure 4.2: Comparison of Lagrangian and Eulerian number density pdf for the test case (HIT1,H) at t=10.8. It shows the probability to find a computational cell with a certain number density.

4.2.2 Comparison of local instantaneous properties (HIT1,H)

Here the local instantaneous number density field and the local instantaneous QBE are selected for comparison. This is done on a cut plane for $z = 0$ in the case of the volume filtered Lagrangian simulation and the Eulerian simulation at $t = 10.8$. In Fig. 4.3 the local instantaneous number densities are compared. The upper graph shows the volume filtered Lagrangian particle number density and the lower graph shows the Eulerian particle number density. Number densities are normalized with respect to their mean value. It can be seen, that the Eulerian simulation does not reproduce the fine small scale structures of the Lagrangian simulation and that the number density field already seems filtered. Extended regions of large and small droplet number densities are however well captured. Fig. 4.4 shows the QB energy at the same cut as the particle number density. Eulerian simulations show structures of QB energy which have a shape comparable to the Lagrangian QBE but are of several magnitudes too small. This puts into question the model used for the QB energy production and the estimation of QB viscosity. An enhanced QB viscosity might on the other hand alter the structure of the small scale mesoscopic velocity. Therefore it is interesting to compare the spectra of the Lagrangian and Eulerian mesoscopic flow field.

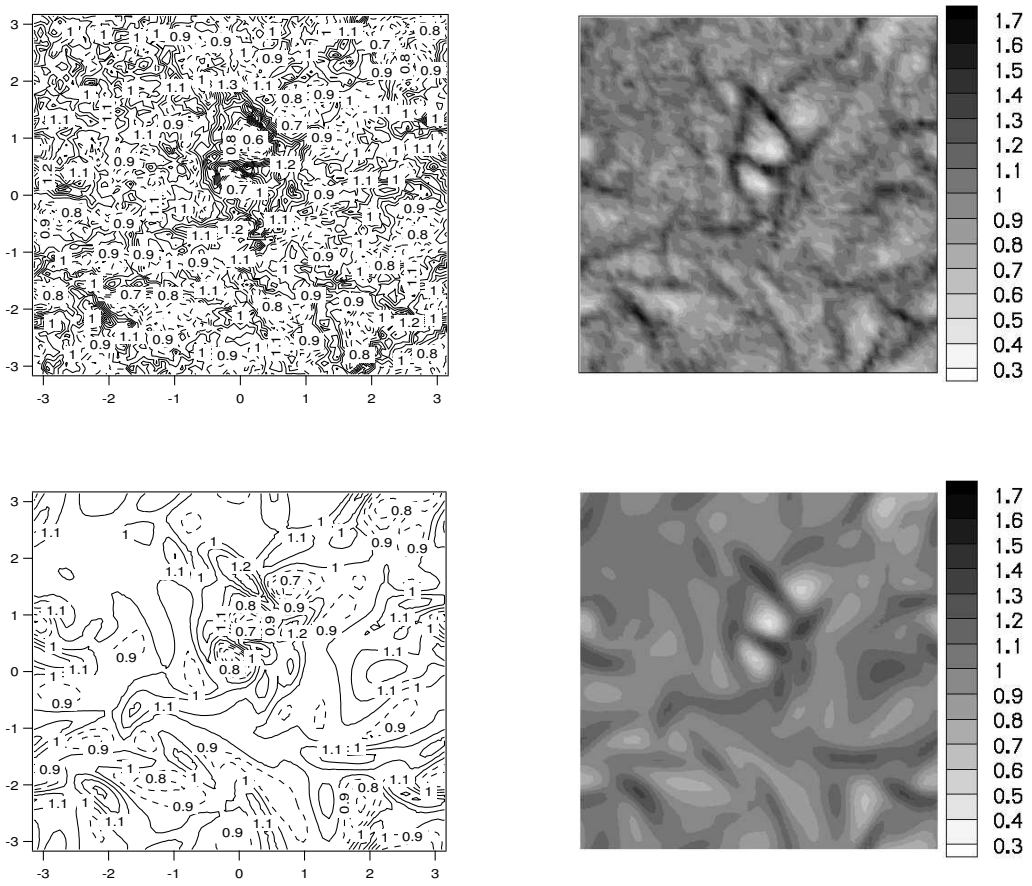

Figure 4.3: Comparison of the normalized droplet number $\check{n}/\langle\check{n}\rangle$ in the Lagrangian computation (upper graph, resolution 64^3) and the Eulerian computation (lower graph, resolution 64^3) at the non-dimensional time t=10.8. The cut plane has been defined a $z = 0$. Values below the mean are indicated by dashed contour lines, values above the mean are indicated by continuous contour lines. The simulation parameters are (HIT1,H)

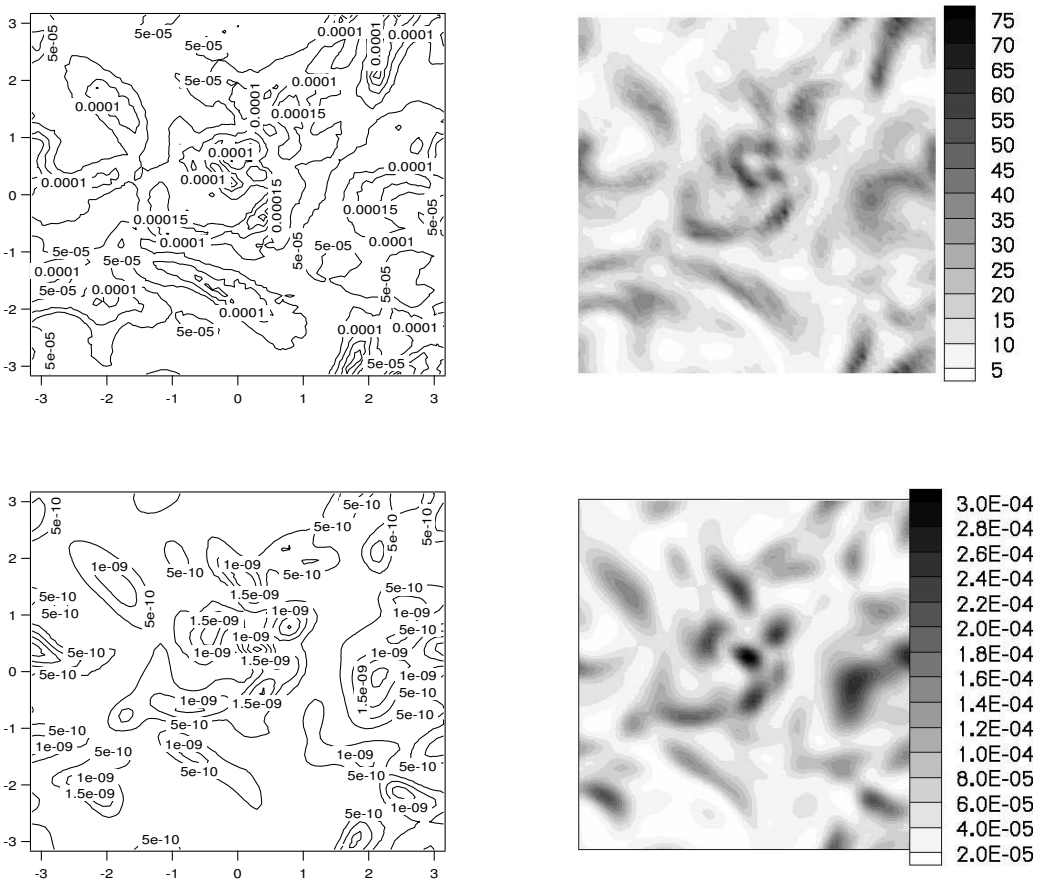

Figure 4.4: Comparison of the Quasi Brownian Energy (QBE) in the Lagrangian computation (upper graph,resolution 64^3) and the Eulerian computation (lower graph,resolution 64^3) at the non-dimensional time t=10.8. The cut plane has been defined a $z = 0$. The simulation parameters are (HIT1, H)

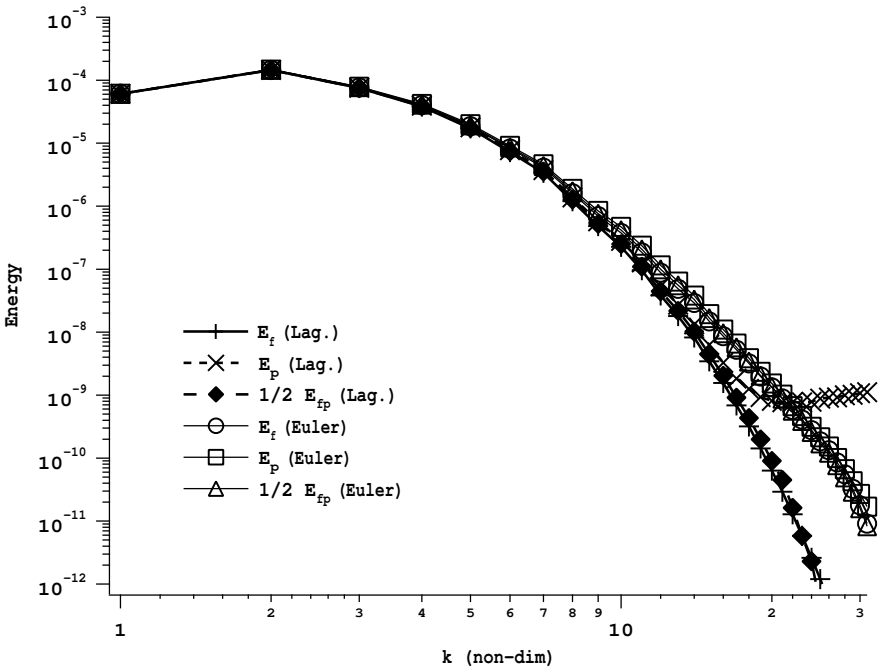

Figure 4.5: Comparison of Lagrangian and Eulerian kinetic energy spectra for the test case (HIT1,H) at t=10.8. Both simulations were performed on a grid with a spatial resolution of 64^3 .

4.2.3 Comparison of spectral properties (HIT1,H)

The spectra of the carrier phase kinetic energy, dispersed phase kinetic energy and the fluid-particle correlation are given in Fig. 4.5. One may remark, that the carrier phase spectra of the Lagrangian simulation and the Eulerian simulation do not coincide. The spectrum of the carrier phase resolved by the NTMIX code with a 6th order spectral like scheme drops more rapidly than the spectrum of the AVBP code with a second order central difference scheme. Spatial resolution of both simulations is 64^3. This difference may be due to different numeric schemes and has to be kept in mind while comparing and interpreting the spectra of dispersed phase kinetic energy.
The carrier phase dispersed phase correlation follows closely the spectrum of the carrier phase. Estimation of the "free path length" as done in section 9 shows, that in this case particles should follow the carrier phase dynamics up to a length scale of $\lambda_p = \tau_p v_p = 0.021$. This length scale is 5 times smaller than the Kolmogorov length scale of the carrier phase and the grid spacing chosen for the simulation. Indeed, the carrier phase dispersed phase correlation follows the carrier phase spectrum down to the very smallest length scales resolved.
The dispersed phase spectrum of the mesoscopic velocity field of the Lagrangian simulation follows closely the spectrum of the carrier phase up to a certain point, where it changes

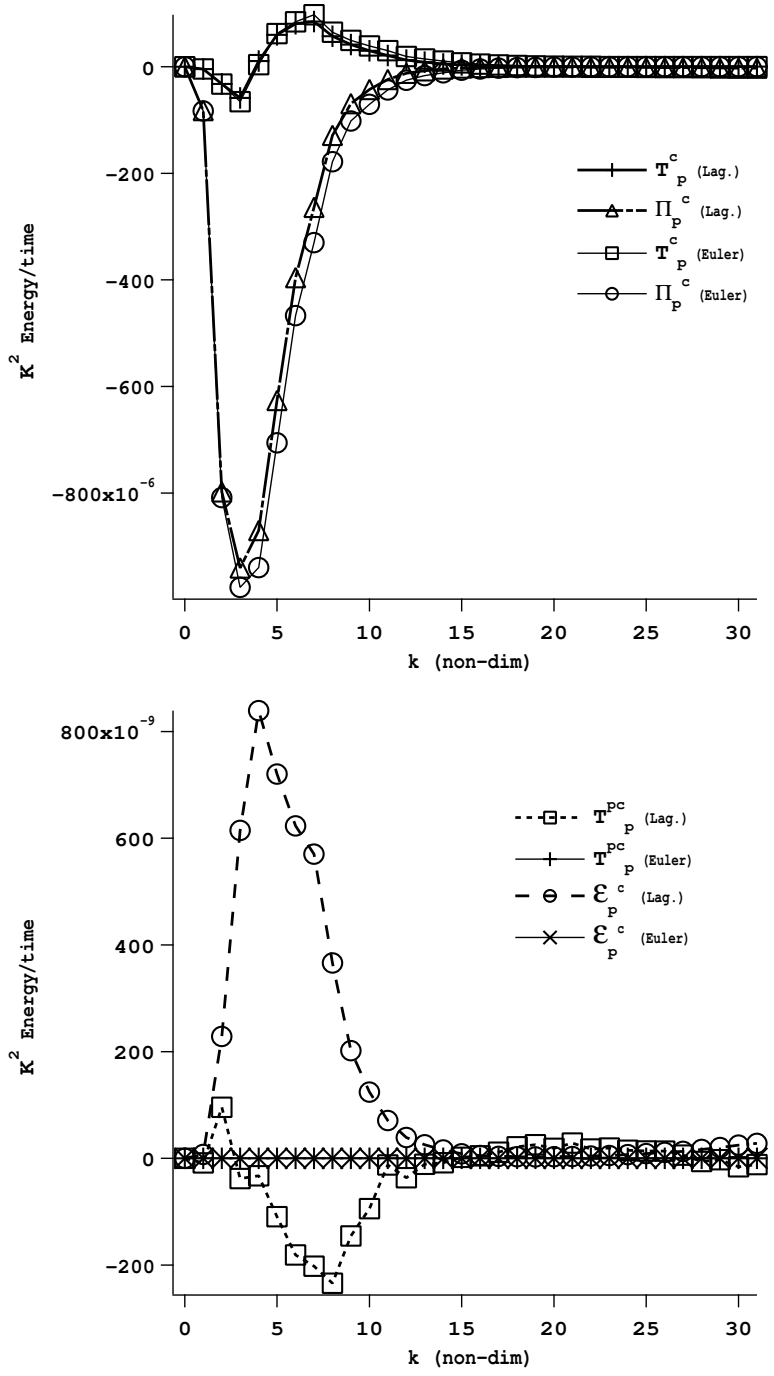

Figure 4.6: Comparison of the temporal development of spectral kinetic energy of the dispersed phase between the Lagrangian computation and the Eulerian computation. The simulation parameters are (HIT1, H). The upper graph shows the nonlinear transfer term and the drag force term. The lower graph shows the redistribution due to QB pressure and QB dissipation.

drastically from the carrier phase. This behavior was already observed in the presentation of the test case (HIT1,CJ) in section 2.7.2. The Eulerian simulation of the mesoscopic velocity field does not reproduce the carrier phase spectrum. Therefore a mechanism that transports kinetic energy to small scales seems to be lacking in the case of the Eulerian simulations. In order to analyze this further, the different transport terms for the temporal development of spectral kinetic energy are compared.
Fig. 4.6 shows the different terms for the temporal development of spectral kinetic energy for the dispersed phase. In the upper graph the transport term and the drag force term of the Lagrangian and Eulerian simulations are compared. Whereas the Lagrangian and Eulerian values of the transport term almost superpose, the drag force term shows slight differences and seems more dissipative in the Eulerian simulation. This transport term is however the consequence of the spectrum of fluid-particle correlation and the dispersed phase kinetic energy spectrum $(1/\tau_p(E_{fp}(\kappa) - E_p(\kappa)))$ and can therefore not be blamed for excessive dissipation of correlated particle kinetic energy in the small scales.
The lower graph in Fig. 4.6 shows the contribution of QB pressure and QB dissipation to the development of the spectrum. Since the values of QBE are of magnitudes too low in this simulation such effects are quasi inexistent in the Eulerian simulation. One remarks however, that both, QB pressure and QB dissipation, dissipate correlated particle kinetic energy in the range of large to medium scales.
In the next step the analysis is extended to the compressible part of the mesoscopic velocity field in order to explain the differences in the particle number density field. Fig. 4.7 shows the dispersed phase kinetic energy spectrum as well as the compressible part of the carrier phase kinetic energy and the compressible part of the dispersed phase kinetic energy for the Lagrangian and the Eulerian simulation. The compressible part of the carrier phase kinetic energy is in both simulations significantly lower than the dispersed phase kinetic energy. The compressible kinetic energy of the dispersed phase of the Lagrangian and the Eulerian simulation are almost identical up to a wave number of 13. At this scale the compressible kinetic energy of the dispersed phase admits a kink in the Lagrangian simulation and flattens of in the Eulerian simulation. This can partially explain the difference in the number density field that captures well the large structures in the Eulerian simulation but not the small scale structures of the Lagrangian simulation.
In order to explain this phenomena the temporal development of the compressible kinetic energy is more closely examined. Fig. 4.8 shows the transport and drag force term of the temporal development of the compressible kinetic energy of the dispersed phase in the upper graph. Contributions due to QB pressure and QB dissipations are shown in the lower graph. First it can be remarked that the production of the transport term is slightly larger in the case of the Eulerian simulation compared to the Lagrangian simulation at large scales. On the other hand the dissipation of compressible kinetic energy due to particle drag is also slightly larger in the Eulerian simulation and compensates partially the surplus of production by the transport term. It is also interesting to note that the term due to particle drag is more dissipative a small scales than the corresponding Eulerian term. This is consistent with the fact that the compressible part of the particle kinetic energy in the Eulerian simulation is smaller than the Lagrangian simulation (Fig. 4.7) since the

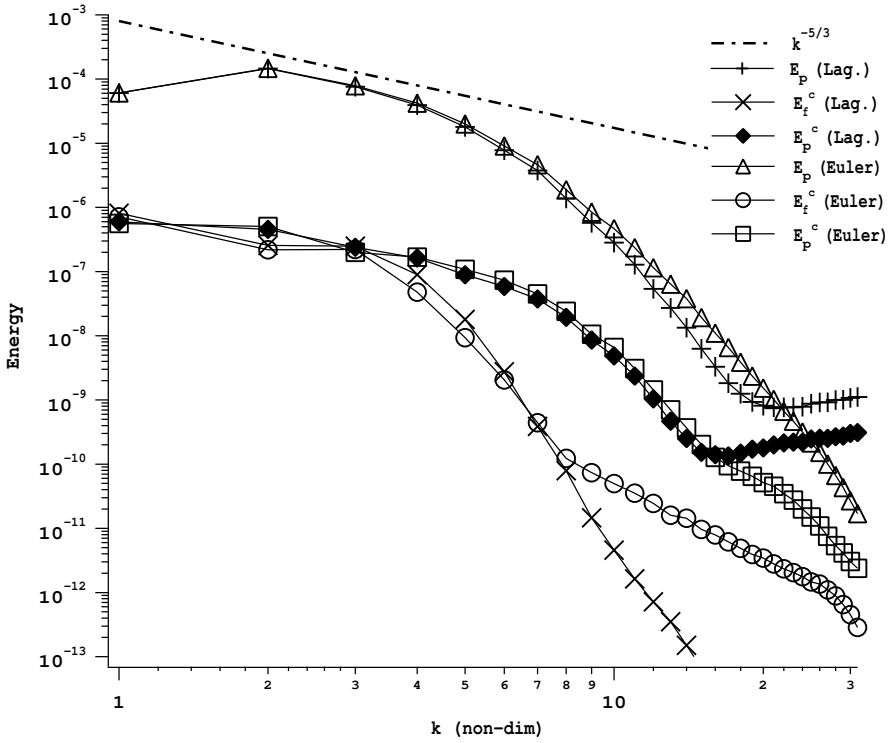

Figure 4.7: Comparison of Lagrangian and Eulerian kinetic energy spectra for the test case (HIT1,H) at t=10.8.

contribution due to drag force is of the form $-1/\tau_p E_p^c(\kappa)$. The contributions due to QB pressure and QB dissipation are inexistent compared to the Lagrangian contributions due to the low QB energy.

4.3 Comparison of Lagrangian and Eulerian simulations for inertial particles

In this section the Eulerian and Lagrangian simulations with of the test case HIT1,CJ are compared. This corresponds to more inertial particles than in the case HIT1,H. Since this test case is placed in a region of maximal segregation, the number density field can only be resolved when filtered and the subgrid term introduced in section 3.3 needs to be applied. In this section first the results of the Eulerian simulations are compared to the results of the Lagrangian simulation. In order to quantify the effect of filtering the number density field, the filter obtained in section 3.3.2 is applied to the Lagrangian instantaneous solutions and those are then post-processed. The filtered Lagrangian results are compared then to the Eulerian and unfiltered Lagrangian results.

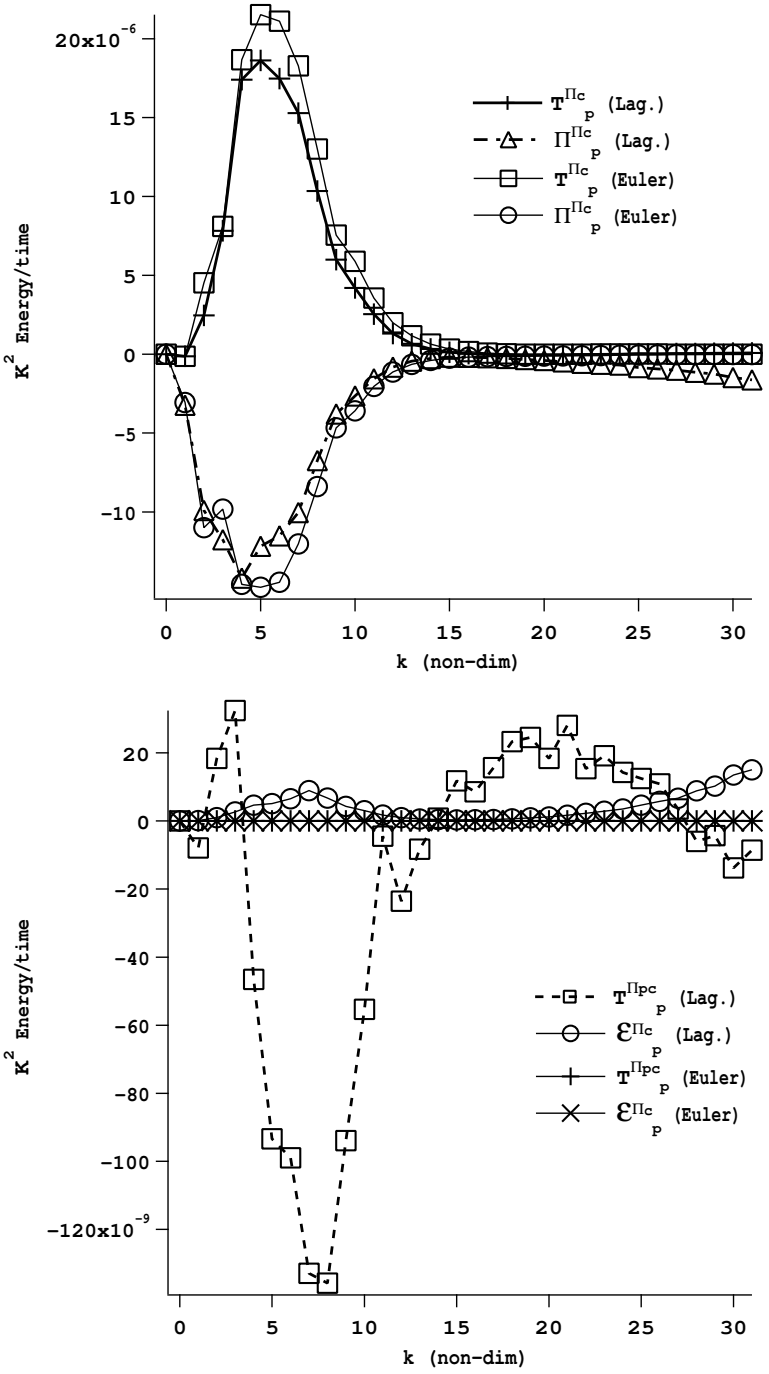

Figure 4.8: Comparison of the temporal development of the compressible spectral kinetic energy of the dispersed phase between the Lagrangian computation and the Eulerian computation. The simulation parameters are (HIT1, H). The upper graph shows the nonlinear transfer term and the drag force term. The lower graph shows the redistribution due to QB pressure and QB dissipation.

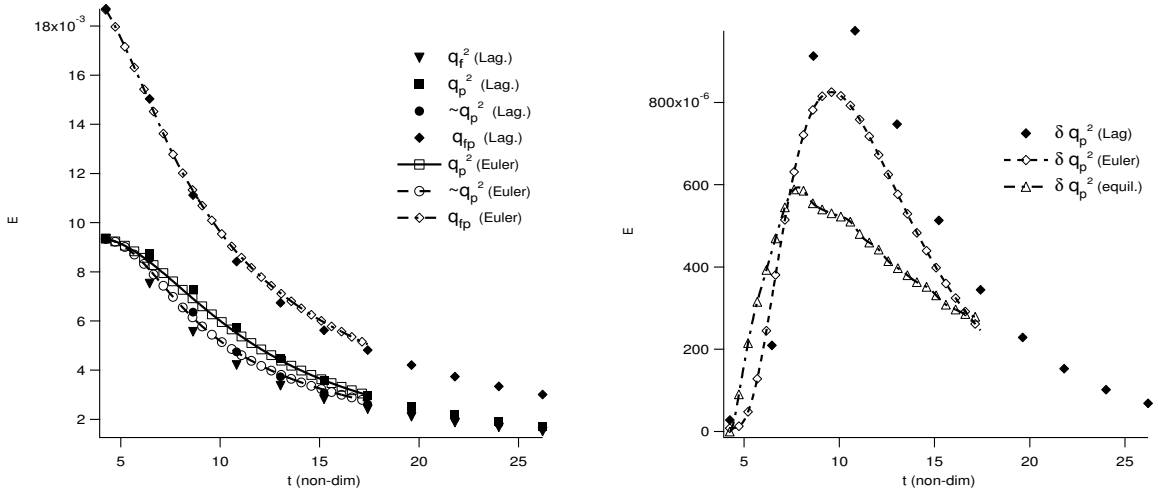

Figure 4.9: Comparison of Lagrangian and Eulerian integral properties in the test case (HIT1, CJ).

4.3.1 Comparison of integral properties (HIT1,CJ)

The integral properties $q_p^2, \breve{q}_p^2, q_{fp}$ and $\delta\breve{\theta}_p$ for the test case HIT1,CJ are shown in Fig. 4.9. All those global values are well predicted by the Eulerian computation compared to the Lagrangian computation. Only the QB energy is slightly smaller than in the Eulerian case compared to the Lagrangian case.

The number density distribution is shown in Fig. 4.10. As in the case of less inertial particles the distribution is less wide in the Eulerian simulation. Furthermore the Lagrangian simulation admits computational cells without particles. This is not the case in the Eulerian simulation. When the particle number density reaches zero, this leads to a difficulty in the definition of the number density pondered quantities. The Lagrangian simulation produces a number density distribution that resembles a Poisson distribution. This is not exactly the case for the Eulerian simulation. It is pointed out that the Eulerian simulation was performed with a filtered number density field. Therefore it is natural for the Eulerian distribution to be less wide than the Eulerian distribution.

4.3.2 Comparison of local instantaneous properties (HIT1,CJ)

Here the local instantaneous properties of the Eulerian and Lagrangian simulation are compared. Fig. 4.11 shows the local instantaneous droplet number on the $z = 0$ cut plane at $t = 10.8$. The upper graph corresponds to the Lagrangian simulation and the lower graph corresponds to the Eulerian simulation. Since the Eulerian droplet number corresponds to a filtered droplet number, it does not admit the strong variations of the Lagrangian particle number density field. The large scale structures are nevertheless well

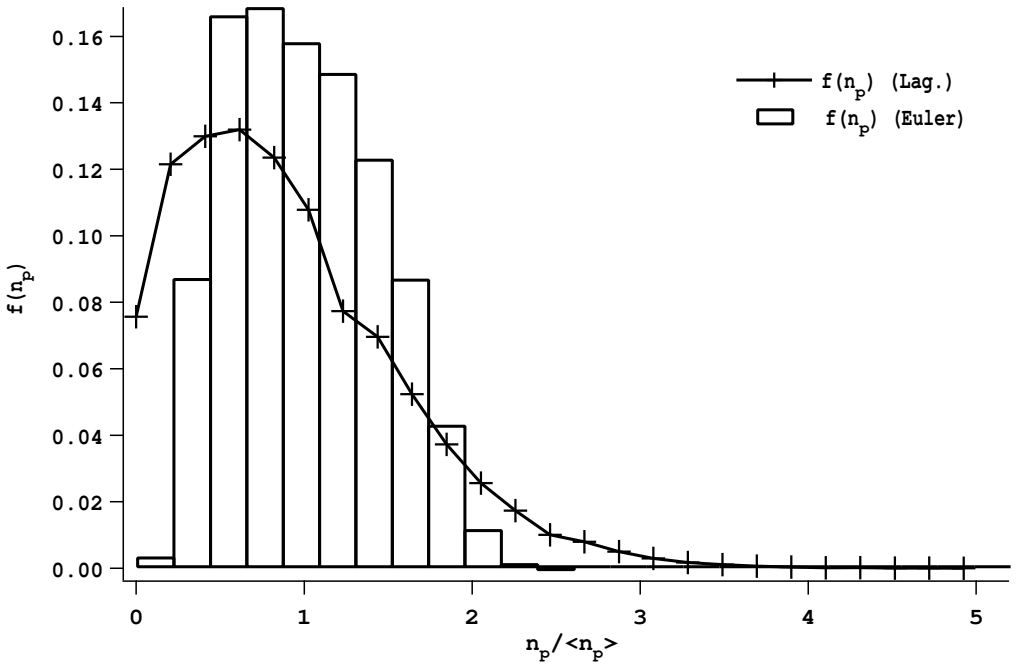

Figure 4.10: Comparison of Lagrangian and Eulerian number density pdf for the test case (HIT1,CJ) at t=10.8. It shows the probability to find a computational cell with a certain number density.

represented in the Eulerian simulation.
In Fig. 4.12 the Quasi Brownian energy of the Lagrangian and Eulerian simulation is compared at $t = 10.8$. The upper graph represents the Lagrangian QBE and the lower graph the Eulerian QBE. Comparison shows, that the structures of QBE and their value are well predicted by the Eulerian simulation.

4.3.3 Subgrid pressure

In Fig. 4.14 the QBP from the Lagrangian computation is compared to the subgrid pressure in the Eulerian computation that leads to filtered number density field. This subgrid pressure has to be larger than the QBP from the Lagrangian computation to diminish the compressible velocity component of dispersed phase velocity. Qualitatively it is clear that the subgrid pressure acts in regions where QBP is high as well. This is in accordance to the idea that compression leads to an increase in QBE.

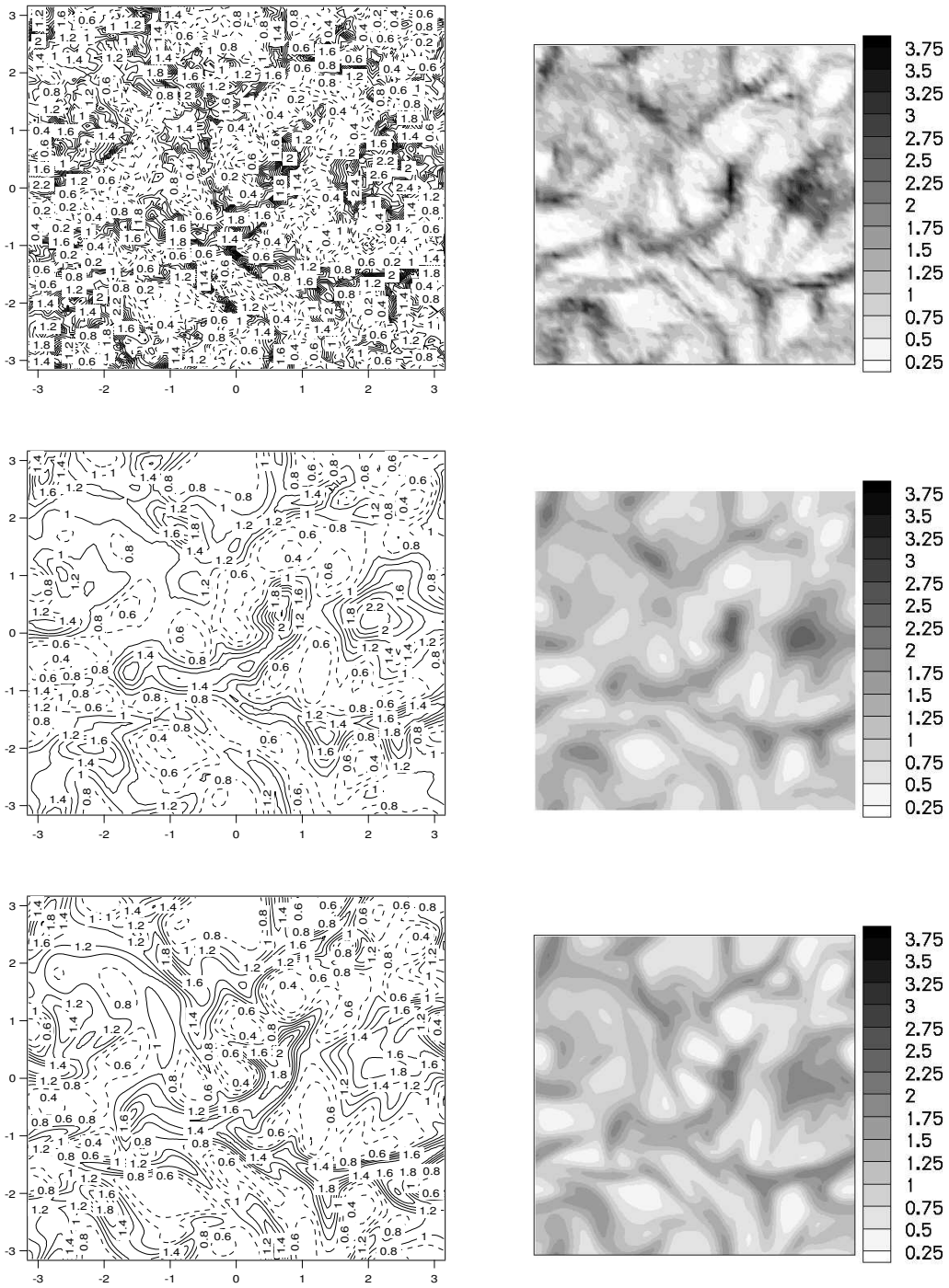

Figure 4.11: Comparison of the normalized droplet number $\check{n}_p/\langle\check{n}_p\rangle$ in the Lagrangian computation (upper graph, resolution 64^3), the filtered Lagrangian computation (middle graph, resolution 64^3) and the Eulerian computation (lower graph, resolution 128^3) after one particle relaxation time (t=10.8). The cut plane has been defined a $z = 0$. Values below the mean are indicated by dashed contour lines, values above the mean are indicated by continuous contour lines. Simulation parameters are (HIT1,CJ)

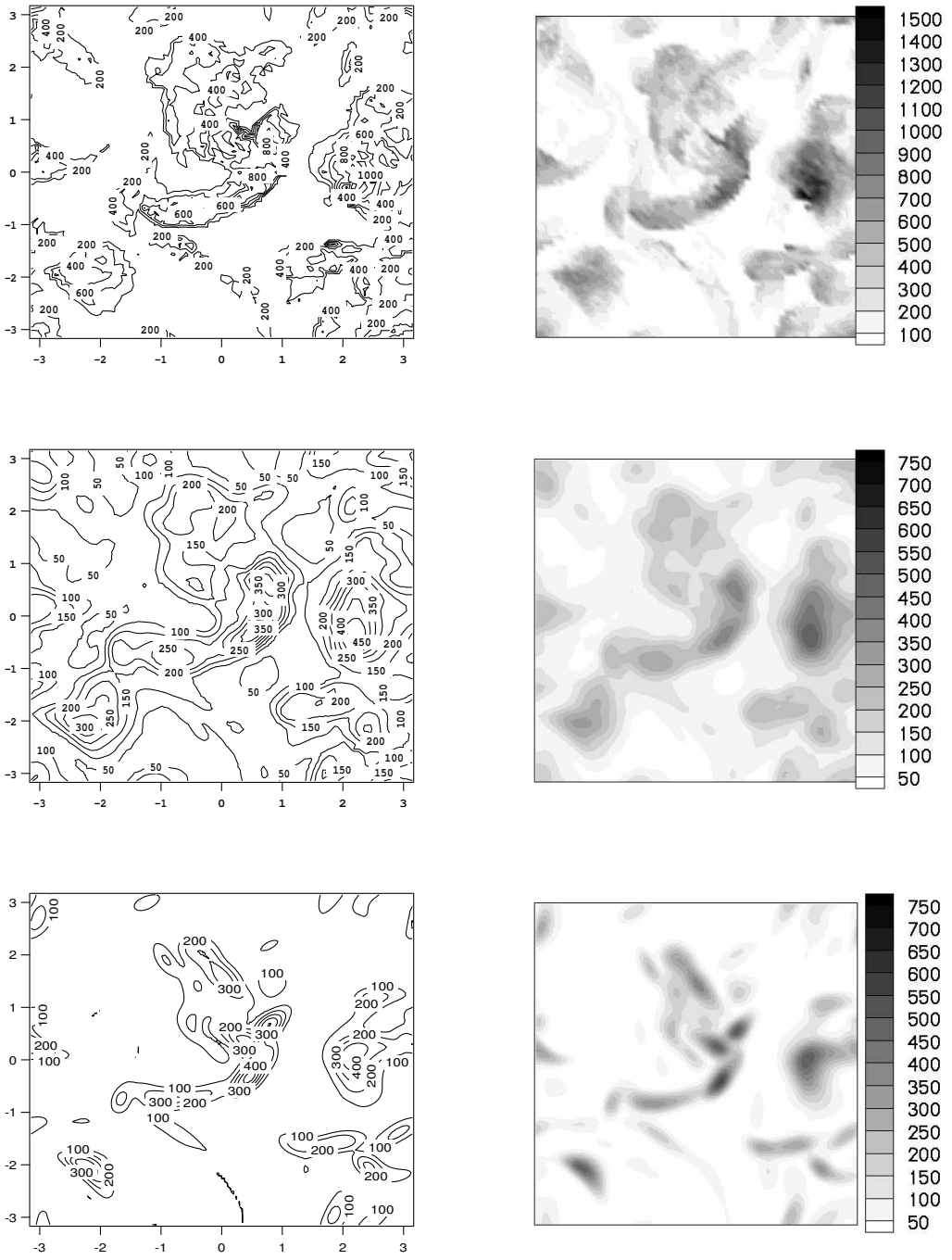

Figure 4.12: Comparison of the Quasi Brownian Energy ($\delta\breve{\theta}_p$) in the Lagrangian computation (upper graph,resolution 64^3) the filtered Lagrangian computation, (middle graph,resolution 64^3) and the Eulerian computation (lower graph,resolution 128^3)after one particle relaxation time (t=10.8) . The cut plane has been defined a $z = 0$. Simulation parameters are (HIT1,CJ)

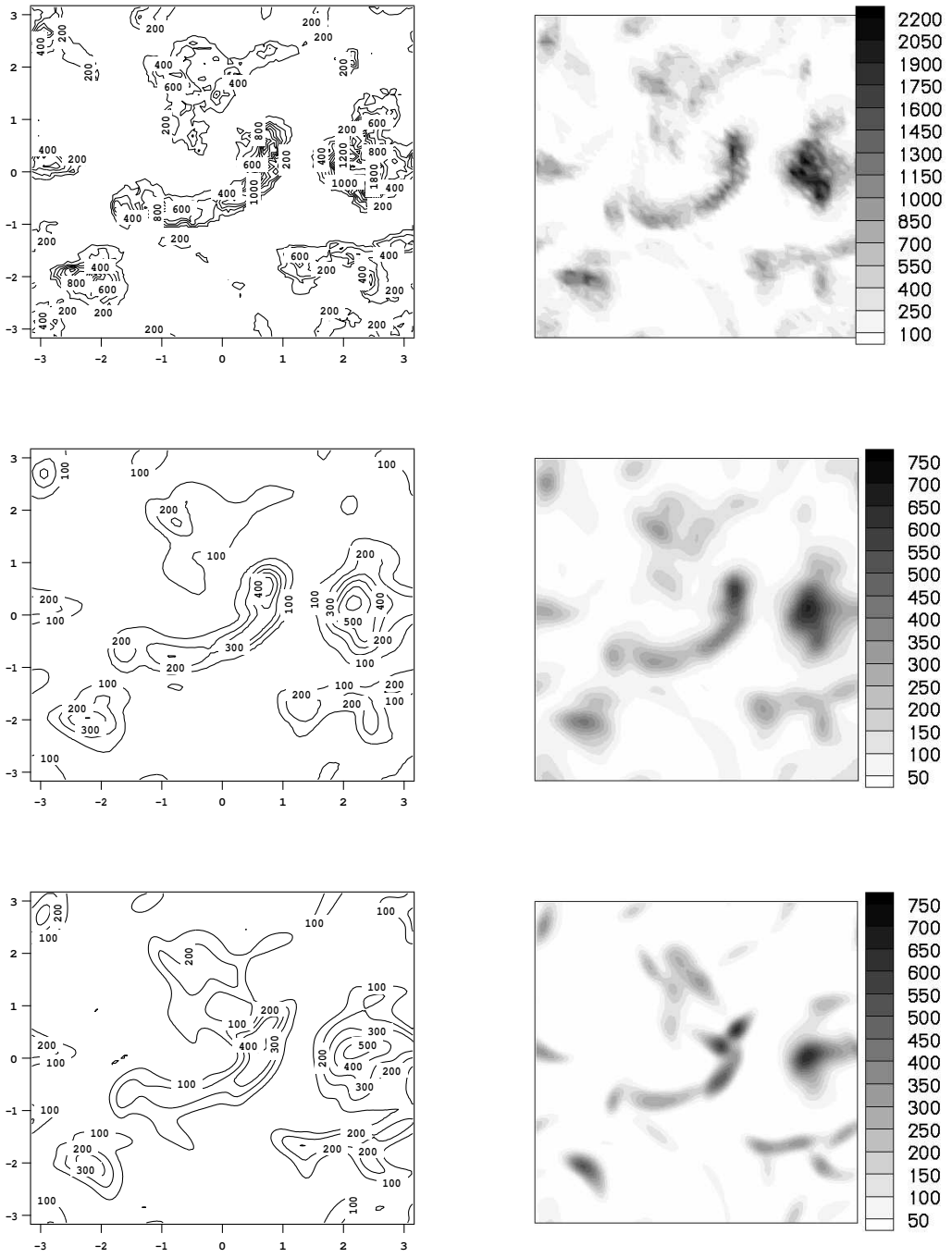

Figure 4.13: Comparison of the Quasi Brownian Pressure ($2/3\check{n}_p\delta\breve{\theta}_p$) in the Lagrangian computation (upper graph,resolution 64^3) the filtered Lagrangian computation, (middle graph,resolution 64^3) and the Eulerian computation (lower graph,resolution 128^3)after one particle relaxation time (t=10.8) . The cut plane has been defined a $z = 0$. Simulation parameters are (HIT1,CJ)

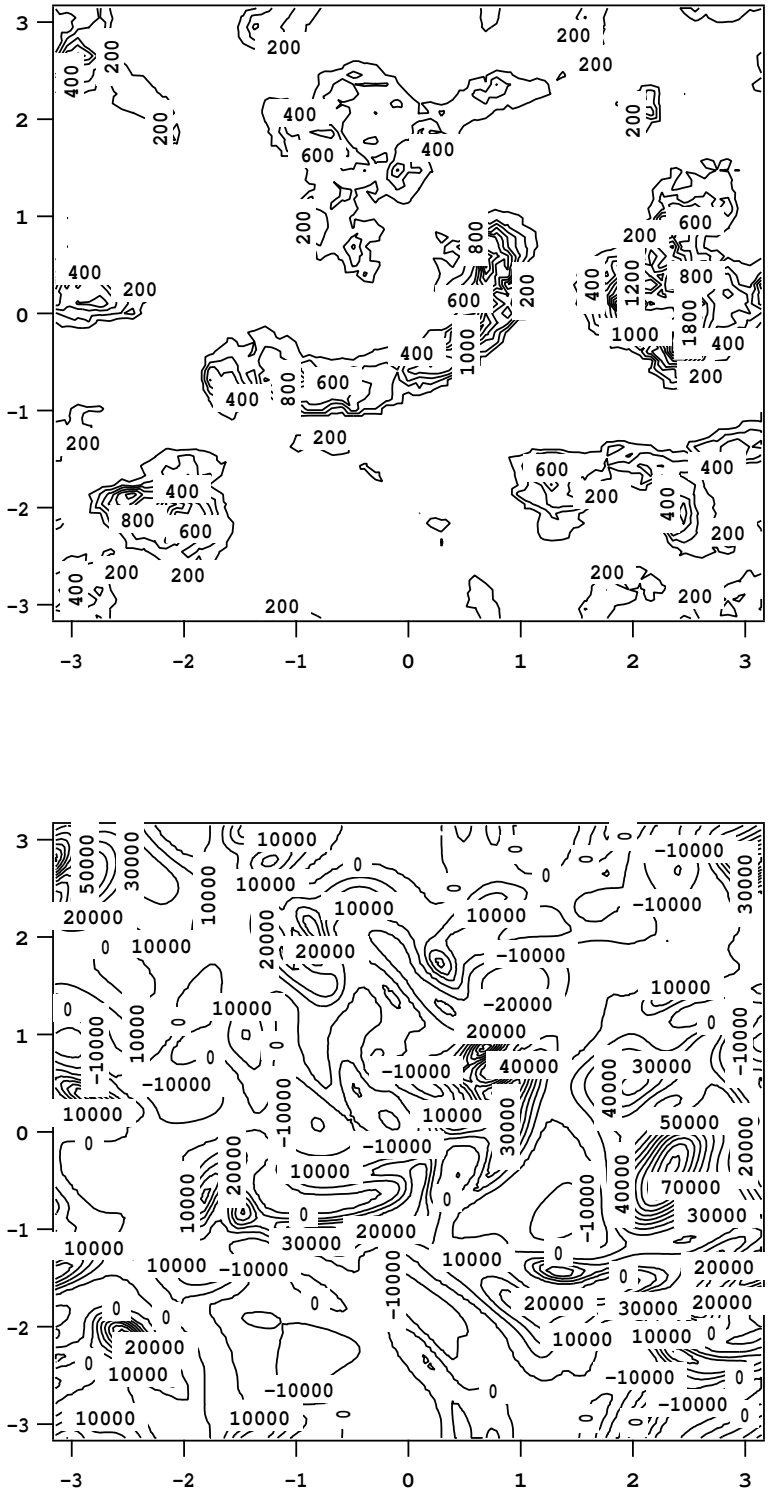

Figure 4.14: Comparison of subgrid pressure in the lower graph to the QBP in the Lagrangian computation upper graph.

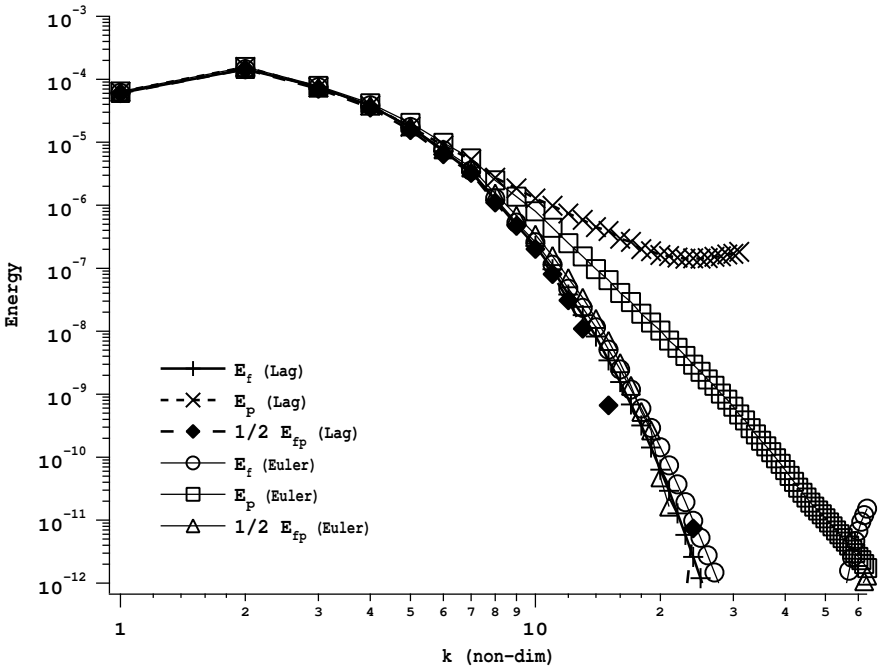

Figure 4.15: Comparison of Lagrangian and Eulerian kinetic energy spectra for the test case (HIT1,CJ) at t=10.8.

4.3.4 Comparison of spectral properties (HIT1,CJ)

Fig. 4.15 shows the kinetic energy spectra of the carrier phase, dispersed phase and fluid particle correlation in the test case (HIT,CJ) at t=10.8. The Eulerian computation was performed on a 128^3 grid and the Lagrangian computation on a 64^3 grid. Carrier phase kinetic energy spectra of the Eulerian and Lagrangian computation coincide at almost all wave numbers. Fluid particle correlation drops more rapidly in the Lagrangian case than in the Eulerian case if going to larger wave numbers. Correlated dispersed phase kinetic energy of the Eulerian simulation compares well to the Lagrangian simulations at small wave numbers. At large wave numbers the Eulerian description admits significantly less kinetic energy than the Lagrangian equivalent. One has to keep in mind that the Eulerian simulation was obtained by a set of equations, that was filtered for the number density. This may influence the small scale kinetic energy.
In order to investigate this energy behavior, the different terms of the temporal development of the particle kinetic energy are investigated. In the Eulerian simulation a subgrid term was however applied to the dispersed phase momentum equation. Using the definition of the subgrid term as a subgrid pressure (eq. 3.45) one can define the contribution of the subgrid term to the kinetic energy transport by analogy to the pressure term in dispersed

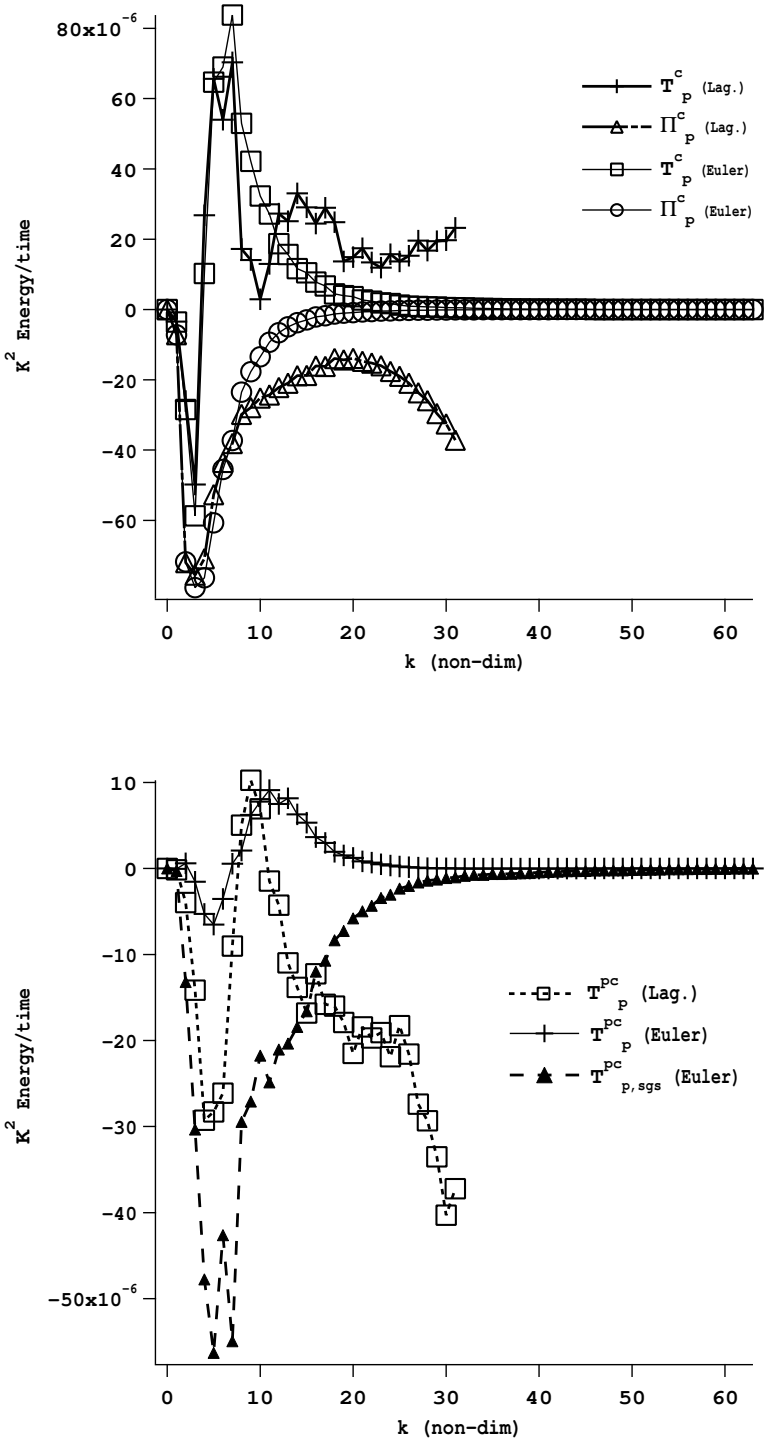

Figure 4.16: Comparison of the temporal development of spectral kinetic energy of the dispersed phase between the Lagrangian computation and the Eulerian computation. The simulation parameters are (HIT1, CJ). The upper graph shows the nonlinear transfer term and the drag force term. The lower graph shows the redistribution due to QB pressure and QB dissipation.

phase momentum equation (eqs. 2.104,2.110).

$$\hat{Q}_{i,sgs}\left(\boldsymbol{\kappa}\right) = \mathcal{F}_{\boldsymbol{\kappa}}\left\{\frac{1}{\breve{n}_p}\frac{\partial}{\partial x_i}P_{sgs}\right\} \tag{4.1}$$

$$\hat{T}^{pc}_{p,sgs}\left(\boldsymbol{\kappa}\right) = -\frac{1}{2}\left(\hat{u}_{p,i}(\boldsymbol{\kappa})\hat{Q}^{*}_{i,sgs}(\boldsymbol{\kappa}) + \hat{u}^{*}_{p,i}(\boldsymbol{\kappa})\hat{Q}_{i,sgs}(\boldsymbol{\kappa})\right) \tag{4.2}$$

Then, the resulting total transport equation of the Eulerian dispersed phase kinetic energy is:

$$\frac{\partial}{\partial t}E_p(\boldsymbol{\kappa}) - \hat{T}^{c}_{p}(\boldsymbol{\kappa}) - \hat{T}^{pc}_{p}(\boldsymbol{\kappa}) - \hat{T}^{pc}_{p,sgs}(\boldsymbol{\kappa}) + \hat{\mathcal{E}}^{c}_{p}(\boldsymbol{\kappa}) - \hat{D}_p(\boldsymbol{\kappa}) = 0 \tag{4.3}$$

The temporal development of the different terms of the transport equation is shown in Fig. 4.16. The upper graph shows the contributions of transport and drag force for the Eulerian and Lagrangian computation. The Eulerian transport term represents acceptably the Lagrangian transport at very low wave numbers. At larger wave numbers the Eulerian contribution levels off, whereas the Lagrangian contribution remains important. The contribution of the drag force term shows a similar behavior. At small wave numbers contributions are comparable and then the dissipative contribution of the Eulerian simulation is much smaller than the Lagrangian contribution.
The lower graph shows the contribution of the QB pressure in the Lagrangian case and the QB pressure and the subgrid pressure in the Eulerian simulation. The QB pressure has the same tendency as the Lagrangian contribution for small wave numbers but not the same magnitude. The contribution of the subgrid pressure term is by far more important than the contribution of QB pressure in this simulation.

The Eulerian simulation reflects the behavior of the dispersed phase at small wave numbers and therefore at large scales, but fails to show the same behavior at large wave numbers.

The subgrid Pressure was introduced to obtain a filtered number density field by acting on the compressible part of the mesoscopic velocity field. The compressible spectra of the carrier and dispersed phase are shown in Fig. 4.17. Compressible components of the carrier phase are almost identical in the Lagrangian and Eulerian simulation. The compressible component of the dispersed phase kinetic energy is however only comparable to the Lagrangian simulation at small wave numbers. At larger wave numbers the subgrid contribution diminishes the compressible kinetic energy.
Furthermore it is interesting to investigate the contribution of the subgrid term to the temporal development of compressible particle kinetic energy. In analogy to the temporal development of the dispersed phase kinetic energy, the contribution of the subgrid pressure to the temporal development of the compressible kinetic energy is defined by:

$$\hat{T}^{\hat{\Pi}pc}_{p,sgs}\left(\boldsymbol{\kappa}\right) = -\frac{1}{2}\left(\hat{u}^{c}_{p,i}(\boldsymbol{\kappa})\hat{\Pi}_{ij}\hat{Q}^{*}_{j,sgs}(\boldsymbol{\kappa}) + \hat{u}^{c*}_{p,i}(\boldsymbol{\kappa})\hat{\Pi}_{ij}\hat{Q}_{j,sgs}(\boldsymbol{\kappa})\right) \tag{4.4}$$

This leads to the following equation for the temporal development of the compressible kinetic energy:

$$\frac{\partial}{\partial t}E^{c}_{p}\left(\boldsymbol{\kappa}\right) - \hat{T}^{\hat{\Pi}c}_{p}\left(\boldsymbol{\kappa}\right) - \hat{T}^{\hat{\Pi}pc}_{p}\left(\boldsymbol{\kappa}\right) - \hat{T}^{\hat{\Pi}pc}_{p,sgs}\left(\boldsymbol{\kappa}\right) + \hat{\mathcal{E}}^{\hat{\Pi}c}_{p}\left(\boldsymbol{\kappa}\right) - \hat{D}^{\hat{\Pi}c}_{p}\left(\boldsymbol{\kappa}\right) = 0 \tag{4.5}$$

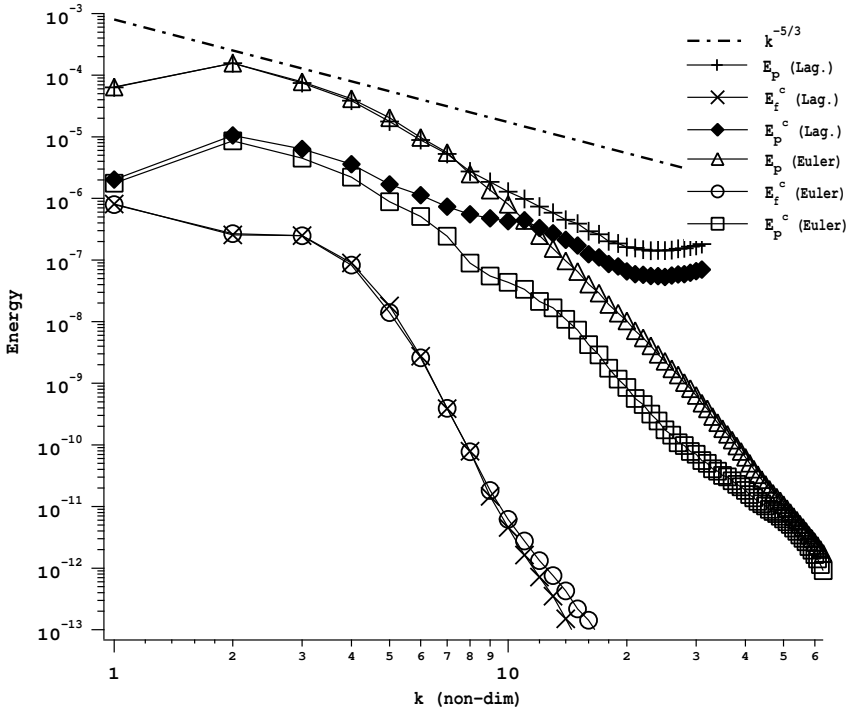

Figure 4.17: Comparison of Lagrangian and Eulerian kinetic energy spectra for the test case (HIT1,CJ) at t=10.8.

Fig. 4.18 shows the different contributions to the temporal development of the compressible kinetic energy. In the upper graph the transport and drag force contributions are compared. Production of compressible energy by the transport term at small wave number is well reproduced by the Eulerian model. At larger wave numbers this production term is absent. The dissipation of compressible energy due to drag is larger in the Lagrangian simulation than the Eulerian simulation. This is due to the larger compressible kinetic energy of the dispersed phase at large wave numbers.
The lower graph shows the contribution of QB pressure in the Eulerian and Lagrangian simulation. The dissipative mechanism of QB pressure for the compressible kinetic energy is not reproduced by either the QB pressure of the Eulerian simulation, its subgrid contribution nor its sum.

Comparison of Lagrangian, Filtered Lagrangian and Eulerian spectral transfer

The spectra of the mesoscopic kinetic energy in the Lagrangian computation, from the Lagrangian results filtered before post-processing and the Eulerian results are shown in figs. 4.19 and 4.20. The kinetic energy of the filtered Lagrangian results is smaller than the kinetic energy of the Lagrangian result since the filtering procedure only retains the filtered velocity. The kinetic energy is however not only significantly smaller at large wave

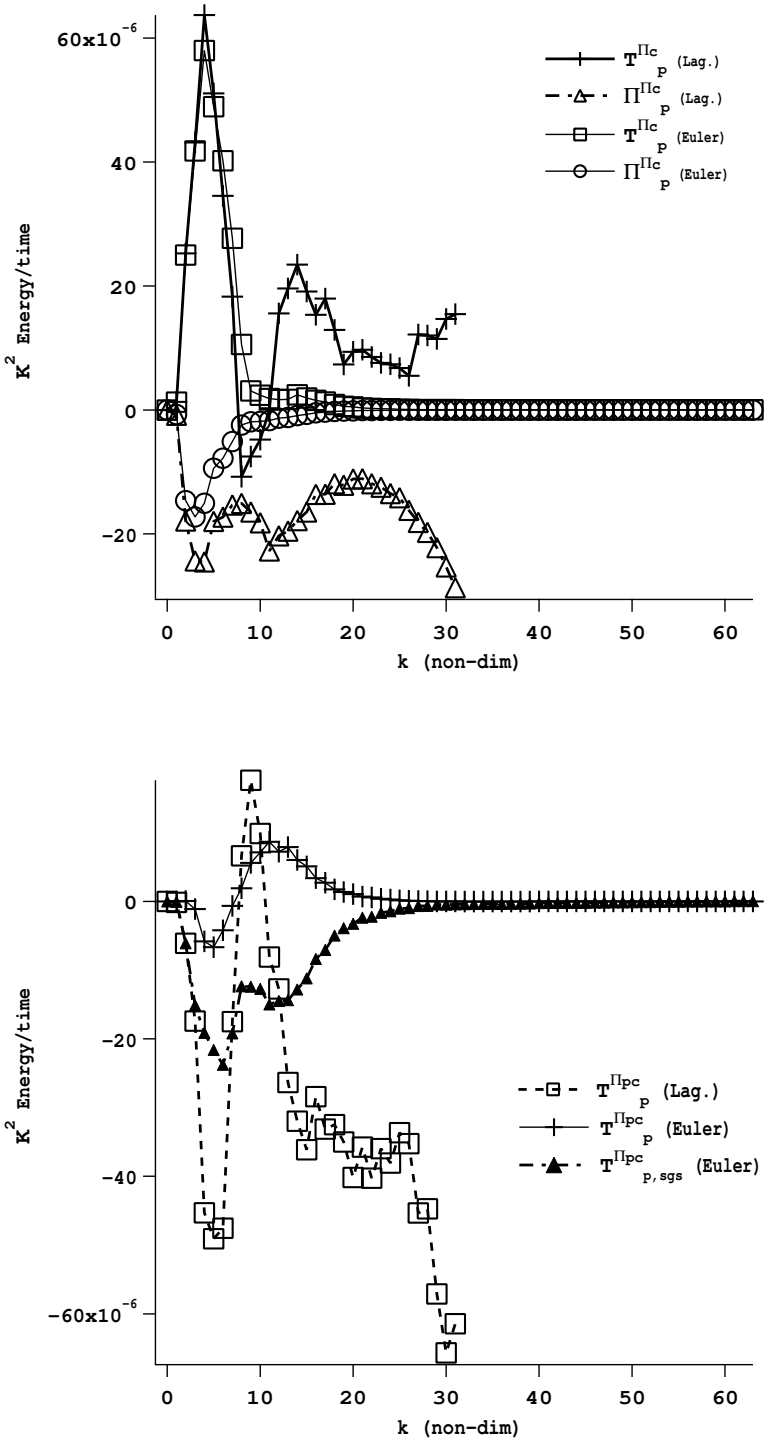

Figure 4.18: Comparison of the temporal development of the compressible spectral kinetic energy of the dispersed phase between the Lagrangian computation and the Eulerian computation. The simulation parameters are (HIT1, CJ). The upper graph shows the nonlinear transfer term and the drag force term. The lower graph shows the redistribution due to QB pressure and QB dissipation.

numbers but also smaller at intermediate wave numbers. The mesoscopic kinetic energy of the Eulerian velocity field is almost identical up to wave numbers of approx. 12 and smaller at larger wave numbers. It is however consistent with the Lagrangian simulation at intermediate wave numbers and coincides with the filtered Lagrangian kinetic energy at large wave numbers.
The compressible component of the Eulerian energy spectrum is closer to the filtered kinetic energy of the Lagrangian simulation than the true Lagrangian simulation. This indicates, that the operator chosen in section 3.3.2 acts principally on the compressible component of the dispersed phase velocity and not on the solenoidal component as small wave numbers. This is confirmed by the solenoidal kinetic energy spectra shown in Fig. 4.20. The solenoidal kinetic energy of the dispersed phase in the Eulerian simulation coincides with the solenoidal kinetic energy of the Lagrangian simulation up to wave numbers of approx. 12.

Fig. 4.21 shows the transfer terms of the carrier-phase dispersed-phase correlation in eq. 2.115. The principal mechanisms of transport, drag and dissipation are comparable in the Lagrangian, filtered Lagrangian and Eulerian simulation. The biggest difference appears in the term related to QBP, which is significantly smaller in the filtered Lagrangian and Eulerian results.

Fig. 4.22 shows the terms of the mesoscopic kinetic energy in eq. 2.114 for the Lagrangian, filtered Lagrangian and Eulerian results. Significant differences between the different results are in the term related to QBP and dissipation. Since the spectral kinetic energy is larger in the Lagrangian computation at large wave numbers, dissipation is also larger at large wave numbers. The mechanisms of transport and drag are well represented at small wave numbers but redistribution of energy to large wave numbers is not well represented in the Eulerian computation.

Fig. 4.23 shows the different terms of the development of the compressible kinetic energy and Fig. 4.24 shows the development of the solenoidal energy. As already observed in the previous graphs, the transport of energy to the small scales is not as well represented in the Eulerian computation than the Lagrangian computation. Furthermore the effects due to dissipation and QBP are not well reflected in the results of the Eulerian computation. If the Eulerian computation is compared to the filtered Lagrangian results, the lack of transport to small scales, smaller QBP effects and the difference in drag force and dissipation are as well observed. Therefore this deficiency can be associated to the filtering in the Eulerian computation. In general, the different terms concerning the development of spectral kinetic energy at large scales are however well represented in the Eulerian simulation.

4.3.5 Summary on the comparison of Euler-Lagrange

The detailed comparison of global and local quantities from the Lagrangian and Eulerian simulation show two results. Large scale motion of particles, large scale structures of particle number density and QBE are well captured by the Eulerian approach. Small scale motion and structures are however not well represented in the Eulerian approach. This is the case for the quantities of droplet number density as well as the correlated small scale

motion of the particles. Especially the small scale "kink" in the dispersed phase spectral kinetic energy is not present in Eulerian simulations. Particle kinetic energy is however larger than the carrier phase kinetic energy showing some inertia effects.

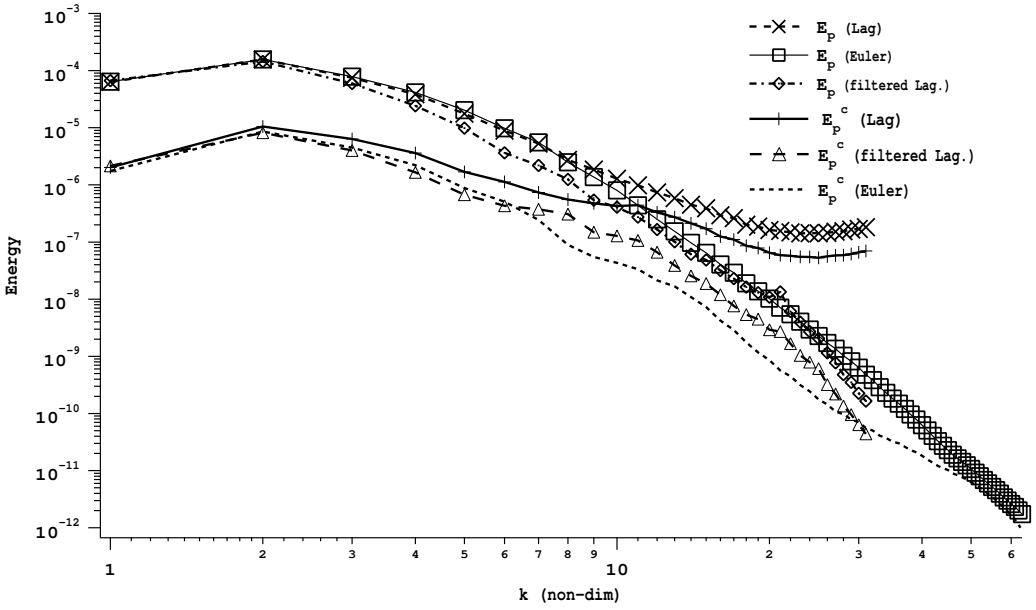

Figure 4.19: Total and compressible kinetic energy for the test case (HIT 1,CJ) in the Lagrangian, filtered Lagrangian and Eulerian computation.

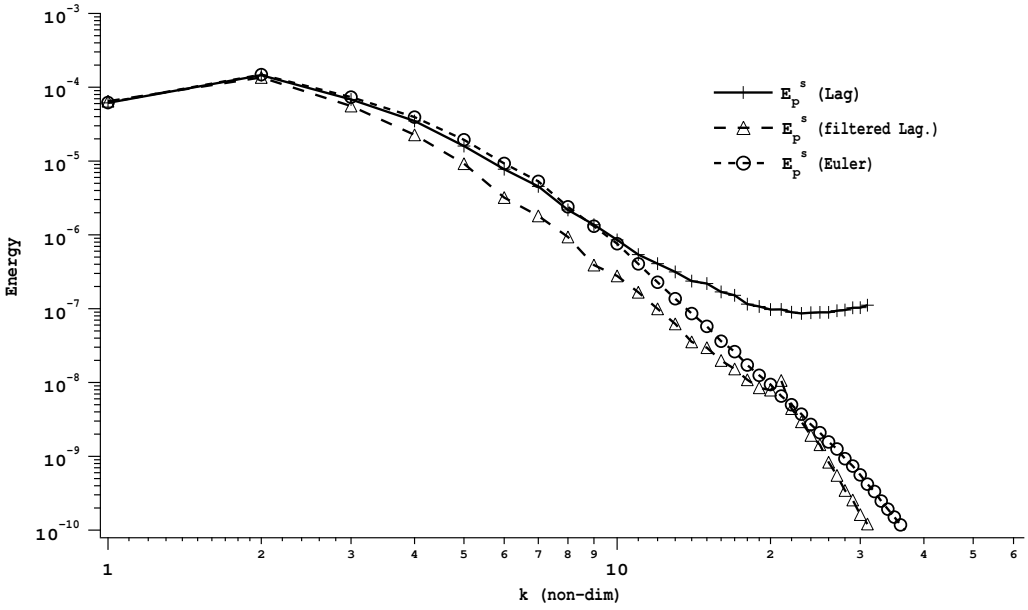

Figure 4.20: Solenoidal kinetic energy for the test case (HIT 1,CJ) in the Lagrangian, filtered Lagrangian and Eulerian computation.

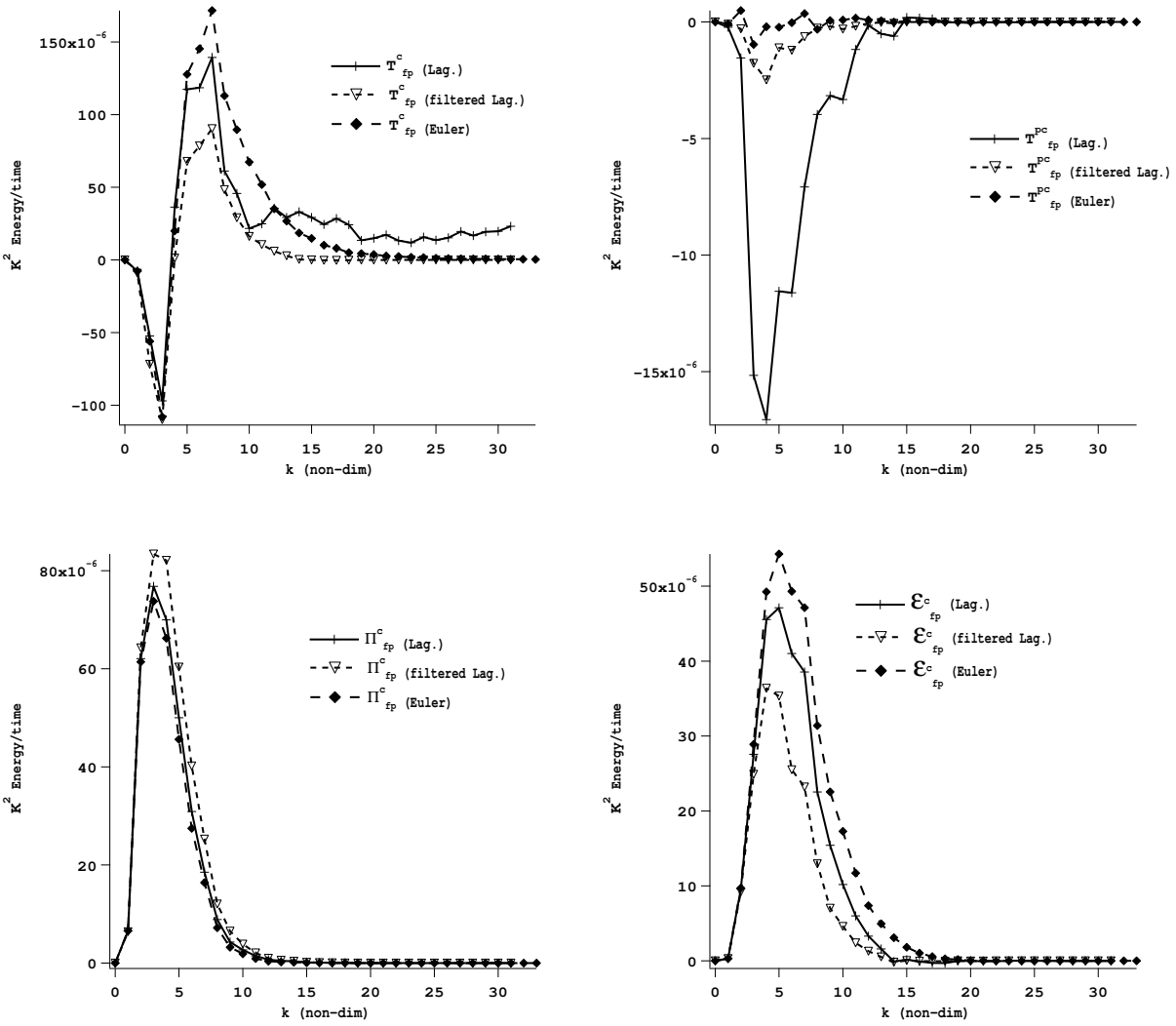

Figure 4.21: Comparison of the carrier phase dispersed phase correlation transport terms in Lagrangian, filtered Lagrangian and Eulerian computation for the test case (HIT1,CJ) at t=10.8.

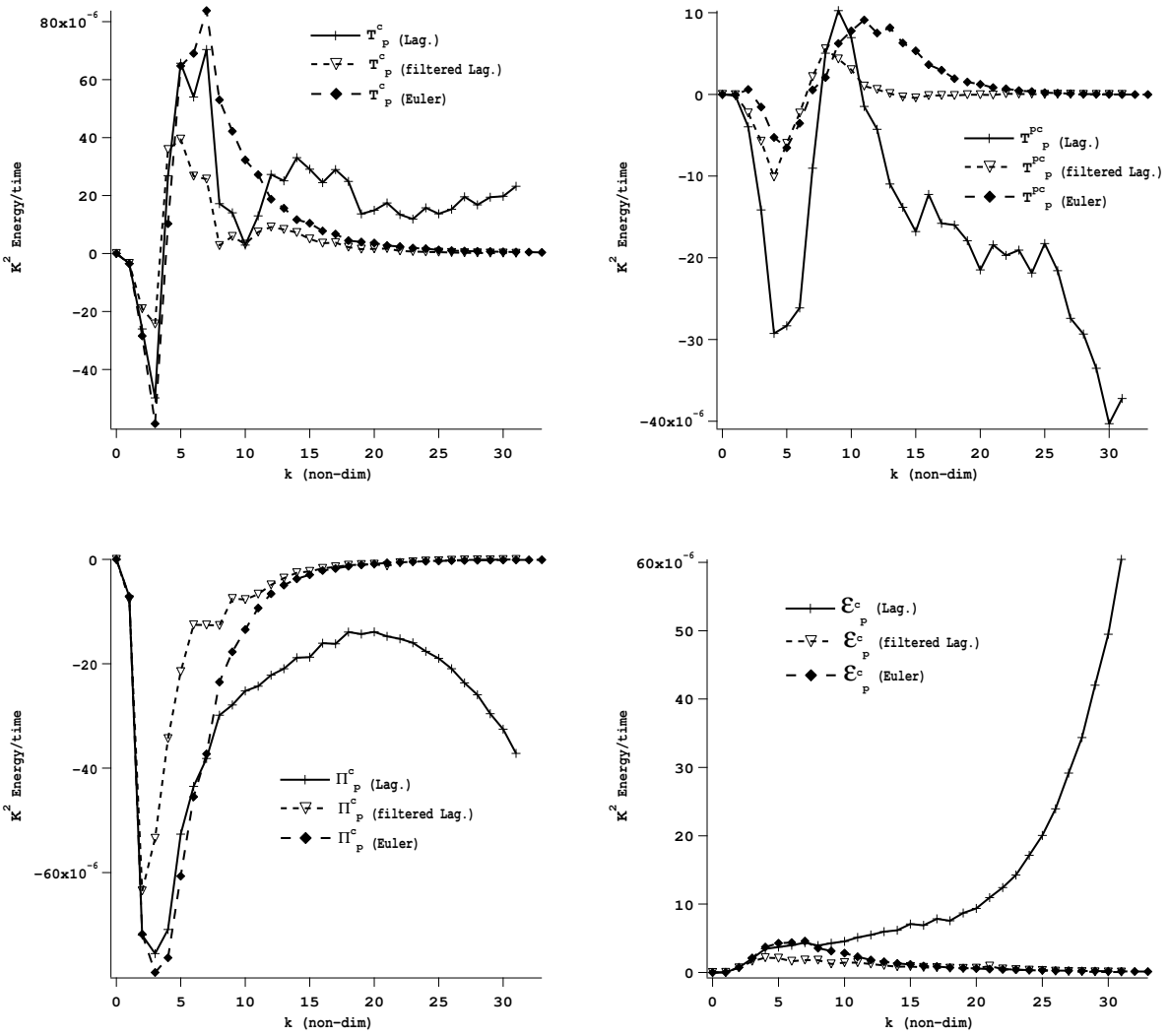

Figure 4.22: Comparison of the dispersed phase transport terms of kinetic energy in Lagrangian, filtered Lagrangian and Eulerian computation for the test case (HIT1,CJ) at t=10.8.

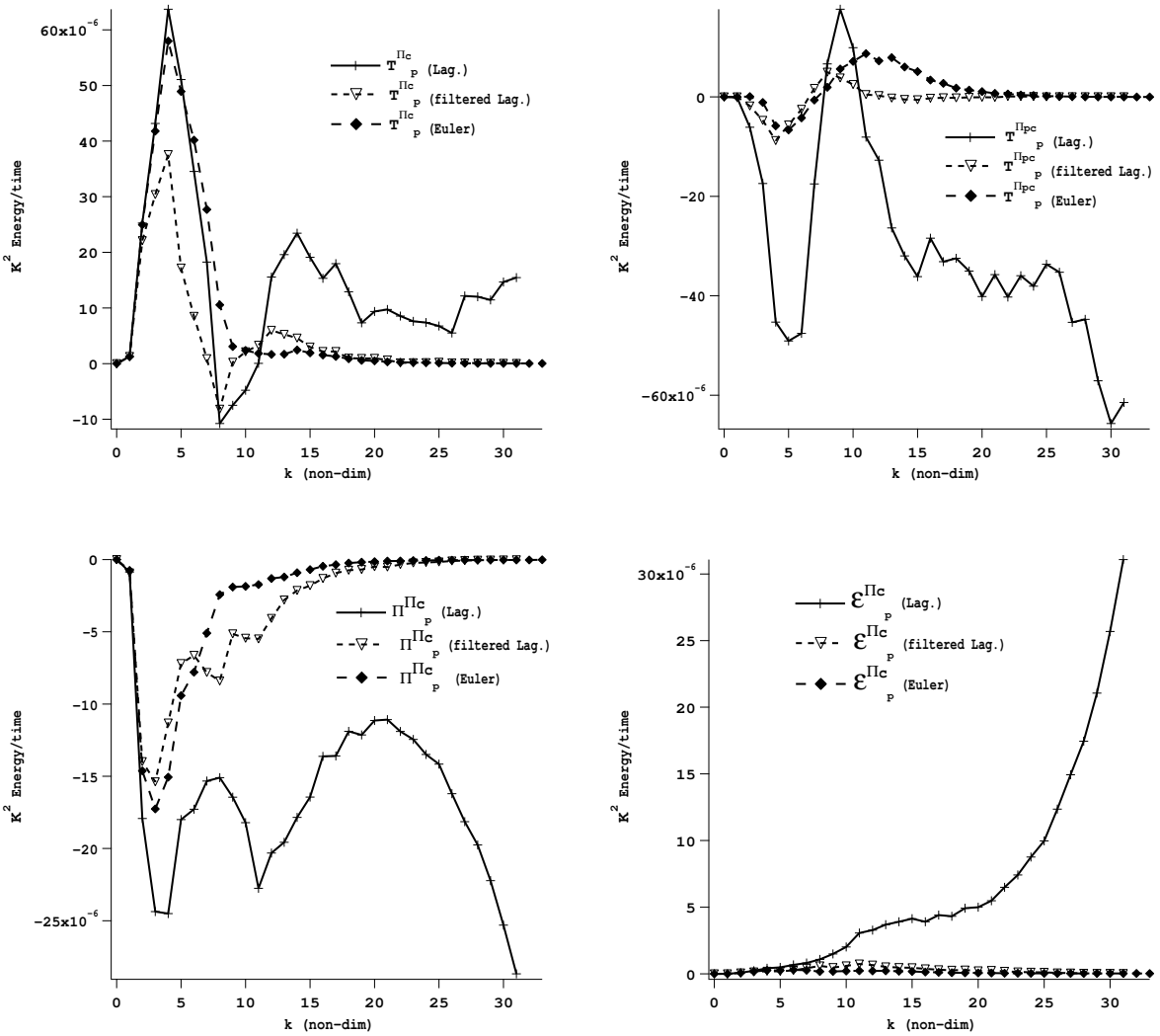

Figure 4.23: Comparison of the dispersed phase transport terms of compressible kinetic energy in Lagrangian, filtered Lagrangian and Eulerian computation for the test case (HIT1,CJ) at t=10.8.

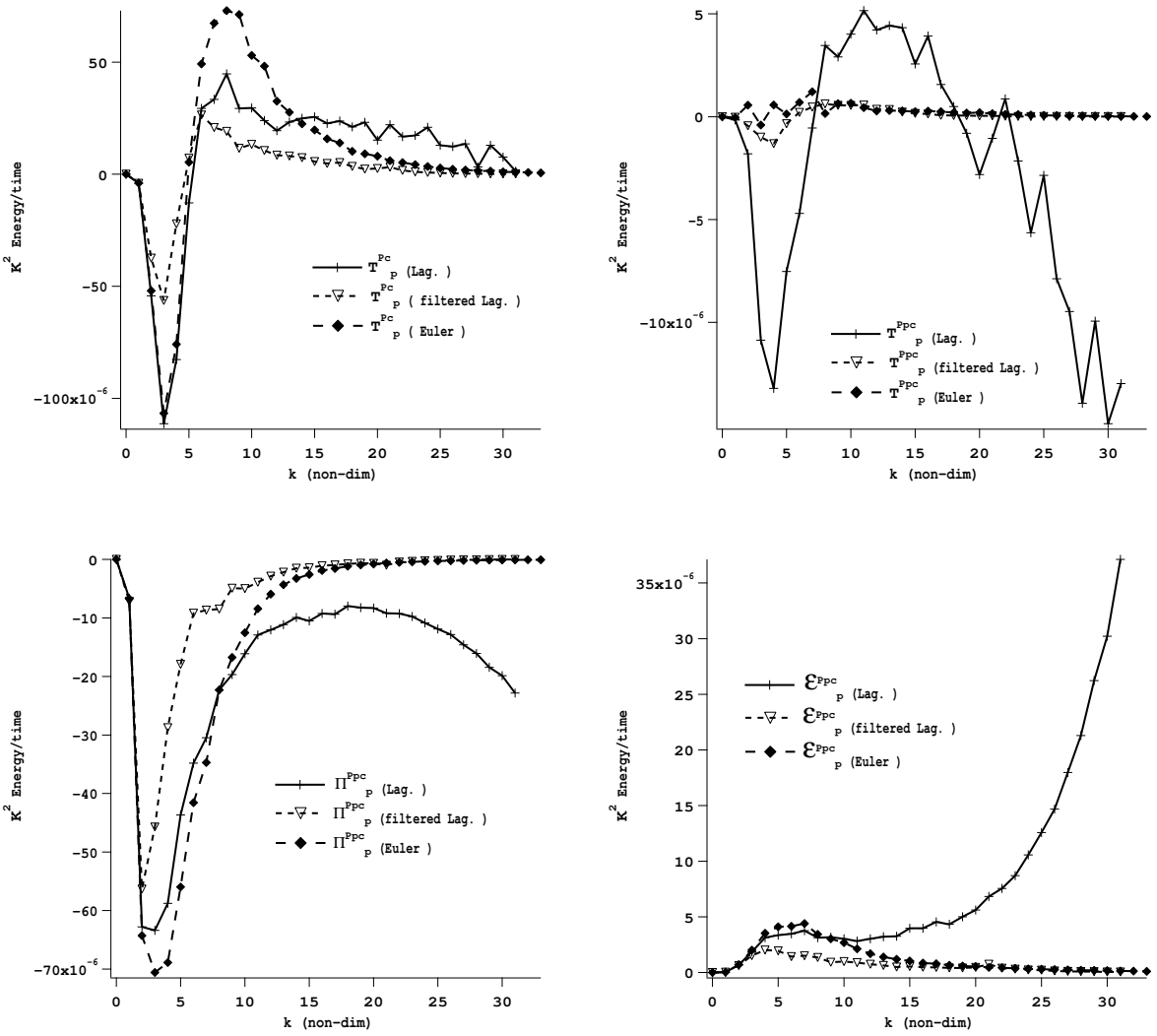

Figure 4.24: Comparison of the dispersed phase transport terms of solenoidal kinetic energy in Lagrangian, filtered Lagrangian and Eulerian computation for the test case (HIT1,CJ) at t=10.8.

Chapter 5

Implications for LES of Eulerian Two Phase Flows

Und sie laufen ! Naß und nässer
Wirds im Saal und auf den Stufen:
Welch entsetzliches Gewässer !
Herr und Meister, hör mich rufen ! -
Ach, da kommt der Meister !
Herr, die Not ist groß !
Die ich rief, die Geister,
Werd ich nun nicht los.
Goethe, Zauberlehrling

Large Eddy Simulation (LES) is becoming a well understood tool for non-reactive single phase flows with moderate Reynolds numbers. The success of such methods for internal and external flows is contributed to the fact that large scale structures are explicitly solved, leading to more detailed information about the physics of the flow then in Reynolds averaged steady computations. The difficulty in common with Reynolds averaged methods is the (subgrid) model used to represent the unresolved stresses. Simulation results are usually very sensitive to the type of subgrid model used and the model parameters.

Computation of reacting flows requires the modeling of subgrid scale chemistry. Those models depend on the chemistry time scale and other parameters such as temperature, radiation and subgrid mixing. LES of reactive flows such as combustion has just left the starting blocks. Several approaches are currently being tested and compared, such as the G-equation (level set methods) [73] or the thickened flame [16].

Large Eddy Simulation of multi-phase flows are still rare. Some encouraging results have already been obtained by coupling carrier phase LES methods to Lagrangian particle tracking methods [59]. By coupling two phases supplementary difficulties occur. They are connected to phase exchange terms such as evaporation and drag force. Besides, if the simulation is reactive, those models have to be coupled to the subgrid chemistry models. The compatibility of those models is however not clear yet.

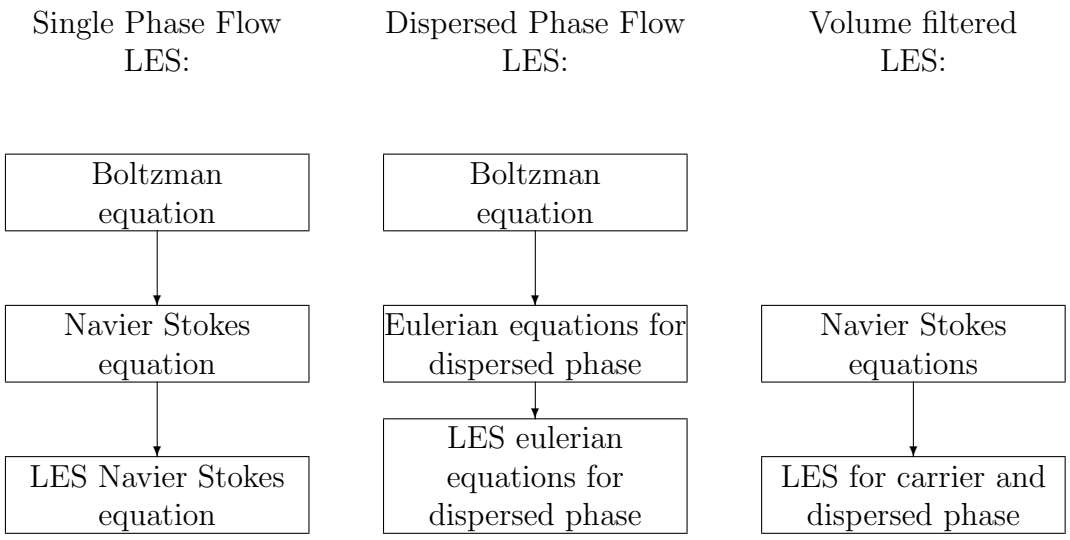

Figure 5.1: Strategies for LES equations for two phase flows.

Eulerian descriptions for the dispersed phase are obtained by some kind of averaging method (for example by ensemble average section 1.3 or volume average 1.4). The different averaging procedures lead however not to exactly the same set of equations. With the filtering the Eulerian field equations in the sense of LES, a second averaging procedure is introduced. This procedure may be compared to the process for obtaining LES equations for single phase flow: the Navier Stokes equations are obtained from kinetic theory of gases by ensemble average of the molecular dynamics. Then they can be filtered to obtain the filtered LES equations (Fig. 5.1). Conceptually the approach used for the dispersed phase is similar in the case of one way coupling. The Eulerian equations of the dispersed phase are obtained from ensemble average of kinetic theory and the filtered equations by application of a LES filter. The major difference concerns the involved length and time scales and the sampling rate. Whereas in gaseous flows 6.0 10^{23} molecules per mole contribute to the average, the corresponding particle number density in the dispersed phase is much smaller. Furthermore, the molecular "diameter" is of the order of some Angström ($10^{-10}m$) whereas the particle diameter is typically of the order of microns ($10^{-6}m$) or larger. In the case of volume average, a filter size sufficiently larger than the typical particle diameter is required to guarantee continuous Eulerian equations. Therefore volume filtered equations can be understood as beeing already LES type equations for the two phases with explicit phase coupling.

The general idea of Large Eddy Simulation is to numerically resolve the energy contained in large scales and to model the small unresolved scales. The idea of separating resolved and modeled scales is sketched in Fig.5.2. Since the Navier-Stokes equations contain non-linear transport terms, there is a redistribution of kinetic energy over a wide range of scales. LES models for the momentum equation usually try to mimic the transport of kinetic energy from the resolved scales to the unresolved scales by dissipation of kinetic

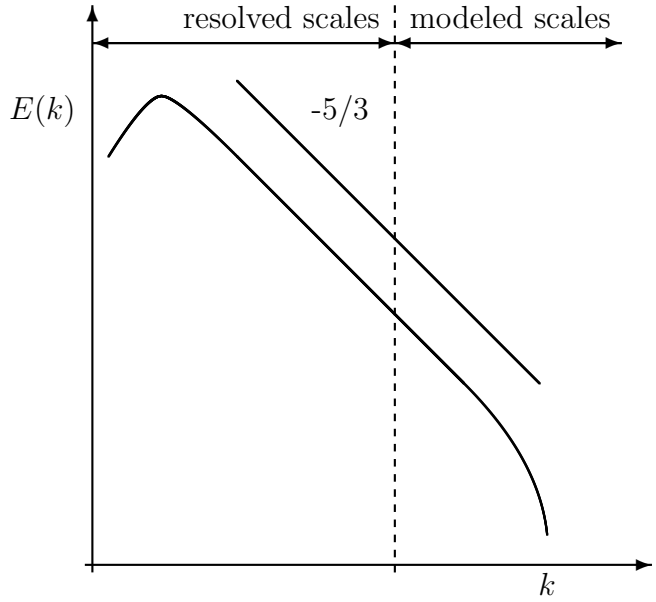

Figure 5.2: Sketch of Spectrum seperation in Large Eddy Simulations

energy at the cut-off scale. Unfortunately dissipation does not only act at the cutoff scale but acts on a broader range of the spectrum. This results in a kinetic energy spectrum different from such obtained by completely resolved flows [84],[74]. Due to the purely dissipative character of most LES models, backscatter effects, that is transport from small scales to large scales, are usually completely neglected. Subject of this chapter is to discuss the possibilities of performing "Large Eddy Simulation" in the Eulerian formulation of the dispersed phase. First, the governing equations of the carrier phase LES and the traditional modeling methods are recalled. Then, the filtered equations for the dispersed phase are developed and possible modeling of unresolved terms for a dispersed phase LES are evoked. The necessary analysis is based on the volume filtered Lagrangian results and the Eulerian results obtained with the ensemble averaged set of equations.

5.1 LES filters

In LES the filtering procedure consists in defining averaged variables that are obtained by a convolution product of the unfiltered variable f with a filter kernel F. Typical examples for filtering kernels are top hat filters or Gaussian functions with the corresponding filtering kernel in spectral space (see for example Sagaut [84],Germano [35] or Piomelli [74]). A filtered quantity is defined as :

$$\bar{f}(x) = \int f(x) F(x' - x) \, dx' \tag{5.1}$$

If flows with varying density are considered, it is common practice to define Favre averaged (mass pondered) quantities *. The Favre filtered quantity is then defined as :

$$\bar{\rho}\tilde{f}(x) = \int \rho(x) f(x) F(x'-x)\, dx' \tag{5.2}$$

Favre averaged quantities differ from standard averages in compressible computations. In a case with combustion for instance, densities are much lower downstream the flame front (on the hot side) than upstream the flame front (on the cold side). Then both averages do not have the same physical interpretation. Experimental hot wire measurements are typically closer to Favre averaged quantities since they measure a heat loss which is proportional to the conductivity and the gas density. For numerical computations, Favre averages are interesting, since they omit a supplementary modeling term in the continuity equation.
In general the filter kernels are not designed so that the filter commutes. Defining $f' = f - \bar{f}$ this implies generally that $\bar{f}' \neq 0$ and $\bar{\bar{f}} \neq \bar{f}$ (ie. if the filter is not idempotent). This applies also to Favre averaged quantities. A supplementary difficulty arises from the fact that the filtering operation does not generally commute with the derivative operators. This point is discussed for the case of incompressible flows by P. Sagaut [84].

5.2 LES equations of the carrier phase

Filtering of the Navier-Stokes equations leads to the following set of conservation equations for the filtered quantities:

$$\frac{\partial}{\partial t}\bar{\rho} + \frac{\partial}{\partial x_j}\bar{\rho}\tilde{u}_j = 0 \tag{5.3}$$

$$\frac{\partial}{\partial t}\bar{\rho}\tilde{Y}_k + \frac{\partial}{\partial x_j}\bar{\rho}\tilde{Y}_k\tilde{u}_j = \frac{\partial}{\partial x_j}\left[\overline{Y_k V_{k,j}^c} - \bar{\rho}\left(\widetilde{Y_k u_j} - \tilde{Y}_k\tilde{V}_{k,j}^c\right)\right] + \bar{\dot{\omega}}_k$$

$$\frac{\partial}{\partial t}\bar{\rho}\tilde{u}_i + \frac{\partial}{\partial x_j}\bar{\rho}\tilde{u}_i\tilde{u}_j = -\frac{\partial}{\partial x_i}\bar{P} + \frac{\partial}{\partial x_j}\bar{\tau}_{ij} + \frac{\partial}{\partial x_j}\left[\bar{\rho}\tilde{u}_i\tilde{u}_j - \bar{\rho}\widetilde{u_i u_j}\right] \tag{5.4}$$

$$\frac{\partial}{\partial t}\bar{\rho}\tilde{E} + \frac{\partial}{\partial x_j}\bar{\rho}\tilde{E}\tilde{u}_j = -\frac{\partial}{\partial x_j}\bar{q}_j + \frac{\partial}{\partial x_j}\overline{\sigma_{ij}u_i} + \bar{\dot{\omega}}_T + \frac{\partial}{\partial x_j}\bar{\rho}\left(\widetilde{u_j E} - \tilde{u}_j\tilde{E}\right) \tag{5.5}$$

The equations for the filtered quantities contain nonlinear unclosed terms. Those unclosed terms are identified as:

- Unresolved subgrid stresses:

$$\tilde{u}_i\tilde{u}_j - \widetilde{u_i u_j} \tag{5.6}$$

- Unresolved species fluxes:

$$\widetilde{Y_k u_j} - \tilde{Y}_k\tilde{V}_{k,j}^c \tag{5.7}$$

*see Poinsot & Veynante [75]

- Filtered laminar species diffusion and species consumption/production:

$$\overline{Y_k V_{k,j}^c} \quad \text{and} \quad \bar{\dot{\omega}}_k \tag{5.8}$$

- Unresolved energy fluxes:

$$\widetilde{u_j E} - \tilde{u}_j \tilde{E} \tag{5.9}$$

- Filtered laminar heat flux and heat release:

$$\bar{q}_i \quad \text{and} \quad \bar{\dot{\omega}}_T \tag{5.10}$$

- filtered pressure-strain correlations:

$$\overline{\sigma_{ij} u_i} \tag{5.11}$$

Those unclosed terms in the filtered balance equations require modeling. Several strategies exist. They can roughly be divided into methods, that use transport equations for higher moments of the filtered quantities (or other physical quantities such as subgrid energy) and methods, that use algebraic subgrid models based on filtered quantities and gradients of filtered quantities.

Filtered laminar fluxes are usually simply treated by using the Ficks law for diffusion on the filtered quantities:

$$\bar{q}_i = \bar{\lambda} \frac{\partial}{\partial x_i} \bar{T} \quad \text{or} \quad \overline{Y_k V_{k,j}^c} = -\bar{\rho} \bar{D}_k \frac{\partial}{\partial x_j} \tilde{Y}_k \tag{5.12}$$

In the same way turbulent species and heat fluxes are usually estimated by a gradient diffusion assumption with a turbulent viscosity ν_t, a subgrid Schmidt number Sc_k for the species flux and a subgrid Prandtl number Pr for the energy flux:

$$\widetilde{Y_k u_j} - \tilde{Y}_k \tilde{V}_{k,j}^c = -\frac{\nu_t}{Sc_k} \frac{\partial}{\partial x_j} \tilde{Y}_k \quad \textit{and} \quad \widetilde{u_j E} - \tilde{u}_j \tilde{E} = -\frac{\nu_t}{Pr} \frac{\partial}{\partial x_j} \tilde{E} \tag{5.13}$$

Filtered species consumption/production $\bar{\dot{\omega}}_k$ and filtered heat release $\bar{\dot{\omega}}_T$ are somewhat more difficult to model. In the case of the Navier-Stokes equations, heat release can well be modeled by an Arrhenius law. For the filtered equations a more detailed analysis of the physics is crucial, since the necessary length and time scales are typically not resolved in a LES computation [75]. Using simply the Arrhenius law with the filtered quantities supposes, that the subgrid mixing is much faster than the species consumption.

Most attention is usually given to the modeling of the unresolved subgrid stresses $\tilde{u}_i \tilde{u}_j - \widetilde{u_i u_j}$. Based on the description given by Sagaut [84] and using the notations introduced in section 2.4 the idea behind the modeling of the subgrid stresses is briefly recalled: The spectral version of the incompressible momentum equation is:

$$\left(\frac{\partial}{\partial t} + \nu \kappa^2 \right) \hat{u}_i \left(\boldsymbol{\kappa} \right) = \mathcal{T}_{f,i}(\boldsymbol{\kappa}) \tag{5.14}$$

Here the shorthand notation $\mathcal{T}_f(\boldsymbol{\kappa}) = -\hat{\mathcal{P}}_{ij}(\boldsymbol{\kappa})\hat{G}_j(\boldsymbol{\kappa})$ is used. Admitting furthermore the use of a spectral filter function $\hat{F}(\boldsymbol{\kappa})$ one obtains a filtered momentum transport equation:

$$\left(\frac{\partial}{\partial t} + \nu\kappa^2\right)\hat{F}(\boldsymbol{\kappa})\hat{u}_i(\boldsymbol{\kappa}) = \hat{F}(\boldsymbol{\kappa})\mathcal{T}_{f,i}(\boldsymbol{\kappa}) \tag{5.15}$$

Formally the term on the right hand side may be split into two components, one depending only on the resolved velocity ($\hat{F}(\boldsymbol{\kappa})\hat{u}_i(\boldsymbol{\kappa}) = \tilde{\hat{u}}_i(\boldsymbol{\kappa})$) and one depending on the resolved and unresolved velocity ($\hat{u}_i''(\boldsymbol{\kappa}) = \hat{u}_i - \tilde{\hat{u}}_i$):

$$\hat{F}(\boldsymbol{\kappa})\mathcal{T}_{f,i}(\boldsymbol{\kappa}) = \mathcal{T}_{r,i}(\boldsymbol{\kappa}, \tilde{\hat{u}}_j(\boldsymbol{\kappa})) + \mathcal{T}_{sgs,i}(\boldsymbol{\kappa}, \tilde{\hat{u}}_j(\boldsymbol{\kappa}), \hat{u}_j''(\boldsymbol{\kappa})) \tag{5.16}$$

In a LES computation one has only information about the resolved velocity. Therefore the transfer term depending on the unresolved velocity requires modeling. Several methods exist to treat this term. The computationally most inexpensive are algebraic models that estimate the unresolved fluxes by an algebraic function of the resolved velocity, its spatial gradients and the cutoff scale κ_c:

$$\mathcal{T}_{sgs,i}(\boldsymbol{\kappa}, \tilde{\hat{u}}_j(\boldsymbol{\kappa}), \hat{u}_j''(\boldsymbol{\kappa})) \approx \mathcal{T}^M_{sgs,i}(\boldsymbol{\kappa}, \tilde{\hat{u}}_j(\boldsymbol{\kappa}), \kappa_k\tilde{\hat{u}}_j(\boldsymbol{\kappa})) \tag{5.17}$$

Other models use supplementary transport equations for the kinetic energy with wave numbers below the cutoff scale or even transport equations for the different terms of the unresolved subgrid stresses. In the latter case, third order terms need to be modeled. This shifts the difficulty of modeling to a different expression.
The usual linear algebraic model for the transport $\mathcal{T}^M_{sgs,i}$ uses a turbulent viscosity ν_{sgs} and the Boussinesq assumption:

$$\mathcal{T}^M_{sgs,i}(\boldsymbol{\kappa}, \tilde{\hat{u}}_j(\boldsymbol{\kappa}), \kappa_k\tilde{\hat{u}}_j(\boldsymbol{\kappa})) = -\nu_{sgs}\kappa^2\tilde{\hat{u}}_i \tag{5.18}$$

In this case the filtered spectral transport equation for the momentum equation is:

$$\left(\frac{\partial}{\partial t} + (\nu + \nu_{sgs})\kappa^2\right)\tilde{\hat{u}}_i(\boldsymbol{\kappa}) = \mathcal{T}_{r,i}(\boldsymbol{\kappa}) \tag{5.19}$$

Some constraints are imposed on the turbulent subgrid viscosity ν_{sgs}: For example, it should vanish, if the resolution of the computation is sufficient to resolve all scales (typically in laminar flows) and it should reproduce the correct log scale behavior in the vicinity of the wall. Two among most popular algebraic models for the subgrid viscosity are:

1. The Smagorinsky model [96], [84]:

$$\nu_{sgs} = (C_{SM}\Delta)^2 2\left|\bar{S}_{ij}\right| \tag{5.20}$$

   This model estimates the subgrid viscosity using the resolved strain rate $\bar{S}_{ij}$ and the numerical grid spacing Δ. The model uses an equilibrium assumption: the kinetic energy transfered to scales smaller than the cutoff scale equals the energy dissipated at

scales smaller than the cutoff scale. The constant C_{SM} can be evaluated theoretically by making an assumption on the form of the spectrum [84]. This model is known to be too dissipative. It does not vanish in laminar flow and does not have the correct log scale behavior in the near wall region. In confined geometries this model tends to laminarise the flow.

2. The Germano dynamic model explicitly estimates the subgrid dissipation by the resolved eddies. This can be obtained by introducing two filters: One at the numerical cutoff scale and at one scale larger than the cutoff scale. The constant C_{SM}, which is fixed in the Smagorinsky model, can be evaluated dynamically from the stresses measured at the two scales.

The choice of the constant C_{SM} usually depends on the type of flow considered and is unfortunately not universal. In order to obtain the correct behavior in the near wall region different models for the turbulent viscosity have been proposed (Nicoud [70]).
Using a subgrid viscosity leads to the computation of a fluid, which is sometimes called a Smagorinsky fluid. The effective Reynolds number of such a flow, due to the subgrid viscosity, is significantly lower than the Reynolds number of the flow under investigation.

5.3 LES equations for the dispersed phase

Here the filtering procedure described in section 5.1 with the definitions of Favre averaging (Eqs. 5.1, 5.2) is applied to the conservation equations of the dispersed phase as obtained from the ensemble averaging procedure (see section 1.3).

This filtering procedure can be compared to the filtering of the compressible Navier Stokes equations (Erlebacher [29]) taking explicitly into account compressibility effects. The conservation equations for the filtered dispersed phase are :

$$\frac{\partial}{\partial t}\breve{\bar{n}}_p + \frac{\partial}{\partial x_j}\breve{\bar{n}}_p\breve{\tilde{u}}_{p,j} = 0 \tag{5.21}$$

$$\begin{aligned}\frac{\partial}{\partial t}\breve{\bar{n}}_p\breve{\tilde{u}}_{p,i} + \frac{\partial}{\partial x_j}\breve{\bar{n}}_p\breve{\tilde{u}}_{p,i}\breve{\tilde{u}}_{p,j} &= -\frac{\partial}{\partial x_i}\bar{P}_{QB} + \frac{\partial}{\partial x_j}\bar{\tau}_{ij} - \frac{\bar{n}_p}{\tau_p}\left(\breve{\tilde{u}}_{p,i} - \tilde{u}_i\right) \\ &\quad + \frac{\partial}{\partial x_j}\left[\breve{\bar{n}}_p\breve{\tilde{u}}_{p,i}\breve{\tilde{u}}_{p,j} - \breve{\bar{n}}_p\widetilde{\breve{u}_{p,i}\breve{u}_{p,j}}\right]\end{aligned} \tag{5.22}$$

$$\begin{aligned}\frac{\partial}{\partial t}\breve{\bar{n}}_p\delta\breve{\tilde{\theta}}_p + \frac{\partial}{\partial x_j}\breve{\bar{n}}_p\delta\breve{\tilde{\theta}}_p\breve{\tilde{u}}_{p,j} &= -\frac{2\breve{\bar{n}}_p\delta\breve{\tilde{\theta}}_p}{\tau_p} - \overline{\left[P_{QB}\delta_{ij} - \breve{\tau}_{ij}\right]\frac{\partial\breve{u}_{p,i}}{\partial x_j}} \\ &\quad + \frac{\partial}{\partial x_j}\breve{\bar{n}}_p\left(\widetilde{\breve{u}_{p,j}\delta\breve{\theta}_p} - \breve{\tilde{u}}_{p,j}\delta\breve{\tilde{\theta}}_p)\right) \\ &\quad + \overline{\frac{\partial}{\partial x_j}\kappa_{QB}\frac{\partial}{\partial x_j}\delta\breve{\theta}_p}\end{aligned} \tag{5.23}$$

Considering the drag related term in the filtered dispersed phase momentum equation, note that the expression $\tilde{u}_i$ corresponds to the Favre averaged carrier phase velocity with Favre-

averaging operator of the dispersed phase. It is therefore different from the carrier phase Favre-averaged velocity. The filtered dispersed phase equations contain three unclosed terms that are due to filtering.

- Unresolved fluxes in the momentum equation :

$$\tau_{p,ij,sgs} = \breve{\tilde{u}}_{p,i}\breve{\tilde{u}}_{p,j} - \widetilde{\breve{u}_{p,i}\breve{u}_{p,j}} \tag{5.24}$$

- Unresolved fluxes of Quasi Brownian Energy :

$$\widetilde{\breve{u}_j\delta\breve{\theta}_p} - \breve{\tilde{u}}_j\delta\breve{\tilde{\theta}}_p \tag{5.25}$$

- Pressure strain relations :

$$\overline{[P_{QB}\delta_{ij} - \breve{\tau}_{ij}]\frac{\partial}{\partial x_j}\breve{u}_{p,i}} \tag{5.26}$$

A rough modeling of the unresolved stresses in the filtered momentum equation due to compressibility effects was given in section 3.3. The analysis of the different terms is refined here. Before addressing the modeling of the different terms, the different contributions to the total particle kinetic energy are investigated. As a consequence a transport equation for the subgrid scale energy is constructed [89]. The construction of the subgrid scale energy requires the knowledge of the mesoscopic kinetic energy. First the corresponding transport equation is constructed.

Mesoscopic kinetic energy

The transport equation for the mesoscopic kinetic energy is deduced from the mesoscopic momentum equation (Eq. 1.46) :

$$\begin{aligned}\frac{\partial}{\partial t}\breve{n}_p\frac{1}{2}\breve{u}_{p,i}\breve{u}_{p,i} + \frac{\partial}{\partial x_j}\breve{n}_p\breve{u}_{p,j}\frac{1}{2}\breve{u}_{p,i}\breve{u}_{p,i} &= \underbrace{-\breve{u}_{p,i}\frac{\partial}{\partial x_i}P_{QB}}_{(A)} + \underbrace{\breve{u}_{p,i}\frac{\partial}{\partial x_j}\breve{\tau}_{p,ij}}_{(B)} \\ &\quad + \frac{\breve{n}_p}{\tau_p}\left(u_i - \breve{u}_{p,i}\right)\end{aligned} \tag{5.27}$$

The first two terms on the right hand side (A) and (B) of Eq. 5.27 can be separated into a diffusion term $\left(\frac{\partial}{\partial x_j}\left(P_{QB}\delta_{ij} - \breve{\tau}_{p,ij}\right)\breve{u}_{p,i}\right)$ and an exchange term $\left(P_{QB}\delta_{ij} - \breve{\tau}_{p,ij}\right)\frac{\partial}{\partial x_j}\breve{u}_{p,i}$. The exchange term corresponds to the transfer of correlated kinetic energy to QBE by QB viscosity and the exchange due to compression and dilatation. The corresponding term can therefore be found in the transport equation for QBE with an opposite sign.

Filtered Energy

In the system of the filtered equations, the situation is more complex than in the case of the "laminar" equations and is therefore described by decomposing the different contributions.
The total kinetic energy of the dispersed phase is the sum of the kinetic energy associated to the mesoscopic velocity field and the QBE.

$$E_p = \frac{1}{2}\breve{u}_{p,i}\breve{u}_{p,i} + \delta\breve{\theta}_p \tag{5.28}$$

Favre averaging the energy equation leads to the following expression:

$$\begin{aligned} \tilde{E}_p &= \frac{1}{2}\widetilde{\breve{u}_{p,i}\breve{u}_{p,i}} + \delta\tilde{\breve{\theta}}_p & (5.29)\\ &= \frac{1}{2}\tilde{\breve{u}}_{p,i}\tilde{\breve{u}}_{p,i} + \frac{1}{2}\left(\widetilde{\breve{u}_{p,i}\breve{u}_{p,i}} - \tilde{\breve{u}}_{p,i}\tilde{\breve{u}}_{p,i}\right) + \delta\tilde{\breve{\theta}}_p & (5.30)\end{aligned}$$

This demonstrates how the filtered total dispersed phase energy $\tilde{E}_p$ can be divided into a resolved mesoscopic kinetic energy $\frac{1}{2}\tilde{\breve{u}}_{p,i}\tilde{\breve{u}}_{p,i}$, an unresolved mesoscopic kinetic energy $\breve{q}^2_{p,sgs} = \frac{1}{2}\left(\widetilde{\breve{u}_{p,i}\breve{u}_{p,i}} - \tilde{\breve{u}}_{p,i}\tilde{\breve{u}}_{p,i}\right)$ and a filtered quasi brownian energy $\delta\tilde{\breve{\theta}}_p$. The unresolved mesoscopic kinetic energy $\breve{q}^2_{p,sgs}$ corresponds to half the trace of the unresolved stresses $\tau_{p,ij,sgs}$ in the filtered dispersed phase momentum equation (Eq. 5.22).

In section 1.4.5 the difference between the volume filtered and the ensemble averaged approach was evoked. Eq. 5.29 makes this difference, concerning the subgrid energy, clearer, since the subgrid correlated kinetic energy $\breve{q}^2_{p,sgs}$ appears explicitly in the filtered energy equation. The equivalent of the volume filtered subgrid kinetic energy $\Delta q^2_{\Omega,l}$is here the sum of subgrid kinetic energy $\breve{q}^2_{p,sgs}$ and the filtered QBE $\delta\tilde{\breve{\theta}}_p$ since the volume filtering procedure does not seperate correlated from uncorrelated kinetic energy.

Unresolved mesoscopic fluxes

The motivation for the introduction of the subgrid kinetic energy $\breve{q}^2_{p,sgs}$ is, other than the explication of the transfer mechanisms, of practical nature. If the stress tensor $\tau_{p,ij,sgs}$ is split into two components the filtered momentum equation can be rewritten.

$$\tau_{p,ij,sgs} = -\bar{\breve{n}}_p\frac{2}{3}\breve{q}^2_{p,sgs}\delta_{ij} + \tau'_{p,ij,sgs} \tag{5.31}$$

Regrouping the QBP with the contribution of the subgrid energy $\breve{q}^2_{p,sgs}$ and the filtered stress tensor with the residual stress tensor $\tau'_{p,ij,sgs}$ the filtered momentum equation takes the following form :

$$\begin{aligned} \frac{\partial}{\partial t}\bar{\breve{n}}_p\tilde{\breve{u}}_{p,i} + \frac{\partial}{\partial x_j}\bar{\breve{n}}_p\tilde{\breve{u}}_{p,i}\tilde{\breve{u}}_{p,j} &= -\frac{\partial}{\partial x_i}\left(\bar{P}_{QB} + \bar{\breve{n}}_p\frac{2}{3}\breve{q}^2_{p,sgs}\right) & (5.32)\\ &\quad + \frac{\partial}{\partial x_j}\left(\bar{\tau}_{ij} + \tau'_{p,ij,sgs}\right)\\ &\quad - \frac{\bar{n}_p}{\tau_p}\left(\tilde{\breve{u}}_{p,i} - u_i\right)\end{aligned}$$

The mesoscopic subgrid kinetic energy $\breve{q}^2_{p,sgs}$ and the stresses $\tau'_{ij,sgs}$ are not known in a LES computation. One possibility is to model those terms directly. The mesoscopic subgrid kinetic energy can be split into a compressible and an incompressible component.

$$\breve{q}^2_{p,sgs} = \breve{q}^2_{p,sgs}{}^{(c)} + \breve{q}^2_{p,sgs}{}^{(s)} \tag{5.33}$$

In section 3.3.2 the incompressible solenoidal component of the mesoscopic subgrid kinetic energy and the non-diagonal subgrid stresses were considered negligible. The compressible component of the mesoscopic subgrid kinetic energy was modeled with a bulk viscosity assumption.

$$\breve{q}^2_{p,sgs}{}^{(c)} = -C\Delta^2 \left| \frac{\partial \tilde{\breve{u}}_{p,k}}{\partial x_k} \right| \frac{\partial \tilde{\breve{u}}_{p,k}}{\partial x_k} \tag{5.34}$$

Note that the right hand side of Eq. 5.34 is not strictly an energy expression since it takes negative values in the case of dilatation. In the case of dilatation, the force counteracting the compressible velocity component needs to take however a different sign than in the case of compression.
This approach may be extended to a general subgrid kinetic energy using an expression like it is proposed in the modeling for compresseible LES of gaseous flows (Moin et al. [65],Yoshizawa [118]). Such a term is usually neglected in the case of subsonic LES computations since the subgrid kinetic energy is of several orders of magnitude smaller than the internal energy of the flow.
The tensor $\tau'_{p,ij,sgs}$ is by construction trace free and addresses the solenoidal component of the velocity. Spectra of the Eulerian computations of the dispersed phase in section 4.3.4 show however, that the solenoidal energy is already smaller than the Lagrangian solenoidal energy at small scales. Therefore the use of a subgrid tensor modeled by a viscous assumption is questionable. Of course the simulations shown in chapter 4 were performed at a small Reynolds number and a generalization to large Reynolds numbers is questionable.
If the stress tensor $\tau'_{p,ij,sgs}$ is constructed with a viscous assumption of Boussinesq type, a subgrid viscosity $\nu_{p,sgs}$ needs to be introduced. Contrary to the QB viscosity ν_{QB} there is no direct reason for this viscosity to depend on the particle relaxation time. Since it is a turbulent viscosity, it should depend on the mesoscopic subgrid kinetic energy $\breve{q}^2_{p,sgs}$.
Another possibility is to develop a transport equation for the subgrid kinetic energy $\breve{q}^2_{p,sgs}$.

Construction of subgrid kinetic energy

The correlated subgrid kinetic energy transport equation is constructed by difference of the transport equations for the filtered mesoscopic kinetic energy $1/2\widetilde{\breve{u}_{p,i}\breve{u}_{p,i}}$ and the resolved mesoscopic kinetic energy $\frac{1}{2}\tilde{\breve{u}}_{p,i}\tilde{\breve{u}}_{p,i}$. The transport equations for the energies obtained from the mesoscopic momentum transport equation (Eq. 1.46) and the filtered mesoscopic momentum transport (Eq. 5.22) equations are :

$$\frac{\partial}{\partial t}\bar{\breve{n}}_p \frac{1}{2}\widetilde{\breve{u}_{p,i}\breve{u}_{p,i}} + \frac{\partial}{\partial x_j}\bar{\breve{n}}_p \tilde{\breve{u}}_{p,j}\frac{1}{2}\widetilde{\breve{u}_{p,i}\breve{u}_{p,i}} = -\overline{\breve{u}_{p,i}\frac{\partial}{\partial x_i}P_{QB}} \tag{5.35}$$

$$
\begin{aligned}
&+\overline{\breve{u}_{p,i}\frac{\partial}{\partial x_j}\breve{\tau}_{p,ij}} \\
&+\frac{\bar{\breve{n}}_p}{\tau_p}\left(u_i\widetilde{\breve{u}_{p,i}}-\breve{u}_{p,i}\widetilde{\breve{u}_{p,i}}\right) \\
&+\frac{1}{2}\frac{\partial}{\partial x_j}\bar{\breve{n}}_p\left(\tilde{\breve{u}}_{p,j}\breve{u}_{p,i}\widetilde{\breve{u}_{p,i}}-\breve{u}_{p,j}\widetilde{\breve{u}_{p,i}}\breve{u}_{p,i}\right)
\end{aligned}
\tag{5.36}
$$

$$
\begin{aligned}
\frac{\partial}{\partial t}\bar{\breve{n}}_p\frac{1}{2}\tilde{\breve{u}}_{p,i}\tilde{\breve{u}}_{p,i}+\frac{\partial}{\partial x_j}\bar{\breve{n}}_p\tilde{\breve{u}}_{p,j}\frac{1}{2}\tilde{\breve{u}}_{p,i}\tilde{\breve{u}}_{p,i} &= -\underbrace{\tilde{\breve{u}}_{p,i}\frac{\partial}{\partial x_i}\bar{P}_{QB}}_{(C)} \\
&\quad+\underbrace{\tilde{\breve{u}}_{p,i}\frac{\partial}{\partial x_j}\bar{\tau}_{p,ij}}_{(D)} \\
&\quad+\frac{\bar{\breve{n}}_p}{\tau_p}\left(\tilde{u}_i\tilde{\breve{u}}_{p,i}-\tilde{\breve{u}}_{p,i}\tilde{\breve{u}}_{p,i}\right) \\
&\quad+\underbrace{\tilde{\breve{u}}_{p,i}\frac{\partial}{\partial x_j}\tau_{p,ij,sgs}}_{(E)}
\end{aligned}
\tag{5.37}
$$

Knowledge of the previous two equations allows to construct the transport equation of the subgrid kinetic energy $\breve{q}^2_{p,sgs}$:

$$
\begin{aligned}
\frac{\partial}{\partial t}\bar{\breve{n}}_p\breve{q}^2_{p,sgs}+\frac{\partial}{\partial x_j}\bar{\breve{n}}_p\tilde{\breve{u}}_{p,j}\breve{q}^2_{p,sgs} &= -\left(\underbrace{\overline{\breve{u}_{p,i}\frac{\partial}{\partial x_i}P_{QB}}}_{(F)}-\underbrace{\tilde{\breve{u}}_{p,i}\frac{\partial}{\partial x_i}\bar{P}_{QB}}_{(C)}\right) \\
&\quad+\left(\underbrace{\overline{\breve{u}_{p,i}\frac{\partial}{\partial x_j}\breve{\tau}_{p,ij}}}_{(G)}-\underbrace{\tilde{\breve{u}}_{p,i}\frac{\partial}{\partial x_j}\bar{\tau}_{p,ij}}_{(D)}\right) \\
&\quad+\frac{\bar{\breve{n}}_p}{\tau_p}\left(\left(u_i\widetilde{\breve{u}_{p,i}}-\tilde{u}_i\tilde{\breve{u}}_{p,i}\right)-2\breve{q}^2_{p,sgs}\right) \\
&\quad+\frac{1}{2}\frac{\partial}{\partial x_j}\bar{\breve{n}}_p\left(\underbrace{\tilde{\breve{u}}_{p,j}\breve{u}_{p,i}\widetilde{\breve{u}_{p,i}}}_{(H)}-\underbrace{\breve{u}_{p,j}\widetilde{\breve{u}_{p,i}}\breve{u}_{p,i}}_{(I)}\right) \\
&\quad-\underbrace{\tilde{\breve{u}}_{p,i}\frac{\partial}{\partial x_j}\tau_{p,ij,sgs}}_{(E)}
\end{aligned}
\tag{5.38}
$$

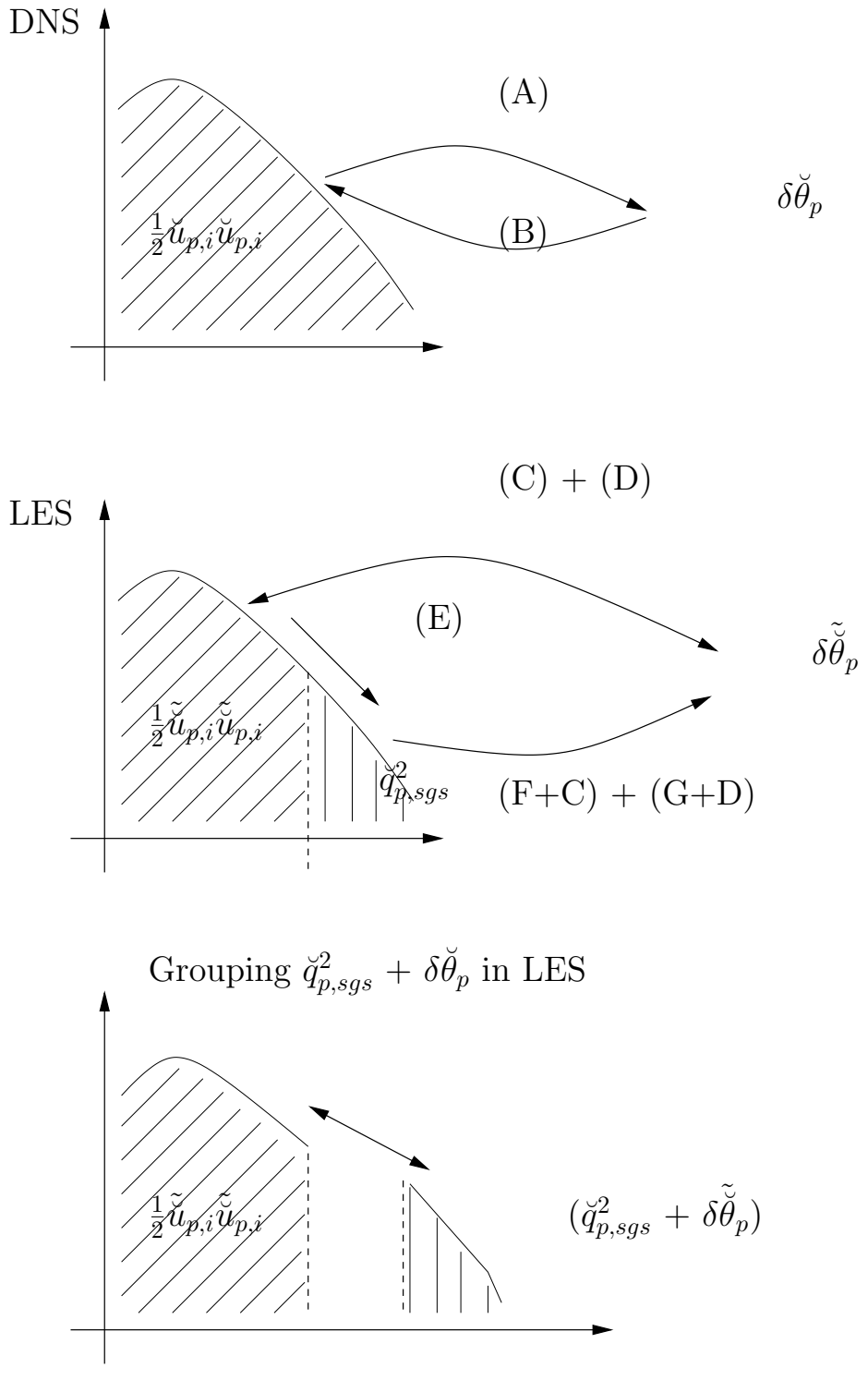

Figure 5.3: Sketch of the Energy transport in DNS, LES and when grouping $\breve{q}^2_{p,sgs} + \delta\breve{\theta}_p$ in the dispersed phase.

In this transport equation for the mesoscopic subgrid kinetic energy appears a new term which is related to the subgrid fluid particle correlation.

$$q_{fp,sgs} = \left(\widetilde{u_i \breve{u}_{p,i}} - \tilde{u}_i \breve{\tilde{u}}_{p,i}\right) \tag{5.39}$$

Note, that in this equation $\tilde{u}_i$ is the carrier phase velocity with the Favre average of the dispersed phase. The existence of a subgrid fluid particle correlation depends a priori on the Stokes number and the cutoff scale of the filter. In section 9 the length scale associated to the mean free particle path λ_p was associated to the smallest fluid particle correlation. If this length scale is larger than the cutoff scale, the subgrid fluid particle correlation is inexistent. If the cutoff scale is larger than the mean free particle path length this contribution needs to be modeled.

Having established the transport equations for the different quantities it is interesting to investigate the different mechanisms concerning the transfer of energy. In the transport equation for the resolved correlated kinetic energy of the dispersed phase (Eq. 5.37) the expression (E) corresponds to the transfer of resolved correlated particle kinetic energy to the subgrid particle kinetic energy $\breve{q}^2_{p,sgs}$ (Eq. 5.38) where the term appears with an opposite sign (expression (E)). The expressions (C) and (D) in Eq. 5.37 correspond to the transfer between resolved correlated particle kinetic energy and QBE. In the same way, one may identify the transfer expressions in Eq. 5.38. Here the terms $(F-C)$ and $(G-D)$ characterize the exchange of mesoscopic kinetic energy with QBE. These transfer mechanisms are roughly sketched in Fig. 5.3.

Grouping $\left(\breve{q}^2_{p,sgs}$ and $\delta\breve{\tilde{\theta}}_p\right)$

The subgrid kinetic energy $\breve{q}^2_{p,sgs}$ and the filtered QBE $\delta\breve{\tilde{\theta}}_p$ can be grouped to form one energy $q^2_{p,sgs} = \breve{q}^2_{p,sgs} + \delta\breve{\tilde{\theta}}_p$. Using the corresponding transport equations (Eq. 5.24 and Eq. 5.38) one may establish a transport equation for this new quantity.

$$\begin{aligned}
\frac{\partial}{\partial t}\bar{\tilde{n}}_p q^2_{p,sgs} + \frac{\partial}{\partial x_j}\bar{\tilde{n}}_p \breve{\tilde{u}}_{p,j} q^2_{p,sgs} \;=\; & -\left(\underbrace{\overline{\frac{\partial}{\partial x_i}\breve{u}_{p,i} P_{QB}}}_{(M)} - \underbrace{\breve{\tilde{u}}_{p,i}\frac{\partial}{\partial x_i}\bar{P}_{QB}}_{(N)} - \underbrace{\breve{\tilde{u}}_{p,i}\frac{\partial}{\partial x_j}\breve{q}^s_{p,sgs}}_{(O)}\right) \\
& + \left(\underbrace{\overline{\frac{\partial}{\partial x_j}\breve{u}_{p,i}\breve{\tau}_{p,ij}}}_{(P)} - \underbrace{\breve{\tilde{u}}_{p,i}\frac{\partial}{\partial x_j}\bar{\tau}_{p,ij}}_{(Q)} - \underbrace{\breve{\tilde{u}}_{p,i}\frac{\partial}{\partial x_j}\tau'_{p,ij,sgs}}_{(R)}\right) \\
& + \frac{\bar{\tilde{n}}_p}{\tau_p}\left(q_{fp,sgs} - 2q^2_{p,sgs}\right) \\
& + \frac{1}{2}\frac{\partial}{\partial x_j}\bar{\tilde{n}}_p\left(\breve{\tilde{u}}_{p,j}\widetilde{\breve{u}_{p,i}\breve{u}_{p,i}} - \breve{u}_{p,j}\widetilde{\breve{u}_{p,i}\breve{u}_{p,i}}\right)
\end{aligned}$$

$$+\frac{1}{2}\frac{\partial}{\partial x_j}\breve{\bar{n}}_p\left(\breve{\tilde{u}}_{p,j}\delta\breve{\tilde{\theta}}_p - \widetilde{\breve{u}_{p,j}\delta\breve{\theta}_p}\right)$$
$$+\overline{\frac{\partial}{\partial x_j}\kappa_{QB}\frac{\partial}{\partial x_j}\delta\breve{\theta}_p}$$

This equation can be simplified, by making some drastic modeling assumptions concerning the unresolved fluxes of mesoscopic subgrid kinetic energy, unresolved fluxes of QBE and grouping of the transfer components. The first modeling assumption concerns the redistribution of subgrid kinetic energy by QBP.

$$\overline{\frac{\partial}{\partial x_j}P_{QB}\breve{u}_{p,j}} \approx \frac{\partial}{\partial x_j}\bar{P}_{QB}\breve{\tilde{u}}_{p,j} + \frac{\partial}{\partial x_j}\frac{2}{3}\breve{\bar{n}}_p\breve{q}_{p,sgs}\breve{u}_{p,j} \tag{5.40}$$

The second modeling assumption concerns the redistribution of subgrid kinetic energy due QB stress.

$$\overline{\frac{\partial}{\partial x_j}\breve{\tau}_{p,ij}\breve{u}_{p,i}} \approx \frac{\partial}{\partial x_j}\breve{\bar{\tau}}_{p,ij}\breve{\tilde{u}}_{p,i} + \frac{\partial}{\partial x_j}\tau'_{ij,sgs}\breve{u}_{p,i} \tag{5.41}$$

Furthermore here the unresolved fluxes of mesoscopic subgrid kinetic energy, unresolved fluxes of QBE and filtered fluxes of QBE are grouped into one single diffusion equation.

$$\frac{\partial}{\partial x_j}\kappa_{q^2_{p,sgs}}\frac{\partial}{\partial x_j}q^2_{p,sgs} \tag{5.42}$$

The resulting simplified transport equation is then

$$\begin{aligned}\frac{\partial}{\partial t}\breve{\bar{n}}_p q^2_{p,sgs} + \frac{\partial}{\partial x_j}\breve{\bar{n}}_p\breve{\tilde{u}}_{p,j}q^2_{p,sgs} \;=\; & -\frac{2}{3}\breve{\bar{n}}_p q^2_{p,sgs}\frac{\partial}{\partial x_j}\breve{\tilde{u}}_{p,j} + \left(\breve{\bar{\tau}}_{p,ij} + \tau'_{ij,sgs}\right)\frac{\partial}{\partial x_j}\breve{\tilde{u}}_{p,i} \\ & \frac{\breve{\bar{n}}_p}{\tau_p}\left(q_{fp,sgs} - 2q^2_{p,sgs}\right) \\ & \frac{\partial}{\partial x_j}\kappa_{q^2_{p,sgs}}\frac{\partial}{\partial x_j}q^2_{p,sgs}\end{aligned} \tag{5.43}$$

The grouped subgrid kinetic energy $q^2_{p,sgs}$ may then be used in the filtered momentum equation of the dispersed phase (Eq. 5.32). Two difficulties persist associated to the simplified transport equation. One is due to the modeling of the subgrid stress tensor $\tau'_{p,ij,sgs}$ and the other one is due to subgrid fluid particle correlation.
The transport equation for the subgrid kinetic energy $q^2_{p,sgs}$ is, other than the difference in volume and ensemble average, equivalent to the transport equation of the subgrid kinetic energy as obtained from the volume filtering approach (see section 1.4.4).

5.4 LES of dispersed two-phase flow

In the preceding sections the transport equations are developed from the ensemble averaged point of view. This was limited to the easiest case of one way coupling. The additional

difficulty with respect to the carrier phase is the compressibility of the dispersed phase. This makes it necessary to consider the spherical contribution of the unresolved fluxes. During this thesis, no LES computation of two-phase flow was performed. Only the theoretical aspects of LES were addressed such as the different contributions of the subgrid kinetic energy that were identified. The "DNS" analysis and comparison to Lagrangian computations of two-phase flows leads to the following remarks for the simulation of such flow.

- The dispersed phase behaves, depending on the Stokes number, like a highly compressible flow. Therefore a numerical scheme is necessary to handle such compressibility effects. If numerical resolution is insufficient to resolve the number density the number density can be filtered. This requires a subgrid model, that acts on the compressible component of the dispersed phase velocity.

- Energy transfer as studied in sections 2.7.2, and 4.1 is more complex in the case of two phase flow than of incompressible energy. For length scales larger than the average "free path" length of the particles are well captured but smaller length scales are badly captured by the Eulerian method. Modeling of subgrid scales in an Eulerian LES should therefore content itself to reproduce the behavior of the dispersed phase at length scales larger than the mean "free path" length.

The reactive component of two-phase flow has not yet been addressed. This is the subject of the next chapter (chapter 6).

Chapter 6

Reactive two phase flows: One-dimensional laminar two-phase flames

Mephistopheles. *Da sieh nur: welch bunten Flammen !*
Es ist ein muntrer Klub beisammen.
Im Kleinen ist man nicht allein.
Faust. *Doch droben möcht ich lieber sein !*
Schon seh ich Glut und Wirbelrauch.
Dort strömt die Menge zu dem Bösen;
Da muß ich manches Rätsel lösen.
Goethe, Faust, 1. Teil, Walpurgisnacht

One-dimensional two-phase flames are an important generic problem for reactive two-phase flows and offer a basic test case for a reactive two-phase code. They allow to test how the models for reactive flows such as source terms for species and internal energy couple with the source terms and models specific to chemical reactions and the terms specific to two-phase flows such as evaporation, heat transfer and drag.

This chapter contains a brief introduction to the continuous conservation equations for a one-dimensional two phase flame. The necessary source terms, evaporation, heat transfer and drag force are then discussed and the chosen approximations justified. The structure of a one-dimensional two-phase flame is presented as a perturbation of a purely gaseous one-dimensional flame and the effects of the different source terms are explained. Numerical results for one-dimensional flame with ethanol droplets are presented and the effect of droplet diameter on the flame structure is discussed.
Since meshes used for numerical computations in realistic geometries hardly ever allow to resolve the flame structure, a turbulent sub-grid combustion model is necessary. This difficulty is found in both purely gaseous and two-phase flames. For the present work, liquid flames are thickened exactly as gaseous flames [17] : this extension is described here

and numerical results for the case of the one-dimensional flame with ethanol droplets is presented.

Experimentally one-dimensional flames are difficult to set up. Usually basic experimental studies on flames are performed on steady strained counterflow flames. Those flames can be measured for several degrees of strain rate and their internal structure can be studied and compared to numerical results obtained with appropriate numerical treatments ([19],[39]). Nevertheless such flames are not easy to handle numerically and were excluded for a first test case. Experimental data on one-dimensional two-phase flames is rare. Some information on flame speed for the ethanol flame is given by Hayashi et al. [40].

One-dimensional two-phase flames have been studied analytically by Lin et al. [55] [56] or Saulnier [85]. They consider the liquid phase as a perturbation on the gaseous flame and perform a perturbation expansion. The perturbative results lead to interesting insight in the response of a two-phase flame on the change of equivalence ratio and droplet diameter. Analytical solutions can furthermore be used to initialize the computation of a one-dimensional two-phase flame and then be used as a reference solution to validate computational results [85].

Numerical studies on one-dimensional two-phase flames have been done by Versaevel [108] and BenDakhlia [18]. BenDakhlia uses an extension of the *CHEMKIN* package with a detailed treatment chemical kinetics and transport coefficients. A multi-class droplet formulation allows to perform computations of realistic droplet size distributions. The numerical formulation is implicit and supposes the existence of a steady state.

In the present study a simplified two-phase flame formulation is considered (one-step chemistry and one droplet size). The main objective is to demonstrate that it is possible to compute a one-dimensional two-phase flame in an Eulerian formulation with the chosen numerical tool and that the extension of the thickened flame (TF) model is valid.

6.1 Laminar two-phase flames

The basic configuration studied here is sketched in Fig. 6.1. While the usual flame prototype for gaseous fuels is the laminar propagating planar flame, which is studied in its own reference flame, the two-phase flame needs more attention : it is useful to characterize 1D two-phase flames by considering three zones: the injection zone (IZ), where liquid and gaseous fuel is mixed with air, the evaporation zone (EZ), where the liquid fuel evaporates and the combustion zone (CZ), where the reaction takes place. A simple classification may be proposed depending on the relative position of the three zones:

1. If the IZ is far away from the CZ, ie. if the flame is far from the place, where liquid fuel is injected and the air is not saturated in gaseous fuel, the fuel evaporation process will be completed before the flame. Then the EZ is located well before the flame and may overlap with the IZ. A sketch of such a flame structure is given in the upper graph of Fig. 6.1.

2. When the air is saturated in gaseous fuel before the flame, evaporation will take place

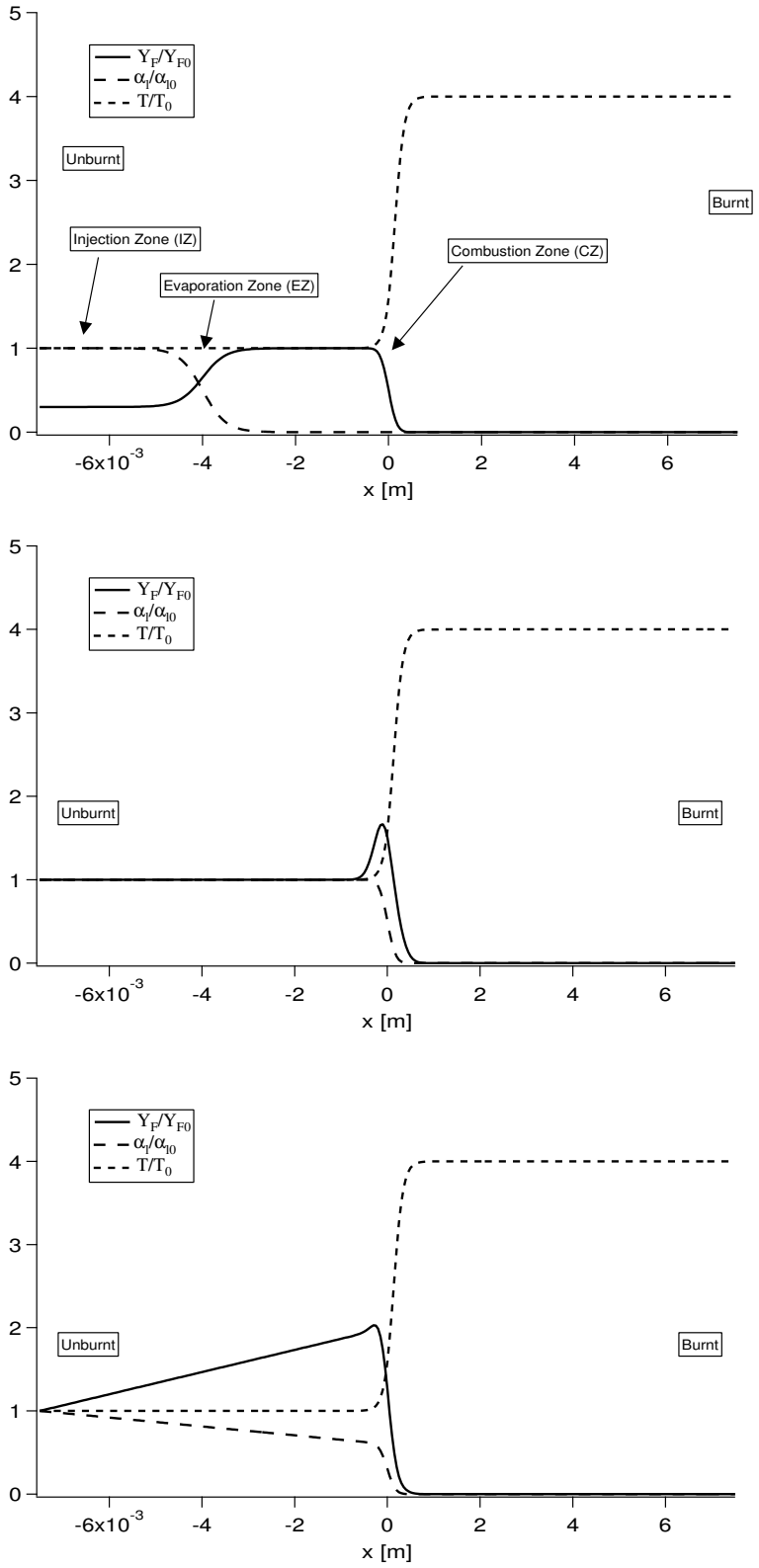

Figure 6.1: Sketch of two-phase flame types: preevaporized flame (upper graph), saturated flame (middle graph), and anchored flame(lower graph). Only the preevaporized and the saturated flame can be computed in their reference frame as steady solutions.

also in the pre-heating zone of the flame. In this case the EZ overlaps with the CZ. Such flames are called "saturated" flames by Ben Dakhlia [18]. What is called an "anchored" flame by Ben Dakhlia, is characterized by an EZ before the flame which is attached to the inlet. If evaporation is taking place in the fresh gases while the flame propagates into it, the problem cannot be formulated in the flame reference frame and must be studied in a fixed frame. In this frame (Fig. 6.1) additional quantities must be used to describe the problem: the distance between the flame and the inlet and the injection speed u_{in}. If the inlet velocity is smaller than the gaseous consumption speed, the flame zone will approach the inlet. Then liquid fuel is typically partially evaporated in the flame zone leading to a lower flame speed. At one point the two-phase flame speed is equal to the inlet velocity and the flame is stationary.

Whereas a flame speed can be defined in the case of the preevaporized and saturated flame in the sense that is an eigenvalue of the associated mathematical problem this is not so in the case of the anchored flame. If the inlet speed is lower than the consumption speed of the equivalent gaseous flame, the flame propagates towards the inlet and becomes stationary if fuel consumption is balanced by the evaporation process. In the case of an inlet speed larger than the equivalent consumption speed, the flame is pushed and there is no steady state.

6.1.1 Estimation of flame characteristics

Evaporation characteristics

One important characteristic of a two-phase flame is, where evaporation occurs: before the flame, in the flame or everywhere. Simple scalings allow to characterize the regimes using the d^2 law for evaporation [95] and the size of the domain of calculation. If the entry speed is $U_l = U_g = s_l$ and the length from the entry to the flame is l_1 the characteristic time of a droplet reaching the flame is $t_f = l_1/s_l$. On the other hand the d^2 law gives $d^2 = d_0^2 - \kappa t$ and the characteristic evaporation time in fresh gases (before the flame) is $t_{evap} = d_0^2/\kappa$. When $t_f > t_{evap}$ evaporation is completed before the flame and the theory of gaseous flames apply. This is the case for the preevaporized flame (Fig. 6.1). If on the other hand $t_f < t_{evap}$, there is evaporation within the flame and perhaps after the flame. (saturated or anchored flame). Therefore one may define a critical droplet diameter d_c as the critical diameter where evaporation is completed at the entry of the flame sheet.

$$d_c = \sqrt{\frac{l_1 \kappa}{s_l}} \tag{6.1}$$

Then two phase flames may be classified according to the critical diameter:
$d < d_c$: preevaporized gaseous flame
$d > d_c$: two-phase flame with evaporation in the flame sheet

Equivalence ratio classification

In a two-phase flame it is necessary to specify the fuel content in each phase. This leads to the definition of four equivalence ratios:

$\phi_t = s \left.\frac{\alpha_g \rho_g Y_F + \alpha_l \rho_l}{\alpha_g \rho_g Y_O}\right\|_{inlet}$	global equivalence ratio: liquid + gaseous fuel at the inlet to gaseous oxygen
$\phi_g = s \left.\frac{Y_F}{Y_O}\right\|_{inlet}$	gaseous equivalence ratio: gaseous fuel at the inlet to gaseous oxygen
$\phi_l = s \left.\frac{\alpha_l \rho_l}{\alpha_g \rho_g Y_O}\right\|_{inlet}$	liquid equivalence ratio: liquid fuel at the inlet to gaseous oxygen
$\phi_f = s \left.\frac{Y_F}{Y_O}\right\|_{flame}$	gaseous and preevaporised equivalence ratio: gaseous fuel at the flame sheet to gaseous oxygen

The sum of gaseous and liquid equivalence ratio lead to the global equivalence ratio.

$$\phi_t = \phi_g + \phi_l \tag{6.2}$$

Furthermore one may define a parameter Ω that compares gaseous to total fuel content as

$$\Omega = \frac{\alpha_g \rho_g Y_F}{\alpha_l \rho_l + \alpha_g \rho_g Y_F} \tag{6.3}$$

This parameter allows to classify flames from pure liquid injection ($\Omega = 0$) to purely gaseous cases ($\Omega = 1$).

6.1.2 Flame classifications

Due to the complexity of two-phase flames, multiple classifications can be introduced. In the next section two-phase flames are classified according to their evaporation characteristics and the equivalence ratio. To some point the two classifications are linked since the evaporation characteristics influence the gaseous fuel content.

Classification based on equivalence ratio

Here the classification of Lin et al. [55, 56] is adopted. Lin et al. consider first gaseous equivalence ratio and then global equivalence ratio: (ϕ_g, ϕ_t). d_{inc} characterizes the inlet droplet diameter, d_{st} the droplet diameter at the flame sheet. The different combustion regimes are illustrated in figure 6.2. Globally two types of flames exist.

1. The simplest case occurs when droplets evaporate completely before the flame sheet (middle sketch in Fig. 6.2): the structure of the flame is that of a usual premixed flame.

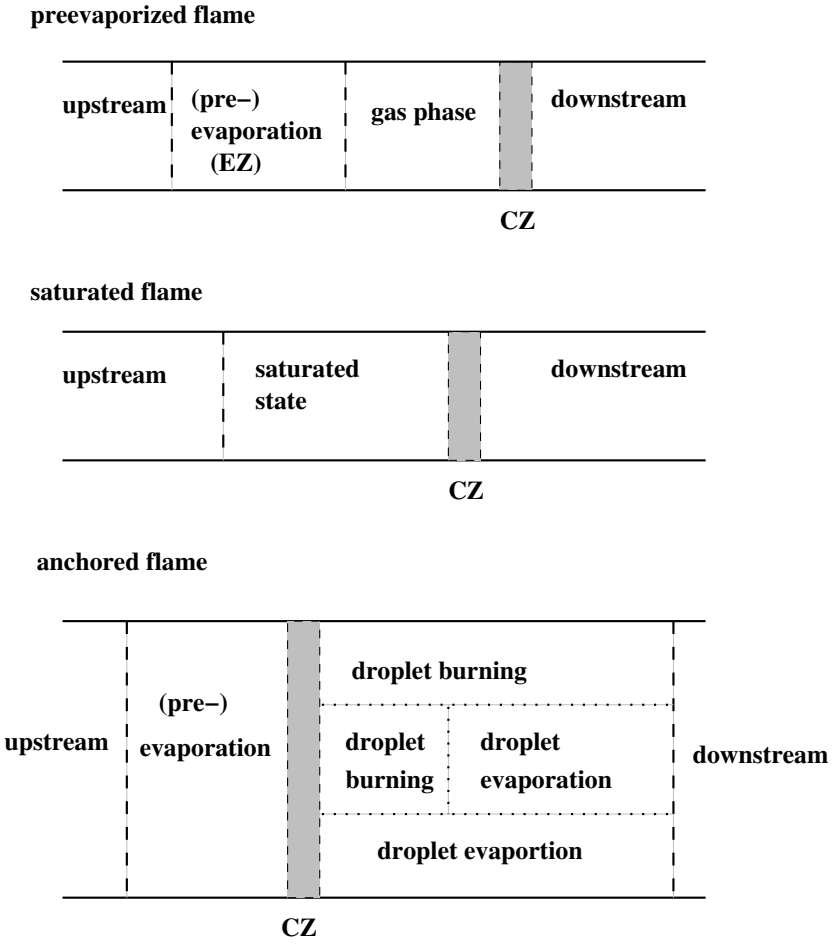

Figure 6.2: Zoology for two phase flames with evaporation before and after the flame sheet

2. The more complicated case occurs when droplets are bigger than the critical droplet diameter and enter the flame sheet. This leads to different combustion regimes explained in the following section.

6.1.3 Structure and properties of a two-phase flame

In order to understand the structure of a two phase flame it is very instructive to begin with a purely gaseous flame and consider fuel droplets as a perturbation on the gaseous flame *. Here the structure of a laminar flame is first recalled to the extend necessary to understand the basic interactions with the dispersed phase.

*See [75], chapter 2 for a detailed discussion on one-dimensional laminar flames

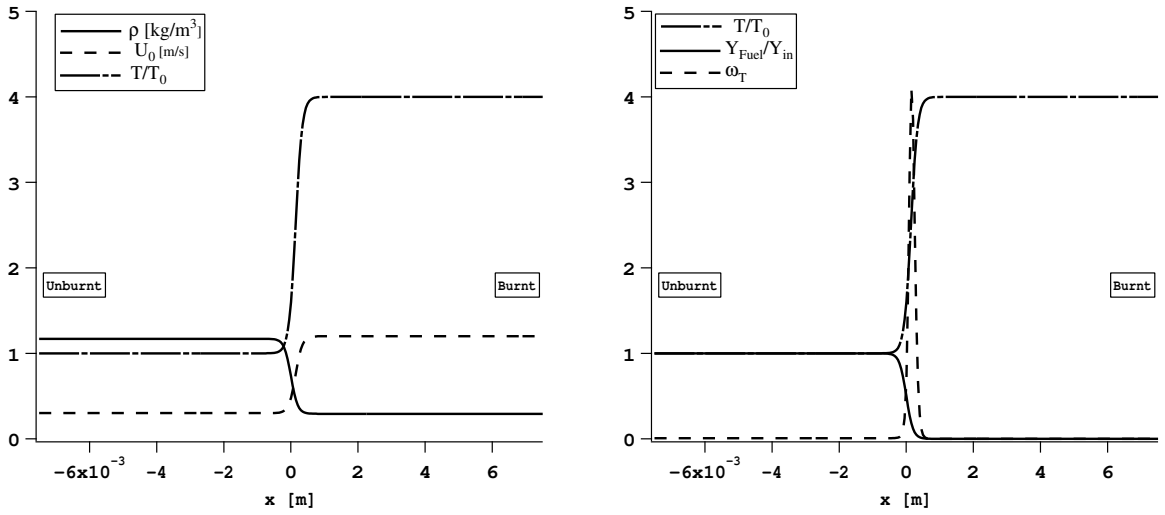

Figure 6.3: Sketch of the structure of a laminar gaseous flame

A simple one-step chemistry with Arrhenius law for the reaction rate and constant heat capacity is considered to explain the basic phenomena. In Fig. 6.3 the density, temperature and velocity profiles for a steady one-dimensional flame are given on the left graph whereas temperature, fuel mass fraction and reaction rate (heat release) are given on the right graph. Neglecting the small pressure jump at the flame sheet, a steady one-dimensional flame has the following properties:

$$\rho T = const \tag{6.4}$$

$$\rho U = const \tag{6.5}$$

$$Y_F = \frac{C_p}{Q}\left(T(x) - T_{in}\right) \tag{6.6}$$

Heat diffuses from the hot burnt side to the side where the un-burnt gases are present. If the temperature is sufficiently high to overcome the necessary activation energy, fuel and oxygen are consumed to produce heat and the corresponding combustion products such as CO_2, H_2O etc. Flame speed and the thickness of the reaction rate are governed by heat (and species) diffusion and the stiffness of the reaction rate [†].

If fuel droplets are added to such a flow, they are subject to heat transfer from the gas and mass exchange with the gas. Usually the heat transfer between the droplets and the gaseous phase is modeled proportional to the temperature difference between the carrier gas and the liquid fuel temperature. Supposing, that the temperatures at the inlet are identical, heat exchange becomes important when the droplets reach the zone of increasing temperature, therefore the flame sheet. Heat exchange is directly coupled to mass transfer

[†]Those properties are used in the thickened flame model to construct a model that can resolve a flame on a coarse grid

since the evaporation rate depends on the fuel mass fraction in the vicinity of the droplet and the fuel vapor content at equilibrium. At the computational inlet fuel vapor content is typically not saturated and therefore moderate evaporation takes place. When the droplets approach the zone of the reaction rate, the temperature of the liquid fuel increases and therefore shifts the fuel saturation pressure to higher values. This increases the fuel vapor content at the droplet surface and the steeper gradient of fuel mass fraction from the droplet surface to the gaseous phase increases fuel diffusion into the carrier gas. Therefore the evaporation source term becomes increasingly important, when the droplet reaches the flame sheet. In the flame sheet fuel is then consumed as in a normal gaseous flame.

Since heat and mass transfer are directly proportional to the surface on which exchange can take place, both heat and mass transfer are proportional to the square of the the fuel droplet diameter. For preevaporized cases, in cases where droplets are smaller then the critical diameter d_c (see Eq. 6.1), that is droplets evaporate completely before the flame sheet with the thermodynamic conditions present at the computational inlet, the flame structure remains essentially unchanged compared to the purely gaseous flame (see Fig.6.2, upper graph). If particles penetrate into the reaction zone the change of flame structure depends on the different equivalence ratios. This is illustrated in Fig. 6.2 [‡]. The droplets themselves will undergo vaporization. Droplet burning is divided by Lin et al. into two different combustion regimes: isolated droplet combustion or group combustion.

- Isolated droplet combustion occurs, if the distance between droplets is sufficiently large and a diffusion flame may exist around the isolated droplet. Then the isolated droplet may burn in a mode illustrated in Fig. 6.4. Heat diffuses from the reaction zone to the droplet and enhances evaporation whereas fuel diffuses from the droplet surface to the reaction zone. The oxidizer diffuses from the gaseous side to the reaction zone. With the assumptions of quasi-steady combustions (constant droplet diameter) and infinitely fast chemistry this two-phase combustion mode can be treated analytically [10].

- Group combustion can be divided into three subtypes [10].
  Depending on the distance between droplets and the radius a diffusion flame an isolated droplet would have in an isolated droplet regime with the same diffusion and fuel properties. A sketch of the group combustion regime is given in Fig. 6.5.
  If the product of the distance between droplets and diffusion flame radius is small, the droplet cloud is said to be dense and a flamelet around a small number of droplets will exist. This corresponds to a diffusion flame around a group of droplets.
  If the product of the distance between droplets and the diffusion flame radius is large the droplet cloud is said to be diluted and small flamelets will exist between the droplets. If the product of the inter-particle distance and the diffusion flame radius is about unity, infinitely long diffusion flamelets coexist with flamelets around groups of particles and gas depending on the local mixture fraction.
  Two group combustion regimes are illustrated in Fig. 6.6.

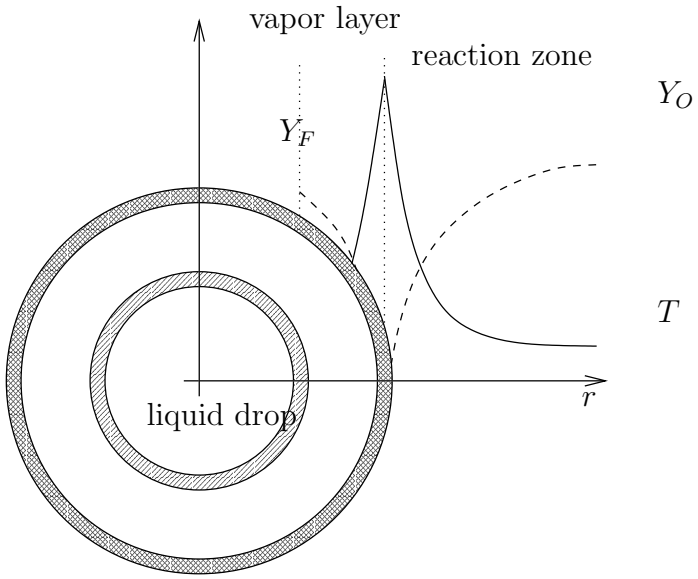

Figure 6.4: Sketch of isolated droplet combustion.

It is questionable, whether the evaporation and heat exchange model derived for an isolated droplet together with a reaction rate model taken from gaseous premixed combustion can be used to describe a laminar two-phase flame, that may undergo the combustion modes previously described. Comparison of experiments with computations of steady strained laminar counterflow flames charged with fuel droplets seem to indicate however, that global non chemical quantities are correctly predicted by such rough models [19],[39]. It is however doubtful, if intermediate species of combustion depending on the combustion regime are correctly predicted.

Experiments and computations of laminar two-phase flames lead to a non-trivial dependence of the flame speed on the global equivalence ratio. If the liquid content tends to zero, the behavior for flame speed of a purely gaseous flame is recovered. If a large amount of fuel is initially in liquid form, elevated flame speeds are also found for large ($\phi_t \gg 1$) equivalence ratios (Fig. 6.7).

Under the assumption that the used evaporation and combustion model correctly describe the evoked combustion types, the basic structure is dominated by evaporation. Given the temperature profile of the gaseous flame evaporation is usually limited before the flame in the region of moderate temperature. As soon as droplets enter regions of elevated temperature, evaporation becomes important and liquid fuel content diminuishes rapidly. The evaporated fuel can then be consumed and heat is released. The thickness of the two-phase flame can be altered, if droplets are sufficiently large to enter the reaction zone and deposit fuel in the region of elevated temperature. If oxidizer is present the fuel will be rapidly consumed. The thickness of this type of flame is then dominated by the evaporation mechanism. As shown by Versaevel [108] and BenDahklia [18] the flame speed

[‡]see also Lin et al. [55]

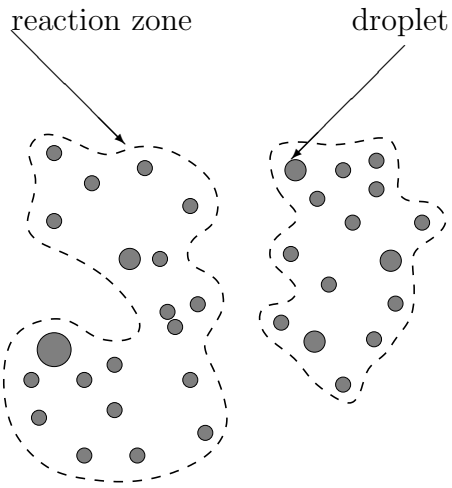

Figure 6.5: Sketch of group combustion.

dependence on equivalence ratios can be significantly modified compared to purely gaseous flames since a considerable part of the fuel is "stored" in liquid form.

In gaseous flames the flame thickness is inversely proportional to the flame speed [75]. This is not necessarily true in two-phase flames, where the thickness of the flame is not only governed by thermal diffusion, but also by the evaporation process in the case of particles entering the reaction zone. Versaevel argues, that the flame speed should be inversely proportional to the droplet diameter. This assumption is based on the idea, that the laminar flame speed is proportional to thermal diffusion and inversely proportional to a length scale ($s_l = D_{th}/\delta$). He estimates the evaporation length scale by $\delta = \tau_{evap} * s_l$ and obtains a flame speed, that is proportional to the square root of diffusion and the evaporation constant of the d^2 law. This seems to be true for very large diameters. This model can be extended by replacing the thermal diffusion with a characteristic evaporation coefficient, for instance d^2/τ_{evap}. Then the flame speed becomes proportional to the evaporation parameter from the d^2 law and inversely proportional to the diameter ($s_l \propto \kappa/d$).

6.2 The set of one-dimensional equations for two phase flows with evaporation and reaction terms

Here the one-dimensional set of equations of the Two-Fluid model as obtained by volume filtering (see [115] or [24]) are recalled and the individual source terms are explained.

The one-dimensional gaseous conservation equations can be reduced to the following set of equations, if viscous effects and geometric constraints are neglected ($\alpha_g \approx 1$) on pressure and momentum exchange terms.

$$\frac{\partial}{\partial t}\alpha_g\rho_g + \frac{\partial}{\partial x}\alpha_g\rho_g U_g = \Gamma \tag{6.7}$$

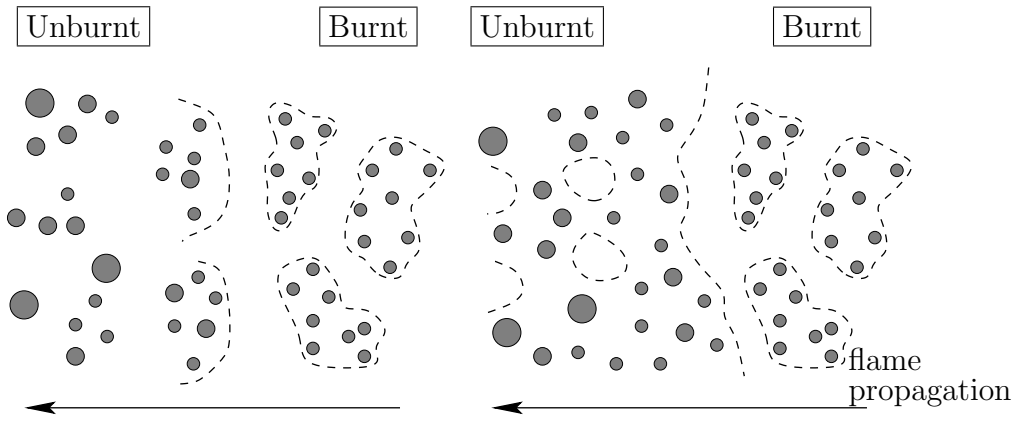

Figure 6.6: Sketch of different group combustion regimes.

$$\frac{\partial}{\partial t}\alpha_g\rho_g U_g + \frac{\partial}{\partial x}\alpha_g\rho_g U_g^2 = -\frac{\partial}{\partial x}P_g + F_{drag} + \Gamma U_g \tag{6.8}$$

$$\frac{\partial}{\partial t}\alpha_g\rho_g E_g + \frac{\partial}{\partial x}\alpha_g\rho_g U_g E_g = -\frac{\partial}{\partial x}P_g U_g - \frac{\partial}{\partial x}q_g - \frac{1}{2}\Gamma U_g^2 - \Phi - \Lambda + \omega_{th} \tag{6.9}$$

The gasesous conservation equations consist of:

- mass conservation (Eq. 6.7) with the gaseous volume fraction α_g, gaseous density ρ_g and the mass exchange term Γ due to evaporation,
- momentum conservation (Eq. 6.8) with the gaseous velocity U_g, the gaseous pressure P_g and the drag force F_g,
- total non-chemical energy (Eq. 6.9) with the energy E_g, the heat diffusion q_g the enthalpy exchange due to mass exchange Λ, the enthalpy transfer due to conduction Φ and the thermal reaction rate $\dot{\omega}_{th}$. (See notations and definitions in section 1.4)

The continuous form of the dispersed phase equations is the following:

$$\frac{\partial}{\partial t}\alpha_l\rho_l\frac{\partial}{\partial x}\alpha_l\rho_l U_l = -\Gamma \tag{6.10}$$

$$\frac{\partial}{\partial t}n + \frac{\partial}{\partial x}nU_l = 0 \tag{6.11}$$

$$\frac{\partial}{\partial t}\alpha_l\rho_l U_l + \frac{\partial}{\partial x}\alpha_l\rho_l U_l^2 = -\Gamma U_l - F_{drag} \tag{6.12}$$

$$\frac{\partial}{\partial t}\alpha_l\rho_l E_l + \frac{\partial}{\partial x}\alpha_l\rho_l U_l E_l = -\frac{1}{2}\Gamma U_l^2 + \Phi + \Lambda \tag{6.13}$$

The dispersed phase conservation equations consist of:

- liquid mass conservation (Eq. 6.10) with the liquid volume fraction α_l, the liquid density ρ_l, the dispersed velocity U_l and the mass exchange term Γ,

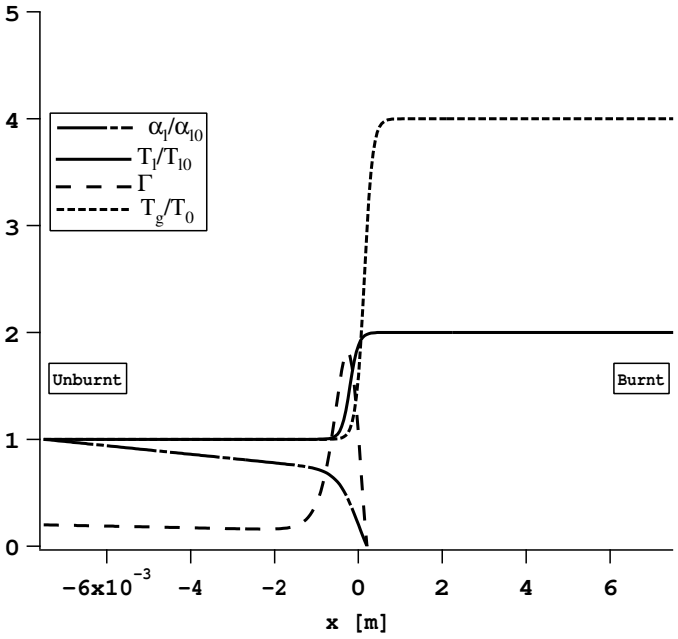

Figure 6.8: Sketch of the structure of an anchored two-phase flame . The gaseous temperature profile is given as a reference for the flame position. Mass exchange rate (evaporation) is indicated by Γ, liquid volume fraction by α_l.

- Drag F_{drag}: The Stokes law for drag has been used to couple the momentum equations. This drag force is described in section 1.1.4.
- Heat flux
- Enthalpy Exchange

6.2.1 Evaporation: mass and enthalpy exchange

The source term connecting the continuity equations for gas and droplet phase is the evaporation (more precisely the mass exchange) source term (Γ). Since evaporation is directly dependent on temperatures and vapor pressure the source term is dependent on the energy equations and the fuel species equation. Furthermore evaporation changes the energy equation since the vapor transports enthalpy from one phase to the other.

The evaporation of an isolated droplet including the physical phenomena of fuel diffusion and temperature distribution is known as the two-phase Stefan problem. Solving the Stefan problem is a numerical challenge in itself.

In a simplified microscopic viewpoint fuel molecules in the liquid droplet have a certain random motion. The mean velocity of the random motion between two collisions is governed by the thermal energy distribution. For the ideal case (black body radiation)

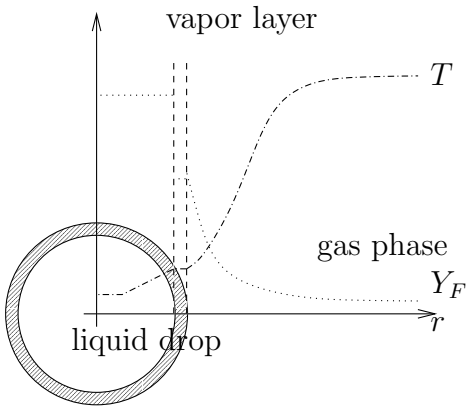

Figure 6.9: Sketch of the physical phenomena of evaporation on an isolated droplet

the thermal velocity distribution is given by Plancks law [§]. Fuel molecules have to overcome a potential barrier due to intermolecular forces in order to escape from the liquid (in the subcritical case). This potential barrier leads to the physical phenomena of surface tension. Some molecules, those in the tail of the energy distribution (Fig. 6.10), have thermal velocities that enable them to overcome the potential barrier of surface tension and escape from the liquid droplet. These molecules then add to the first layer around the droplet. Partial pressure of vapor with the local thermodynamic conditions is given by the Clausius-Clapeyron equation 6.17 (see also Fig. 6.12). The energy consumed by the molecule to overcome the potential barrier of surface tension leads to the introduction of the latent heat of evaporation in the macroscopic model. Since the most energetic molecules leave the liquid at the surface, the mean temperature of the droplet will decrease and so will the temperature distribution. This causes a temperature difference between the droplet and the surrounding gas. If the molecules of the gas have a thermal velocity distribution corresponding to a higher temperature, they will transfer energy via collisions at the liquid surface. The temperature difference depends therefore on the mass flow rate of fuel molecules leaving the liquid droplet and the thermal diffusion in the surrounding gas heating the droplet.

This picture of the isolated droplet in the absence of convective motion of the carrier phase gas is the idealized case. A relative velocity of the carrier phase gas and the droplet may induce an internal convection in the droplet via surface friction. This internal flow tends to make the temperature distribution in the droplet more uniform. For small droplets (some microns) and small relative velocities the Reynolds number for the internal motion are however small and this can be considered as a second-order effect. The other effect of

[§]Plancks law for black body radiation gives a thermal energy distribution of the form

$$E(\omega)d\omega \approx \frac{\hbar}{\pi^2 c^3} \frac{\omega^3 d\omega}{\exp(\hbar\omega/kT) - 1} \tag{6.16}$$

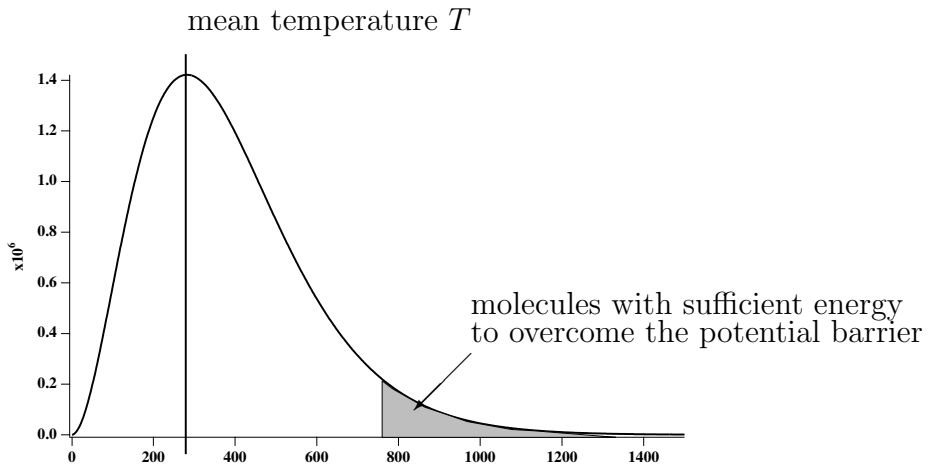

Figure 6.10: Thermal energy distribution of a black body.

a relative velocity between the droplet and the carrier phase is the enhanced transport of fuel molecules from the droplet surface to the gas lowering the gaseous fuel mass fraction in the vicinity of the droplet and the enhanced exchange of enthalpy. Those rather complex phenomena of heat and mass transport in the presence of a convection velocity require the solution of the gaseous Navier-Stokes equations around the droplet for an exact solution. Since it is numerically expensive to solve those equations for a large number of droplets this effect is typically taken into account by empirical correlations for the *Nusselt* and *Sherwood* numbers.

Fuel molecules, once escaped from the droplet, may encounter an oxidizer in the vicinity of the droplet and chemical reactions may occur. Typically activation energies for hydrocarbon fuels are nevertheless well above the boiling temperatures of the liquid fuel, so that this can also be classified as a second-order effect.

Realistic fuels are multicomponent mixtures of hydrocarbons containing small amounts of sulfur and other species. Evaporation of such mixtures is significantly more complicated. "Light" molecules tend to evaporate more quickly since their kinetic energy is typically bigger after a collision with a "heavy" molecule due to energy and momentum conservation. Spurious amounts of other species may be sufficient to change surface tension and the associated potential barrier. Multicomponent evaporation has been addressed by Sirignano [95]. It is not considered here since the gasesous combustion model currently assumes a single fuel species and multicomponent fuel combustion is not yet considered.

This microscopic description of evaporation has to be formulated so that it can be treated with the macroscopic conservation equations of mass and fuel species conservation and temperature or enthalpy conservation.

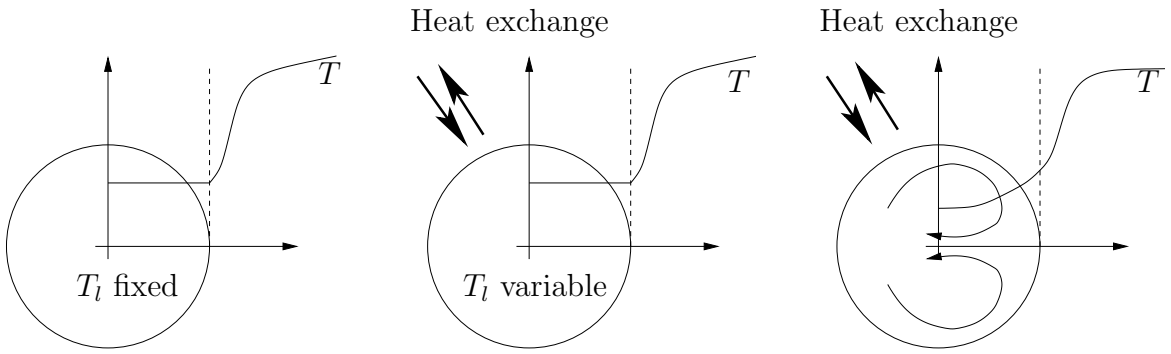

Figure 6.11: The different evaporation models: from left to right, fixed temperature model, uniform temperature model and resolved temperature model

Existing models

In the literature several evaporation models exist. They usually assume the existence of an isolated droplet and evaluate the mass flux from a local thermodynamic equilibrium at the droplet surface. The existing evaporation models have been discussed for instance by Siringano [15] [1] [94] and Bellan [63].

Depending on the degree of physics desired and the amount of computational effort that can be afforded, evaporation models for isolated droplets can be divided into four groups.

1. d^2 **law:** This model assumes constant mass transfer per unit surface from the liquid phase to the gaseous phase depending only on the droplet surface. Effects related to varying droplet temperature and fuel vapor concentrations are not directly taken into account. The droplet temperature is actually directly imposed by the quasi-steady assumption used for heat and species transport. The model is numerically very simple and stable. Since the evaporation time can be computed algebraically, numerical instabilities can be avoided.

2. **fixed droplet temperature model:** This model does not require an energy or temperature equation for the liquid phase since the droplet temperature is assumed constant. Partial pressure of fuel at the droplet surface can only change with the surrounding gaseous pressure and therefore the mass transfer rate depends essentially on the fuel mass fraction of the gas in the vicinity of the droplet.

3. **uniform temperature model:** The droplet temperature is assumed to be uniform within the droplet but can vary with time. This is equivalent to assuming infinitely fast temperature conduction in the droplet. The partial pressure of fuel vapor of the droplet depends on the droplet temperature and the surrounding gaseous pressure. Since the fuel vapor content at the droplet surface depends on the partial pressure of fuel, the evaporation rate depends indirectly on droplet temperature and directly on the fuel mass fraction of the gas in the vicinity of the droplet.

4. **resolved temperature model:** In this model the temperature distribution within the droplet is resolved. This requires a numerical solution of the temperature distribution in the droplet. Some models also take the internal convection of the liquid due to drag into account. This requires to solve the full Navier-Stokes equations in the droplet. Therefore this model is the most physical and but also the most expensive.

The list of evaporation models is not exhaustive: subclasses and variations of these evaporation models do exist. Here the uniform temperature model is chosen. It provides a reasonable tradeoff between computational effort and treatment of physical phenomena, since it captures the desired effects of temperature-dependent heating and evaporation essential to treat evaporation in a correct manner in the vicinity of the flame front. If droplets are small compared to the surrounding length scales, this model is quite reasonable.

The uniform temperature model and the corresponding thermodynamic state at the droplet surface

Two essential hypothesis are made for this evaporation model:

1. infinite conductivity for temperature
2. other thermodynamic mechanisms are fast compared to evaporation: the droplet is in quasi-equilibrium.

With those two drastic assumptions we assume that the droplet and its surrounding surface vapor layer have a uniform temperature T_d. Then the partial pressure of the vapor at the droplet surface $p_{F,\zeta}$ is given by the Clausius Clapeyron equation ([120],[42]):

$$p_{F,\zeta} = p_{cc} \exp\left(\frac{\Delta H W_F}{R}\left(\frac{1}{T_{cc}} - \frac{1}{T_l}\right)\right) \tag{6.17}$$

Knowing the partial vapor pressure one may determine the fuel mass fraction at the droplet surface as:¶

$$Y_{F,\zeta} = \frac{p_{F,\zeta} W_F}{p_{F,\zeta} W_F + (p - p_\zeta) W_g} \tag{6.18}$$

The total density at the droplet surface is then:

$$\rho_\zeta = \frac{p_{F,\zeta}/p_{tot} W_F + (p - p_{F,\zeta})/p W_g}{R T_\zeta} \tag{6.19}$$

the partial fuel vapor density is given by:

$$\rho_{F,\zeta} = \frac{p_{F,\zeta}/p W_F}{R T_\zeta} \tag{6.20}$$

¶If the molar mass of the gas is not assumed constant but dependent on the species this equation needs to be corrected for varying gaseous molar mass. This can be done by introducing a correction factor and leads to $Y_{F,\zeta} = \frac{P_{F,\zeta} W_F}{P_{F,\zeta} W_F + (P_g - P_{F,\zeta}) \bar{W}_g \frac{1 - Y_{F,g}}{1 - Y_{F,g} \bar{W}_g / W_F}}$ see appendix C.1.

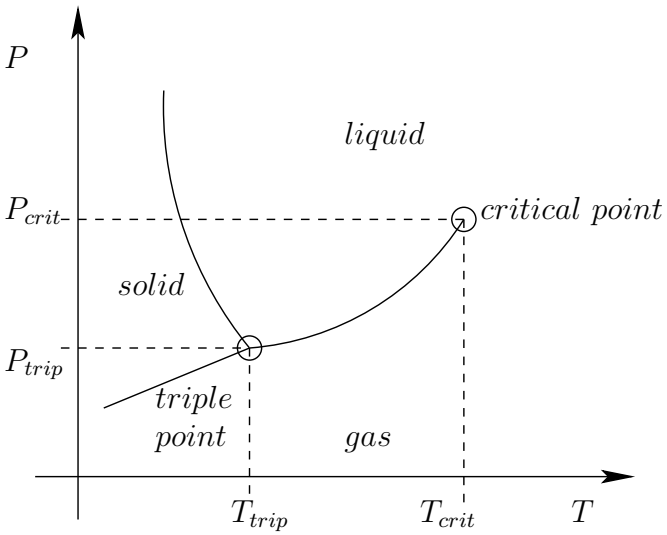

Figure 6.12: Clausius Clapeyron Graph: Given the values of one point of (T, P) on the Clausius Clapeyron line connecting the triple point with the critical point the Clausius Clapeyron equation (Eq. 6.17) defines the partial pressure of the liquid vapor on the droplet surface

and the partial density of the other gas is given by:

$$\rho_{F,\zeta} = \frac{\left(p - p_{F,\zeta}\right)/pW_F}{RT_\zeta} \tag{6.21}$$

Once the thermodynamic properties at the droplet surface are known, the fuel mass flux from the liquid surface corresponding the molecules leaving the liquid needs to be modeled. This is done in the following section.

Mass transfer model

Obviously, solving the Navier-Stokes equations around each droplet is impossible. The usual technique is to solve these equations around an isolated droplet and assume, that the result for the evaporation rate can be used for all droplets. Traditionally a quasi steady assumption for the flow around each droplet is made [120]. This enables one to neglect the temporal derivatives in the conservation equations. The fluxes of the gaseous continuity equation and the gaseous fuel species conservation equation in absence of the reaction term can be combined to obtain the following flux balance equation at the droplet surface (indexed with ζ).

$$\rho_g u_g|_\zeta = \rho_g u_g Y_F|_\zeta - \rho_g D \frac{\partial}{\partial x} Y_F \bigg|_\zeta \tag{6.22}$$

This allows to determine the gaseous bulk velocity normal to the surface by solving Eq. 6.22 for u_g:

$$u_g = \frac{D\frac{\partial}{\partial x}Y_F\Big|_\zeta}{Y_{F,\zeta} - 1} \tag{6.23}$$

Spalding introduced at this point a parameter that allows to compare the fuel mass fraction at some distance r from the surface to the fuel mass at the droplet surface $r = r_\zeta$.

$$b = \frac{Y_F}{Y_{F,\zeta} - 1} \tag{6.24}$$

In the case of an isolated droplet the mass transfer due to evaporation can be evaluated analytically ([120]) using the conservation equation for fuel mass fraction in spherical coordinates outside the droplet and thus omitting the evaporation source term. The objective is then to obtain an analytical expression for the fuel diffusion outside the droplet with a matching condition at the surface:

$$r^2\rho_g u_g b = r^2\rho_g D\frac{\partial}{\partial x_b} + const. \tag{6.25}$$

Application of boundary conditions and partial integration supposing $\rho_g D$ to be constant then yields an analytical expression:

$$-\frac{r_\zeta^2 u_{g,\zeta}}{rD_\zeta} = \ln\left(b - b_\zeta + 1\right) + const. \tag{6.26}$$

Finally Spalding introduced the mass transfer number B. It measures the difference in fuel vapor at the droplet surface and the surrounding gas is then weighted by $\frac{1}{1-Y_{F,\zeta}}$:

$$B = \frac{Y_{F,\zeta} - Y_{F,g}}{1 - Y_{F,\zeta}} \tag{6.27}$$

Physically, this implies that by approaching the Clausius Clapeyron line, the mass transfer number would tend to infinity. Combination of the previous definitions leads then to the final expression for the mass transfer term:

$$\Gamma = \alpha_l\frac{6}{d^2}Sh\left[\rho_\zeta D_\zeta\right]\ln\left(1 + B\right). \tag{6.28}$$

Here the *Sherwood* number is used (Sh) to correct for enhanced evaporation if a relative velocity is present:

$$Sh = 2.0 + 0.55Re_d^{1/2}Sc^{1/3} \tag{6.29}$$

This correlation for the Sherwood number depending on the Reynolds number of the droplet[‖] and the Schmidt number Sc for fuel diffusion is often called the Ranz-Marshall law.

[‖] The Reynolds number of the droplet is defined with the droplet diameter, the relative velocity and the gaseous viscosity $Re_d = \frac{d|u_g - u_d|}{\nu}$

The mass transfer model Eq. 6.28 does not reproduce perfectly the measured values of evaporation and an empirical correction of the evaporation law that corrects temperature and fuel mass fraction at the surface [47]:

$$\tilde{T} = T_\zeta + A(T_\infty - T_\zeta) \tag{6.30}$$
$$\tilde{Y}_F = Y_{F,\zeta} + A(Y_{F,\infty} - Y_{F,\zeta}) \tag{6.31}$$

Since experimental data is best fitted when choosing $A = 1/3$, this is often referred to as the 1/3 law [47]. Since here only mono-dispersed sprays are considered, the droplet diameter is obtained from the following relations:

$$\alpha_l = \frac{n\pi}{6} d^3, \qquad d = \left(\frac{6\alpha_l}{n\pi}\right)^{1/3}, \quad \frac{1}{d^2} = \left(\frac{n\pi}{6\alpha_l}\right)^{2/3} \tag{6.32}$$

Using the above relations the source term for droplet evaporation is written as follows:

$$\Gamma = \alpha_l^{1/3} 6^{1/3} (n\pi)^{2/3} Sh \left[\rho D\right]_{1/3} \ln(1+B) \tag{6.33}$$

Enthalpy Exchange

The enthalpy exchange in between the two phases (Eqs. 6.9, 6.13) can be divided into two components: Λ due to mass exchange and Φ due to conduction. The construction of the macroscopic enthalpy exchange Λ depends on the definition of the latent heat of evaporation. For a consistent enthalpy exchange that takes into account the total energy loss due to phase change the definitions of enthalpies and latent heat of Miller and Bellan [62] are used and their argumentation is followed here. As for mass transfer the objective is to formulate a model such as the macroscopic conservation equations describe the microscopic physical behavior. The enthalpy of the liquid phase for the incompressible liquid is defined as $h_l = \int_0^T C_L(T')dT'$. The enthalpy of vapor for the same species is defined as $h_V = h_V^0 + \int_0^T C_{p,V}(T')dT'$ and the reference enthalpy is taken to be zero at $T = 0$. The index V stand for fuel vapor. Enthalpies of fuel in the vapor phase and liquid fuel are not independent. The latent heat of evaporation is defined as the enthalpy difference $L_V = h_{V,\zeta} - h_{L,\zeta}$ between liquid and vapor phase at equal temperatures at the liquid surface. Combining the definition of latent heat of evaporation with the definitions for liquid and vapor enthalpies yields:

$$h_V^0 = L_V(T^*) + \int_0^{T^*} \left(C_L(T') - C_V(T')\right) dT' \tag{6.34}$$

For constant heat capacities (perfect gases) the enthalpy equation is with the above considerations:

$$h_{V,\zeta} = C_{p,V} T + h_V^0 \tag{6.35}$$
$$L_V = h_V^0 - (C_L - C_{p,V}) T_\zeta \tag{6.36}$$

and the gaseous internal energy at the droplet surface is defined as:

$$e_i = (1 - Y_{F,\zeta}) (C_{v,g} T_\zeta) + Y_{F,\zeta} \left(C_{v,V} T_\zeta + h_V^0 \right) \tag{6.37}$$

In order for the assumption of constant heat capacities to be consistent, the heat capacity of fuel vapor at the droplet surface must be equal to the liquid heat capacity ($C_L = C_{p,V}$). The transfer of enthalpy due to heat conduction, Φ is again modeled by a gradient assumption. Then the heat transfer is proportional to a conductivity constant (λ_g) the droplet surface (d^2) and the temperature difference (ΔT):

$$\Phi = -\alpha_l \lambda_g Nu \frac{6}{d^2} (T_l - T_g) \tag{6.38}$$

As in the mass transfer model, this law needs to be corrected for unsteady and turbulent effects. For a constant Nusselt number Nu this model is valid only in steady atmosphere. For the Nusselt number often a Ranz-Marshall type correlation is assumed:

$$Nu = 2.0 + 0.55 Re_d^{1/2} Pr^{1/3} \tag{6.39}$$

Pr is the Prandtl number that compares the diffusion of temperature to the diffusion of momentum.

6.2.2 Consumption flame speed of a saturated two-phase flame

Here a formula for the consumption flame speed of a saturated two-phase flame is derived (Fig. 6.1a). It is not possible to apply this formula to an anchored flame, since its flame speed is equal to the inlet velocity. In order to calculate the consumption flame speed of a two-phase flame the equations of continuity (Eq. 6.7, 6.10) and fuel balance (Eq. 6.14) are written in the reference frame of the flame sheet and integrated:

$$\int_{-\infty}^{\infty} \alpha_g \rho_g U_g dx = \int_{-\infty}^{\infty} \Gamma dx \tag{6.40}$$

$$\int_{-\infty}^{\infty} \alpha_l \rho_l U_l dx = -\int_{-\infty}^{\infty} \Gamma dx \tag{6.41}$$

$$\int_{-\infty}^{\infty} \alpha_g \rho_g U_g Y_F dx = \int_{-\infty}^{\infty} \dot{\omega}_F dx + \int_{-\infty}^{\infty} \Gamma dx \tag{6.42}$$

The integral fuel consumption is $\dot{\Omega}_F = \int_{-\infty}^{\infty} \dot{\omega}_F dx$. For a steady flame, the fresh gas velocity is equal to the consumption speed and one obtains by combining equations 6.40, 6.41 and 6.42 the following relations:

$$[\alpha_g \rho_g U_g Y_F]_{-\infty} = [\alpha_g \rho_g U_g Y_F]_{\infty} - \dot{\Omega}_F + [\alpha_g \rho_g U_g]_{-\infty} - [\alpha_g \rho_g U_g]_{\infty} \tag{6.43}$$

$$[\alpha_g \rho_g U_g (Y_F - 1)]_{-\infty} = [\alpha_g \rho_g U_g (Y_F - 1)]_{\infty} - \dot{\Omega}_F \tag{6.44}$$

$$[\rho_g U_g]_{\infty} = [\alpha_g \rho_g U_g]_{-\infty} + [\alpha_l \rho_l U_l]_{\infty} \tag{6.45}$$

Gas		Liquid	
C_p	1437.0 J/kgK	C_l	2431.0 J/kgK
W_m	0.029 $kg/mole$	W_m	0.046 $kg/mole$
ρ_{in}	1.17 kg/m^3	ρ_l	816.0 kg/m^3
E_{activ}	20000 cal/mol	L_V	911000 J/kg
Q_{reac}	23653 J/g	p_{cc}	101330 Pa
A	10^{10}	T_{cc}	351 K
		D	$6 * 10^{-5}$ m^2/s
		λ	$1 * 10^{-2}$ J/smK

Table 6.1: Physical and thermo-chemical properties of the one-dimensional two-phase flame. Thermo-chemical data on ethanol was taken from the web-site *http://webbook.nist.gov*. Diffusion and heat conductivity parameters are adjusted such as to find typical evaporation times found in literature. The pre-exponential constant A of the Arrhenius law has not been fitted, so that the gaseous flame would match the experimental flame speed and the computed flame speed is too low.

Here complete droplet evaporation $\left((\alpha_g)_\infty = 1\right)$ and equal inlet speeds ($U_l = U_g = s_l$) are assumed to obtain the expression for the consumption speed :

$$s_c = \frac{\dot{\Omega}}{[\alpha_g \rho_g + \alpha_l \rho_l]_{-\infty} Y_{F,\infty} - [\alpha_g \rho_g Y_F]_{-\infty} - [\alpha_l \rho_l]_{-\infty}} \tag{6.46}$$

For a purely gaseous flame, $\alpha_l \to 0$ and the above equation for the consumption flame speed becomes

$$s_c = \frac{\dot{\Omega}}{[\rho_g]_{-\infty} (Y_{F,\infty} - Y_{F,-\infty})} \tag{6.47}$$

which corresponds to the gaseous consumption flame speed of a gaseous flame, as expected. **

6.3 Numerical results for a one-dimensional anchored two-phase flame

In this section numerical results for a one-dimensional two-phase flame are presented. This is done for a sample one-step chemistry with the gaseous and liquid thermo-chemical properties given in table 6.1. The flame is anchored: inlet gases are not saturated and evaporation proceeds everywhere upstream of the flame front. Those thermo-chemical properties are close to a two-phase flame with ethanol droplets, keeping in mind, that the one-step Arrhenius law and the simple evaporation law may not mimic the complex thermo-chemical process, if droplets enter the reaction zone. The inlet conditions are chosen, so

**see Poinsot [75],p.38 Eq. 2.26 for a derivation of the consumption flame speed

d $[micron]$	ϕ_g	ϕ_t	ϕ_f
10	0.53	1.19	0.8
20	0.53	1.19	
30	0.53	1.19	
40	0.53	1.19	0.56

Table 6.2: The different equivalence ratios for the computed flames

that a totally rich flame ($\phi_t = 1.19$), which is initially lean at the inlet ($\phi_g = 0.53$), is computed with an initial droplet diameter of 10 micron. The computational domain has a length of two centimeters and a spatial discretization of 300 points. Fig. 6.13 shows selected numerical results of the two-phase flame. The upper four graphs show properties of the gaseous phase whereas the lower four graphs show properties of the dispersed phase. The density and velocity profiles of the gas phase are almost identical to a purely gaseous flame whereas the fuel mass fraction increases due to evaporation and reaches a maximum just before the reaction zone where fuel is consumed. Since the total equivalence ratio is slightly rich ($\phi_t = 1.19$), there is excess fuel (Y_{fuel}) on the product side of the flame. The volume fraction of liquid fuel (α_l) decreases due to evaporation (Γ) first slowly and then faster in the vicinity of the reaction zone. The evolution of the particle diameter (d) corresponds (as expected) to the third root of the volume fraction. The particle number density n varies due to the acceleration of the droplets in the combustion products. Note here a classical paradox of an Eulerian computation: if liquid volume fraction and droplet diameter go to zero, fuel droplets are physically non-existent. Numerically the conservation equations are however continuous and give values for profiles such as velocity even in areas where the liquid volume fraction are close to zero. Therefore some care has to be taken in the interpretation of the numerical results in this regions.

It is interesting to compare fuel production by evaporation to fuel consumption by the flame. This is done in Fig. 6.14 for the two-phase flame with an initial droplet diameter of 10 micron. The evaporation rate for this configuration is maximal, when droplets enter the reaction zone. Evaporation finishes before the end of the reaction zone and the form of the reaction rate is similar to the reaction rate of a purely gaseous flame. Spatially evaporation and combustion occur simultaneously and this is handled without problem by the numerical solver. The importance of the droplet diameter on the flame structure is illustrated in Fig. 6.15. Four different droplet diameters are considered. Table 6.2 summarizes inlet conditions for the four flames. The total (ϕ_t) and gas (ϕ_g) equivalence ratios are identical for the different flames. Fig. 6.15 shows the gas phase properties on the left side and the corresponding droplet properties on the right side. With decreasing droplet diameter the droplet surface for phase exchange decreases as the square of the diameter and so does the evaporation source. Whereas the equivalence ratio just before the reaction rate is $\phi_f \approx 0.8$ in the case of the two-phase flame with droplets of 10 microns, the equivalence ratio is almost identical ($\phi_f \approx 0.56$) to the inlet equivalence ratio at the inlet (ϕ_g) in the case of the flame with diameters of 40 microns since the evaporation source term is

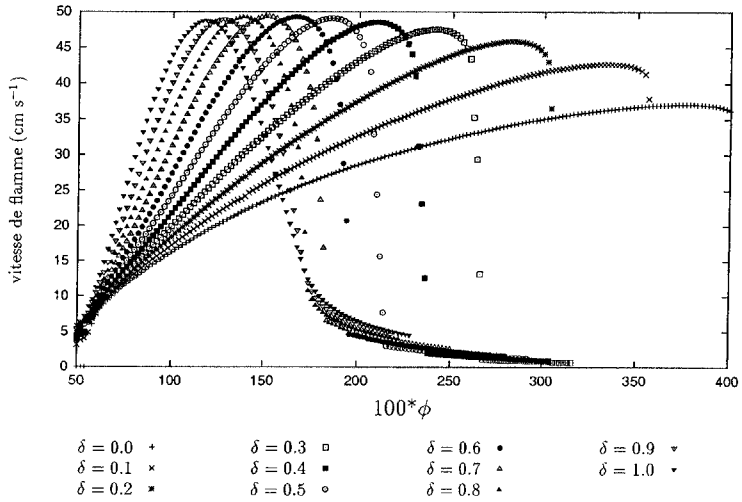

Figure 6.7: Flame speed for a laminar two-phase flame versus total equivalence ratio (Ben Dakhlia [18]). The initial droplet diameter is 20 micron. δ compares the initially gaseous equivalence ratio to the total equivalence ratio ($\delta = 1$ purely gaseous flame)

- liquid droplet number density n conservation,
- liquid momentum conservation (Eq. 6.12) with the dispersed velocity U_l and the momentum exchange term F_{drag},
- liquid sensible energy conservation E_l with the phase exchange terms Λ for the enthalpy exchange due to mass exchange and the heat conduction Φ.

Further more it is necessary to transport fuel and oxygen in the gaseous phase:

$$\frac{\partial}{\partial t}\alpha_g\rho_g Y_F + \frac{\partial}{\partial x}\alpha_g\rho_g Y_F U_g = \alpha_g\frac{\partial}{\partial x}\left(D_F\frac{\partial}{\partial x}Y_F\right) + \Gamma + \dot{\omega}_F \tag{6.14}$$

$$\frac{\partial}{\partial t}\alpha_g\rho_g Y_O + \frac{\partial}{\partial x}\alpha_g\rho_g Y_O U_g = \alpha_g\frac{\partial}{\partial x}\left(D_O\frac{\partial}{\partial x}Y_F\right) + \dot{\omega}_O \tag{6.15}$$

This yields a total of nine conservation equations that have to be fulfilled simultaneously to solve the one-dimensional two-phase flame compared to five conservation equations in a purely gaseous flame (Eqn.6.7-6.9 and 6.14,6.15).

The coupling terms for the gaseous and dispersed phase need to modeled. Theses terms are:

- Mass exchange due to evaporation (Γ): Evaporation is the coupled effect of mass and enthalpy exchange. This is briefly explained in the next section.

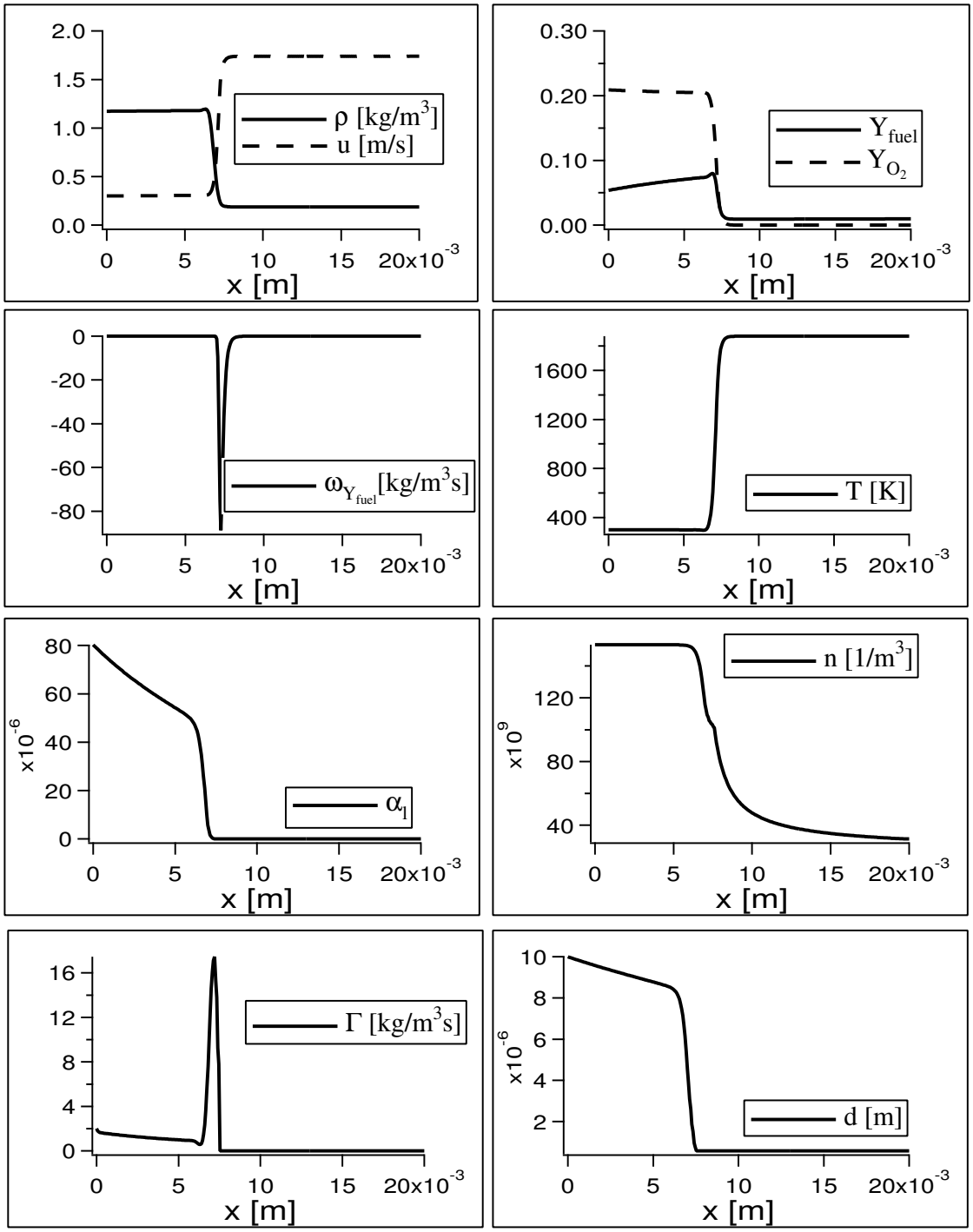

Figure 6.13: Selected properties of the numerical solution of a sample flame. The total equivalence ratio is slightly rich and the inlet diameter for the fuel droplets is 10 microns.

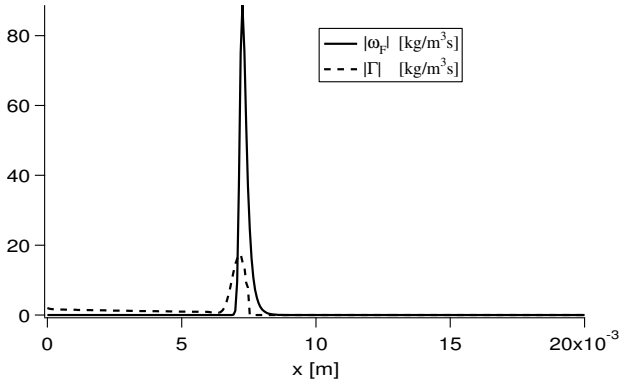

Figure 6.14: Comparison of the magnitude of fuel consumption by the flame (ω_F) and fuel production by evaporation (Γ). The droplet diameter is 10 micron.

significantly smaller. For flames with large droplets (Fig.6.16), the reaction zone can be divided into two zones: In the first zone the gaseous fuel is consumed first and leads to a lean flame and the fuel mass fraction becomes zero. The second part of the reaction zone is governed by the evaporation process and is significantly thicker. The evaporated fuel is almost instantly consumed by the flame and the fuel mass fraction of the totally rich flame increases only, if the oxidizer becomes rare. This process can be identified by comparing the gaseous fuel production by evaporation to fuel consumption of the flame (Fig. 6.16). In the case of larger droplets, the form of the reaction zone differs from the reaction rate of a purely gaseous flame or a flame with small droplets (Fig. 6.14). One clearly distinguishes the reaction zone of the gaseous lean flame from the reaction zone due to fuel evaporation in the hot gases with remaining oxidizer. In the second zone the fuel consumption by the flame is controlled by the evaporation rate of the large droplets.
Note that the view of the large droplet flames given in Fig. 6.15 matches the equation of our model but it is not clear however if this numerical solution of the eulerian conservation equations reflects the microscopic behavior when fuel droplets enter the flame sheet: droplets might burn in a completely different regime.

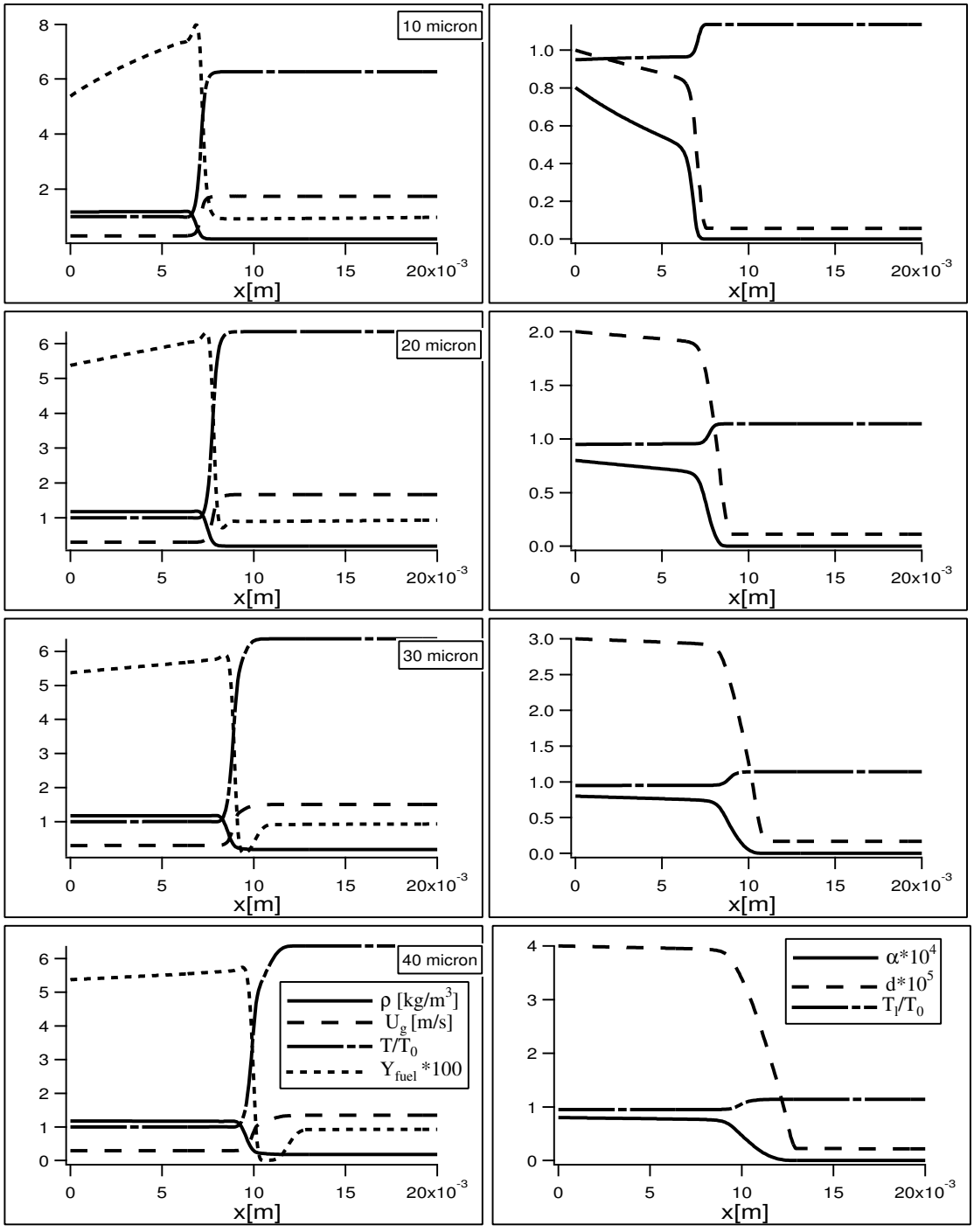

Figure 6.15: Parametric study of the influence of the particle diameter on the combustion regime

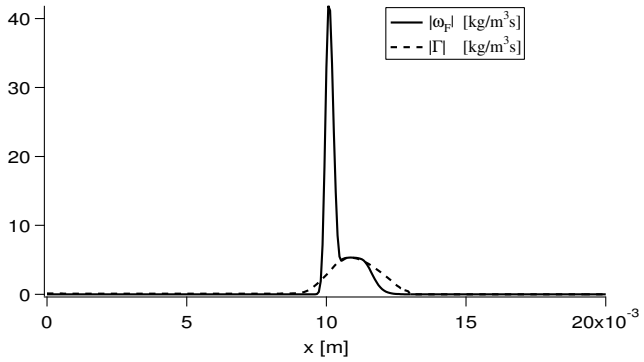

Figure 6.16: Comparison of the magnitudes of fuel consumption by the flame (ω_F) and fuel production by evaporation (Γ). The droplet diameter is 40 micron.

6.4 Turbulent combustion modeling in two-phase flows.

As in LES of reacting gaseous flows, flame sheets in two-phase flows are usually not resolved in a calculation and modeling of the reacting terms is necessary. Several methods exist for LES modeling of turbulent flames, one of them is the thickened flame (TF) model [11] [17]. This model is used here and extended to a two-phase flame.

6.4.1 Derivation of the thickened flame model for two-phase flames

The idea of the thickened flame model is to change the diffusive length and time scales of the flow while conserving the dynamic length scales. The scale transformation is: $x \leftarrow x = Fx$ and $t \leftarrow t = Ft$. If this transformation is applied to the gaseous species equation,

$$\frac{\partial}{\partial t}\alpha_g\rho_g Y_{g,k} + \frac{\partial}{\partial x}\alpha_g\rho_g U_g Y_{g,k} = \alpha_g \frac{\partial}{\partial x}\left(\rho_g D_{g,k}\frac{\partial}{\partial x}Y_{g,k}\right) + \omega_k \tag{6.48}$$

it becomes:

$$F\frac{\partial}{\partial t'}\alpha_g\rho_g Y_{g,k} + F\frac{\partial}{\partial x'}\alpha_g\rho_g U_g Y_{g,k} = F\frac{\partial}{\partial x'}\left(\rho_g D_{g,k}F\frac{\partial}{\partial x'}Y_{g,k}\right) + \omega_k \tag{6.49}$$

and after division by the factor F equation 6.49 becomes:

$$\frac{\partial}{\partial t'}\alpha_g\rho_g Y_{g,k} + \frac{\partial}{\partial x'}\alpha_g\rho_g U_g Y_{g,k} = \frac{\partial}{\partial x'}\left(\rho_g D_{g,k}F\frac{\partial}{\partial x'}Y_{g,k}\right) + \frac{\omega_k}{F} \tag{6.50}$$

This equation 6.50 is identical to equation 6.48 if one multiplies the diffusion coefficient by F. The same operation can be carried out on the equation of internal energy or temperature. Using Ficks law for the heat flux one finds the original equation after multiplication

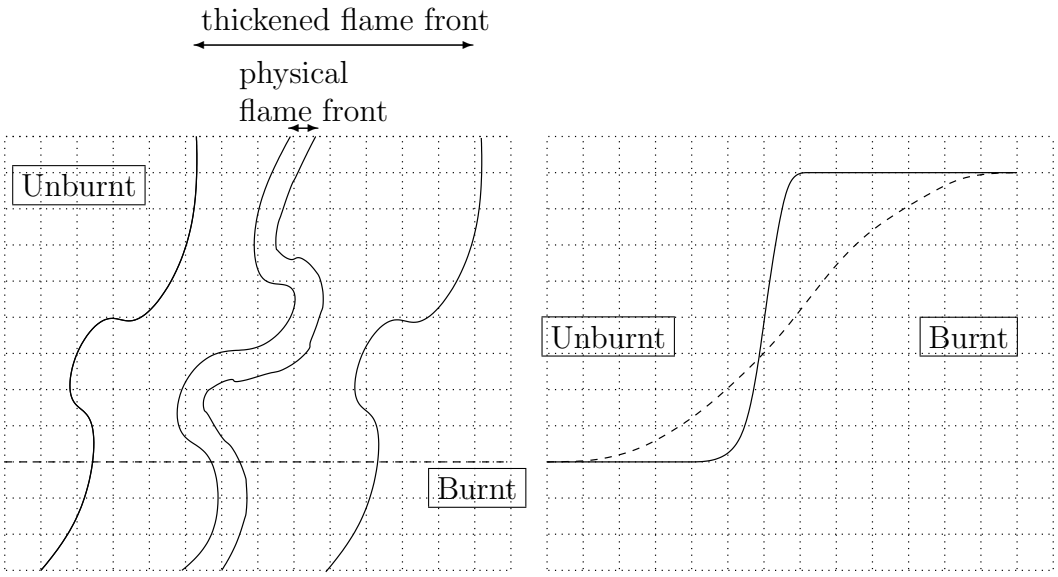

Figure 6.17: The thickened flame: A typical computational mesh for LES computations is indicated by the dotted lines, on the left sketch the physical flame is compared to the artificially thickened flame and on the right sketch the temperature profiles through the flame sheet on the dashed line are given.

of the heat diffusion coefficient by F and division of the thermal reaction rate by the factor F. This operation is not carried out on the momentum equation since the flow dynamics are not to be changed. A detailed discussion on the coupling of the thickened flame to the dynamics of the flow field can be found in Colin [17]. The previous algebraic operation conserves the laminar flame speed since

$$s_l \propto \sqrt{D_{th} A} = \sqrt{(D^0_{th} F)\,\frac{A^0}{F}} \tag{6.51}$$

and thickens the reaction zone by a factor F since: See Poinsot [75] for a detailed analysis of the thickened flame model and its consequences on flame speed and reaction zone thickness.

$$\delta_l \propto \frac{D_t h}{s_l} \propto \sqrt{\frac{D_{th}}{A}} = F\sqrt{\frac{D^0_{th}}{A^0}} = F\delta^0_l \tag{6.52}$$

Here the exponent 0 is used to indicate the un-thickened flame properties and A is the pre-exponential constant in the Arrhenius reaction law. The advantage of the TF model is, to provide a way to numerically propagate a flame front at the right speed without having to use a dense mesh. Since the thickened flame front thickness $\delta_l = F\delta^0_l$ depends directly on the thickening factor F it allows to thicken the flame front sufficiently to resolve its structure even on a coarse mesh. The drawback of the TF model is that the interaction of turbulence and chemistry may be modified since the Damköhler number is modified.

The Damköhler number is defined as the comparison of turbulent (τ_t) to chemistry time scale (τ_c).

$$Da = \frac{\tau_t}{\tau_c} = \frac{l_t}{u'}\frac{s_l}{\delta_l^0} \tag{6.53}$$

In two-phase flames the other important source term besides reaction rates, that is governed by diffusion is the evaporation. To keep the flame structure, conservation equations containing source terms related to evaporation have to undergo the same treatment as the species conservation equation.
The procedure of scale transformation, detailed for the species conservation procedure in eqs. 6.48-6.50, gives the following set of equations for the one-dimensional two-phase flow equation:

$$\frac{\partial}{\partial t'}\alpha_g\rho_g + \frac{\partial}{\partial x'}\alpha_g\rho_g U_g = \frac{\Gamma}{F} \tag{6.54}$$

$$\frac{\partial}{\partial t'}\alpha_g\rho_g Y_{g,k} + \frac{\partial}{\partial x'}\alpha_g\rho_g U_g Y_{g,k} = \frac{\partial}{\partial x'}\left(\rho_g D_{g,k} F \frac{\partial}{\partial x'} Y_{g,k}\right) + \frac{\omega_k}{F} \tag{6.55}$$

$$\frac{\partial}{\partial t'}\alpha_g\rho_g E_g + \frac{\partial}{\partial x'}\alpha_g\rho_g U_g E_g = -\frac{\partial}{\partial x'}P_g U_g - \frac{\partial}{\partial x'}Q_g - \frac{1}{2F}\Gamma U_l^2 - \frac{\Phi}{F} - \frac{\Lambda}{F} + \frac{\omega_{th}}{F} \tag{6.56}$$

$$\frac{\partial}{\partial t'}\alpha_l\rho_l + \frac{\partial}{\partial x'}\alpha_l\rho_l U_l = -\frac{\Gamma}{F} \tag{6.57}$$

$$\frac{\partial}{\partial t'}n + \frac{\partial}{\partial x'}nU_l = 0 \tag{6.58}$$

$$\frac{\partial}{\partial t'}\alpha_l\rho_l E_l + \frac{\partial}{\partial x'}\alpha_l\rho_l U_l E_l = -\frac{1}{2F}\Gamma U_l^2 + \frac{\Phi}{F} + \frac{\Lambda}{F} \tag{6.59}$$

For the set of the coupled equations the scaling factor F enters the equations for continuity via the evaporation term and the equations for temperature or energy via the heat exchange terms and the heat diffusion in the case of the gaseous energy equation. Therefore the extension of the thickened flame model to the one-dimensional two-phase flame modifies the source terms for evaporation and heat exchange.

6.4.2 Numerical results for the two-phase thickened flame model

Numerically this extension of the TF model to the two-phase thickened flame model (TPTF) is tested for a flame with droplets of 50 microns.

Fig. 6.18 presents the un-thickened two-phase flame that is to be compared to the thickened two-phase flame in Fig. 6.19. The thickening factor is ($F = 10$). As expected, the thickened flame is larger and easier to resolve numerically. The un-thickened flame is compared to the thickened flame in Fig. 6.20. For the ease of comparison, the flame has been shifted to the origin of the x axis. The profiles of the thickened flame areas expected significantly smoother than the un-thickened flame while the characteristic behavior of profiles remain unchanged.

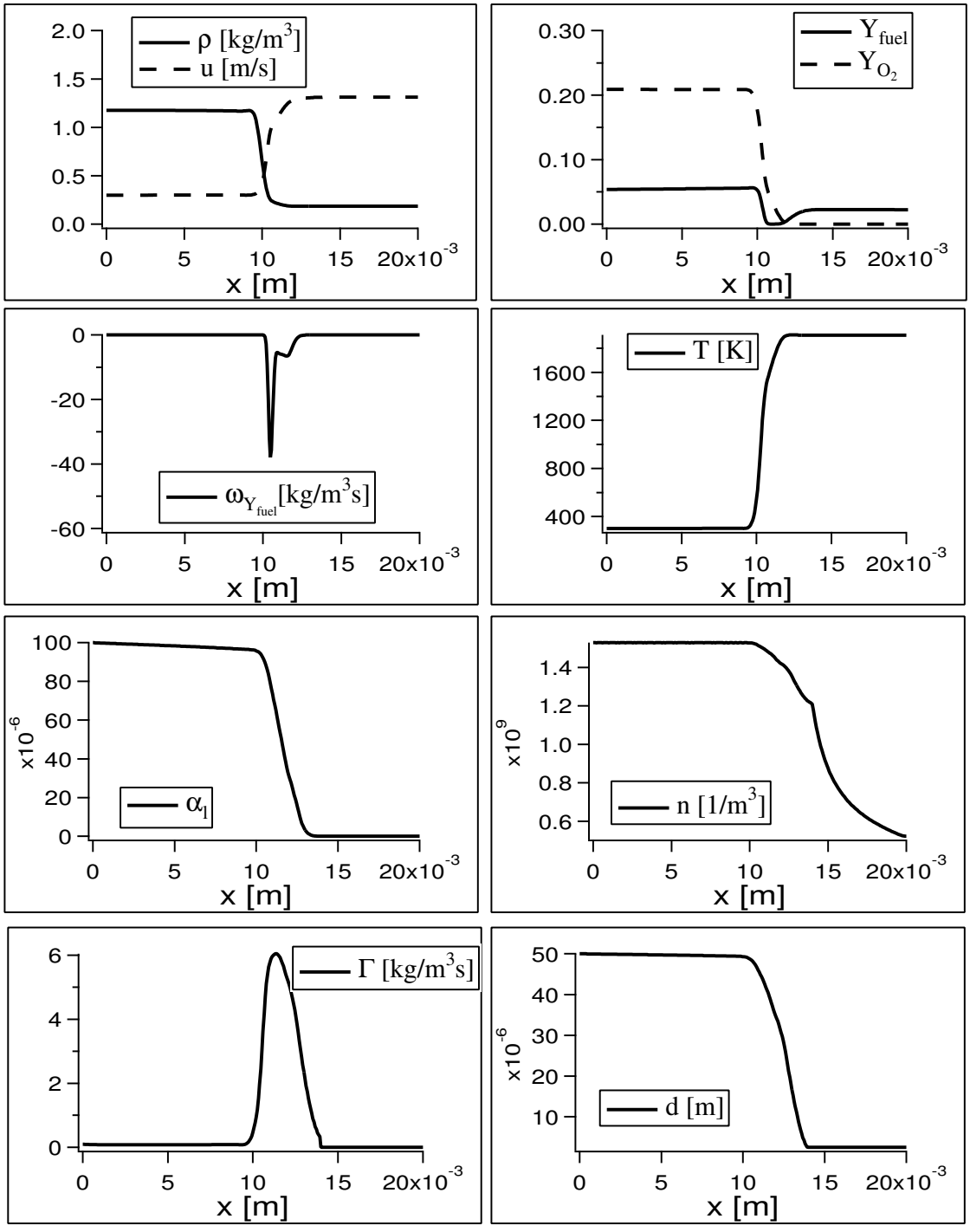

Figure 6.18: Selected properties of the numerical solution of the unthickened flame that is to be compared to the thickened flame. The total equivalence ratio is slightly rich and the inlet diameter for the fuel droplets is 50 microns.

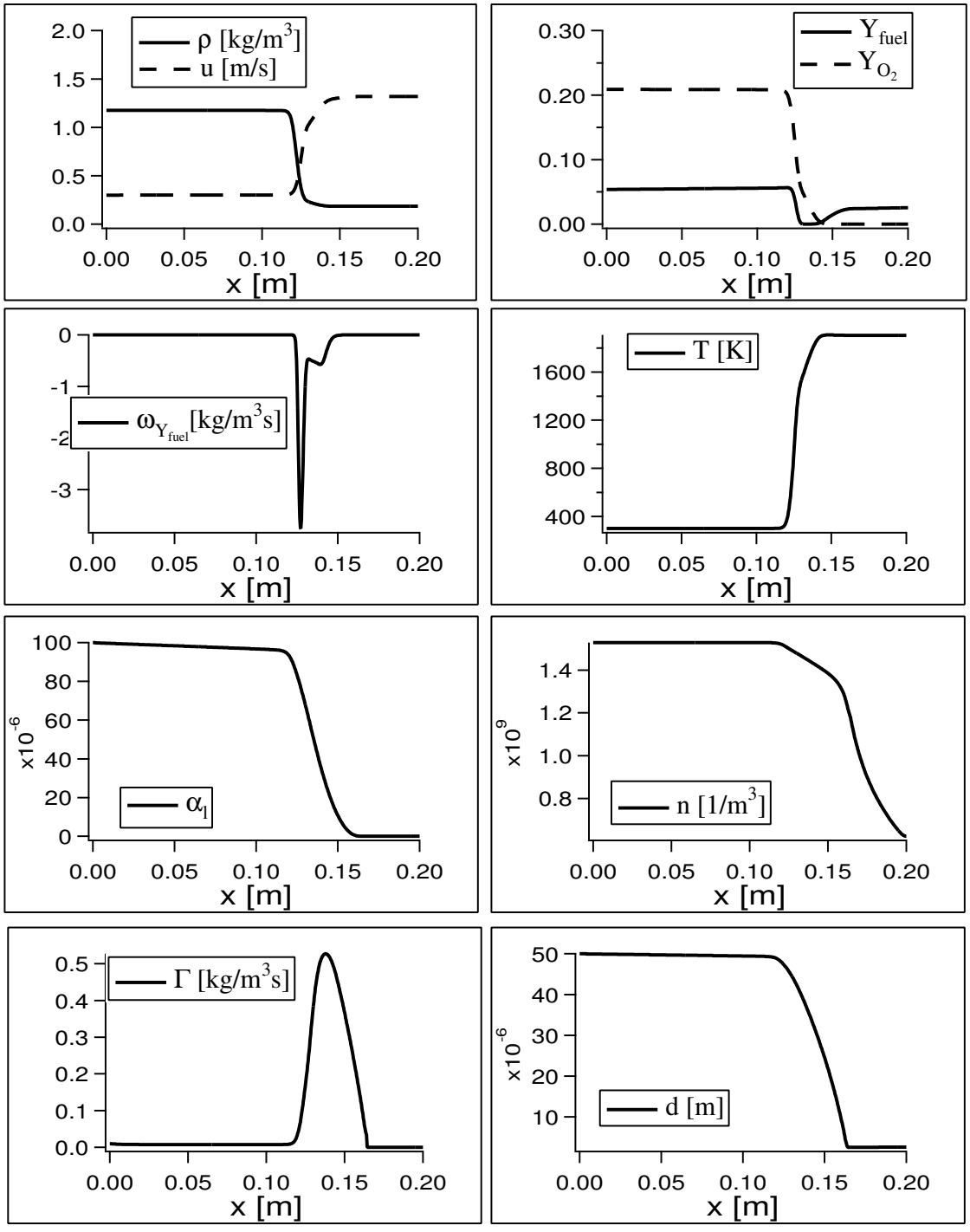

Figure 6.19: Selected properties of the numerical solution of an artificially thickened flame. The total equivalence ratio is slightly rich and the inlet diameter for the fuel droplets is 50 microns. The thickening factor is $F = 10$.

To verify that the thickening operator performs exactly as expected, it is interesting to compare the un-thickened flame with a "scaled" thickened flame (figs. 6.21, 6.22). The scaling is obtained as follows: the spatial abscissa of a thickened flame is divided by F and the source terms magnitude is multiplied by the thickening factor F. After this scaling, the results of the thickened and unthickened flame should match.

This is true for the gaseous properties of the flame (Fig. 6.21). The liquid properties show however a small difference on the evaporation rate (Fig. 6.22). One of the possible sources of the difference is related to particle drag. The momentum equation for the liquid phase has not been rescaled like eqs.6.54-6.59 in order not to alter the particle dynamics that should be conserved. Like the Damköhler number in the case of a gaseous turbulent flame here the time scale of drag (τ_p) does not compare after rescaling to the time scale of chemistry ($\tau_c = \delta_l^0/s_l$). This leads to "chemical" Stokes number:

$$St_c = \frac{\tau_p}{\tau_c} = \frac{\tau_p s_l}{\delta_l^0} \tag{6.60}$$

This non-dimensional quantity decreases with the thickening procedure therefore by the amount of the thickening factor F. Compared to the original flame after rescaling particles are less inertial and follow more the gaseous flow field. This leads to a slightly larger evaporation zone since particles undergo a different acceleration as particle relaxation time was not altered in the flame thickening procedure. This is the effect of the altered "chemical" or "reactive" Stokes number St_c. This slightly larger evaporation zone can be seen in Fig. 6.22. Note that the differences remain small and acceptable.

Now, even though the thickening operation works for laminar flames, it will introduce differences in turbulent flames. The turbulent wrinkling of the physical flame is reduced by increased diffusion. Since the reaction rate is proportional to the flame surface, an artificially thickened flame has a reduced reaction rate. This can be compensated by introducing an efficiency function that estimates subgrid wrinkling and modifies the reaction rate by the corresponding factor. The effects of flame thickening and sub-grid efficiency have been investigated by Angelberger [4] and Colin [16] for the gaseous flame. The efficiency function estimates sub-grid turbulence and its calculations is based on velocity gradients. The reaction rate corrected with this efficiency factor then produces a reaction rate, that corresponds to the total physical reaction rate of the turbulent flame and has the corresponding turbulent flame speed.

The extension of the efficiency function to the thickened two-phase flame has not been studied. Evaporation is (to first order) proportional to the liquid fuel surface (D^2 law). This is not altered by turbulence. The diffusion process is nevertheless enhanced and steeper gradients of fuel mass fraction and temperature in the vicinity of the droplet surface should accelerate the evaporation process. In the present evaporation models this is taken into account by the *Nusselt* (Eq. 6.39) and *Sherwood* (Eq. 6.29) numbers that are functions of the droplet Reynolds number. Therefore the efficiency for evaporation should be taken into account via the droplet Reynolds number.

This test shows how to extend the thickened flame model to two-phase flames. No complete turbulent two-phase reacting simulations were performed during this study and

the present work will have to be completed by a real application in a turbulent flow. This work is currently undertaken by the PhD students J.B. Mossa, S. Pascaud and M. Boileau.

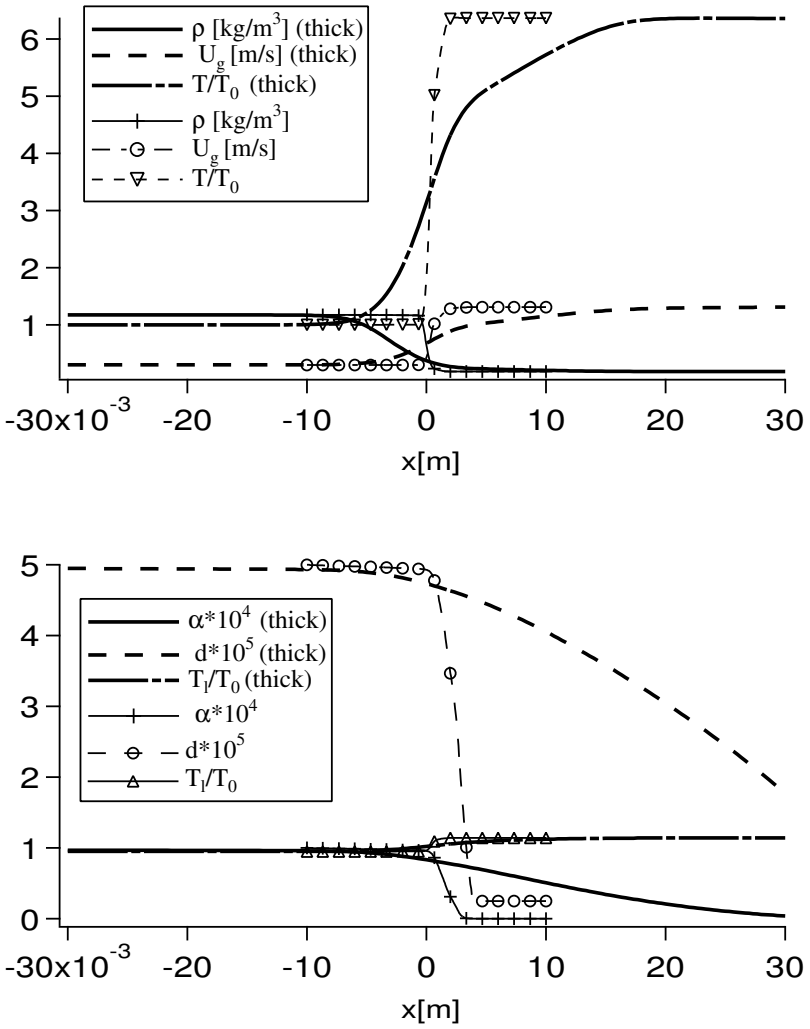

Figure 6.20: Comparison of the un-thickened to the thickened two-phase flame profiles.

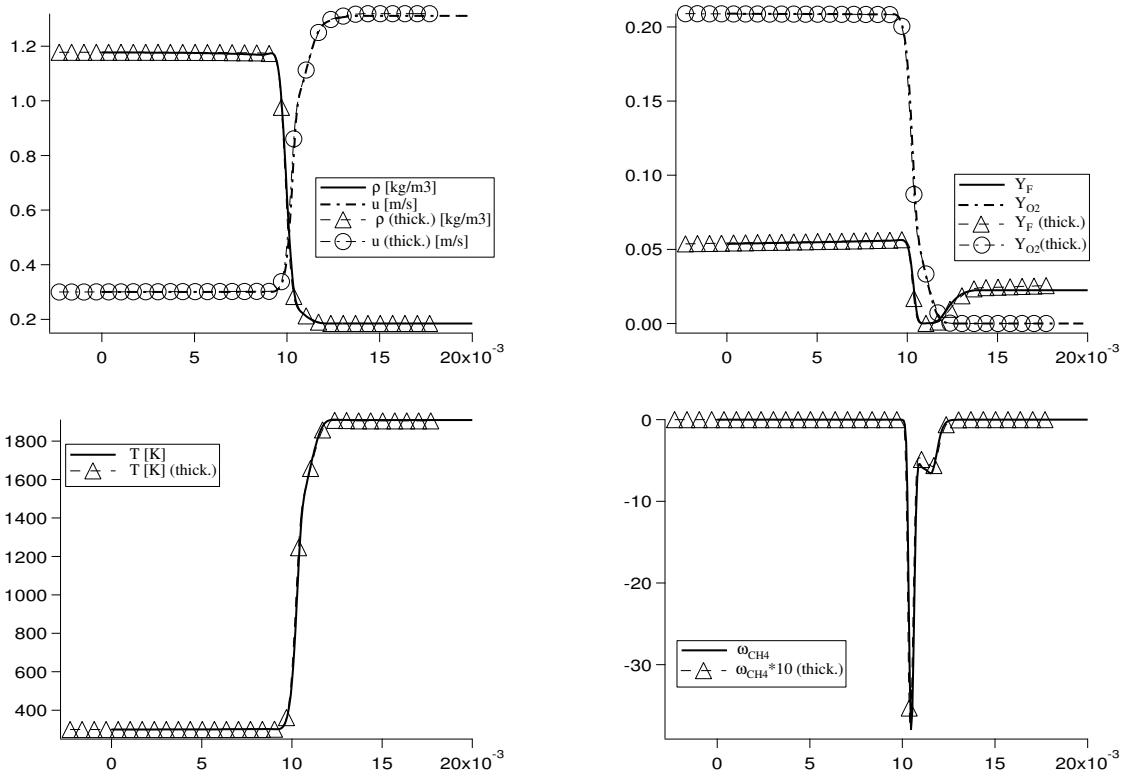

Figure 6.21: Comparison of the gas flow field parameters of the thickened flame to an ordinary flame after rescaling.

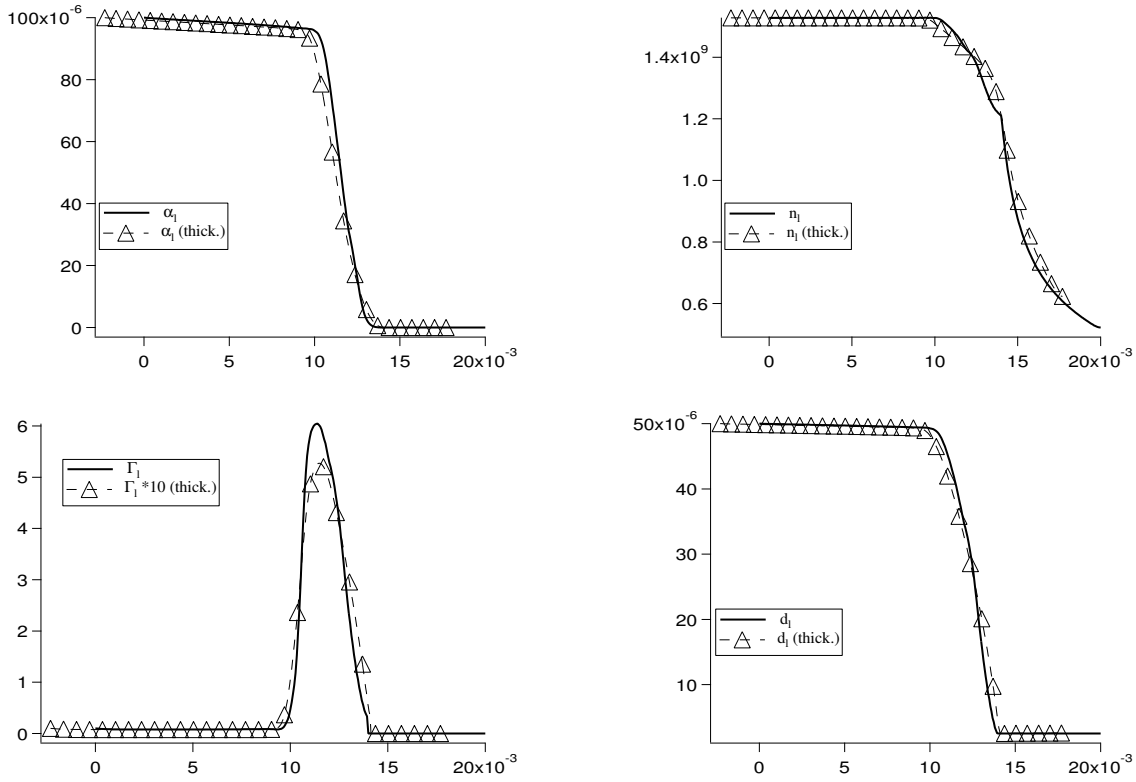

Figure 6.22: Comparison of the dispersed flow field parameters of the thickened flame to an ordinary flame after rescaling.

Conclusion

It's not numbers, it's insight !
Author unknown.

The objective of the present thesis was a feasibility study for unsteady two-phase flow simulations in an Eulerian framework, having in mind a further extension to Large Eddy Simulation of reactive two-phase flow. Whereas no Large Eddy Simulations of reactive two-phase flow were actually performed in the present thesis, the test cases of "direct numerical simulation" at small Reynolds numbers revealed some information about the behavior of the dispersed phase in an Eulerian formulation.

Numerical experiments in the simple case of particle laden homogeneous isotropic turbulence revealed, that the continuum description of the dispersed phase behaves like a highly compressible, supersonic gas. Since the compressibility depends on the inertia of the considered particles, simulations with inertial particles could only be performed when a filtered particle number density field was considered. This filtering of the number density was achieved by modifying the compressible velocity component in form of a subgrid pressure in the momentum equation. Such a modeling of the compressibility effects has therefore to be considered in the case of two-phase flow LES.

Different models for the stress tensor that arises in the averaging procedure are proposed. An isentropic approximation for the Quasi Brownian Energy (QBE) of the dispersed phase seems to be a good model that takes into account local variances due to compression and dilatation. Transport equation models perform poorly for small Stokes numbers and do not reproduce the right amount of QBE. When the transport equation model for QBE is solved, it is questionable whether or not to include the compressible energy modeled by a subgrid pressure into the production mechanism for QBE. When it is omitted, QBE levels remains too low and when it is included it violates the isentropic behavior found in the Lagrangian simulations.

The spectra of the mesoscopic kinetic energy reveal a large compressible component of kinetic energy at small scales. This is consistent with effects of compressibility observed. Furthermore in these simulations at small Reynolds numbers the kinetic energy of the dispersed phase was significantly larger than the kinetic energy of the carrier phase at small scales. This allows an analogy to flows at large Prandtl numbers where small scale diffusion of heat is smaller than the diffusion of kinetic energy and the scalar spectrum of temperature is larger than the scalar spectrum of kinetic energy. This can be explained by the evolution of the average "free path" length of the particles. When particles interact with carrier phase structures that have a time scale smaller than the particle relaxation

time, particles are almost not influenced. Small scale energy is not captured in the Eulerian formulation which admits less kinetic energy at small scales. This is probably due to the modeling of the stress tensor by a simple pressure-viscous approach that does not mimic correctly the fluxes due to the uncorrelated motion of the particles.

The coupling of the Eulerian formulation to an Arrhenius formulation for combustion does not pose particular difficulties. A preliminary test for the coupling of the Eulerian formualtion to the extended thickened flame model for turbulent combustion does not show any difficulties either and opens one possibility for the simulation of turbulent two-phase combustion.

The comparison of predictions made by Eulerian simulations to volume filtered Lagrangian results reveals to be a powerful tool. One the one hand the Eulerian diagnostics allow to isolated for instance the compressible component of the mesoscopic velocity in the Lagrangian simulation and on the other hand measures of the number density and Quasi Brownian Energy (QBE) in the Lagrangian simulation reveal the current deficiencies of the Eulerian approach. To overcome those deficiencies, it would be interesting not only to measure the QBE but all components of the unresolved fluxes such that more appropriate models for Eulerian computations can be developed. For the modeling of those fluxes more general algebraic models as used in *Reiner Rivilin Fluids* [107] which introduce a natural time scale may provide a useful base. Concerning Large Eddy Simulation of two phase flow in an Eulerian framework, a similar approach using volume filtered results of the unresolved stresses at high Reynolds numbers may help to identify the fluxes that require modeling. Even if the small scale motion in the Eulerian framework still requires some work, the large scale motion is well captured. Since LES is based on resolving the large scales of the flow it might be possible to perform Eulerian two phase LES with simple algebraic or dynamic models for the unresolved and subgrid stresses. Nevertheless some more development is necessary for the subgrid scale fluxes that occur when filtering the equations. Indeed the study of the different transfer terms in the equation for the mesoscopic kinetic energy of the dispersed phase revealed that the energy transfer is more complicated than in the case of the incompressible Navier-Stokes equations.

Acknowledgments

Financial support for this thesis was furnished by the European Training Research Network *STOPP*.
Numerical simulations have been performed on COMPAQ α machines (CEA,CERFACS) using up to 24 processors and excellent speed-up was obtained *.
Simulations with high grid resolutions were performed on the SGI ORIGIN 3000 of the supercomputing center CINES in the framework of the EXTREME COMPUTING FOR TURBULENT COMBUSTION project using up to 128 processors.
Simulations using Lagrangian particle tracking were performed by Jerome Helie using the DNS code NTMIX at the supercomputing center IDRIS in the framework of the project : ECOULEMENTS REACTIFS DIPHASIQUES: SIMULATIONS DIRECTES ET AUX GRANDES ECHELLES.

*see www.cerfacs.fr

Related Publications and Reports

- A. Kaufmann, O. Simonin, T. Poinsot and J. Helie; *Dynamics and Dispersion in Eulerian-Eulerian DNS of Two Phase Flow*; Proceedings of the Summer Program, Center for Turbulence Research, NASA AMES/Stanford University, USA; kaufmann.pdf

- A. Kaufmann, B. Cuenot, O. Simonin and J. Helie; *Dynamics and Dispersion in 3D Unsteady Eulerian-Eulerian Simulation of Two-phase Flows*; International Conference on Supercomputing in Nuclear Applications (SNA); Palais de Congrés, Paris 2003;

- A. Kaufmann,J. Helie, O. Simonin and T. Poinsot; *Comparison between Lagrangian and Eulerian particle simulations coupled with DNS of homogeneous isotropic decaying turbulence*; EUROMECH COLLOQUIM 447 - Interaction Phenomena in Turbulent Particle-Laden Flows; Estonian Akademy of Sciences , Tallinn, Estonia 2003;

- A. Kaufmann, O. Simonin and T. Poinsot; *Direct Numerical Simulation of Particle-Laden homogeneous isotropic turbulent flows using a two-fluid model formulation*; 5th International Conference on Multiphase Flow - Paper No.443; Yokohama, Japan 2004;

- For related technical reports see Cerfacs CFD Publications

Appendix A

Obtaining the transport equation for the stress tensor

In this part the conservation equations for the second order transport equations are developed for the two different approaches for the Eulerian equations. The first section is devoted to the stress tensor as obtained from ensemble average and the second section is devoted to the derivation of the stress tensor by volume filtering.

A.1 stress tensor of Quasi Brownian Motion $\langle \delta u_{p,i} \delta u_{j,p} \rangle_p$

The phase space velocity of the individual particle can be decomposed into a contribution of the mesoscopic eulerien velocity field and the residual (or peculiar) velocity of the individual particle ($c_i = u_{p,i} + \delta u_i$). The velocity correlation $c_i c_j$ can then be decomposed.

$$c_{p,i}c_{p,j} = \breve{u}_{p,i}\breve{u}_{p,j} + \breve{u}_{p,i}\delta u_j + \delta u_i \breve{u}_{p,j} + \delta u_i \delta u_j \tag{A.1}$$

The transport equation obtained by applying the equivalent of Enskogs general equation of change (Eq.1.30) to the product $\psi = c_i c_j$ is in absence of collisions

$$\begin{aligned}
\frac{\partial}{\partial t}\breve{n}_p\langle c_i c_j\rangle_p + \frac{\partial}{\partial x_k}\breve{n}_p\langle c_i c_j c_k\rangle_p + \breve{n}_p\langle\frac{F_{p,k}}{m_p}\frac{\partial}{\partial c_{k,p}}(c_i c_j)\rangle_p + \breve{n}_p\langle\frac{\partial}{\partial t}c_i c_j + c_k\frac{\partial}{\partial x_k}c_i c_j\rangle_p = \\
+\frac{\partial}{\partial t}\breve{n}_p\breve{u}_{p,i}\breve{u}_{p,j} + \frac{\partial}{\partial x_k}\breve{n}_p\breve{u}_{p,i}\breve{u}_{p,j}\breve{u}_{p,k} \\
+\frac{\partial}{\partial t}\breve{n}_p\langle\delta u_i\delta u_j\rangle_p + \frac{\partial}{\partial x_k}\breve{n}_p\breve{u}_{p,k}\langle\delta u_{p,i}\delta u_{p,j}\rangle_p \\
+\frac{\partial}{\partial x_k}\breve{n}_p\breve{u}_{p,i}\langle\delta u_{p,j}\delta u_{p,k}\rangle_p \\
+\frac{\partial}{\partial x_k}\breve{n}_p\breve{u}_{p,j}\langle\delta u_{p,i}\delta u_{p,k}\rangle_p \\
+\frac{\partial}{\partial x_k}\breve{n}_p\langle\delta u_{p,i}\delta u_{p,j}\delta u_{p,k}\rangle_p
\end{aligned} \tag{A.2}$$

$$-\frac{1}{\tau_p}\left((\breve{u}_i\breve{u}_{p,j}+\breve{u}_j\breve{u}_{p,i})-2\breve{u}_{p,i}\breve{u}_{p,j}\right)$$
$$+\frac{2}{\tau_p}\breve{n}_p\langle\delta u_{p,i}\delta u_{p,j}\rangle_p$$

The mesoscopic velocity correlation $\breve{u}_{p,i}\breve{u}_{p,j}$ can be obtained from the momentum transport equation.

$$\begin{aligned}\frac{\partial}{\partial t}\breve{n}_p\breve{u}_{p,i}\breve{u}_{p,j}+\frac{\partial}{\partial x_k}\breve{n}_p\breve{u}_{p,i}\breve{u}_{p,j}\breve{u}_{p,k}&\\ +\breve{u}_{p,i}\frac{\partial}{\partial x_k}\breve{n}_p\langle\delta u_{p,j}\delta u_{p,k}\rangle_p&\\ +\breve{u}_{p,j}\frac{\partial}{\partial x_k}\breve{n}_p\langle\delta u_{p,i}\delta u_{p,k}\rangle_p&\\ -\frac{1}{\tau_p}\left((u_i\breve{u}_{p,j}+u_j\breve{u}_{p,i})-2\breve{u}_{p,i}\breve{u}_{p,j}\right)&=0\end{aligned}\tag{A.3}$$

Then, subtracting Eq. A.3 from Eq. A.2 one yields a transport equation for the QB stresses.

$$\begin{aligned}\frac{\partial}{\partial t}\breve{n}_p\langle\delta u_{p,i}\delta u_{p,j}\rangle_p+\frac{\partial}{\partial x_k}\breve{n}_p\breve{u}_{p,k}\langle\delta u_i\delta u_{p,j}\rangle_p&\\ +\breve{n}_p\langle\delta u_{p,i}\delta u_{p,k}\rangle_p\frac{\partial}{\partial x_k}\breve{u}_{p,j}&\\ +\breve{n}_p\langle\delta u_{p,j}\delta u_{p,k}\rangle_p\frac{\partial}{\partial x_k}\breve{u}_{p,i}&\\ +\frac{\partial}{\partial x_k}\breve{n}_p\langle\delta u_{p,i}\delta u_{p,j}\delta u_{p,k}\rangle_p&\\ +\frac{2}{\tau_p}\breve{n}_p\langle\delta u_i\delta u_j\rangle_p&=0\end{aligned}\tag{A.4}$$

QBE is defined as half the trace of the stress tensor $\delta\breve{\theta}_p=\langle\delta u_{p,k}\delta u_{p,k}\rangle_p$. Then the QBE transport equation can be obtained form Eq. A.4.

$$\begin{aligned}\frac{\partial}{\partial t}\breve{n}_p\delta\breve{\theta}_p\frac{\partial}{\partial x_j}\breve{n}_p\delta\breve{\theta}_p\breve{u}_{p,j}&=-\langle\delta u_{p,k}\delta u_{p,j}\rangle_p\frac{\partial}{\partial x_j}\breve{u}_{p,i}\\ &\quad-\frac{\partial}{\partial x_j}\langle\delta u_{p,k}\delta u_{p,k}\delta u_{p,j}\rangle_p-\frac{2\breve{n}_p}{\tau_p}\delta\breve{\theta}_p\end{aligned}\tag{A.5}$$

In this transport equation the stress tensor $\langle\delta u_{p,k}\delta u_{p,j}\rangle_p$ and the triple correlation $\langle\delta u_{p,k}\delta u_{p,k}\delta u_{p,j}\rangle_p$ need to be modeled. When the stress tensor is closed making a pressure and viscosity assumption it can be written in the following form.

$$\breve{n}_p\langle\delta u_{p,k}\delta u_{p,j}\rangle_p=\frac{2}{3}\breve{n}_p\delta\breve{\theta}_p-\breve{\tau}_{p,ij}\tag{A.6}$$

Viscous stresses are abbreviated by $\breve{\tau}_{p,ij}$. Assuming that third order correlations can be modeled by a diffusion assumption the transport equation for QBE can be closed.

$$\begin{aligned} \frac{\partial}{\partial t}\breve{n}_p\delta\breve{\theta}_p\frac{\partial}{\partial x_j}\breve{n}_p\delta\breve{\theta}_p\breve{u}_{p,j} &= -\left[P_{QB}\delta_{ij}-\breve{\tau}_{p,ij}\right]\frac{\partial}{\partial x_j}\breve{u}_{p,i} \\ -\frac{\partial}{\partial x_j}\kappa_{QB}\frac{\partial}{\partial x_j}\delta\breve{\theta}_p - \frac{2\breve{n}_p}{\tau_p}\delta\breve{\theta}_p & \end{aligned} \tag{A.7}$$

Here the definition of QBP was used ($P_{QB} = 2/3\breve{n}_p\delta\breve{\theta}_p$).

A.2 Stress tensor of as obtained by volume filtering

For the derivation of the stress tensor for the volume filtered approach some important assumptions are made. Those assumptions are

1. The particles do not admit an internal flow and the surface tension is neglected such that the stress tensor σ_{ij} is zero.

2. Control volumes are such that only complete particles are in the control volume.

3. All particles have the same density.

4. All particles have the same mass.

5. All internal degrees of freedom such as rotation of the particle are neglected.

6. Particles with the finite extension behave like point particles.

7. Particles do not undergo collisions.

8. Drag force is limited to Stokes drag.

With the previous assumptions the velocity of every particle $V_i^{(k)}$ in the control volume may divided into the favre averaged mean velocity of all particles in the control volume $U_{l,i}$ and a residual velocity $\Delta u_i^{(k)}$, so that the the mass pondered average of the residual velocities over the control volume is zero. Then, under the previous assumptions, the velocity $u_i(x)$ of the Navier Stokes equation to filter can be identified with the individual particle velocity $V_i^{(k)}$ if x is in the particle volume. Here the N particles in one control volume Ω are considered.

$$V_i^{(k)} = U_{l,i} + \Delta u_i^{(k)} \tag{A.8}$$

$$U_{l,i} = \frac{1}{N}\sum_k V_i^{(k)} = \frac{1}{\alpha_l\rho_l}\langle\chi_l\rho u_i\rangle_\Omega \tag{A.9}$$

Then second order correlations of the particle velocities can then be written as follows:

$$\begin{aligned}
\langle \chi_l \rho u_i u_j \rangle_\Omega &= \alpha_l \rho_l \frac{1}{N} \sum_k V_i^{(k)} V_j^{(k)} \qquad (A.10)\\
&= \alpha_l \rho_l \frac{1}{N} \sum_k \left(U_{l,i} + \Delta u_i^{(k)} \right) \left(U_{l,j} + \Delta u_j^{(k)} \right) \\
&= \alpha_l \rho_l \frac{1}{N} \sum_k U_{l,i} U_{l,j} + \left(\Delta u_i^{(k)} \Delta u_j^{(k)} \right) \\
&\quad + \alpha_l \rho_l \frac{1}{N} \sum_k \left(\left(U_{l,i} \Delta u_j^{(k)} \right) + \left(\Delta u_i^{(k)} U_{l,j} \right) \right) \\
&= \alpha_l \rho_l \frac{1}{N} \sum_k U_{l,i} U_{l,j} + \alpha_l \rho_l \frac{1}{N} \sum_k \left(\Delta u_i^{(k)} \Delta u_j^{(k)} \right)
\end{aligned}$$

Then, the stress tensor has the following properties:

$$\begin{aligned}
\left(\langle \chi_l \rho u_i u_j \rangle_\Omega - \alpha_l \rho_l U_{l,i} U_{l,j} \right) &= \alpha_l \rho_l \frac{1}{N} \sum_k \left(\Delta u_i^{(k)} \Delta u_j^{(k)} \right) \qquad (A.11)\\
&= \alpha_l \rho_l \frac{1}{N} \sum_k \langle u_i'' u_j'' \rangle_{\Omega,l} \qquad (A.12)
\end{aligned}$$

In the previous equation the last line has to be understood as the definition of the stress tensor. Under the same assumptions as above the third order correlations can be decomposed into the following terms:

$$\begin{aligned}
\langle \chi_l \rho u_i u_j u_k \rangle_\Omega &= \alpha_l \rho_l U_{l,i} U_{l,j} U_{l,k} + \alpha_l \rho_l \langle u_i'' u_j'' u_k'' \rangle_{\Omega,l} \qquad (A.13)\\
&\quad + \alpha_l \rho_l U_{l,i} \langle u_j'' u_k'' \rangle_{\Omega,l} + \alpha_l \rho_l U_{l,j} \langle u_j'' u_k'' \rangle_{\Omega,l} + \alpha_l \rho_l U_{l,k} \langle u_i'' u_j'' \rangle_{\Omega,l}
\end{aligned}$$

In the next step the transport equation for the velocity correlations is constructed from the momentum equation.

$$\frac{\partial}{\partial t} \rho u_i + \frac{\partial}{\partial x_j} \rho u_i u_j = \frac{\partial}{\partial x_j} \sigma_{ij} \qquad (A.14)$$

Using the continuity equation this leads to the transport equation for the velocity correlations.

$$\frac{\partial}{\partial t} \rho u_i u_j + \frac{\partial}{\partial x_k} \rho u_i u_j u_k = u_i \frac{\partial}{\partial x_k} \sigma_{jk} + u_j \frac{\partial}{\partial x_k} \sigma_{ik} \qquad (A.15)$$

Then volume filtering the correlation equation with the characteristic functions leads to the following transport equation for the dispersed phase assuming that σ_{ij} in the droplet is zero.

$$\begin{aligned}
&\frac{\partial}{\partial t} \alpha_l \rho_l U_{l,i} U_{l,j} + \frac{\partial}{\partial x_k} \alpha_l \rho_l U_{l,i} U_{l,j} U_{l,k} + \frac{\partial}{\partial t} \alpha_l \rho_l \langle u_i'' u_j'' \rangle_{\Omega,l} \frac{\partial}{\partial x_k} \alpha_l \rho_l \langle u_i'' u_j'' u_k'' \rangle_{\Omega,l} \qquad (A.16)\\
&\quad + \frac{\partial}{\partial x_k} \alpha_l \rho_l U_{l,i} \langle u_j'' u_k'' \rangle_{\Omega,l} + \frac{\partial}{\partial x_k} \alpha_l \rho_l U_{l,j} \langle u_i'' u_k'' \rangle_{\Omega,l} + \frac{\partial}{\partial x_k} \alpha_l \rho_l U_{l,k} \langle u_i'' u_j'' \rangle_{\Omega,l} \\
&\quad - U_{l,i} U_{l,j} \Gamma - \langle u_i'' u_j'' \rangle_{\Omega,l} \Gamma \\
&\quad + F_i U_j + F_j U_i + F_{ij}'' = 0
\end{aligned}$$

Here F_i is the drag force contribution to the volume averaged velocity and F''_{ij} the contribution of drag force to the stress term. In the same manner the volume filtered momentum equation (Eq.1.87) can be used to obtain a transport equation for the volume filtered velocity correlations. Here again it is assumed, that the stress tensor σ_{ij} in the droplet is zero.

$$\begin{aligned}\frac{\partial}{\partial t}\alpha_l\rho_l U_{l,i}U_{l,j} + \frac{\partial}{\partial x_k}\alpha_l\rho_l U_{l,i}U_{l,j}U_{l,k} &= -U_{l,j}\frac{\partial}{\partial x_k}\alpha_l\rho_l\langle u''_i u''_k\rangle_{\Omega,l} - U_{l,i}\frac{\partial}{\partial x_k}\alpha_l\rho_l\langle u''_j u''_k\rangle_{\Omega,l} \quad \text{(A.17)}\\ &\quad -F_iU_j - F_jU_i + U_{l,i}U_{l,j}\Gamma \quad \text{(A.18)}\end{aligned}$$

The difference between equations A.16 and A.17 then leads to the transport equation for the stresses.

$$\begin{aligned}\frac{\partial}{\partial t}\alpha_l\rho_l\langle u''_i u''_j\rangle_{\Omega,l} + \frac{\partial}{\partial x_k}\alpha_l\rho_l U_{l,k}\langle u''_i u''_j\rangle_{\Omega,l} &= -\frac{\partial}{\partial x_k}\alpha_l\rho_l\langle u''_i u''_j u''_k\rangle_{\Omega,l} \quad \text{(A.19)}\\ &\quad -\langle u''_i u''_k\rangle_{\Omega,l}\frac{\partial}{\partial x_k}U_{l,j} - \langle u''_k u''_k\rangle_{\Omega,l}\frac{\partial}{\partial x_k}U_{l,i}\\ &\quad -F''_{ij} + \langle u''_i u''_j\rangle_{\Omega,l}\Gamma\end{aligned}$$

Here the, term that needs to be modeled, is the contribution of drag force F''_{ij} on the stress tensor.
Furthermore one may define an energy associated to this stress tensor

$$\Delta q^2_{\Omega,l} = \frac{1}{2}\langle u''_k u''_k\rangle_{\Omega,l} \quad \text{(A.20)}$$

The transport equation for this subgrid energy can then be obtained from the trace of Eq. A.19.

$$\begin{aligned}\frac{\partial}{\partial t}\alpha_l\rho_l\Delta q^2_{\Omega,l} + \frac{\partial}{\partial x_j}\alpha_l\rho_l U_{l,j}\Delta q^2_{\Omega,l} &= -\frac{\partial}{\partial x_k}\alpha_l\rho_l\langle u''_i u''_j u''_k\rangle_{\Omega,l} \quad \text{(A.21)}\\ &\quad -\langle u''_k u''_j\rangle_{\Omega,l}\frac{\partial}{\partial x_j}U_{l,k}\\ &\quad -\frac{1}{2}F''_{kk} + \Delta q^2_{\Omega,l}\Gamma\end{aligned}$$

Unless the stress tensor $\langle u''_i u''_j\rangle_{\Omega,l}$ is modeled making some kind of assumption, the previous equation is unclosed. If the stress tensor is modeled, as in the case of the ensemble average, by the trace and a viscous term this term of the equation can be closed.

$$\langle u''_i u''_j\rangle_{\Omega,l} = \tau_{l,ij} = \frac{2}{3}\Delta q^2_{\Omega,l} - \nu_{\Omega,l}\left(\frac{\partial U_{l,i}}{\partial x_j} + \frac{\partial U_{l,j}}{\partial x_i} - \frac{2}{3}\frac{\partial U_{l,k}}{\partial x_k}\delta_{ij}\right) \quad \text{(A.22)}$$

Third order correlations are not modeled and the drag force contribution is expressed in analogy to the dissipation in the ensemble average the transport equation for the subgrid

energy. Then the transport equation can be written as follows.

$$\begin{aligned}\frac{\partial}{\partial t}\alpha_l\rho_l\Delta q^2_{\Omega,l} + \frac{\partial}{\partial x_j}\alpha_l\rho_l U_{l,j}\Delta q^2_{\Omega,l} &= -\tau_{l,kj}\frac{\partial}{\partial x_j}U_{l,k} \\ &\quad + \frac{\alpha_l\rho_l}{\tau_p}\left(\Delta q_{\Omega,fp} - 2\Delta q^2_{\Omega,l}\right) + 2\Delta q^2_{\Omega,l}\Gamma \\ &\quad - \frac{\partial}{\partial x_k}\alpha_l\rho_l\langle u_i'' u_j'' u_k''\rangle_{\Omega,l}\end{aligned}$$

At subgrid scale, some of the dispersed phase kinetic energy is correlated and therefore the fluid particle correlation is not necessarily zero. By analogy to the LES equations obtained by filtering the ensemble averaged approach the term related to drag force F''_{kk} is modeled by the difference between a subgrid scale fluid particle correlation $\Delta q_{fp,\Omega,l}$ and the subgrid scale dispersed phase kinetic energy $\Delta q^2_{\Omega,l}$. This is the transport equation corresponding to QBE in the ensemble average. Interpretation of this equation has to be done carefully considering all of the assumptions made at the beginning of the section.

Appendix B

A Different approach for ensemble averaged equations

B.1 Alternative derivation of ensemble averaged equations

Using Stokes drag for Lagrangian particle tracking the particle velocity changes according to the following law:

$$\frac{\partial}{\partial t} V_i^{(k)}(x,t) = \frac{1}{\tau_p}\left(u_i(x,t) - V_i^{(k)}(x,t)\right) \tag{B.1}$$

Here $u_i(x,t)$ is the carrier phase velocity at the particle location. If it is assumed that the carrier phase velocity is not altered by the dispersed phase presence, for an infinity of realisation with particle velocity $c_{p,i}$, every particle relaxes to the carrier phase velocity according to the drag law above (eq. B.1). Here the probability density function (pdf) of the particle velocity is $\check{f}(x,t,c_{p,i}$. The integral over all velocity space of the pdf is the local instantaneous particle number density in the considered flow.

$$\check{n}_p = \int \check{f}(x,t,c_{p,i}) dc_{p,i} \tag{B.2}$$

The velocity pdf will temporarily change due to transport and to relaxation towards the carrier phase velocity. Since the carrier phase velocity is not altered by the particle presence it does not admit any fluctuation and can be expressed as a dirac function in space and time at the particle location. This (dirac) pdf is required to have as integral value the number density $\check{n}_p$. Therefore the velocity pdf of the carrier phase is defined as $f_F = \check{n}_p \delta(u_i(x,t) - c_{p,i})$. The temporal change of the particle velocity pdf due to drag can than be expressed as

$$\frac{\partial}{\partial t}\check{f} + \frac{\partial}{\partial x_j}\check{f} c_{p,j} = \frac{1}{\tau_p}\left(f_F - \check{f}\right) \tag{B.3}$$

In this kinetic equation the force term was suppressed since drag force is taken into account by the relaxation towards the carrier phase velocity distribution.

Then using the usual derivation for the equations one obtains the following set without modeling :

$$\frac{\partial}{\partial t}\check{n}_p + \frac{\partial}{\partial x_j}\check{n}_p\check{u}_{p,j} = 0 \tag{B.4}$$

$$\frac{\partial}{\partial t}\check{n}_p\check{u}_{p,i} + \frac{\partial}{\partial x_j}\check{n}_p\check{u}_{p,j}\check{u}_{p,i} = -\frac{\partial}{\partial x_j}\check{n}_p\langle\delta u_{p,i}\delta u_{p,j}\rangle_p - \frac{1}{\tau_p}\left(\check{u}_{p,i} - u_{f,i}\right) \tag{B.5}$$

$$\begin{aligned}\frac{\partial}{\partial t}\check{n}_p\langle\delta u_{p,i}\delta u_{p,j}\rangle_p + \frac{\partial}{\partial x_k}\check{n}_p\check{u}_{p,k}\langle\delta u_{p,i}\delta u_{p,j}\rangle_p &= \frac{\partial}{\partial x_k}\check{n}_p\langle\delta u_{p,i}\delta u_{p,j}\delta u_{p,k}\rangle_p \\ &-\check{n}_p\langle\delta u_{p,i}\delta u_{p,k}\rangle_p\frac{\partial}{\partial x_k}\check{u}_{p,j} - \check{n}_p\langle\delta u_{p,j}\delta u_{p,k}\rangle_p\frac{\partial}{\partial x_k}\check{u}_{p,i} \\ &-\frac{\check{n}_p}{\tau_p}\langle\delta u_{p,i}\delta u_{p,j}\rangle_p \\ &+\frac{\check{n}_p}{\tau_p}\left(\check{u}_{p,i}\check{u}_{p,j} + u_iu_j - \check{u}_{p,i}u_j - \check{u}_{p,j}u_i\right)\end{aligned} \tag{B.6}$$

The only difference in this set of equations is the last line that comes up if deriving the correlations of the QB velocities. Therefore the equation of QBE admids a supplementary source term and takes the form:

$$\begin{aligned}\frac{\partial}{\partial t}\check{n}_p\delta\check{\theta}_p + \frac{\partial}{\partial x_j}\check{n}_p\check{u}_{p,j}\delta\check{\theta}_p &= -2\frac{\check{n}_p}{\tau_p}\delta\check{\theta}_p - \left[P_{QB}\delta_{ij} - \check{\tau}_{p,ij}\right]\frac{\partial\check{u}_{p,i}}{\partial x_j} \\ &+\frac{\partial}{\partial x_j}\check{n}_p\check{k}_{QB}\frac{\partial}{\partial x_j}\delta\check{\theta}_p + \frac{\check{n}_p}{\tau_p}\frac{1}{2}\left(\check{u}_{p,k}\check{u}_{p,k} + u_ku_k - 2\check{u}_{p,k}u_k\right)\end{aligned} \tag{B.7}$$

Again, new in the equation above (eq.B.7) is the last term. Supposing that the quation above is an equilibrium as in stationary turbulence one may assume that the terms due with the relaxation time τ_p balance each other. Then, after integration over the entire domain, one obtains the following equilibrium equation.

$$\delta q_p^2 = \check{q}_p^2 + q_{f@p}^2 - q_{fp} \tag{B.8}$$

This equilibrium equation can be compared to the other equilibrium equation.

$$\delta q_p^2 = \breve{q}_p^2 * \left(\frac{4\breve{q}_p^2 q_{f@p}^2}{q_{fp}} - 1\right) \tag{B.9}$$

Appendix C

Numerical Details for Eulerian Two Phase Flows

C.1 Calculation of Fuel Mass Fraction at the Droplet Surface

The gaseous fuel mass fraction of fuel vapor in the vicinity of the droplet surface is defined by

$$Y_{F,\zeta} = \frac{W_F P_{F,\zeta}}{\bar{W} P_g}. \tag{C.1}$$

W_F is molecular mass of fuel, $P_{F,\zeta}$ is the vapor pressure of fuel in the vircintiy of the droplet, $\bar{W}$ is the gaseous mean molecular mass in the vircintiy of the droplet and P_g is the gaseous pressure. Furthermore the gaseous fuel mass fraction in the gas is defined by $Y_{F,g}$. The gaseous mean molecular mass $\bar{W}$ in the vicinity of the droplet is calculated by

$$\bar{W} \;=\; 1/\left\{ Y_{F,\zeta}/W_F + \frac{1-Y_{F,\zeta}}{1-Y_{F,g}} \sum_{k\neq F} Y_{k,g}/W_k \right\} \tag{C.2}$$

then combining eq. C.1 and eq. C.2 one obtains the following expression.

$$Y_{F,\zeta}\left(1/\left\{ \frac{Y_{F,\zeta}}{W_F} + \frac{1-Y_{F,\zeta}}{1-Y_{F,g}} \sum_{k\neq F} Y_k/W_k \right\}\right) = \frac{W_F P_{F,\zeta}}{P_g} \tag{C.3}$$

Additionally a mean gaseous mass fraction W_g is introduced

$$\frac{1}{\bar{W}_g} = \frac{Y_{F,g}}{W_F} + \sum_{k\neq F} Y_k/W_k \tag{C.4}$$

Then, with some algebra, eq. C.3 can be solved for the fuel mass fraction at the droplet surface.

$$Y_{F,\zeta} = \frac{P_{F,\zeta} W_F}{P_{F,\zeta} W_F + (P_g - P_{F,\zeta})\, \bar{W}_g \frac{1-Y_{F,g}}{1-Y_{F,g}\bar{W}_g/W_F}} \tag{C.5}$$

One may define the fuel mass at the surface without the definition of eq. C.4 solving simply for $Y_{F,\zeta}$.

$$Y_{F,\zeta} = \frac{\frac{1}{1-Y_{F,g}} \sum\limits_{k \neq F} \frac{Y_k}{W_k}}{\frac{P}{W_F P_{F,\zeta}} \left\{ \frac{1}{W_F} - \frac{1}{1-Y_{F,g}} \sum\limits_{k \neq F} \frac{Y_k}{W_k} \right\}} \tag{C.6}$$

In eq. C.5 it is easy to see that a correction factor arises

$$\frac{1 - Y_{F,g}}{1 - Y_{F,g} \bar{W}_g / W_F} \tag{C.7}$$

compared to the equation where the mean molecular mass of the vapor in the vicinity of the droplet is assumed as the mean gasesous molecular mass ignoring fuel mass .

$$\hat{Y}_{F,\zeta} = \frac{P_{F,\zeta} W_F}{P_{F,\zeta} W_F + (P_g - P_{F,\zeta}) \bar{W}_g} \tag{C.8}$$

C.2 Exact Integration of the Evaporation law

If the characteristic particle time scale for evaporation $1/\kappa$ is small compared the characteristic time scales of the carrier phase T_f, the numerical timestep can be limited by evaporation. This can be overcome using the d^2 law assuming that κ is constant.

$$d^2 = d_0^2 - \kappa t \tag{C.9}$$

The inverse of the characteristic evaporation time κ can be related directly to the evaporation source term Γ since $\alpha_l = n\pi/6d^3$.

$$\kappa = \frac{4}{n\pi d \rho_l} \Gamma \tag{C.10}$$

Then eq. C.9 can be used to discretise the local conservation law for the dispersed phase volume fraction.

$$\frac{d_{n+1}^3 - d_n^3}{\delta t} = \frac{\left(d_n^2 - \kappa \delta t\right)^{3/2} - d_n^3}{\delta t} \tag{C.11}$$

Taylor development of $\left(d_n^2 - \kappa \delta t\right)^{3/2}$ leads to

$$\frac{d_{n+1}^3 - d_n^3}{\delta t} = -\frac{3 d_n}{2} \kappa + \frac{3}{8 d_n} \delta t \kappa^2 \ldots \tag{C.12}$$

In the small time step limit $\delta t \to 0$ one finds the discrete expression of the local conservation of the third moment. Therfore the source term Γ should be replaced by $\tilde{\Gamma}$

$$\tilde{\Gamma} = \rho_l \frac{\pi n}{6} \frac{\left(d_n^2 - \frac{4\Gamma}{\pi n d \rho_l} \delta t\right)^{3/2} - d_n^3}{\delta t} \tag{C.13}$$

to obtain exact integration. The second difficulty that arrises from the evaporation law is, that the evaporation source term becomes large, if the dispersed phase surface is large compared to the dispersed phase volume. Numerically evaporation may be limited by satifying the conditions for minmal dispersed phase volume $\alpha_{l,min}$

$$\alpha_{l,n} + \Gamma > \alpha_{l,min} \tag{C.14}$$

or a minimal droplet diameter d_{min}

$$d_n^3 - \left(d_n^2 - \frac{4\Gamma}{\pi n d \rho_l} \delta t \right)^{3/2} > d_{min} \tag{C.15}$$

Bibliography

[1] B. Abramzon and W. A. Sirignano. Droplet vaporisation model for spray combustion calculations. *Int. Journal Heat Mass Transfer*, 9:1605–1618, 1989.

[2] A.M. Ahmed and S. Elghobashi. On the mechanisms of modifying the structure of turbulent homogeneous shear flows by dispersed particles. *Physics of Fluids*, 12(11):2906–2930, 2000.

[3] J.C. Andre and M. Barrere. Turbulence fluide, ecoulements complexes. Cours d'options c1, Ecole Polytechnique, 1984.

[4] C. Angelberger, D. Veynante, F. Egolfopoulus, and T. Poinsot. Large eddy simulations of combustion instabilities in premixed flames. *Proceedings of the Summer Program at the Center of Turbulence Research*, pages 61–82, 1998.

[5] Ch. Bailley and G. Compte-Bellot. *Turbulence*. CNRS Editions, sciences et techniques de l'ingénieur edition, 2002.

[6] F. Bataille, Ye Zhou, and Jean-Pierre Bertoglio. Energy transfer in compressible turbulence. ICASE Report 95-65, NASA, 1995.

[7] G.K. Batchlor. Small-scale variation of convected quantities like temperature in turbulent fluid. part1. general discussion and the case of small conductivity. *Journal of Fluid Mechanics*, 5:113, 1959.

[8] Jean-Pierre Bertoglio, Francoise Bataille, and Jean Denis Marion. Two-point closures for weakly compressible turbulence. *Physics of Fluids*, 13(1):290–310, 2001.

[9] M. Boivin, O. Simonin, and K. D. Squires. Direct numerical simulation of turbulence modulation by particles in isotropic turbulence. *Journal of Fluid Mechanics*, 375:235–263, 1998.

[10] R. Borghi and M. Champion. *Modélisation et théorie des flammes*. TECHNIP, editions technip edition, 2000.

[11] T.D. Butler and P.J. O'Rourke. A numerical method for two-dimensional unsteady reacting flows. In *Sixteenth Symposium (International) on Combustion*, pages 1503–1515. The Combustion Institute, 1977.

[12] Tchen Chan-Mou. Mean value and correlation problems connected with the motion of small particles supended in a turbulent fluid, 1947.

[13] S. Chapman and T.G. Cowling. *The Mathematical Theory of Non-Uniform Gases*. Cambridge University Press, cambridge mathematical library edition, 1939 (digital reprint 1999).

[14] P. Chassaing. *Turbulence en mécanique des fluides*. Cépaduès éditions, collections polytech edition, 2000.

[15] C. H. Chiang and W.A. Sirignano. Interacting,convecting, vaporizing fuel droplets with variable properties. *Int. Journal Heat Mass Transfer*, 36,Nr 4:875–886, 1993.

[16] O. Colin, F. Ducros, D. Veynante, and T. Poinsot. A thickened flame model for large eddy simulations of turbulent premixed combustion. *Physics of Fluids*, 12(7):1843–1863, 2000.

[17] O. Colin, F. Ducros, D. Veynante, and T. Poinsot. A thickened flame model for les of turbulent premixed combustion. *Physics of Fluids*, 12(7):1843–1863, 2000.

[18] Rafik Ben Dakhlia. Combustion stationaire et instationaire de mélanges diphasiques, 2001.

[19] N. Darabiha, F. Lacas, J.C. Rolon, and S. Candel. Laminar counterflow spray diffusion flames: A comparison between experimental results and complex chemistry calculations. *Combustion and Flame*, 95:261–275, 1993.

[20] S.R. de Groot and P. Mazur. *Non-Equilibrium Thermodynamics*. Dover, 1984.

[21] Paul J. Dellar. Bulk and shear viscosities in lattice boltzmann equations. *Phys. Rev. E*, 64.031203, 2001.

[22] E. Deutsch. Dispersion de particules dans une turbulence homogen isotrope stationaire calculee par simulation numerique directe des grandes echelles, 1992.

[23] E. Deutsch and O. Simonin. Large eddy simulation applied to the motion of particles in stationary homogeneous fluid turbulence. *Turbulence Modification in Multiphase Flow*, 110:35–42, 1991.

[24] Donald A. Drew and Stephen L. Passman. *Theory of Multicomponent Fluids*. Springer, springer applied mathematical sciences 135 edition, 1999.

[25] O.A. Druzhini and S. Elghobashi. Direct numerical simulations of bubble-laden turbulent flows using the two-fluid formulation. *Physics of Fluids*, 10(3):685–697, 1998.

[26] O.A. Druzhini and S. Elghobashi. On the decay rate of isotropic turbulence laden with microparticles. *Physics of Fluids*, 11(3):602–610, 1999.

[27] S. Elghobashi and G.C. Truesdell. Direct simulation of particle dispersion in a decaying isotropic turbulence. *Journal of Fluid Dynamics*, 242:655–700, 1992.

[28] S. Elghobashi and G.C. Truesdell. On the two-way interaction between homogeneous turbulence and dispersed solid particles. i: Turbulence modification. *Physics of Fluids A*, 5(7):1790–1801, 1993.

[29] G. Erlebacher, M.Y.Hussaini, and C.G. Speziale T.A. Zang. Torward the large eddy simulation of compressible turbulent flows. *Icase*, 90-76:1–43, 1990.

[30] Fabre and Legendre. Diphasique. Cours d'options, Ecole Nationale Superieure d'Electrotechnique, d'Electronique, d'Informatique, d'Hydraulique et des Télécommunications., 2002.

[31] P. Fevrier and O. Simonin. Statistical and continuum modelling of turbulent reactive particulate flows. Lecture Series 2000-06, von Karman Institute for Fluid Dynamics, 2000.

[32] Pierre Fevrier. Etude numerique des effets de concentration preferentielle et de correlation spatiale entre vitesses des particules solides en turbulence homogene isotrope stationaire, 2000.

[33] J.C.H. Fung, J.C.R. Hunt, N.A. Malik, and R.J. Perkins. Kinetmatic simulation of homogeneous turbulence by unsteady random fourier modes. *Journal of Fluid Mechanics*, 236:281–318, 1992.

[34] T.B. Gatski and C.G. Speziale. On explicit algebraic stress models for complex turbulent flows. *Journal of Fluid Mechanics*, 254:59–78, 1991.

[35] M. Germano. Turbulence: the filtering approach. *Journal of Fluid Mechanics*, 238:325–336, 1992.

[36] J. Glimm, D. Saltz, and D.H. Sharp. *Nonlinear Partial Differential Equations*, chapter Two-Pressure Two-Phase Flow. 1998.

[37] Harold Grad. On the kinetic theory of rarified gases. *Communications on Pure and Applied Mathematics*, 2,Nr.4:331–407, 1949.

[38] W.G. Gray and P.C.Y. Lee. On the theorems for local volume averaging of multiphase systems. *International Journal of Multiphase Flow*, 3:333–340, 1977.

[39] E. Gutheil. *Modellierung technischer Sprayflammen*. Fortschritt-Berichte VDI, reihe 6 energietechnik nr.390 edition, 1998.

[40] S. Hayashi and S. Kumagai. Flame propagation in fuel droplet-vapor-air mixtures. In *Fifteenth (International) Symposium on Combustion*, pages 445–452. The Combustion Institute, 1975.

[41] J. He and O. Simonin. Modélisation numérique des ecoulements turbulents gaz-solides en conduite verticale. Technical Report HE 44/94/021A, EDF, Septembre 1994.

[42] Charles Hecht. *Thermodynamics and Kinetic Theory*. Dover Publications, 1990.

[43] Jerome Helie. Private communication. 2003.

[44] J.O. Hinze. *Turbulence*. McGraw-Hill, mcgraw-hill classic textbook reissue edition, 1987.

[45] Hirschfelder, Curtis, and Bird. *Molecular Theory of Gases and Liquids*. John Wiley & Sons, 1954 edition, 1954.

[46] F. A. Howes and St. Whitaker. The spatial averaging theorem revisted. *Chemical Engineering Science*, 40,No.8:1387–1392, 1985.

[47] G.L. Hubbard, V.E. Denny, and A.F. Mills. Droplet evaporation: effects of transient and variable properties. *International Journal of Heat and Mass Transfer*, 18:1003–1008, 1975.

[48] J.C.R. Hunt, J.C. Buell, and A.A. Wray. Big whorls carry little whorls. In *Proceedings of the Summer Program 1987, Center for Turbulence Research Stanford,Ca*, pages 77–94, 1987.

[49] A. Kaufmann, O. Simonin, T. Poinsot, and J. Helie. Dynamics and dispersion in eulerian-eulerian dns of two-phase flows. In *Proceedings of the Summer Program 2002, Studying Turbulence Using Numerical Simulation Databases IX, Center for Turbulence Research Stanford,Ca*, pages 381–392, 2002.

[50] M. Kohler. Reibung in mäßig verdünten Gasen als Folge verögerter Einstellung der Energie. *Zeitschrift für Physik*, 125:715–732, 1949.

[51] R.H. Kraichnan. An alomost markovian galilean-invariant turbulence model. *Journal of Fluid Mechanics*, 47:513, 1971.

[52] J. Laviéville. Simulations numeriques et modelisation des interactions entre l'entrainement par la turbulence et les collisions interparticulaires en ecoulements gaz-solides, 1997.

[53] S. K. Lele. Compact finite difference schemes with spectral-like resolution. *Journal of Computational Physics*, 103:16–42, 1992.

[54] Randall J. LeVeque. *Numerical Methods for Conservation Laws*. Birkäuser Verlag, 1992.

[55] T.H. Lin, C.K.Law, and S.H. Chung. Theory of laminar flame propagation in off stochiometric dilute sprays. *International Journal Heat Mass Transfer*, 31(5):1023–1034, 1988.

[56] T.H. Lin and Y.Y. Sheu. Theory of flame propagation in near-stochiometric dilute sprays. *Combustion and Flame*, 84:333–342, 1991.

[57] Lumley. *A first course in Turbulence*. MIT Press, 1972.

[58] J. Magnaudet, M. Rivero, and M. Fabre. Accelerated flows past a solid sphere or a spherical bubble. part 1. steady straining flow. *Journal of Fluid Mechanics*, 284:97–135, 1995.

[59] K. Mahesh, G. Consantinescu, S. Apte, G. Iaccarino, and P. Moin. Large eddy simulation of gas turbine combustors. *Center for Turbulence Research, Annual Research Briefs*, pages 1–15, 2001.

[60] Alexandre Massol. Simulations numeriques d'ecoulements a travers des reseaux fixes de spheres monodisperses et bidisperses, pour des nombres de reynolds moderes, 2003.

[61] Martin R. Maxey. The gravitational settling of aerosol particles in homogeneous turbulence and random flow fields. *Journal of Fluid Mechanics*, 174:441–465, 1987.

[62] R. S. Miller and J.Bellan. Direct numerical simulation of a confined three-dimensional gas mixing layer with one evaporating hydrocarbon-droplet-laden stream. *Journal of Fluid Mechanics*, 384:293–338, 1999.

[63] R.S. Miller, K. Harstad, and J. Bellan. Evaluation of equilibrium and non equilibrium evaporation models for many-droplet gas-liquid flow simulations. *International Journal of Multiphase Flow*, 24:1025–1055, 1998.

[64] J.P. Minier and E. Peirano. The pdf apporach to turbulent polydispersed two-phase flows. *Physics Reports*, 352:1–214, 2001.

[65] P. Moin, K. Squires, W. Cabot, and S. Lee. A dynamic subgrid-scale model for compressible turbulence and scalar transport. *Physics of Fluids*, A 3(11):2746–2757, 1991.

[66] Parviz Moin and Krishnan Mahesh. Direct numerical simulation: A tool in turbulence research. *Annual Review of Fluid Mechanics*, 30:539–578, 1998.

[67] A. S. Monin and A. M. Yaglom. *STATISTICAL FLUID MECHANICS: Mechanics of Turbulence*. MIT Press, Cambridge Ma, 1987.

[68] Christophe Morel. Modelisation multidimensionnelle des écoulements diphasique gaz-liquide. application à la simulation des écoulements 'a bulles ascendants en conduite verticale., 1997.

[69] Bertrand Naud. Pdf modeling of turbulent sprays and flames using a particle stochastic approach, 2003.

[70] F. Nicoud and F. Ducros. Subgrid-scale stress modelling based on the square of the velocity gradient tensor. *Flow, Turbulence and Combustion*, 62(3):183–200, 1999.

[71] R. Paoli, J. Helie, T. Poinsot, and S. Ghosal. Contrail formation in aircraft wakes using large eddy simulation. In *Proceedings of the Summer Program 2002, Studying Turbulence Using Numerical Simulation Databases IX, Center for Turbulence Research Stanford,Ca*, pages 229–241, 2002.

[72] T. Passot and A. Pouquet. Numerical simulation of compressible homogeneous flow in the turbulent regime. *Journal of Fluid Mechanics*, 181:441–466, 1987.

[73] Norbert Peters. *Turbulent Combustion*. Cambridge University Press, 2000 edition, 2000.

[74] U. Piomelli. Large-eddy simulation: achievements and challenges. *Progress in Aeorspace Sciences*, 35:335–362, 1999.

[75] T. Poinsot and D. Veynante. *Theoretical and Numerical Combustion*. Edwards, 2001 edition, 2001.

[76] S.B. Pope. A more general effective-viscosity hypothesis. *Journal of Fluid Mechanics*, 72(2):331–340, 1975.

[77] S.B. Pope. Stochastic lagrangian models of velocity in homogeneous turbulent shear flow. *Physics of Fluids*, 14(5):1696–1702, 2002.

[78] Stephen B. Pope. *Turbulent Flows*. Cambridge University Press, cambridge edition, 2000.

[79] M.W. Reeks. On a kinetic equation fo the transport of particles in turbulent flows. *Physics of Fluids A*, 3(3):446–456, 1991.

[80] M.W. Reeks. On the constitutive relations for dispersed particles in nonuniform flows 1: Dispersion relations in a simple shear flow. *Physics of Fluids A*, 5(3):750–761, 1993.

[81] E. Riber. Modélisation et calcul de jets diphasiques. Rapport de DEA WN/CFD/03/74, CERFACS, August 2003.

[82] E. Riber. Rapport de fin d' études - PFE. Technical Report WN/CFD/03/72, CERFACS, June 2003.

[83] F.W. Roos and W.W. Wilmarth. Some experimental results on sphere and disk drag. *AIAA Journal*, 9:285–291, 1971.

[84] Pierre Sagaut. *Introduction á la simulation des grandes échelles*. Springer, mathematiques & applications edition, 1998.

[85] C. Saulnier. Analyse thérique et simulation numérique d'une flamme monodimensionelle. DEA report WN/CFD/02/64, CERFACS, Juin 2000.

[86] R. Saurel and R. Abgrall. A multiphase godunov method for compressible multifluid and multiphase flow. *Journal of Computational Physics*, 150:425–467, 1999.

[87] L. Schiller and A. Nauman. A drag coefficient correlation. *VDI Zeitung*, 77:318–320, 1935.

[88] T. Schönfeld and M. Rudgyard. Steady and unsteady flows simulations using the hybrid flow solver avbp. *AIAA Journal*, 37(11):1378–1385, 1999.

[89] U. Schumann. Subgrid scale model for finite difference simulations of turbulen flows in plane channels and annuli. *Journal of Computational Physics*, 18:376–404, 1975.

[90] W.T. Sha, B.T. Chao, and S.L. Soo. Time and volume-averaged conservation equations for multiphase flow. In *Second Int. Symp. Multiphase Flow and Heat Transfer*, pages 1028–1046, 1989.

[91] O. Simonin. Combustion and turbulence in two phase flows. Lecture Series 1996-02, von Karman Institute for Fluid Dynamics, 1996.

[92] O. Simonin, P. Fevriér, and J. Laviéville. On the spatial distribution of heavy particle velocities in turbulent flow: from continous field to particulate choas. *Journal of Turbulence*, 3:040, 2002.

[93] Olivier Simonin. Gas particules. Cours d'options, Ecole Nationale Superieure d'Electrotechnique, d'Electronique, d'Informatique, d'Hydraulique et des Télécommunications., 2002.

[94] W. A. Sirignano. Fuel droplet vaporisation and spray combustion theory. *Progress Energy Combustion Science*, 9:291–322, 1983.

[95] W. A. Sirignano. *Fluid Dynamics and Transport of Droplets and Sprays*. Cambridge University Press, 1999.

[96] J. Smagorinsky. General circulation experiments with the primitive equations. i: The basic experiment. *Monthly Weather Review*, 91(3):99–165, 1963.

[97] W.H. Snyder and J.L. Lumley. Some measurements of particle velocity autocorrelation functions in a turbulent flow. *Journal of Fluid Mechanics*, 48, part 1:41–71, 1970.

[98] Arnold Sommerfeld. *Vorlesungen über theoretische Physik: Band 5 Thermodynamik und Statistik*. Verlag Harri Deutsch, 1988.

[99] Charles G. Speziale. On nonlinear $k - l$ and $k - \varepsilon$ models of turbulence. *Journal of Fluid Mechanics*, 178:459–475, 1987.

[100] K.D. Squires and J.K. Eaton. Lagrangian and eulerian statistics obtained from direct numerical simulations of homogeneous turbulence. *Physics of Fluids A*, 3(1):130–143, 1991.

[101] Kyle D. Squires and John K. Eaton. Particle response and turbulence modification in isotropic turbulence. *Physics of Fluids A*, 2(7):1191–1203, 1990.

[102] Kyle D. Squires and John K. Eaton. Measurements of particle dispersion obtained from direct numerical simulations of isotropic turbulence. *Journal of Fluid Mechanics*, 226:1–35, 1991.

[103] Kyle D. Squires and John K. Eaton. Preferential concentration of particles by turbulence. *Physics of Fluids A*, 3(5):1169–1178, 1991.

[104] G. G. Stokes. On the effect of the internal friction of fluids on the motions of pendulums. *Trans. Cambridge Phil. Soc.*, 9:8–23, 1851.

[105] S. Sundram and L.R. Collins. A numerical study of the modulation of isotropic turbulence by suspended particles. *Journal of Fluid Mechanics*, 379:105–143, 1999.

[106] Dale B. Taulbee. An improved algebraic reynolds stress model and corresponding nonlinear stress model. *Physics of Fluids*, A 4 (11):2555–2561, 1992.

[107] C. Truesdell. The mechanical foundations of elasticity and fluid dynamics. *Journal of Rational Mechanics and Analysis*, 1:152–300, 1952.

[108] Philippe Versaevel. Combustion laminaire diphasique: Etude théorique et experimentale, 1996.

[109] D. Veynante and T. Poinsot. Large eddy simulation of combustion instabilities in turbulent premixed burners. *Center of Turbulence Research, Annula Research Briefs 1997*, pages 253–274, 1997.

[110] P.L. Viollet and O. Simonin. Introduction a la modelisation des ecoulements d une phase continue contenant des inclusions dispersees en mouvement. Technical report, Ecole Nationale des Ponts et Chaussées, Janivier 1993. Aérodynamique de la combustion.

[111] C. Vit, I. Flour, and O. Simonin. Modelling of a confined bluff body flow laden with polydispersed particles. In *Two-Phase Flow Modelling and Experimentation 1999*, pages 1877–1884. Edizioni ETS, 1999.

[112] Lian-Ping Wang and Martin R. Maxey. Settling velocity and concentration distribution of heavy particles in homogeneous isotropic turbulence. *Journal of Fluid Mechanics*, 256:27–68, 1993.

[113] W.G.Gray and P.C.Y. Lee. On the theorems for local volume averaging of multiphase systems. *International Journal Multiphase Flow*, 3:333–340, 1977.

[114] St. Whitaker. A simple geometrical derivation of the spatial averaging theorem. *Chemical Engeneering Education*, Winter 1985:18–52, 1985.

[115] Stephen Whitaker. *The method of Volume Averaging*. Kluwer Academic Publishers, theory and applications of transport in porous media edition, 1999.

[116] Forman A. Williams. *Combustion Theory, The Fundamental Theory of Chemically Reacting Flow Systems*. Addison-Wesley, second edition edition, 1985.

[117] P.K. Yeung and Pope S.B. An algorithm for tracking fluid particles in numerical simulations of homogeneous turbulence. *Journal of Computational Physics*, 79:373–416, 1988.

[118] Akira Yoshizawa. Simplified statistical approach to complex turbulent flows and ensemble-mean compressible turbulence modeling. *Physics of Fluids*, 7(12):3105–3117, 1995.

[119] M.I. Yudine. Physical considerations on heavy-particle dispersion. *Adv. Geophys.*, 6:185–191, 1959.

[120] Kenneth Kuan yun Kuo. *Principles of Combustion*. John-Wiley & Sons, paperback edition, 1986.

Index